Organometallic Routes to Colloidal Zinc Oxide Nanoparticles and Layered Zinc Hydroxides

Alice Hei Man Leung

Department of Inorganic Chemistry

St Edmund Hall

University of Oxford

July 2018

Thesis submitted in partial fulfilment of the requirement for the degree of Doctor of Philosophy in Inorganic Chemistry

For my parents and family

Declaration

The work described in this thesis was conducted in University of Oxford and Imperial College London, and written by the author unless otherwise stated.

Abstract

The thesis focuses on the controlled hydrolysis of organozinc precursors to form colloidal, surface-functionalised, ZnO nanoparticles (2–4 nm) and exfoliated nanosheets of layered zinc hydroxides (3 nm thick), with a primary application in the catalytic hydrogenation of CO_2 to methanol.

An introduction to the topic and a literature review are provided in Chapter 1. Chapter 2 entails a description of characterisation techniques.

Chapter 3 presents the synthesis of layered zinc hydroxides, intercalated with a range of carboxylates (acetate, hexanoate, decanoate, oleate and benzoate). Exfoliation of layered zinc hydroxide into monolayers was achieved by stirring the material intercalated with oleate ligand, in toluene, for 2 h. The dimensions of the nanostructures are 3 nm thick × ~ 26 nm (AFM and TEM). In addition, a nanoporous ZnO film (1 μm thick) was formed after annealing a film of solution-deposited material at 500 °C, for 15 mins.

Chapter 4 details the synthesis of ZnO nanoparticles (< 3 nm) by hydrolysis of diethylzinc, with di(octadecyl)phosphinate (5 : 1 Zn/ligand loading) . The use of such ligand halts the solid-state ripening of the nanoparticles. The ZnO nanoparticles, combined with Cu(0) or Cu_2O nanoparticles, demonstrate catalytic activity for the hydrogenation of CO_2 to methanol, using a liquid-phase continuous flow stirred tank reactor (mesitylene, 210 °C, 50 bar, 3:1 molar ratio of H_2:CO_2, 150 mL min^{-1} flow). The colloidal Cu/ZnO nanocatalysts exhibit 2-3 times higher rates when compared to the standard commercial heterogeneous Cu-ZnO-Al_2O_3 catalyst (~20 vs. 7 $mmol_{MeOH}\ g_{CuZnO}^{-1}\ h^{-1}$). The use of either Cu(0) or Cu_2O nanoparticles results in the

same catalytic activity and selectivity, but the use of smaller ZnO nanoparticles results in slightly higher activity. Post-catalysis analysis shows an increase in the oxidative stability of Cu(0) nanoparticles. One explanation may be the migration, under catalytic conditions, of ZnO onto Cu(0) nanoparticles that generates a protective layer against oxidation.

Chapter 5 describes the substitutional doping of ZnO nanoparticles, with 5 mol% of Mg(II), Al(III) and Cu(I). Characterisation of electronic properties (UV-Vis, Tauc plot), solid-state structure (XRD) and composition (ICP-OES, XPS) confirms the substitutional doping in all cases. Under the same catalysis conditions outlined in Chapter 4, all the nanocatalysts display higher activity and better stability than the commercial heterogeneous catalyst. Nonetheless, when compared to ZnO, Mg-doping reduces activity, whilst Al-doping increases activity (600 vs. 1020 μmol $mmol_{metal}^{-1}$ h^{-1}).

Chapter 6 summarises the findings from Chapter 3, 4 and 5, followed by the outlook of these chapters. Finally, the experimental methods are presented in Chapter 7.

Acknowledgements

Firstly, I would like to thank my two supervisors, Prof. Charlotte Williams and Prof. Milo Shaffer (Imperial College London). I am grateful they have given me the opportunity to carry out my PhD under their supervision. Their constant support, passion for science and an endless depth of knowledge have driven me to where I am today and without them, the work presented in this thesis would not have been possible, nor as successful and enjoyable.

Throughout my PhD journey, I have received a tremendous amount of support, patience and encouragement from the three PDRAs in the "Methanol Team". Dr Sebastian Pike, Dr Andrés García Trenco and Dr Edward White have made great contributions to the methanol project, where some of their work is featured in this thesis. Not only were they great mentors, they have been good friends which I can have a chat/laugh with, over a pint, at the pub. Special thanks to the methanol reactor (an often forgotten member) for producing methanol over the past 4 years.

There are many people, in both Imperial College London and University of Oxford, which I would like to mention. Special thanks go to Dr Anna Regoutz (XPS), Richard Sweeney (XRD), Pete Haycock (NMR) and Victoria Bemmer, at Imperial College London, for their hard work and support in carrying out some of the characterisations and experiments. Also, thanks to Nick Rees (solid-state NMR) for helping out with some additional characterisation that was carried out in University of Oxford.

To both Williams and Shaffer groups, you all have provided endless entertainment and fun throughout my PhD and thanks for sticking by me. A special

thank you to all the following people: Arron, Tom, Charlie, Ni, Arnaud, Tim, Leti, Sumesh, Georgina, Greg, Gemma, Chris, Duncan, Peck and Giulia. The "Magnificent Seven" PDRA team when I first started my PhD, thanks for your incredible knowledge and support: Dr Andrés García Trenco, Dr Sebastian Pike, Dr Charles Romain, Dr Jennifer Garden, Dr Junjuda Unruangsri, Dr Prabhjot Saini and Dr Anish Cyriac. Some members of Shaffer group should also be mentioned: Dr Adam Clancy, Dr Hin Chun Yau and Dr Wonjun Lee, thanks for helping me to understand materials chemistry.

I have endless gratitude for all my London & Oxford housemates, friends and lastly, my badminton teams (ICSM & OUBaC). They have all done an excellent job at keeping me sane. A massive thank you and love go to 57 Ongar Road crew: Christian, Medic (Hannah), Christine, James, Emily, Ed, Martin and Sam Brown. They are the definition of 'true friends' and I know I can always rely on them, #OngarForever.

I would like to thank Cherlyn, for her love and support. Your unending faith in my abilities have tremendously helped me through the last stage of DPhil, *i.e.* this thesis. You have made Oxford an extra special place for me and I can certainly say I do not regret moving to this city.

Finally, I cannot thank my family enough for their love and support throughout my whole life. My parents are the most incredible people I know. They have sacrificed so much for me and my brother to get us to where we are today, and I am forever in their debt. I hope I can continue to make you both proud.

Publications

Work in this thesis has resulted in, or will result in, the following publications:

Colloidal Cu/ZnO catalysts for the hydrogenation of carbon dioxide to methanol: investigating catalyst preparation and ligand effects

S. D. Pike, A. García-Trenco, E. R. White, A. H. M. Leung, J. Weiner, M. S. P. Shaffer and C. K. Williams, *Catal. Sci. Technol.*, **2017**, 7, 3842-3850.

Layered zinc hydroxide monolayers by hydrolysis of organozincs

A. H. M. Leung, S. D. Pike, A. J. Clancy, H. C. Yau, W. J. Lee, K. L. Orchard, M. S. P. Shaffer and C. K. Williams, *Chem. Sci.*, **2018**, 9, 2135-2146.

Doping of colloidal ZnO nanoparticles: Preparation of Cu/M:ZnO (M = Mg, Al, Cu) nanocatalysts for the hydrogenation of carbon dioxide to methanol

A. H. M. Leung, A. García-Trenco, A. Regoutz, M. Schuster, S. D. Pike, M. S. P. Shaffer and C. K. Williams. *In preparation*.

The role of ZnO on colloidal Cu/ZnO catalysts for the hydrogenation of CO_2 to methanol

A. García-Trenco, A. H. M. Leung, M. Hart, E. R. White, M. S. P. Shaffer and C. K. Williams. *In preparation*.

Table of Contents

Chapter 2: Characterisation Techniques

Chapter 3: Layered Zinc Hydroxide Monolayers by Hydrolysis of Organozincs

Chapter 4: Hydrogenation of CO_2 to Methanol using Colloidal Cu/ZnO Nanocatalysts

Chapter 5: Colloidal M:ZnO Nanoparticles (M = Mg, Al, Cu) in Hydrogenation of CO_2 to Methanol

Chapter 6: Summary & Outlook

Chapter 7: Experimental

Appendix

List of Abbreviations

δ	*Chemical Shift (ppm)*
ε	*Dielectric Constant*
acac	*Acetylacetonate*
AFM	*Atomic Force Microscopy*
$AlEt_3$	*Triethylaluminium*
Al_2O_3	*Alumina*
atm	*Atmospheres (pressure)*
C_{crit}	*Critical Concentration of Solute*
C_S	*Supersaturation of Solute*
CdSe	*Cadmium Selenide*
CL	*Cathodoluminescence*
CO_3	*Carbonate anion*
CSTR	*Continuous Flow Stirred Tank Reactor*
Cu(0)	*Metallic Copper*
Cu_2O	*Copper(I) Oxide*
CuMes	*Mesitylcopper (I)*
DFT	*Density Functional Theory*
DODPA–H	*Di(octadecyl)phosphinic acid*
DODPA	*Di(octadecyl)phosphinate*
DOPA–H	*Dioctylphosphinic acid*
DOPA	*Dioctylphosphinate*
DS	*Dodecylsulphate*
DSSCs	*Dye-sensitised Solar Cells*

DTA	*Differential Thermal Analysis*
EA	*Elemental Analysis*
EDX	*Energy Dispersive X-ray*
EELS	*Electron Energy Loss Spectroscopy*
Equiv.	*Equivalents*
EXAFS	*Extended X-ray Absorption Fine Structure*
FEG	*Field Emission Gun*
FEI	*Field Emission Ionisation*
FFT	*Fast Fourier Transform*
FT-IR	*Fourier Transform Infrared*
FWHM	*Full Width Half Maximum*
HAADF	*High Angle Annular Dark Field*
HOMO	*Highest Occupied Molecular Orbital*
I	*Spin Number*
Jsc	*Short-circuit Current*
HR-TEM	*High Resolution Transmission Electron Microscopy*
ICP-OES	*Inductively Coupled Plasma Optical Emission Spectrometry*
In_2O_3	*Indium(III) Oxide*
IR	*Infrared*
ITO	*Indium Tin Oxide*
LDH	*Layered Double Hydroxides*
LUMO	*Lowest Unoccupied Molecular Orbital*
LZH	*Layered Zinc Hydroxide*
MAS-NMR	*Magic Angle Spinning Nuclear Magnetic Resonance*

Mg(^{n}Bu)(^{s}Bu)	*n-butyl-sec-butylmagnesium*
MODPA–H	*Mono(octadecyl)phosphinic acid*
mol%	*Molar percentage*
NMR	*Nuclear Magnetic Resonance*
OA	*Oriented Attachment*
OR	*Ostwald Ripening*
OAc	*Acetate*
OBz	*Benzoate*
ODec	*Decanoate*
OHex	*Hexanoate*
Ole	*Oleate*
PEG	*Polyethylene Glycol*
PL	*Photoluminescence*
r_{crit}	*Critical Radius of Crystals*
r_{ion}	*Ionic Radius*
SAXS	*Small Angle X-ray Scattering*
SEM	*Scanning Electron Microscopy*
SMSI	*Strong Metal Support Interaction*
SnO_2	*Tin (IV) Oxide*
SSP	*Single Source Precursor*
STEM	*Scanning Transmission Electron Microscopy*
St	*Stearate*
TEM	*Transmission Electron Microscopy*
TGA	*Thermogravimetric Analysis*

TGA-MS	*Thermogravimetric Analysis coupled with Mass Spectrometry*
THF	*Tetrahydrofuran*
TOS	*Time-on-stream*
TPR	*Temperature-programmed Reduction*
V_O	*Oxygen Vacancies (in ZnO)*
V_{OC}	*Open-circuit Voltage*
wt%	*Percent by weight*
XANES	*X-ray Absorption Near Edge Structure*
XPS	*X-ray Photoelectron Spectroscopy*
XRD	*Powder X-ray Diffraction*
$ZnCy_2$	*Dicyclohexylzinc*
$ZnEt_2$	*Diethylzinc*
$ZnPh_2$	*Diphenylzinc*
Zn_i	*Interstitial Zinc (in ZnO)*
ZnO	*Zinc Oxide*
ZnS	*Zinc Sulphide*
ZnSe	*Zinc Selenide*

List of figures

Chapter 1

Chapter 2

Chapter 3

Chapter 4

Chapter 5

List of schemes

Chapter 3

Chapter 4

Chapter 5

Chapter 7

List of tables

Chapter 1

Chapter 3

Chapter 4

Chapter 5

Chapter 1

Introduction

1.1 Introduction to Nanoparticles

Nanomaterials have been extensively explored in the recent decades, with a range of applications from their simple incorporation into composites and solar cells,[1, 2] to more complex systems like catalysis.[3, 4]

Interest in nanomaterials stem from their unique properties which bulk materials cannot access. Nanoparticles (diameters from 1–100 nm) have a high surface-area-to-volume ratio and as such are excellent candidates for surface catalysis. With decreasing particles size, the total surface area increases and hence nanocatalysts may show enhanced activity compared to an equivalent volume of a bulk solid.[5] In addition, more reactive facets, edges and corners may be preferentially exposed in nanoscale systems which can further increase the activity.[6] For example, the activation of methane, using Pt nanoparticles, showed that by changing from bulk Pt(111) facets to nanoscale Pt(111), the energy of C–H bond activation was lowered by ~70 kJ mol^{-1}.[7]

For nanoparticles of sizes < 10 nm, quantum confinement effects may also be relevant; these occur when the exciton Bohr radius is smaller than the particle's radius and the confined movement of electrons leads to quantisation of energy states (Figure 1.1).[6] In addition, quantum confinement causes an increased separation of energy levels and an increased bandgap (E_g). It is mainly beneficial for solar cells where a wide bandgap material (*e.g.* CdSe) is desired for the *n*-type conductor layer.[8]

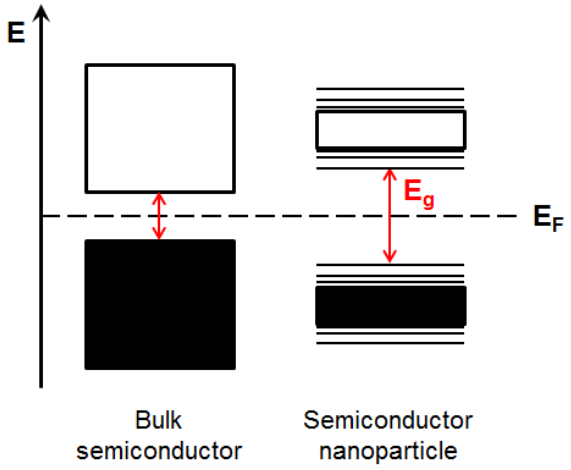

Figure 1.1. Diagram illustrating the increase in band gap (E_g) from bulk semiconductor to semiconductor nanoparticle. E_F is the fermi level.

In order to control the properties of nanoparticles, particle size uniformity must be controlled, with the nucleation and growth being the crucial steps. One mechanism for particle formation suggests that nucleation and growth occur by separate stages (Figure 1.2).[9] The mechanism is divided into three parts: (I) rapid increase in solute concentration, in solution, to reach a critical concentration, C_{crit}; (II) "burst nucleation" associated with the rapid decrease in solute concentration and (III) steady nucleation growth at supersaturation (C_S), under diffusion control of solutes. Consequently, all nanoparticles have a common growth history.[9, 10]

Classical nucleation theory provides a thermodynamic explanation for the nucleation step. If a stable particle critical size (r_{crit}) can be achieved, without dissolution, nucleation can occur (Equation 1.1):[10]

$$r_{crit} = \frac{-2\gamma}{\Delta G_v} = \frac{2\gamma v}{k_B T \ln(S)} \qquad (1.1)$$

γ is the surface free energy, ΔG_v is the crystal free energy, v is the molar volume, k_B is the Boltzmann's constant, T is temperature and S is the supersaturation of solution.

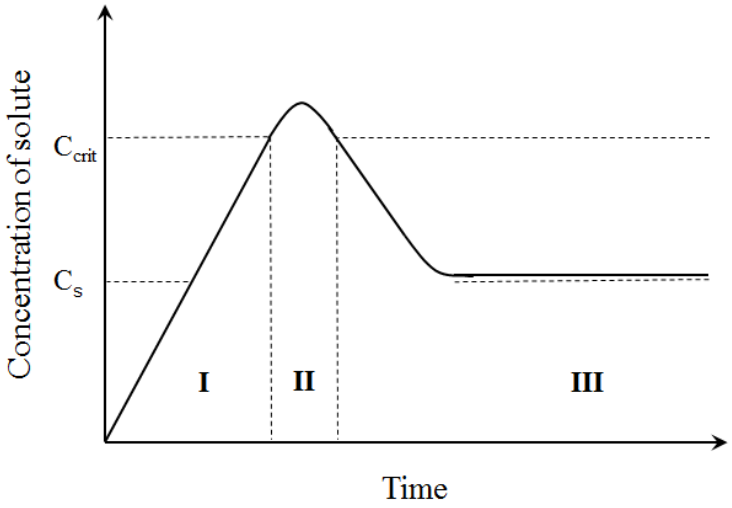

Figure 1.2. LaMer diagram, demonstrating the conditions required for the nucleation and growth of nanoparticles. *Figure reproduced with permission from La Mer et al.*[9] *Copyright 1950 American Chemical Society.*

The rate of nucleation of *N* particles, with respect to time (t), may be described by an Arrhenius type equation (Equation 1.2). It shows dependence on various experimental parameters, such as supersaturation concentration, temperature and surface free energy, with *A* as the pre-exponential factor:

$$\frac{dN}{dt} = A \exp\left(\frac{16\pi \gamma^3 v^2}{3k_B{}^3 T^3 (\ln S)^2}\right) \quad (1.2)$$

One aim of this thesis is to determine the synthetic parameters that control nanoparticle size, shape and surface chemistry/morphology. Another stage of nanoparticle formation is the growth of pre-formed particles; several mechanisms are proposed: Ostwald ripening (OR), digestive ripening, coalescence and oriented attachment (OA) of nanoparticles.[10]

Ostwald ripening, first proposed in 1900, is the growth of larger, more thermodynamically favoured particles at the expense of smaller particles.[11] Under dynamic equilibrium, the high surface energy of smaller particles causes the surface monomer layer to dissolve and re-deposit onto the surface of larger particles.[11] Digestive ripening occurs when smaller particles grow at the expense of larger particles, in the presence of a digesting agent.[12] For example, oleic acid has been used to "digest" trioctylphosphine oxide capped cobalt nanoparticles to form cobalt molecular cluster species, but the mechanism remains unclear.[13]

Coalescence involves the initial aggregation of separate particles, followed by particle growth *via* surface atom diffusion to minimise surface area.[14] Oriented attachment of nanoparticles is the same process as coalescence, but with growth on particular crystal facets (Figure 1.3).[15, 16] Coulombic and, potentially Van der Waal interactions, are proposed to be the driving force for the crystal planes of nanoparticles to align for OA to proceed. This process was observed in ZnO nanoparticles, using HR-TEM and lattice spacing analysis, with the polar (001) facets as the preferred planes for oriented attachment to occur.

One popular method to control nanoparticle nucleation and growth is to use a

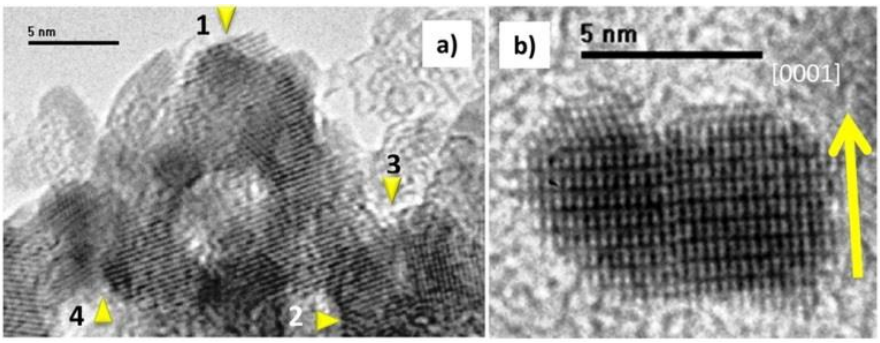

Figure 1.3. Oriented attachment occurring during the growth of ZnO nanoparticles (marked by yellow arrows). *Reprinted with permission from Melinon et al.[16] Copyright 2013 American Chemical Society.*

ligand in the nanoparticle synthesis.[13] In the nucleation stage, the ligand reduces the surface free energy of the resulting crystals and determines the supersaturation of solutes. The ligand stabilisation effects on solutes affect the rate at which supersaturation concentration can be reached. Hence, the more stabilised the solutes are, the quicker the supersaturation concentration is reached and therefore, "burst" nucleation can take place. By accelerating the rate of nucleation, the solute concentration depletes rapidly and the nanoparticles remain small due to the limited availability of solutes for growth. Furthermore, based on equation 1.1, the lower surface free energy provided by the ligand may favour the stabilisation of small nanoparticles.[17]

By modifying the synthetic parameters so as to control rates of nucleation and growth, nanoparticles properties can be tailored to a specific application. This thesis explores zinc oxide and layered zinc hydroxides nanomaterials prepared *via* the hydrolysis of organozinc reagents. The resulting ZnO nanoparticles are tested as catalysts for the catalytic hydrogenation of CO_2 to methanol.

In this chapter, the syntheses of ZnO nanoparticles will be reviewed, with a focus on the controlled hydrolysis of organometallic reagents. It will also provide an introduction to properties and uses of ZnO nanoparticles and layered zinc hydroxides (LZH), and strategies employed to make doped ZnO nanoparticles. An overview of methanol synthesis, using CO_2, and briefly syn-gas, will be provided. Finally, the overall aims of the thesis will be presented.

1.2 Zinc Oxide Nanoparticles

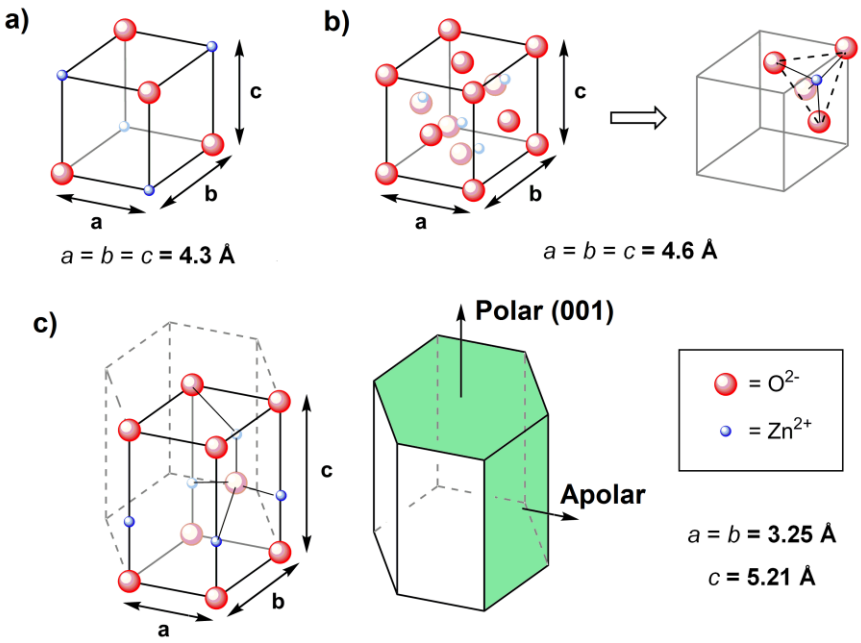

Figure 1.4. Unit cells of known crystal structure of ZnO: (a) cubic rock salt, (b) cubic zinc blend and (c) hexagonal Wurzite.

ZnO is a *n*-type semiconductor which has been extensively investigated for the past half a century.[18] Its wide bandgap (3.37 eV at 300 K), high exciton binding energy (60 meV) and easy access to high-quality bulk single crystals have led to a wide range of applications, including in optoelectronics, sensing and catalysis.[18-21] There are three known phases of ZnO: cubic zinc blend, cubic rock salt and hexagonal Wurzite. The Wurzite structure is the thermodynamically stable phase under ambient conditions (Figure 1.4). In this thesis, all reported ZnO nanoparticles have the Wurzite structure. Due to the presence of polar and apolar facets in Wurzite, it has led to the fabrication of anisotropic nanostructures, such as rings,[22] rods,[23] and pyramidal shapes.[24]

Bulk ZnO exhibits a visible green fluorescence due to surface defects: oxygen vacancies (V_O) and zinc interstitials (Zn_i).[18] Nanoscale ZnO displays enhanced

luminescence properties due to quantum confinement effects, making it attractive for applications such as quantum dots or as an electron transfer layer for quantum dot light-emitting diode (QLED).[25, 26] For example, by changing the size of ZnO nanoparticles (5.5 nm to 2.9 nm; determined by TEM), the electron mobility increases from 7.2 x 10^{-4} cm^2/V s to 4.8 x 10^{-3} cm^2/V s, with the resulting QLED displaying an external quantum efficiency of 4.2%.[27] The enhanced electronic properties of ZnO nanoparticles, combined with optical transparency, had led to its use in photovoltaic devices as *n*-type conductor. Nanoscale ZnO is also applied in dye-sensitized solar cells, as conductor and dye-absorbent layer (*see section 1.5.3*), or in bulk heterojunction solar cells.[28, 29] Furthermore, hybrid ZnO conjugated polymer composites showed good performance as the active layer. For example, a composite of ZnO nanoparticles (~5 nm) and a *p*-type π-conjugated polymer (poly[2-methoxy-5-(3',7'-dimethyloctyloxy)-1,4-phenylenevinylene]) was spin-coated onto indium tin oxide (ITO) to form a hybrid solar cell. It showed an external quantum efficiency of 40%, with a fill factor of 0.53, open-circuit voltage (V_{OC}) of 844 mV and short circuit current (J_{SC}) of 5.4 mA cm^{-2}.[30]

The semiconducting properties of ZnO nanoparticles are also useful in catalysis, such as methanol synthesis (discussed in detail in *section 1.4*) or photocatalysis. The photo-excitation of ZnO generates excitons (electron-hole pairs) that enable redox catalysis, for example the degradation of 4-chlorophenol.[31] ZnO nanoparticles of 35 nm in size (synthesised by the sol-gel method) displayed 70% degradation of 4-chlorophenol, over 5 h and under ambient light conditions. The photoactivity was attributed to the high surface area of ZnO nanoparticles, which readily allowed access for organic pollutant molecules, and bulk ZnO showed no photoactivity.[32]

1.3 Synthesis of Colloidal Nanoparticles

1.3.1 Existing Routes to ZnO

ZnO nanoparticles can be synthesised through several different routes: 1) mechanical, 2) thermolysis and 3) solution-based methods. Ball milling, a mechanical process, involves the grinding of crystalline precursor powders, such as $ZnCl_2$ and Na_2CO_3, using a heavy metal ball. The method generates pressure and heat, enabling the reaction between the two precursors to form $ZnCO_3$.[33] Subsequent calcination, at 400 °C, of $ZnCO_3$ leads to the formation of ZnO nanoparticles. A recent development, high energy ball milling, has also allowed the milling of bulk ZnO to nanoparticles of 30 nm in size.[34] The facile scale-up and low cost of operation of this route are both desirable, but it often generates large size distributions due to particle agglomeration. Furthermore, the lack of morphological control leads to particles with irregular morphologies.

The thermal degradation of organozinc oxo/hydroxide clusters is a facile route to generate ZnO nanoparticles.[35, 36] Upon heating of sub-nanoscale ZnO clusters, they would subsequently nucleate ZnO nanoparticles, with only volatile alkane byproducts produced (Figure 1.5).[37, 38] For example, the thermolysis of a hexameric *tert*-butylzinc hydroxide cluster, $[^tBuZn(\mu\text{-}OH)]_n$, led to the formation of nanocrystalline ZnO particles (3.4 nm, at 150 °C; Figure 1.6).[38] Despite its simplicity, sintering of ZnO nanoparticles was observed by *in-situ* variable temperature powder X-ray diffraction (XRD) and a particle size of 6.2 nm was only obtained when the temperature was increased up to 450 °C. In order to obtain a small, stable ZnO colloid, organic ligands should be present. For example, the decomposition of a zinc-silyl alkoxide cluster,

$[MeZnOSiMe_3]_4$, with added hexadecylamine occurred at 160 °C, and produced colloidal ZnO nanoparticles, capped with the amine, which were as small as 2–3 nm.[39]

Sol-gel syntheses are common solution-based synthetic routes to ZnO nanoparticles. This process involves the initial formation of a solution of oxygenated zinc species (sol). The solution then undergoes a series of hydrolysis, condensation and aggregation reactions resulting in the formation of a gel.[40] The formation of ZnO nanoparticles was achieved by heating zinc acetate dihydrate in ethanol (80 °C) followed by hydrolysis with lithium hydroxide.[41] The addition of ions and polar solvents (*e.g.* alcohols and water) to the synthesis aids control of nanoparticle morphology. The removal of solvent from the gel, at 100–200 °C, produces small ZnO nanoparticles (3 nm). Low size dispersity was proposed to be the result of templating by "magic-sized" zinc oxoacetate clusters.[42] These clusters are proposed to form prior to hydrolysis and to act as nuclei for subsequent nanoparticle growth.

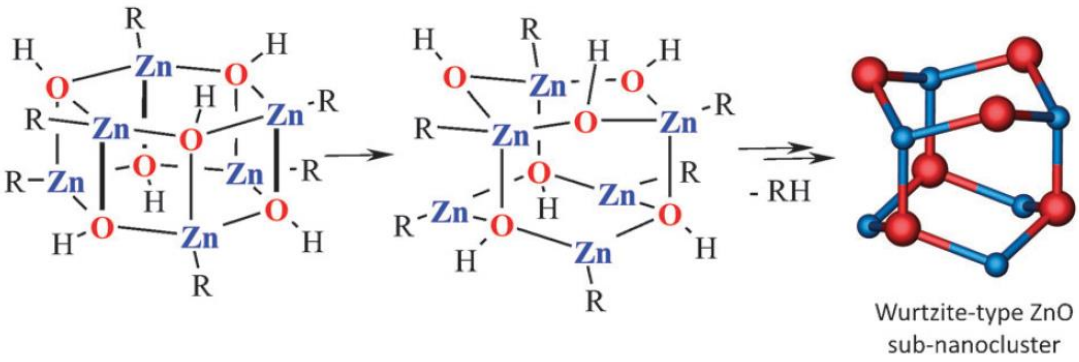

Figure 1.5. Scheme showing the resemblance between zinc hydroxide cluster and Wurzite ZnO sub-nanoclusters. Through thermolysis, the sub-nanoclusters are formed, with the generation of volatile alkane (RH). *Reprinted with permission Lewinski et al.[38] Copyright 2011 Royal Society of Chemistry.*

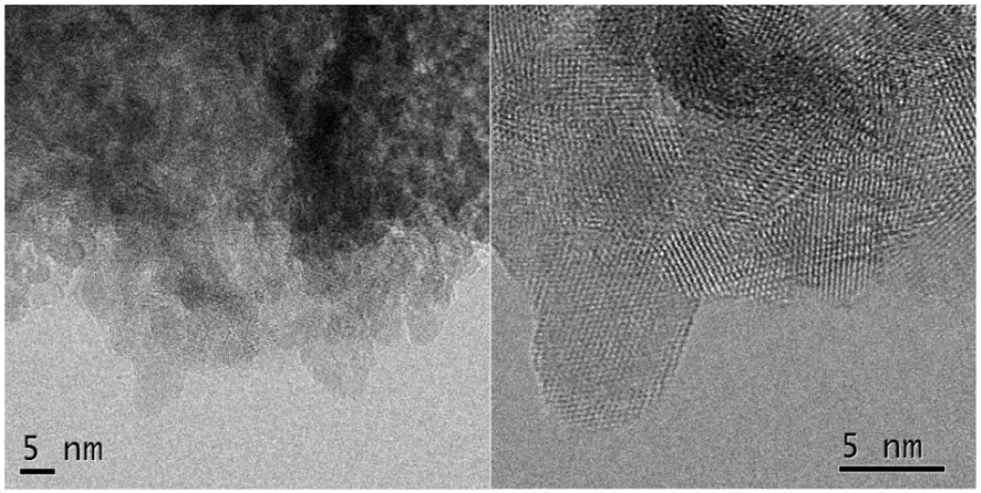

Figure 1.6. HR-TEM images of ZnO nanoparticles obtained from the thermolysis of $[^{t}BuZn(\mu\text{-}OH)]_n$ at 150 °C. *Reprinted with permission from Lewinski et al.[38] Copyright 2011 Royal Society of Chemistry.*

1.3.2 Controlled Hydrolysis of Organometallics to ZnO Nanoparticles

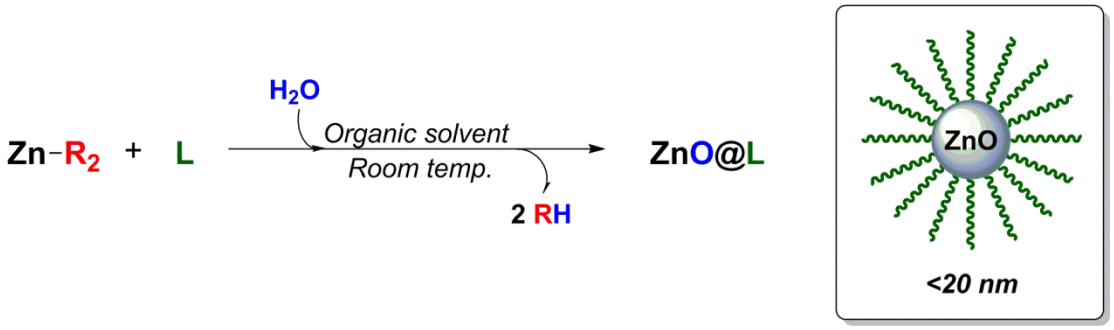

Figure 1.7. General scheme of organozinc hydrolysis to synthesise colloidal ZnO nanoparticles, capped with ligands (L).

An alternative route involves the controlled hydrolysis of organozinc precursors to produce ZnO nanoparticles (Figure 1.7).[43-45] This method mitigates the need for high temperatures which may result in sintering of the nanoparticles. The high reactivity towards water/protic compounds of the Zn–C bond allows for rapid hydrolysis to form Zn–OH bonds, which then undergo a series of condensation reactions to form zinc oxide.[46, 47] Another advantage is the formation of volatile byproducts (*e.g.* alkanes) which are easily removed, simplifying the particle purification process.[48, 49] A range of precursors, from simple dialkylzincs to the more complex zinc-alkyl clusters, have been explored to form colloidal ZnO nanoparticles (Figure 1.8).[50-52]

The first example was the reaction of $ZnEt_2$, with isopropanol and water (complex **1**, Figure 1.8).[53] The mechanism was proposed to proceed *via* the initial formation of ethylzinc hydroxide, [EtZnOH], which then acted as a nucleating agent for ZnO. The proposed nucleation from [EtZnOH] was suggested, on the basis of IR spectroscopy, where the disappearance of the Zn–OH signal was observed as the reaction progressed. Further studies on the hydrolysis of methylzinc *tert*-butoxide cubane, $[MeZn(O^tBu)]_4$, showed the formation of a methylzinc intermediate,

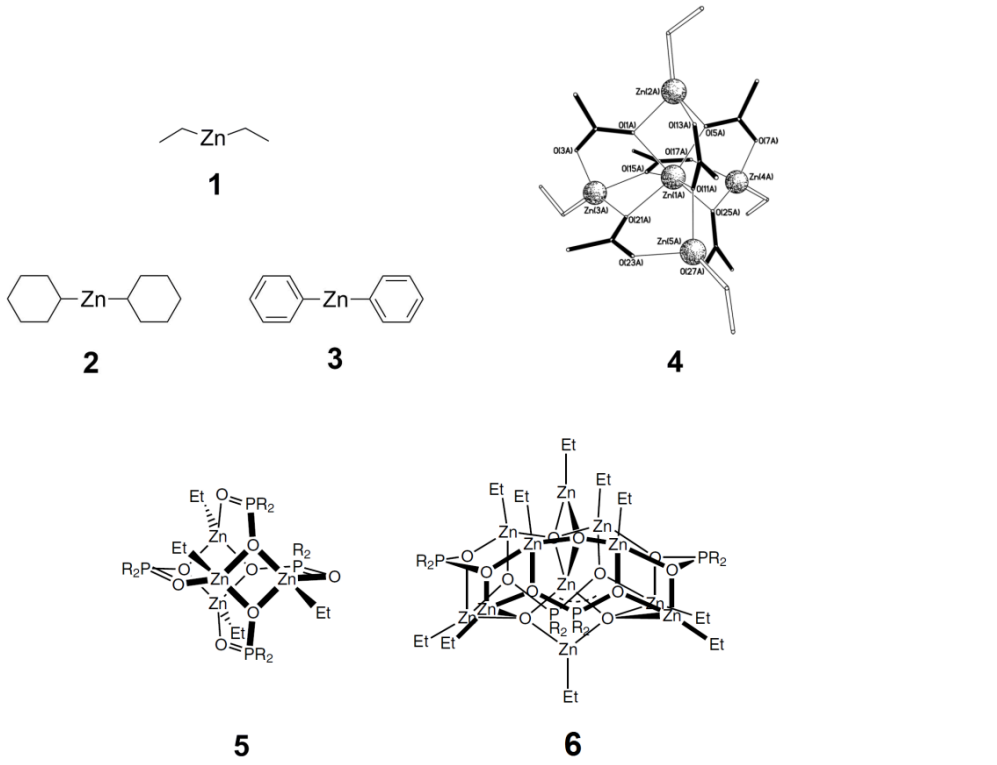

Figure 1.8. Structures of organozinc complexes which have been reported for synthesis of ZnO nanoparticles through hydrolysis.

[MeZnOH], using ^{1}H NMR spectroscopy.[54] The formation of this intermediate suggests the reactivity of Zn–CH_3, with water, is lower than that of the Zn–OCH_3 bond (Figure 1.9). The opposite trend was observed when the methyl alkoxides were substituted with ethyl alkoxides.[55] A possible explanation is the increase in steric bulk from methyl to ethyl, on the alkoxide, stabilises the Zn–OCH_2CH_3 bond.[54]

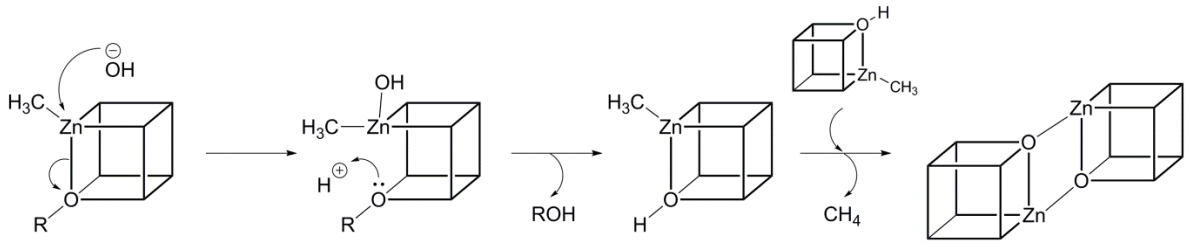

Figure 1.9. The mechanism of hydrolysis proposed for alkylzinc alkoxides cubane. *Reprinted with permission from Polarz et al.[54] Copyright 2008 American Chemical Society*.

Chaudret and co-workers have extensively explored the hydrolysis of various organozinc precursors to form ZnO nanoparticles. The hydrolysis of dicyclohexylzinc ($ZnCy_2$; complex **2**, Figure 1.8) or diphenylzinc ($ZnPh_2$; complex **3**, Figure 1.8) was achieved by exposing the precursor solution to atmospheric moisture over a period of 4 days.[49] Both amines and carboxylic acid were introduced into the precursor solution as ligands. Broadening of the ligand signals, in both ^{1}H and $^{13}C\{^{1}H\}$ NMR spectra, suggested that they were bound to the surface of the nanoparticles (resulting in a long T_1 relaxation time). By changing the solvent from THF to toluene caused the morphology of ZnO to change from nanorods to nanoparticles (<10 nm, $ZnCy_2$ and amine as precursors). An increase in reaction time (4 days to 2 weeks) and a decrease in concentration (0.042 M to 0.01 M) or an increase in temperature (25 °C to 45 °C) all led to the isotropic growth of ZnO nanoparticles (2–5 nm) instead of ZnO nanorods (width x length = ~2 x ~8 nm) as proven by TEM analysis.[50] Furthermore, a change in ligand, from an amine to a carboxylate, was shown to promote the anisotropic growth of ZnO nanoparticles.[56] The formation of nanorods, using the amine (~2.8 x ~11 nm), was found to be more facile compared to oleic acid. It was proposed that the binding of hexadecylamine to the (001) facet of ZnO is less favourable than that of oleic acid. In addition to the anisotropic growth, the particles displayed interesting optical properties, such as additional emissions alongside the common ZnO emission at ~570 nm.[56] The emission spectrum of ZnO nanoparticles, capped with hexadecylamine, showed an additional emission signal at 440 nm (2.82 eV) which was tentatively attributed to the hole trapping on the ZnO surface by the amine groups.

A similar approach was used by our group to synthesise ZnO nanoparticles capped with carboxylate ligands.[52] The reaction between $ZnEt_2$ and sub-stoichiometric amount of zinc *bis*(carboxylate), in apolar organic solvents, was found to form well-defined zinc-ethyl-carboxylate clusters, in the form of $[Zn_5(Et)_4(COOR)_6]$ (complex **4**; Figure 1.8). The controlled hydrolysis of the cluster, in the presence of excess $ZnEt_2$, led to the formation of monodispersed, small spherical ZnO nanoparticles (2–4 nm).[57] The rapid hydrolysis is proposed to promote nucleation and the ligand provided by the nanoparticles enables the reproducible synthesis of small particles. The loading of ligand does not affect the particle size or morphology, but does affect the surface coverage of the particle which increases with increasing ligand loading. Furthermore, the ligands were bound to the surface *via* a bridging coordination mode, confirmed by IR spectroscopy. Although the ligand is coordinated, there are also vacant surface sites available for further functionalisation or catalytic application (*see section 1.4.3*).

A recent study has extended this route to phosphinate capping ligands.[58] The reaction between $ZnEt_2$ with phosphinic acid, in both polar and apolar solvents, forms zinc-ethyl-phosphinate cluster, in the form of $[Zn_4(Et)_4(POOR_2)]$ (complex **5**, Figure 1.8). The subsequent hydrolysis yielded ZnO nanoparticles, capped with phosphinate on the surface, and showed particle size of 2–3 nm. Furthermore, the phosphorus proved useful for studying the hydrolysis pathway by $^{31}P\{^1H\}$ NMR spectroscopy. A series of reversible equilibria between cluster species and ZnO units was observed throughout the hydrolysis process (complex **6**, Figure 1.8). This suggests the ligand does not stay on the nanoparticle surface throughout growth, but instead it is only bound to the surface when full hydrolysis is reached.

1.3.3 Importance of Ligands

Ligands play multiple roles in the synthesis of colloidal nanoparticles. The ZnO Wurzite crystal structure contains polar hexagonal (001) facets and non-polar facets, such as (110), with the former having the highest surface energy and, therefore expected to be the fastest growing plane in nanoparticle synthesis. The polarity difference may promote anisotropic nanoparticles growth, but it can also be moderated through the addition of ligands.[59] Ligands may preferentially bind to certain facets and thereby affect the resulting shape of the nanoparticles. For example, the hot-injection synthesis of cadmium selenide (CdSe) nanoparticles, also of the Wurzite structure, was achieved using hexylphosphonic acid. This resulted in an array of morphologies, from rods-, arrows-, tetrapod- and teardrop-shaped nanoparticles.[60] It was proposed that the selective binding enhances the growth rate of the (001) facet and hence anisotropic growth is promoted.

Anisotropic nanoparticle growth can also be dependent on the chain length of the ligand. Chaudret and co-workers investigated a series of amines with different chain lengths (octyl-, dodecyl- and hexadecyl-amine) and the effect on the morphology of ZnO nanoparticles.[50] The nanomaterials were synthesised by the hydrolysis of $ZnPh_2$, with an equimolar of amine, in THF. By increasing the chain length from octyl- to hexdecyl-amine, ZnO nanorods were formed instead of nanoparticles (Figure 1.10). The change in morphology was tentatively proposed to result from different diffusion rates of Zn^{2+} ions through the ligand layer.[50] The diffusion rate is lowered using long-chain amines, which reduces the growth rate of the slow growing facets and hence promotes nanorod formation.

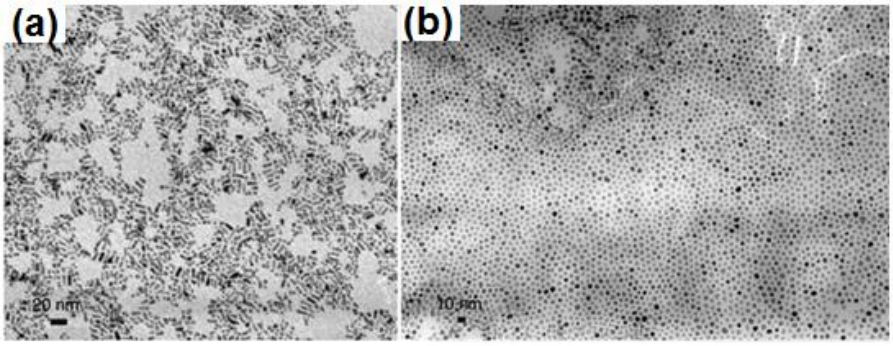

Figure 1.10. Controlled hydrolysis of $ZnPh_2$, in THF, with (a) hexadecylamine to form ZnO rods and (b) octylamine to yield ZnO spheres. *Reprinted with permission from Chaudret et al.[49] Copyrights 2003 WILEY-VCH Verlag GmbH & co. LGaA, Weinheim.*

Once the nanoparticles are formed, the ligands are important in moderating the interactions between nanoparticles. The ligands may create a steric or electrostatic barrier on the nanoparticle surface which prevents particle agglomeration.[61] For example, a molecule, containing three thiol groups, was used as a ligand to cap the surface of Au nanoparticles (20–50 nm). A high dispersity in toluene of such particles was achieved, whilst mono-thiol capped Au nanoparticles exhibited particle agglomeration.[62] A high surface ligand density for tri-thiol capped particles was observed, by XPS, which suggests the tri-thiol moiety binds stronger to the particle surface and its steric bulk prevents particle agglomeration. The importance of ligand-particle surface interactions has also been studied in alkylamine-capped ZnO nanoparticles using ^{1}H NMR and DOSY spectroscopy.[63] Three modes of interactions were determined: strongly bound amines, weakly bound amines and the formation of a second ligand shell. It was suggested that all three modes contribute to stabilising the nanoparticle surface, with the first having the slowest rate of surface desorption ($k_{desorp} \approx 13\ s^{-1}$).

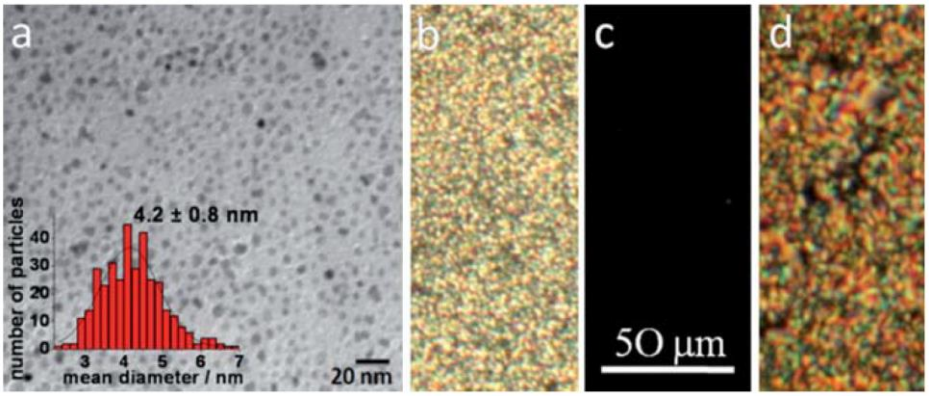

Figure 1.11. (a) TEM image of liquid crystal-ZnO hybrid. Polarised optical micrographs of the hybrid material at (b) 80 °C, (c) 140 °C and (d) cooling down to 84 °C. *Reprinted with permission from Chaudret et al.*[64] *Copyrights 2011 Royal Society of Chemistry.*

Modification of the ligand shell can affect the properties of the nanoparticles. Liquid crystals composed of ZnO nanoparticles were prepared using short chain amine ligands.[64] Exchange between an amine containing mesogenic liquid crystal and octylamine bound to the ZnO surface was achieved through ultrasonication (THF, 30 min, room temperature). Partial replacement of the surface-bound octylamine with liquid crystal-amine was confirmed by ^{1}H NMR spectroscopy, where a change in the N–H signal of the liquid crystal-amine from the free ligand to bound ligand was observed (δ 2.63 ppm to 2.68 ppm). The liquid crystal-ZnO nanoparticles displayed birefringence in polarised optical microscopy and the presence of diffused rings in the X-ray scattering pattern confirmed that the liquid crystal existed in a nematic phase (Figure 1.11). Furthermore, superlattice structures of nanoparticles can be generated, in THF, by using electrostatic interactions between ligands (Figure 1.12).[65] The interaction between ZnO, capped with carboxylate, and ZnO, capped with amine, generates a ligand bilayer, which can then lead to the self-assembly to form organised

superlattices (100–300 nm in size by TEM). This was driven by Coloumbic and Van der Waal interactions between the carboxylate and amine.

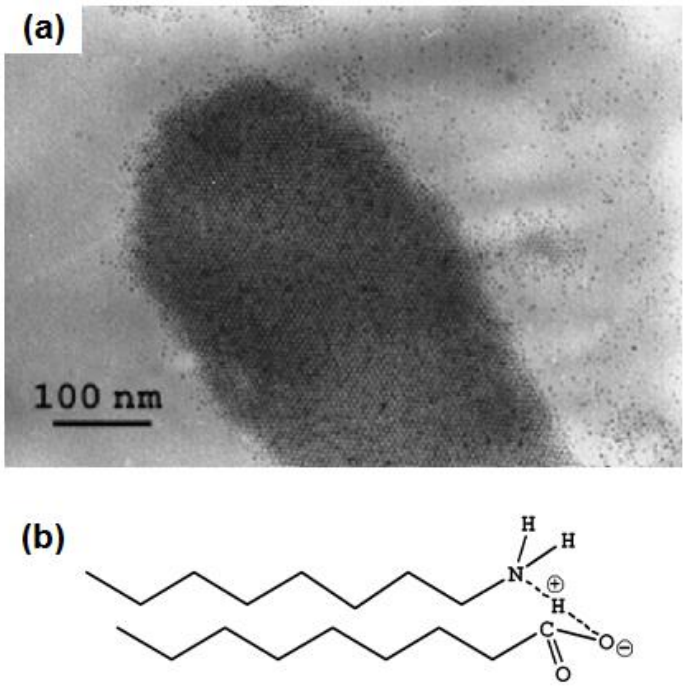

Figure 1.12. (a) 3D superlattice of ZnO nanoparticles using (b) a carboxylate-amine ion-pair ligand, in THF. *Reprinted with permission from Chaudret et al.*[65] *Copyrights 2009 WILEY-VCH Verlag GmbH & co. LGaA, Weinheim.*

1.3.4 Doping of Colloidal Nanoparticles

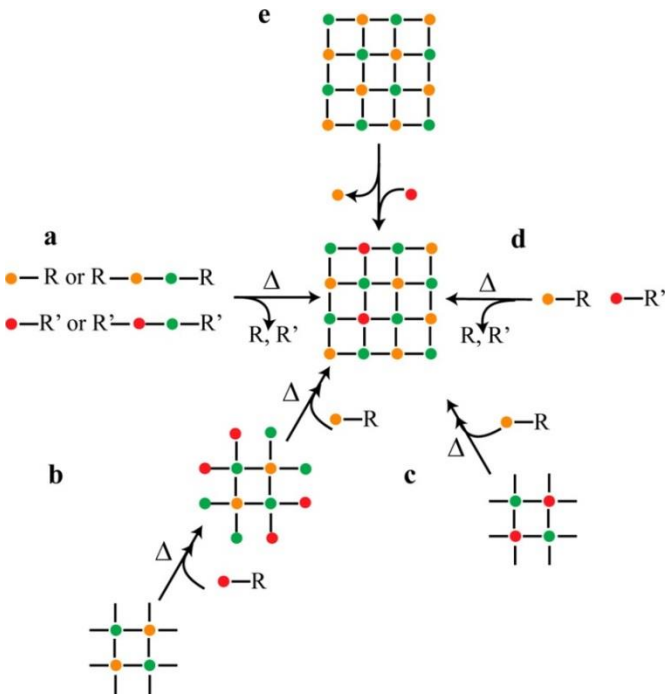

Figure 1.13. General scheme showing synthetic approaches to doped colloidal nanoparticles: (a) use of single-source precursor, (b) growth-doping, (c) nucleation doping, (d) tuning of metal–ligand bond strength and (e) cation diffusion. *Reprinted with permission from Milliron et al.*[66] *Copyright 2013 American Chemical Society*.

With increasing demand for advances in applications such as photovoltaics and catalysis (*see section 1.4.2*), new materials or enhancements to existing material properties must be explored.[2, 67, 68] One method to alter material properties is to incorporate dopants, specifically by substitutional doping (*i.e.* replacement of host atoms with dopant atoms).[66]

The doping of bulk semiconductors, under thermodynamic equilibrium, involves the fast diffusion of dopants into the host lattice. Dopant incorporation as high as 50% has been reported, for example doping of Mn(II) in ZnS and ZnSe.[69] In the case of doping nanoparticles under the same conditions, lower dopant incorporation was typically achieved. This was attributed to the slower diffusion of

dopants into the nanoparticles and hence a kinetic mechanism is proposed instead. The kinetics of the nanoparticle surface reactions determine the success of doping and the three dominant factors are: morphology, shape and type of ligand.[70, 71]

Several kinetically controlled synthetic approaches have been used to improve nanoparticle doping efficacy (Figure 1.13). Overall, the nanoparticle nucleation and growth reactions must be under kinetic control to avoid leaching of dopants from the host's framework.[66, 72] The use of single source organometallic precursors (SSP), prepared using both Zn and dopant metal, ensures close proximity of host and dopant atoms prior to nucleation (Figure 1.13a). Careful design of the precursor molecule is required as the doping level is controlled by access to the appropriate precursor molecule. In the case of doping ZnO nanoparticles, magnesium alkylzinc heterocubanes have been employed to synthesise Mg-doped ZnO nanoparticles (Figure 1.14).[73] The cubane was synthesised by reaction of 6 : 1 : 8 quantities of $ZnMe_2$, $MgMe_2$ and an alcohol (ethanol, 1-propanol, 1-butanol), in toluene. The subsequent thermolysis (600 °C, 2 h) of the cubanes produced Mg-doped ZnO nanoparticles, of sizes 20–80 nm and with Mg levels as high as 5 wt% (confirmed by

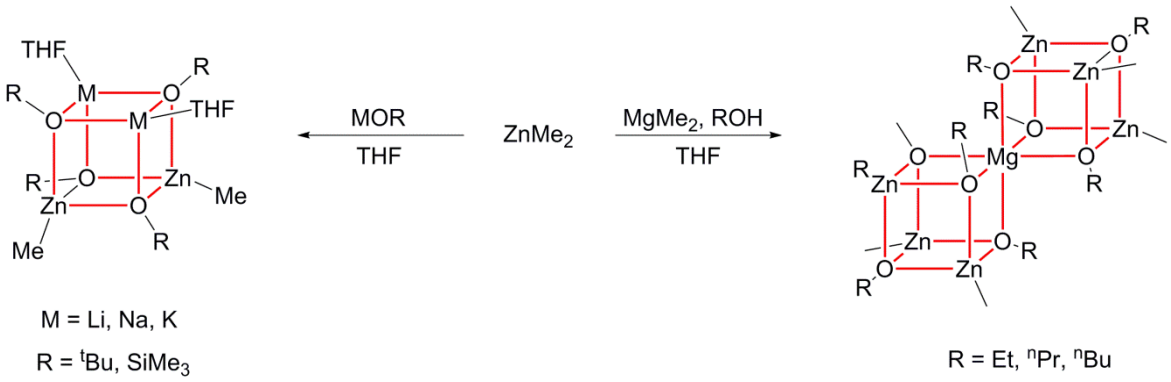

Figure 1.14. The synthesis of bimetallic alkyl zinc heterocubanes, using $ZnMe_2$ and the corresponding dopant precursor in THF.

ICP-OES). A uniform distribution of Mg throughout the samples was indicated by energy-dispersive X-ray spectroscopy (EDX), coupled with SEM. Photoluminescence (PL) measurements revealed an increase in the optical band gap, from 3.1 to 3.3 eV, and it was attributed to Mg^{2+} ions forming deep donor defect levels in the ZnO band structure. A series of Group 1 alkaline metal-zinc heterocubanes was also synthesised to target *p*-type doped-ZnO (Figure 1.14).[37, 74] In general, *p*-type doping of ZnO is difficult due to *n*-type intrinsic defect sites (V_O and Zn_i).[18] The cubanes were prepared by reaction of $ZnEt_2$ with alkaline metal alkoxides and were then thermally degraded, at 750 °C for 3 h, to yield doped ZnO nanoparticles.[75] Successful dopant incorporation was achieved with 1–10 mol% of metals. The PL measurements for Li-doped ZnO nanoparticles showed an increase in optical bandgap from 3.01 to 3.13 eV, with increasing Li^+ levels (0–3 mol% Li). The *p*-type character of ZnO is proposed to arise from the introduction of Li^+ acceptor levels in the ZnO band structure. Furthermore, powder XRD showed the *c*-axis lattice parameter was contracted by 5 pm, which is consistent with Li^+ substitution for Zn^{2+} in the Wurzite lattice.[74]

Two approaches were developed: growth doping and nucleation doping (Figure 1.13b & c).[66] The first approach involves the nucleation of the nanoparticle in the presence of dopant precursor, whilst the second approach requires the dopant precursor to be added once the nanoparticles are formed. Both methods lead to the formation of core-shell nanoparticles, as demonstrated in ZnSe nanoparticles.[76] The Mn(II) doping of ZnSe, *via* growth doping, was achieved by heating manganese stearate with selenium at 280 °C initially, followed by the addition of zinc *bis*(acetate), at 180 °C, to start the growth of the ZnSe shell around the dopant core. The decrease in reaction temperature is to prevent the diffusion of dopant from the core to the surface. The nucleation Cu(II) doping of ZnSe first form the ZnSe core

from zinc *bis*(stearate) and selenium, followed by the addition of copper *bis*(acetate) to initiate the growth of the dopant shell on ZnSe nanoparticles. TEM analysis of both samples showed a zinc blend structure and quantum confinement effects were observed (Figure 1.15).

Another strategy is to use different ligand-metal bond strengths, based on Lewis acidity values (Figure 1.13d). For successful doping, the dopant metal should be more Lewis acidic than the host metal. Furthermore, by using mismatched ligands on the dopant and host precursor, the reactivity of the two species is controlled to ensure homogeneous dopant distribution in the final nanomaterial. For example, the reaction between zinc *bis*(stearate) with [Al(acac)$_3$], using the hot injection method, produced Al-doped ZnO nanoparticles with Al^{3+} incorporation as high as 4.2 mol% (Figure 1.16).[77] When [Al(acac)$_3$] was substituted with less reactive Al(stearate)$_3$, no Al^{3+} incorporation was observed.

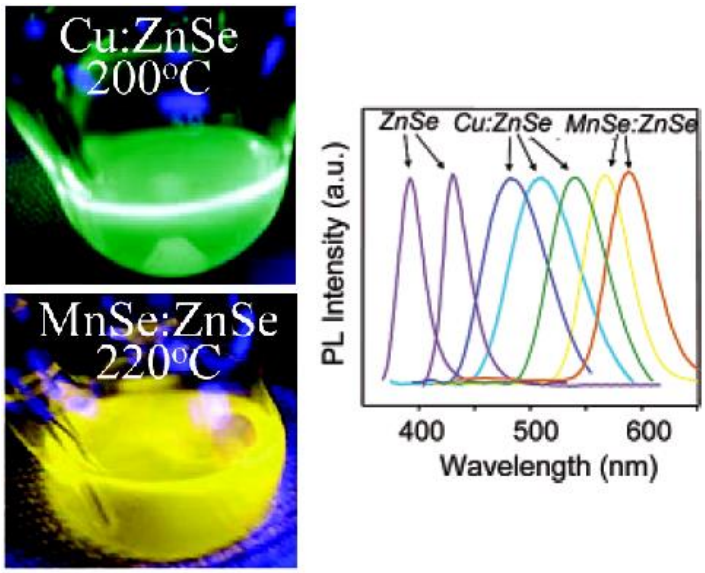

Figure 1.15. (Left) Photos of photoluminescence of Cu-doped and Mn-doped ZnSe nanoparticles above 200 °C. (Right) PL spectra of Zn-based emitters. *Reprinted with permission from Peng et al.*[76] *Copyright 2005 American Chemical Society*.

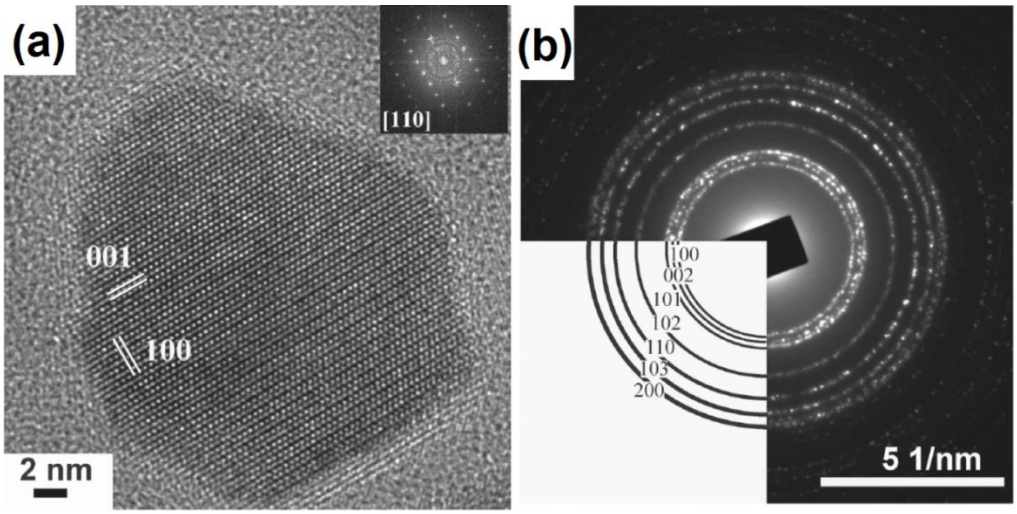

Figure 1.16. (a) HR-TEM of Al-doped ZnO nanoparticles oriented along the [110] zone axis with the corresponding FFT in the inset. (b) Electron diffraction of Al-doped ZnO nanoparticles showing the pattern of Wurzite ZnO. *Reprinted with permission from Milliron et al.[77] Copyright 2011 American Chemical Society*.

An alternative strategy allows the incorporation of dopant in the host lattice through diffusion (Figure 1.13e). It utilises the high energy host edges, steps and facets as sites for the preferential adsorption of dopant precursors; adsorption is proposed to accelerate dopant diffusion.[66] Both adsorption and diffusion rates are temperature dependent and specific to the dopant-host system. The Cu(II) doping of ZnSe was achieved using copper oleate adsorbed onto preformed ZnSe nanoparticles.[78] Temperatures above 60 °C promoted the doping of ZnSe through diffusion, as proven by temporal and thermal evolution of PL measurements. A decrease in the ZnSe PL signal was observed alongside the appearance of the Cu dopant PL signal (Figure 1.17). The quenching of the ZnSe PL was caused by surface adsorbed Cu where they act as surface traps, whilst the appearance of Cu PL signal was attributed to the formation of electron-hole recombination sites by dopant lattice diffusion.

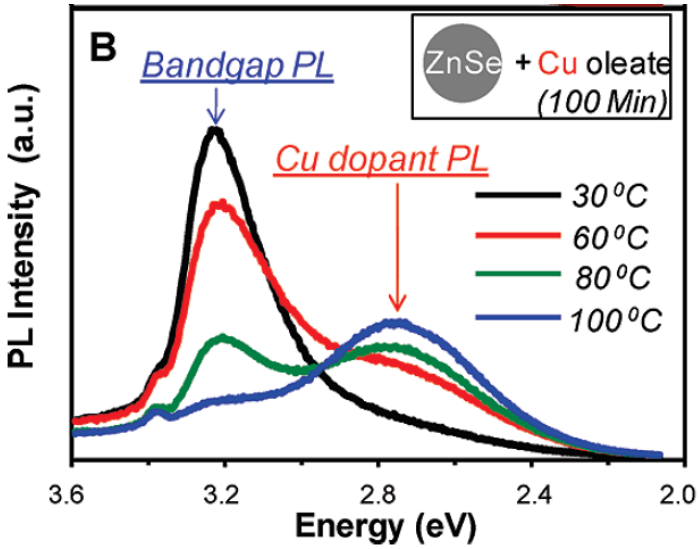

Figure 1.17. PL spectra showing the emergence of Cu dopant PL signal and the disappearance of ZnSe PL signal as the temperature of the reaction increases. *Reprinted with permission from Peng et al.*[78] *Copyright 2009 American Chemical Society*.

1.4 Methanol Synthesis

Methanol is an essential commodity chemical, where over 100 million metric tonnes are produced annually.[80, 81] George Olah, and others, have promoted the "Methanol Economy", whereby methanol is an alternative liquid fuel to petrol. It is particular interesting due to its compatibility with existing fuel infrastructure, ease of transport and storage, ability to use in blends with petrol and clean burning properties.[82] On the other hand, it has only 50% of the energy density of petrol.[81]

Industrially, methanol is produced using a heterogeneous ternary catalyst, Cu-ZnO-Al_2O_3, from synthesis gas (*aka* syn-gas, $CO/CO_2/H_2$, 10:10:80), often in a fixed bed reactor (250 °C, 50 bar). The commonly used ternary catalyst was first developed by Imperial Chemical Industries (ICI) in the 1960s. The optimal Cu:ZnO ratio is 70:30 and the catalyst can show methanol selectivity as high as 99%, but with low overall

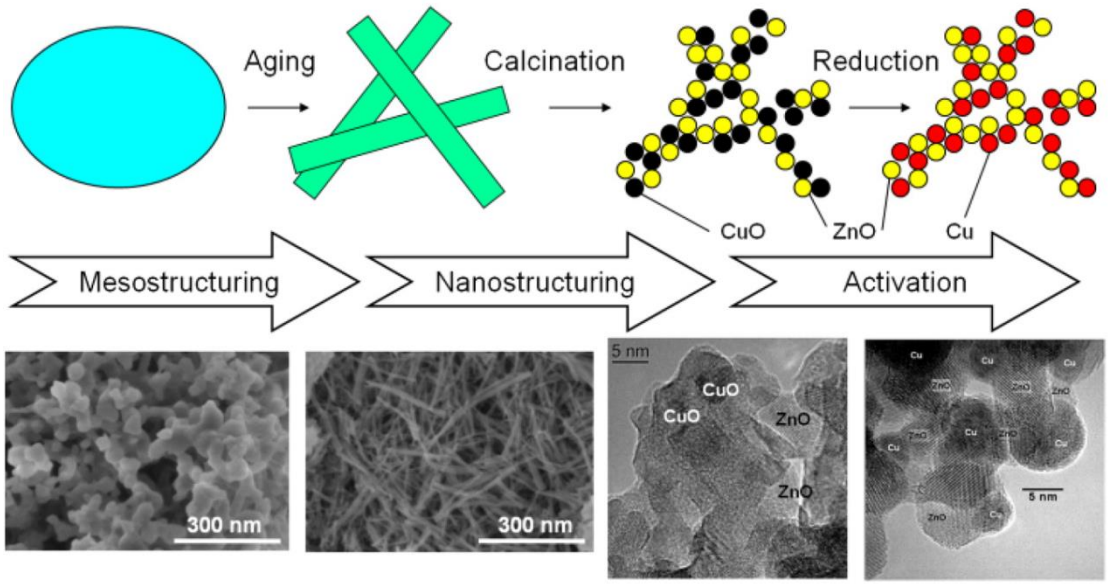

Figure 1.18. Simplified scheme to the synthesis of ternary heterogeneous catalyst, Cu-ZnO-Al_2O_3, using co-precipitation method, with SEM and TEM images showing the morphology of the catalyst through every synthetic steps. *Reprinted with permission from Behrens et al.[79] Copyright 2013 American Chemical Society.*

conversion (<10%, 240 °C, 50 bar) and hence re-feeding the unreacted syn-gas is performed.[79, 83] The catalyst preparation first involves the co-precipitation of Cu, Zn and Al carbonates or nitrates (60 °C, pH 6–7). The precursors are then subjected to ageing, washing and drying steps to yield a mixture of structures (*i.e.* zincian malachite, rosasite, aurichacite & hydrotalcite). The calcination and subsequent reduction of these structures, more specifically zincian malachite, lead to formation of dispersed Cu(0) and ZnO nanoparticles (<10 nm) on the alumina support (Figure 1.18).[84]

Methanol synthesis is a rather complex reaction, and several processes can be occurring concurrently (depending on conditions and catalyst):[85]

Methanol synthesis:

$$CO + 2\,H_2 \rightleftharpoons CH_3OH \qquad \Delta H_{298K} = -90.5\ kJ/mol$$

$$CO_2 + 3\,H_2 \rightleftharpoons CH_3OH + H_2O \qquad \Delta H_{298K} = -90.7\ kJ/mol$$

rWGS:

$$CO_2 + H_2 \rightleftharpoons CO + H_2O \qquad \Delta H_{298K} = +41.2\ kJ/mol$$

Methanol formation from the reduction of CO and CO_2 is exothermic (*see equations above*) and this may be formed by increasing pressure and decreasing temperature. The catalyst requires elevated temperatures (> 240 °C) and is typically applied under 50 bar of gas pressure.[86] A major competing side reaction, the reverse water-gas shift (rWGS), is endothermic (*see equation above*). One strategy to supress rWGS reaction is to employ catalysts with higher selectivity towards methanol formation and to use lower reaction temperatures.[85]

In order to understand the origin of catalyst selectivity towards methanol formation, the mechanism of reduction of CO and CO_2, has been explored in detail for the heterogeneous catalysts, Cu-ZnO-Al_2O_3. Early research, in 1980s, logically assumed CO as the source of carbon for the methanol produced, with additional CO provided by rWGS reaction from CO_2.[87] This was soon disproved by Chinchen and co-workers, who employed carbon-14 labelling to determine the carbon source as CO_2, where CO could be converted to CO_2 through the WGS reaction (50 bar, 250 °C, 10:10:80 CO/CO_2/H_2).[88] DFT calculations and industrial studies further consolidated this finding, with calculations and experiments performed under industrially relevant conditions.[89, 90] With a CO_2/H_2 gas stream, the rate of methanol production was 100 times faster than with CO/H_2 mixture, which was attributed to the different hydrogenation pathways for CO_2 and CO. A lower energy pathway, *via* formate intermediates (such as $HCOO^{\bullet}$ and $HCOOH^{\bullet}$), was proposed for CO_2 hydrogenation. Whereas for the CO hydrogenation pathway, relatively high energy intermediates are generated instead (*e.g.* $HCO^{\bullet}$) before reaching the common intermediate, $CH_3O^{\bullet}$, for the two pathways.[89] Subsequent DFT studies proposed the intermediates in the CO_2 reduction pathway are lower in energy when Cu(0) surfaces are decorated with Zn atoms (Figure 1.19).[91] The intermediates were proposed to be bound to the surface of the catalyst *via* metal–oxygen bonds and the formation of these is promoted by the presence of Zn atoms (*see section 1.4.1 for more details*). In the case of CO hydrogenation, the intermediates are bound to the surface through higher energy metal–carbon bonds and, therefore, the reaction proceeds more slowly due to it higher activation energy barrier.

Although these studies suggest the use of a CO_2/H_2 feed is preferable compared to syn-gas, the thermodynamic methanol yield is only 20% for CO_2/H_2 and 60% for CO/H_2 (molar ratio of 1:3, 50 bar, 227 °C). Also, CO_2/H_2 leads to more rapid catalyst deactivation, likely due to the water byproduct.[84]

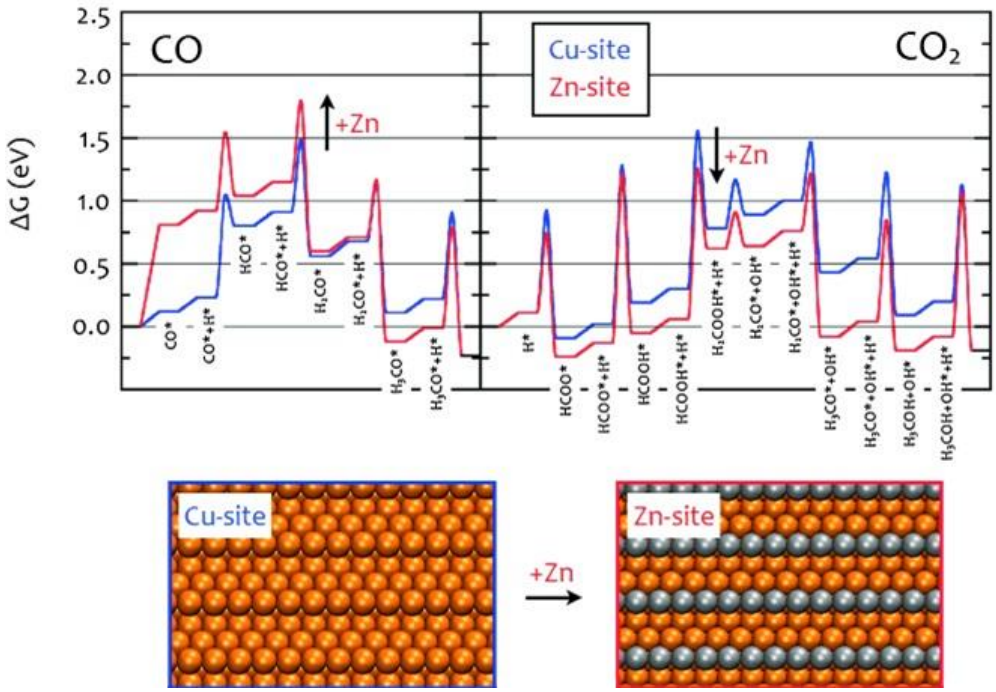

Figure 1.19. Free energy diagram of CO and CO_2 hydrogenation to methanol, at 503 K, on Cu surface (blue line) and Cu surface decorated with Zn (red line). *Reprinted with permission from Schlögl et al.*[91] *Copyright 2015 WILEY-VCH Verlag GmbH & co. LGaA, Weinheim.*

1.4.1 Cu/ZnO Synergy

For the industrial Cu-ZnO-Al_2O_3 catalyst, the role of ZnO has been under vigorous debate. Some early reports proposed that the ZnO acts as a support to prevent the agglomeration of Cu nanoparticles.[92, 93] However, later research instead proposed that ZnO acts as a promoter. The promotional effect of ZnO was substantiated by studies of Cu nanoparticles on various metal oxide supports (Ga_2O_3, ZrO_2, Al_2O_3, SiO_2, MgO) demonstrating lower activity than Cu/ZnO catalyst.[91, 94] The term "strong metal support interaction (SMSI)" has been coined to describe the synergistic effect of Cu and ZnO.

The Cu/ZnO synergy was first proposed by Frost, in 1988.[95] It was proposed that when Cu and ZnO are in close proximity (~ 30 Å), a Schottky-Mott junction can form at the interface, which lowers the enthalpy of oxygen vacancy formation in ZnO,

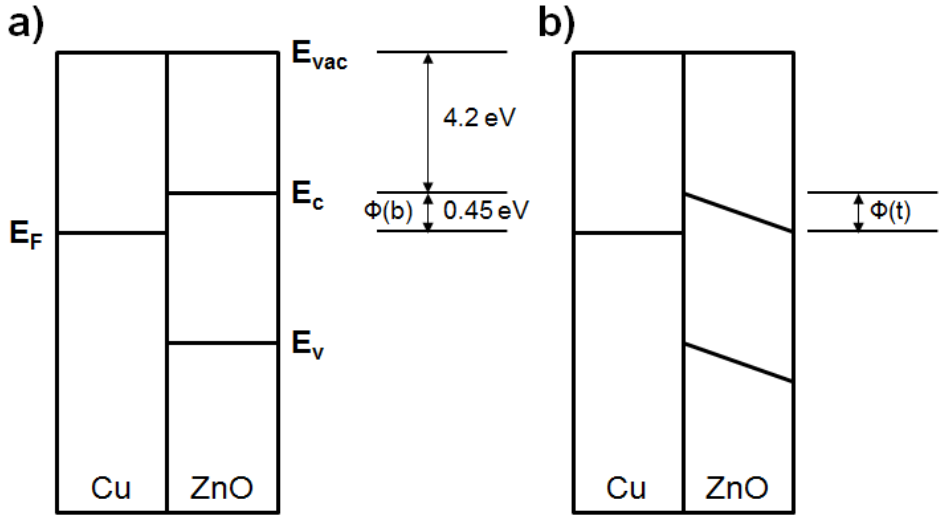

Figure 1.20. Band diagram for the Cu/ZnO Schottky-Mott junction. a) unrelaxed contact, b) contact after the oxygen vacancy and electron transfer to copper. E_{vac} = vacuum level, E_v = valence band edge, E_F = Fermi level, E_c = conduction band edge, Φ(b) = Schottky-Mott barrier height and Φ(t) = band-bending height. Diagram adapted from Frost.[95]

through electron transfer from the conduction band of ZnO to Fermi level of Cu (Figure 1.20). The Cu/ZnO interfaces were proposed to be the active site for methanol formation. This electronic promotional effect was once again demonstrated in a recent study into the influence of different ZnO facets on the Schoktty-Mott junction.[96] The polar (001) facet of ZnO showed a higher density of oxygen vacancies compared to non-polar facets, (100) and (110). It also exhibited superior methanol selectivity (71.6% vs. 39.1%) and CO_2 conversions (15.3% vs. 12%) in the hydrogenation of CO_2 to methanol (1:2.2 CO_2:H_2 feed, 45 bar, 260 °C). The addition of electron-rich CdSe quantum dots to the same system led to further increase in the methanol selectivity (up to 80%), proposed as due to enhanced electron density in the ZnO conduction band.[97]

In addition to electronic promotion by ZnO, some structural effects were also proposed. Under reductive conditions and high temperatures, the re-arrangement and migration of ZnO to the surface of the catalyst has been investigated using extended X-ray absorption fine structure (EXAFS), HR-TEM, Fourier transform infrared spectroscopy (FT-IR) and X-ray photoelectron spectroscopy (XPS).[98-101] HR-TEM showed the formation of 4–6 overlayers of metastable ZnO on Cu nanoparticles (under reductive conditions of methanol synthesis), using both syn-gas and pure CO_2/H_2 feeds (Figure 1.21).[100] In addition, EXAFS analysis indicated that the ZnO overlayer is a non-aggregated oxygen-deficient ZnO phase.[101]

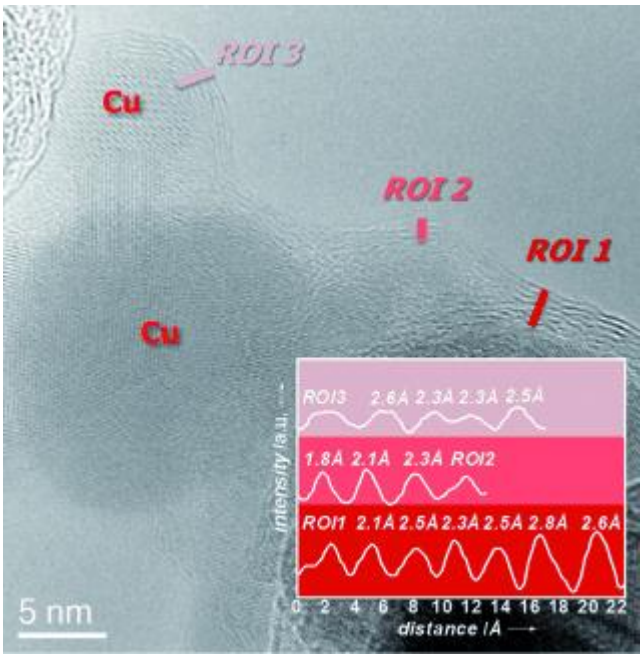

Figure 1.21. HR-TEM micrograph of Cu-ZnO-Al_2O_3 catalyst showing the presence of ZnO overlayers marked by regions of interests (ROI 1, ROI 2 and ROI 3). *Reprinted with permission from Behrens et al.[100] Copyright 2015 Wiley.*

It was proposed that the structural changes to ZnO was triggered by its reducibility and the morphological change of Cu, upon exposure to H_2 and CO.[102, 103] The reducibility of ZnO was substantiated by studies of Cu/MgO catalyst, the latter is a non-reducible metal oxide. The Cu/MgO catalyst displayed no activity for methanol synthesis using syn-gas (30 bar, 230 °C). Furthermore, some studies proposed that the migration of Zn leads to the formation of a CuZn alloy at the interface and that such alloy species promote hydrogenation reactions.[98, 99] In contrast, recent studies suggest that activity arises from the spillover of H_2 from Cu surfaces onto a CO_2-saturated Cu/ZnO interface.[104-106] This idea was proposed following investigation into H_2 and CO_2 chemisorption on Cu and ZnO surfaces and supported by models to understand the contact of Cu with ZnO. The authors proposed that the Cu/ZnO catalyst consists of a graphitic ZnO/Cu layer at the interface (Figure 1.22). It is also

worth noting that a CuZn alloy is also present but it is not involved in the mechanism proposed.

Despite some controversies over the mechanism of Cu/ZnO synergy, all literature highlights the importance of both Cu and ZnO components in the methanol synthesis catalyst. When designing a Cu/ZnO catalyst, two important aspects must be taken into consideration: surface area available for Cu and ZnO interaction and the promotion of Cu/ZnO interface formation.

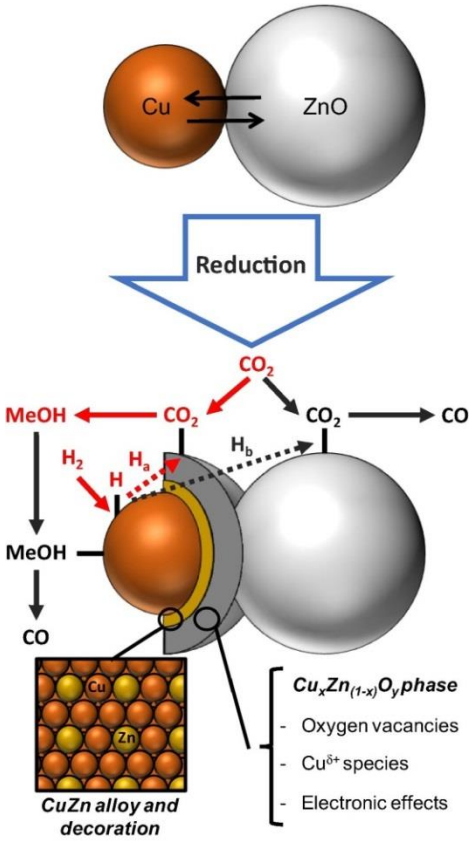

Figure 1.22. General scheme for methanol synthesis, using Cu/ZnO-based catalysts. Close contact and intimate interaction between Cu and ZnO are in support of SMSI effects for the enhanced catalytic activity. *Reprinted with permission from Pouilloux et al.[106] Copyright 2016 Elsevier.*

1.4.2 Hydrogenation of CO_2 to Methanol

Perhaps most widely studied catalysts for direct hydrogenation of CO_2 is the same Cu/ZnO system used in syn-gas to methanol. In addition to Cu/ZnO, other metals have also been explored, in both heterogeneous and homogeneous catalytic systems, to try to improve performance.

Heterogeneous systems

In the 1970s, catalyst development for methanol production was mainly focused on using precious metals (Rh, Ir, Pt, Pd) on metal oxide supports (*e.g.* ZnO, MgO).[107] The precious metal carbonyl clusters were deposited on metal oxide supports, forming highly dispersed metal nanoparticles upon reduction. These catalysts were active for methanol production from CO/H_2, under atmospheric pressure and low temperatures (150–250 °C).[108] However, they were more vulnerable to sulphur poisoning from impure gas streams.[108] Improved sulphur tolerance was obtained by treating the metals with a dilute stream of H_2S to form a metal sulphide catalyst, but poor activity resulted when using a clean gas stream.[109]

Synergistic metal/support interactions, similar to that of Cu/ZnO, were also observed in Pd/Ga_2O_3.[110] The support of Pd nanoparticles on the (002) facet of Ga_2O_3 rods resulted in a high methanol selectivity (51.6%) from CO_2/H_2 (50 bar, 250 °C), which was rationalised to result from electronic promotional effects. Other studies have suggested that the active phase for methanol production may be a Pd_2Ga alloy formed *in-situ*.[111-113] Environmental TEM studies demonstrated Pd_2Ga alloy formation under 4 mbar H_2, at 550 °C. An EXAFS study further confirmed Pd_2Ga formation under catalytic conditions (30 bar, 200 °C) using CO_2/H_2, and the resulting catalyst showed high selectivity towards methanol (two times higher than the

standard industrial ternary catalyst). Furthermore, the promotional effects of Ga have been extensively studied in Cu/ZnO systems. The addition of Ga is proposed to improve dispersion of Cu, which enhances electronic promotional effects and facilitates the formation of the Cu/Zn alloy.[114, 115] A recent study employed layered double hydroxides (LDHs) containing Cu, Zn and Ga, as a precursor to produce Ga^{3+}–modified Cu/ZnO catalysts.[116] The LDH precursor increased the Cu dispersity, perhaps due to the presence of positively charged metal hydroxide sheets during catalyst reduction (indicated by TEM). The most active catalyst, with LDH of composition of $[(Cu_{0.47}Zn_{0.32}Ga_{0.21})(OH)_2]$, displayed 50% methanol selectivity and activity almost twice as high as industrial Cu-ZnO-Al_2O_3 catalyst (45 bar, 3:1 H_2:CO_2, 270 °C).

Binary systems consisting of reducible metal oxides, supported on non-reducible metal oxides, have also demonstrated exceptional activity. In particular, reducible In_2O_3 was already active in other catalytic CO_2 transformations.[117, 118] When In_2O_3 is supported on ZrO_2, 100% selectivity towards methanol was achieved, with activity three times higher than that of Cu-ZnO-Al_2O_3, and exceptional catalyst stability over 1000 h (50 bar, 300 °C).[119]

Promoters & dopants

Promoters can induce beneficial structural and/or electronic effects and are typically applied in low quantities (<10 mol%).[120, 121] Al_2O_3 (5–10 mol% incorporation) is a known promotor in the industrial methanol ternary catalyst, but its interaction with the Cu/ZnO nanoparticles has historically been poorly understood. Recent studies suggest that the Al^{3+} acts as a dopant in ZnO and may induce both structural and electronic promoting effects.[79, 122] By carefully controlling

the concentration of Al^{3+} in synthesis, the successful diffusion of the ions into the catalyst promotes Cu dispersion perhaps through forming surface Al^{3+} species to prevent sintering of Cu(0) nanoparticles. The homogeneous distribution of Al^{3+} throughout the catalyst was confirmed by EDX. Similar structural promoting effects were also observed when using promoters such as Mg^{2+}, Ga^{3+} and Cr^{3+}, or when MgO, Ga_2O_3 and Cr_2O_3 were used as supports. All four catalysts were tested in the hydrogenation of syn-gas to methanol ($CO/CO_2/H_2$ 6:8:59.5, 60 bar, 250 °C), and showed similar conversions of ~ 6% and ~ 42% for CO and CO_2, respectively.[79] Whilst Al^{3+}, Ga^{3+} and Cr^{3+} dopants demonstrated beneficial effects, Mg^{2+} was found to be detrimental, with activity half that of the Al^{3+} promoted catalyst. The doping of the ZnO with Al^{3+}, Ga^{3+} and Mg^{2+} prior to catalyst formation was also investigated (Figure 1.23). The characterisation of the catalysts, using UV-Vis spectroscopy and temperature programmed reduction (TPR), indicated that $Al^{3+}$and Ga^{3+} dopants enhance the *n*-type conductivity of ZnO and promote the formation of oxygen vacancies.[68] In catalysis, these *n*-type dopants may facilitate Zn migration onto Cu, hence promoting Cu/ZnO interface formation. For the Mg-doped catalyst, the ZnO was more insulating (its band increased to 3.20 eV) and this is proposed to reduce the formation of Cu/ZnO interfaces.

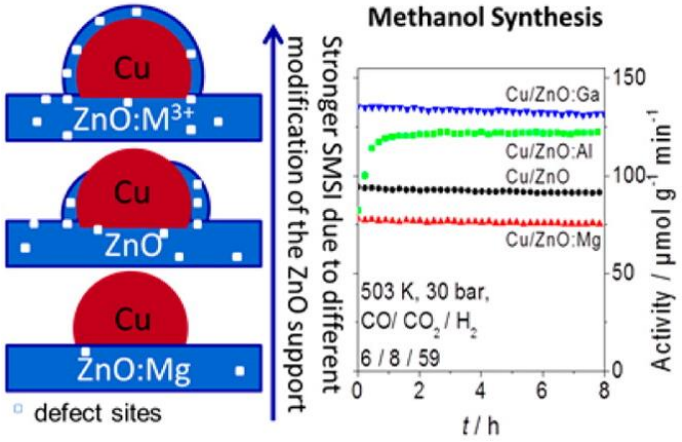

Figure 1.23. Hydrogenation of syn-gas, using doped Cu/ZnO catalysts, in a fixed bed flow reactor (230 °C, 30 bar, $CO:CO_2:H_2$ 6:8:59, 100 mL min^{-1}). The study was performed to demonstrate the effect of SMSI on the catalytic activity. *Reprinted with permission from Behrens et al.[68] Copyright 2015 American Chemical Society.*

Homogeneous catalysts

Early work on homogeneous systems often employed a stoichiometric reducing agent, such as a borane, silane or frustrated Lewis pair, to achieve CO_2 transformation.[123, 124] Ruthenium complexes have been applied for the homogeneous CO_2 hydrogenation to methanol, with both direct and indirect routes being reported.[125, 126] One indirect route utilised a ruthenium pincer complex to catalyse the hydrogenation of urea or dimethyl carbonate (products derived from CO_2) to methanol (< 14 bar, at 110 °C), with turnover number (TON) of 4400 (complex **1**, Figure 1.24).[127, 128] Sandford and co-workers employed a catalytic cascade to form methanol in one-pot using both ruthenium and scandium catalysts (complexes **1** and **2**, Figure 1.24).[125] The ruthenium complex **1** catalyses the hydrogenation of CO_2 to formic acid and this is followed by its esterification (by scandium complex in complexes **2**), with an alcohol, to methyl formate. The second ruthenium complex (in complexes **2**; Figure 1.24) then further hydrogenates the methyl formate to form

methanol. The overall catalytic activity was low, with TON of 2.5, at 40 bar and 135 °C. Furthermore, a large excess of alcohol for the esterification steps is required which is problematic since it is both reagent and product.

Other catalytic systems are capable of performing the hydrogenation with one complex and without any alcohol additives.[129] The ruthenium complex **3,** in Figure 1.24, combined with sub-stoichiometric amount of an acid, such as. trifluoromethanesulphonimide, achieved TON of 220 (80 bar).[126] In addition, this homogeneous catalyst was applied in a biphasic continuous flow system.[129] The system consists of 2-methyltetrahydrofuran-water medium, with the ruthenium complex soluble in the organic phase and the methanol separated in aqueous phase, allowing for its continuous removal.

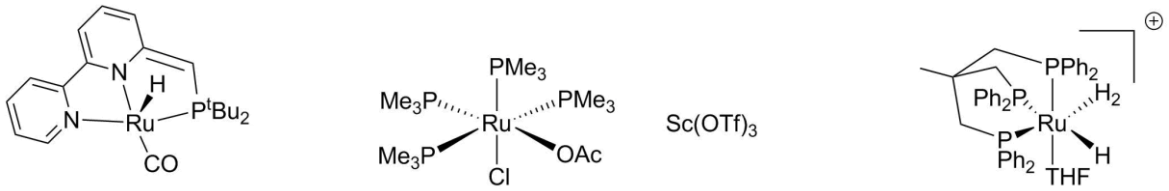

1 **2** **3**

Figure 1.24. Ru complexes reported in literature to be active in direct and indirect hydrogenation of CO_2 to methanol. For complex **3** depicts the active state of the catalyst, with '*Sol*' as the solvent molecule bound to the Ru metal centre.

1.4.3 Liquid Phase Methanol Synthesis

Fixed bed reactors are a very well-developed technology for the industrial methanol synthesis but do suffer from some disadvantages. Traditional fixed bed reactors require efficient temperature control to avoid thermal runaway and catalyst burning.[130] This is often achieved by limiting the loading of CO/CO_2 gases and cooling with H_2, but the limited carbon content decreases the per pass methanol yield.[131] Also, the current fixed bed reactors take time to activate and deactivate – *i.e.* they are not compatible with responsive manufacturing.[132, 133] Rapid cooling or removal of feedstock can cause irreversible catalyst damage and the replacement of catalyst (*i.e.* reactor decommission, catalyst replacement, followed by reactivation) often requires significant reactor down-time.

Alternatively, a three phase or a liquid phase system (slurry reactor) may overcome some of these problems.[134, 135] In slurry reactors, the ternary catalyst is ground to a fine powder and suspended in an inert solvent, often mineral oil or squalane. The liquid medium allows more uniform temperature control and it provides better temperature management for the exothermic reaction, allowing higher CO/CO_2 loading, increased per pass conversion and hence, lower costs.[136] A further attraction is the potential to replace catalyst during reactor operation.[94, 132, 133] Overall, the promising attributes of liquid phase reactor might lower the cost of methanol production, but some limitations to commercialisation remain, mainly the higher catalyst deactivation rate in liquid medium (0.17–1.0% deactivation per day).[136]

Colloidal Nanocatalysts

A logical catalyst modification for liquid phase heterogeneous catalysts is to develop colloidal nanocatalysts. These colloidal nanocatalysts are typically small (<10 nm) and soluble in relevant solvents.[137, 138] As briefly mentioned in *section 1.1,* nanoparticles are expected to have higher number of surface active sites and may show enhanced activity compared to the bulk. [139, 140]

Colloidal nanocatalyst systems might also allow new characterisation and understanding of mechanism.[5, 141] In a recent study, the surface chemistry of Pd nanoparticles was controlled through the addition of dopant atoms on specific facets and edges.[142] Te-doping inhibited formic acid dehydrogenation by blocking the active sites, whereas promoting effects were observed with Bi-doping. The preferential binding of Bi atoms, on high energy sites of Pd, electronically promoted the catalysis, whereas Te atoms bind to the active sites and hence inhibiting catalysis.

Many nanocatalysts undergo particle aggregation, which reduces surface area and decreases activity.[143] One method to prevent ripening is through the introduction of a ligand.[140] Ligands with long alkyl chains, such as stearate, are often used to provide high catalyst solubility, with squalane as a common solvent used.[101, 144] Good stabilisation is achieved with the ligand, at the expense of possible catalyst inhibition due to occupation of active sites.[5]

A range of colloidal nanocatalysts have been explored for methanol synthesis. For example, colloidal Pd/Ga and Pd/In systems showed good activity and selectivity using a CO_2/H_2 feed (molar ratio of 1:3).[145, 146] Pd_2Ga and PdIn were proposed as the active components and for Pd/Ga catalyst, the optimal ratio was 1:2 Pd:Ga, with an average particle size of 5.6 nm. The methanol activity was ~3 times higher than that

of industrial Cu-ZnO-Al_2O_3 catalyst (210 °C, 50 bar, squalane). For the Pd/In system, high methanol selectivity (90%; 210 °C, 50 bar CO_2/H_2 3:1, squalane) was tentatively attributed to a mechanistic difference in the CO_2 activation between Pd/In and Cu-ZnO-Al_2O_3.[146]

Colloidal Cu/ZnO Nanocatalysts

Despite some promising results observed with Pd-based systems, the combination of Cu/ZnO remains the most popular choice due to the low cost of the metals and the wealth of literature available on the corresponding heterogeneous systems.[101, 144, 147] As discussed previously in *section 1.4.1*, the formation of a Cu/ZnO interface is crucial for catalytic activity. Various synthetic strategies were used to try to enhance interface formation, including reduction and hydrogenolysis routes, which they will be outlined below and in Table 1.1.

The reduction of Cu precursor to colloidal Cu(0) nanoparticles, using alkyl metal reagents, was first demonstrated by the reduction of $Cu(acac)_2$ using $ZnEt_2$, in buta-1,3-diene.[148] A brown colloidal solution was formed, but the Cu(0) particle size was not reported. The catalyst was used for CO hydrogenation and a distribution of products formed, including ethanol, methanol and other hydrocarbons (entry 1, Table 1.1). EXAFS analysis found that Cu(0) nanoparticles of 1.2 nm were present, alongside molecular Zn–O cubanes.[149] An organoaluminium reagent, $Al(Oct)_3$, was also used to reduce $Cu(acac)_2$ to small Cu(0) nanoparticles (3–6 nm).[150] Despite the absence of ZnO within the system, the catalyst was quite active for methanol production using syn-gas ($CO/CO_2/H_2$ 10:4:86, 150 °C, THF; entry 2, Table 1.1), but extremely high pressures were required (175–215 bar). Al was proposed to play a similar role to ZnO in the ternary system.[101] In a recent study, $ZnEt_2$ was used to

reduce $Cu(St)_2$ to Cu(0) and ZnO colloid (~7 nm in size), which was highly active for CO_2/H_2 to methanol (entry 3, Table 1.1).[151] Close contact between the Cu and ZnO phases was observed by TEM, with the ZnO forming by the hydrolysis of $ZnEt_2$ and ethyzinc stearate clusters (Figure 1.25). The source of water was proposed to be from either the hydrogenation of CO_2 or residual water in the feed gas. The stability of the catalyst was attributed to the presence of excess stearate ligand.

The sequential pyrolysis of $Cu(OCHMeCH_2NMe_2)_2$ and $ZnEt_2$ (at 220 °C, squalene) produced an active catalyst for the hydrogenation of syn-gas (entry 4, Table 1.1).[101] No ligand was added into this catalyst, but very small nanoparticles were produced (1–3 nm). Electrostatic repulsions between the small particles was tentatively assigned to rationalise the particle stability over several days. Furthermore, UV-Vis spectroscopy studies showed that the Cu component of the catalyst exhibited an enhanced resistance to oxidation.

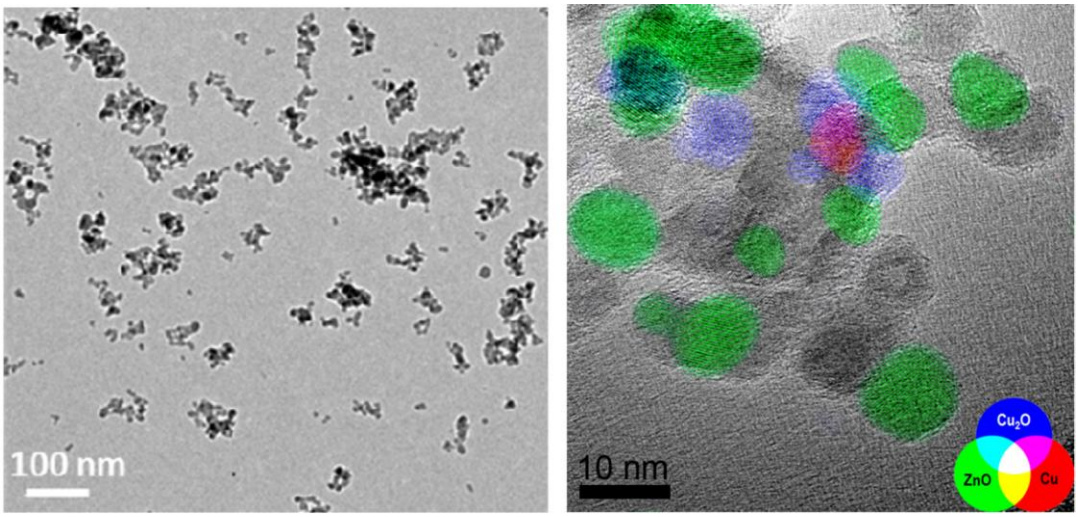

Figure 1.25. (Left) Low-resolution TEM image of the post-catalysis sample after 16 h in methanol production using CO_2/H_2. (Right) HR-TEM image of a nanoparticle cluster containing ZnO, Cu(0) and CuO; colours indicate phases unambiguously identified by lattice spacing analysis. *Reprinted with permission from Williams et al.[151] Copyright 2015 American Chemical Society.*

Hydrogenolysis is a widely applied method for the generation of metal nanoparticles, such as Ru, Ag and Pd.[152] It is generally straightforward to carry out and the only byproduct is water. The reduction of $Cu(St)_2$, in the presence of stearate-capped ZnO nanoparticles (5 bar H_2, 220 °C, 16 h) generated a colloidal Cu/ZnO catalyst, but it showed lower activity compared to the industrial Cu-ZnO-Al_2O_3 catalyst (26 bar syn-gas, 220 °C, squalane; entry 5, Table 1.1).[153] Post-catalysis analysis, using TEM, indicated the formation of large Cu(0) nanoparticles (20–50 nm), with ZnO nanoparticles decorating some Cu surfaces. Although Cu/ZnO interfaces were identified, the mismatch between Cu and ZnO particle size, and decreased Cu surface area were proposed to be the cause of the low activity. Further studies were carried out to reduce the size of Cu(0) nanoparticles; the method involved reducing $Cu(St)_2$ and $Zn(St)_2$ precursors in squalane (5 bar H_2, 220 °C).[154] The resulting 8 nm Cu(0) nanoparticles (confirmed by TEM) appeared to be decorated with $Zn(St)_2$. It was proposed that under catalytic conditions, the Zn

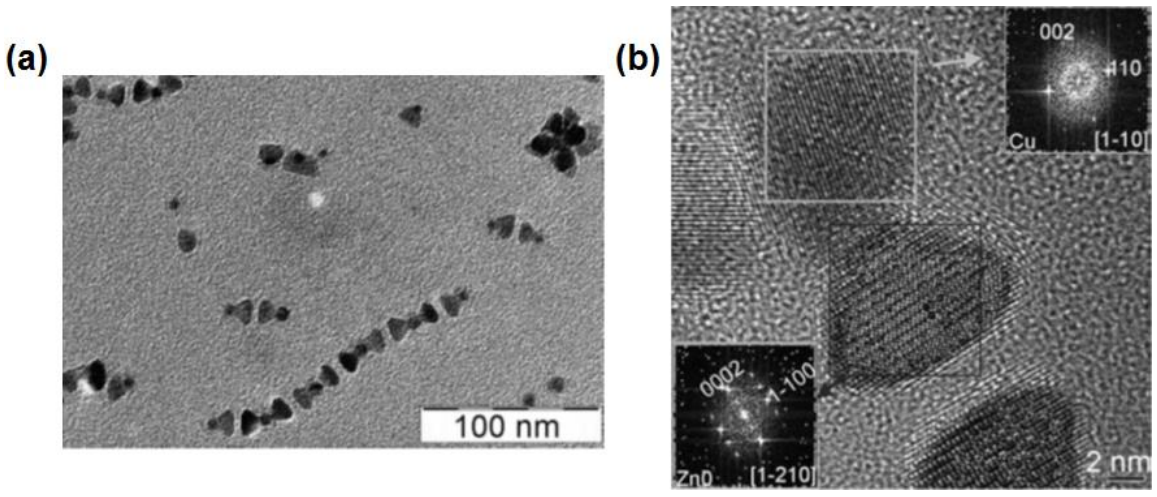

Figure 1.26. (a) Colloidal Cu/ZnO nanoparticles after 22 h in methanol production from syn-gas. Agglomerates display a "bow-tie" structure, with (b) HR-TEM clearly showing spherical Cu(0) nanoparticles attached to pyramidal ZnO nanoparticles in the agglomerates. *Reproduced with permission of Muhler et al.[144] © 2010 Wiley-VCH Verlag GmbH&Co. KGaA, Weinheim.*

complex was hydrolysed to ZnO. The best Cu:ZnO molar ratio was 50:50 and its performance was comparable to the industrial Cu-ZnO-Al_2O_3 catalyst (26 bar syn-gas, 220 °C, squalane). In order to ensure even closer proximity of Cu and Zn prior to hydrogenolysis, melting of the two metal stearate salts was performed under inert atmosphere.[144] An enhancement in the activity was observed (~50% increase) and agglomerates with a "bow-tie" structure were found in the post-catalysis TEM study (Figure 1.26). Such a structure consists of a central spherical Cu(0) nanoparticles, with two pyramidal-shaped ZnO nanoparticles on its surface.

In 2013, our group developed a Cu/ZnO nanocatalyst combining Cu(0) nanoparticles (~ 5 nm) and ZnO nanoparticles (3–4 nm), applied in a continuous flow stirred reactor (CSTR) for the hydrogenation of CO_2 to methanol.[147] The hydrolysis of $ZnEt_2$, with dioctylphosphinate, was employed to synthesise ZnO nanoparticles (ZnO@DOPA). Cu(0) nanoparticles were synthesised from the reduction of $Cu(St)_2$, using two equivalents of hydrazine, forming a colloidal red solution in squalane. At a molar ratio of 35:65 Cu:ZnO, high activity was observed. After catalysis, inverse "bow-tie" structured agglomerates were observed, which were similar to the catalyst reported for syn-gas to methanol. To maximise Cu/ZnO interface formation, the control of ligand loading is important as it determines the available surface area for Cu-ZnO interaction. Next, the effect of varying the ligand on catalytic activity was studied. The formation of Cu(0) nanoparticle (~ 6 nm) was achieved by the hydrogenolysis of CuMes (2.5 bar H_2, 110 °C), in the presence of ZnO@DOPA (2–3 nm; entry 8, Table 1.1). The only ligand source is from ZnO nanoparticles and formation of Cu/ZnO interfaces in the pre-catalyst was observed. When subjected to CO_2 hydrogenation, this catalyst was 2–3 times more active than industrial Cu-ZnO-

Al_2O_3 catalyst. Further increase of ligand loading led to a decrease in activity, with no activity at all when ligand loading is an excess of one equivalent. The loss of activity was attributed to the presence of isolated nanoparticles in the post-catalysis samples (TEM) and the formation of molecular clusters. In addition, studies of various catalyst synthetic routes and their impact on catalysis were explored and will be presented in this thesis (*see Chapter 4*).

Comparisons between the catalytic activity of colloidal systems, in methanol synthesis, is not straightforward as conditions and processes differ, including variation of solvent, temperature, pressure and reactor set-up. Nevertheless, some colloidal nanocatalysts displayed higher activity than the industrial Cu-ZnO-Al_2O_3 catalyst, under the same reactor setup and conditions and this warrants investigation. The emphasis on the Cu/ZnO synergy is clear throughout the literature colloidal nanocatalysts and the formation of a Cu/ZnO interface appears critical to performance. Thus, variation in the catalyst synthetic parameters is a logical approach to promote its formation.

	Precursors						Reaction conditions				
Entry	**Cu**	**Zn**	**Cu:Zn**	**Reducing agent**	**Ligand**	**Solvent**	**T/ °C**	**P/ bar**	**Gas feed**	**% Activity [a]**	**Ref.**
1	$Cu(acac)_2$	$ZnEt_2$	50:50	$ZnEt_2$	Buta-1,3-diene	Buta-1,3-diene	260	60	50% CO 50% H_2	*Not reported*	*148*
2	Cu(acac)	$Al(Oct)_3$	-	$Al(Oct)_3$	$Al(Oct)_3$	THF	150	175–215	10% CO 4% CO_2 86% H_2	73	*150*
3	$Cu(St)_2$	$ZnEt_2$	55:45	$ZnEt_2$	Stearate	Squalane	250	50	66% CO_2 33% H_2	100	*151*
4	$Cu(OCHMeCH_2NMe_2)_2$	$ZnEt_2$	50:50	*Pyrolysis*	-	Squalene	220	60	10% CO 4% CO_2 72% H_2 14% N_2	84	*101*
5	$Cu(St)_2$	ZnO	67:33	H_2	Stearate	Squalane	220	26	32% CO 2% CO_2 64% H_2 2% N_2	65	*153*
6	$Cu(St)_2$	$Zn(St)_2$	50:50	H_2	Stearate	Squalane	220	26	10% CO 4% CO_2 72% H_2 14% N_2	>250	*144, 154*
7	Cu@St	ZnO@DOPA	35:65	Hydrazine	DOPA	Squalene	250	50	66% CO_2 33% H_2	>270	*147*
8	CuMes	ZnO@DOPA	50:50	H_2	DOPA	Mesitylene	210	50	66% CO_2 33% H_2	>260	*155*

Table 1.1. Table showing the comparison of colloidal methanol synthesis catalysts reported in literature. [a] the methanol activity, relative to the industrial ternary catalyst, Cu-ZnO-Al_2O_3. Abbreviations: acac = acetylacetonate, St = stearate, Mes = mesityl, DOPA = dioctylphosphinate.

1.5 Layered Zinc Hydroxides

1.5.1 Introduction & Existing Syntheses

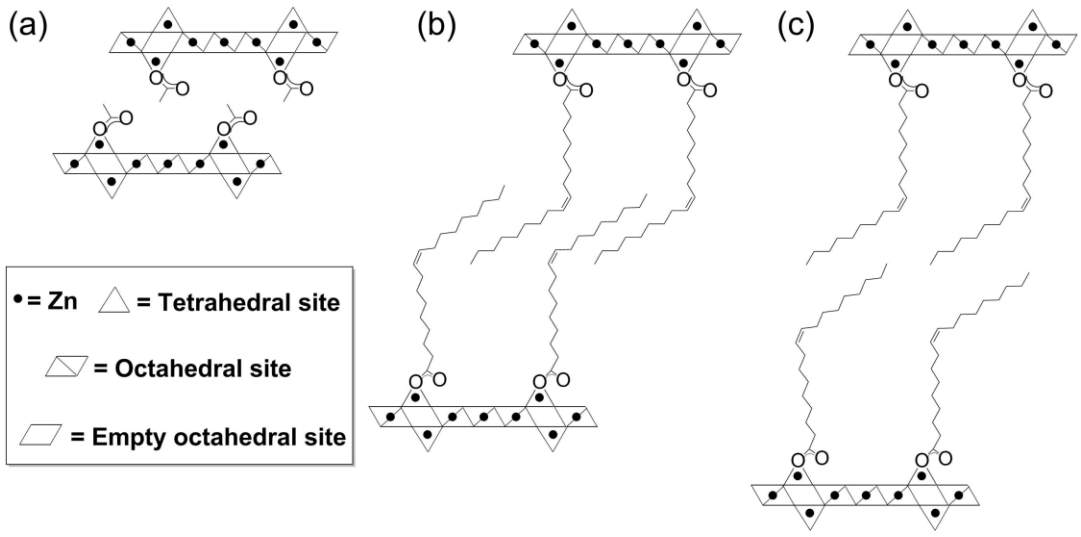

Figure 1.27. Structure of (a) LZH–OAc, (b) LZH–Ole with partial interdigitation and (c) LZH–Ole with no interdigitation occurring between the oleate chains.

Exfoliated 2D inorganic materials are of fundamental interest due to the potential to alter a material's electronic and chemical properties by separation into atomic layer thick, crystalline nanosheets.[156] For example, TiO_2 nanosheets exhibit a considerably larger band gap than the bulk due to a size quantisation effect (3.8 vs. 3.2 eV).[157] These nanosheets generate anodic photocurrents, under UV irradiation (< 320 nm), making them viable photocatalysts.[158] Significant research has been devoted to obtaining 2D inorganic nanosheets,[159-168] such as transition metal chalcogenides, other metal oxides and inorganic clays.[169-171]

Layered zinc hydroxides (LZHs) are a sub-class of inorganic clays with the general formula, $[Zn_5(OH)_8(A^n)_{2/n} \cdot nH_2O]$, where A^n is an intercalated anion, *e.g.* carboxylates, sulphate, chloride, carbonate or nitrate.[172-176] The structure of LZH is similar to that of Brucite (a uniform layer of octahedral units), with a quarter of the octahedral units

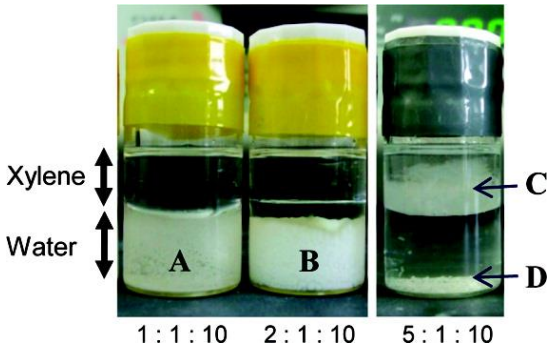

Figure 1.28. Appearance of the biphasic xylene–water systems with [benzoate]:[zinc]:[urea] = 1:1:10, 2:1:10, and 5:1:10 after the reaction at 80 °C for 24 h. Sample A, B, and D were formed in the aqueous phase of the system of [B]:[Z]:[U] = 1:1:10, 2:1:10, and 5:1:10, respectively. Sample C was formed in the xylene phase of only the system of [B]:[Z]:[U] = 5:1:10. *Reprinted (adapted) with permission from Inoue et al.*[177] *Copyright 2010 American Chemical Society.*

being replaced by tetrahedral units located above and below the octahedral plane (Figure 1.27).[94, 98, 99, 108, 113, 114] The intercalated anions are typically coordinated to tetrahedral zinc atoms at the apex of the tetrahedron. LZHs are commonly synthesised *via* base hydrolysis of zinc oxide or zinc salts (zinc carboxylates, zinc nitrate etc.) at elevated temperatures (> 60 °C).[173, 175, 178, 179] Despite the simplicity of these syntheses, LZHs often contain impurities such as hydrozincite, $[Zn_5(OH)_6(CO_3)_2]$, or zinc oxide, detectable by powder XRD.[180] These impurities are either formed by the over-hydrolysis of zinc salts, the presence of CO_2 during synthesis or unreacted zinc oxide contaminating the product. The presence of impurities may alter properties and hinder exfoliation.

In an attempt to eliminate these impurities and to improve yield, a biphasic system, operating at 80 °C for 24 h, produced LZHs at the organic–aqueous interface (Figure 1.28). [177, 181] A range of hydrophobic carboxylates were compatible with the method (benzoate, heptanoate, decanoate and dodecanoate). The optimal ratio was 1 : 1 : 10 ([carboxylate] : [zinc] : [urea]), which resulted in a yield of 89% (based on

Zn). Although the formation of hydrozincite was supressed, other impurities, such as ZnO, were still observed in XRD pattern (*see section 3.6 for further discussions*).[177]

1.5.2 Liquid Exfoliation of LZHs

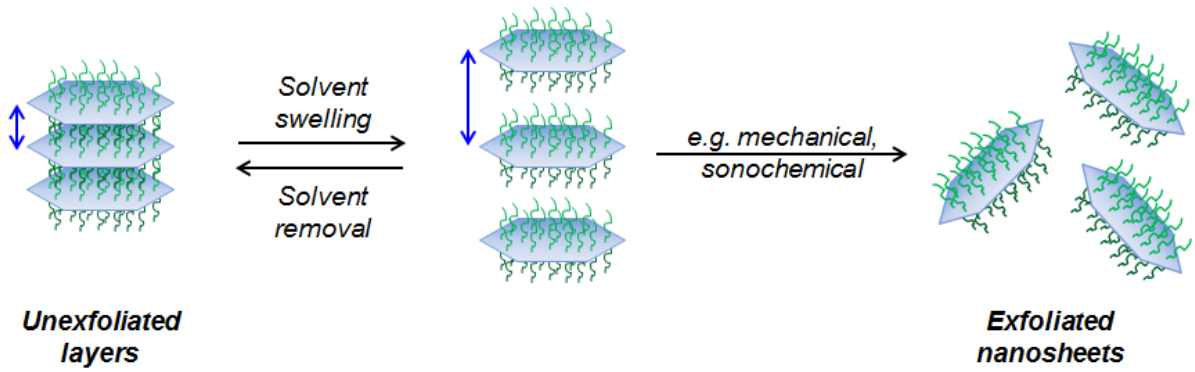

Figure 1.29. The exfoliation (or delamination) of a stack of 2D inorganic material. *Adapted from Sasaki et al.*[167] *Copyright 2006 American Chemical Society.*

Exfoliation (or delamination) is the physical separation of stacked layers into individual stable layers, *i.e.* monolayers (Figure 1.29). The reported thicknesses for monolayers range from 1–5 nm, dependent on the intercalated ions, and lateral sizes are typically 20–100 nm.[180, 182] Bulk 2D inorganic materials are weakly stacked structures which may be disrupted by external stimuli, such as mechanical or sonochemical processes. This disruption provides access to exfoliated monolayers, which have higher surface area and in some cases, enhanced electronic properties. For example, the exfoliation of graphite to graphene increases carrier mobility significantly (> 4000 $cm^2 V^{-1} s^{-1}$).[160, 183] The prospect of successful exfoliation of LZHs might lead to a wide range of applications, for example, high surface area catalytic supports.

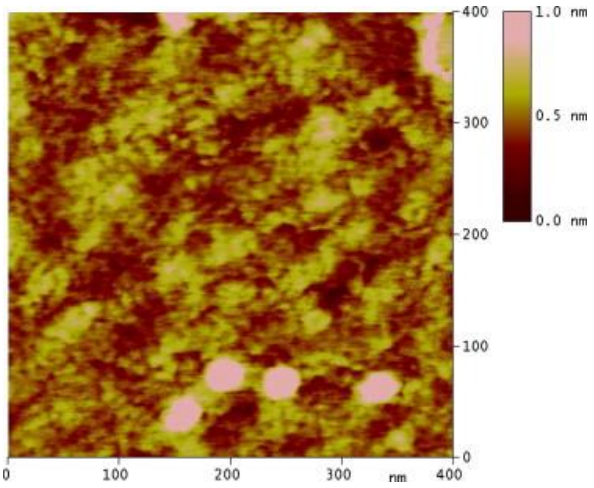

Figure 1.30. AFM image of exfoliated LZH–DS in butanol at 60 °C. *Reprinted with permission from Demel et al.[180] Copyright 2011 Elsevier.*

The most common method of exfoliation is top-down approach, *i.e.* synthesis of bulk material, followed by exfoliation into monolayers. So far, there are no reports of a bottom-up approach to LZH monolayers, *i.e.* the direct synthesis of monolayers. The following strategies are often implemented in exfoliation: 1) ion exchange, *e.g.* the exchange of intercalated NO_3^- with dodecylsulphate to weaken interlayer attractive forces, and 2) sonication of material in a solvent, *e.g.* 1-butanol, formamide, which can stabilise the exfoliated layers.[176, 180, 184] For methods 1 and 2, some form of agitation, such as thermal, shear or ultrasonication, is generally required to physically separate the layers.[110, 126, 132, 134]

The exfoliation of a series of layered compounds, LZH–OAc, LZH–OBz, LZH–DS and LZH–NO_3, was attempted using two methods: 1) mechanical stirring at room temperature or 2) heating to reflux in 1-butanol or formamide (60–118 °C) for 24 h.[180] Whilst most of the LZHs did not exfoliate, LZH–DS monolayers were formed using both methods. The highest solubility was for the LZH–DS in formamide (22 mg/mL). Atomic force microscopy (AFM) analysis showed a nanoplatelet

structure, with thicknesses below 1 nm (Figure 1.30). HR-TEM showed separated layers with some re-stacking due to the experimental conditions (Figure 1.31). In a different study, ultrasonication for 10 mins was employed to obtain LZH–OBz monolayers in alcoholic solvents (0.68 mg/mL in 1-butanol).[176]

In all the aforementioned methods, the isolated yields of monolayers and/or the extent of degradation were not addressed.[185] Furthermore, the exfoliated LZH colloids readily re-aggregate or decompose to zinc oxide (5–7 days). This means they are less stable than other metal hydroxide layers, such as Co(II) and Ni(II) hydroxide layers which typically take one week to decompose.[186-188]

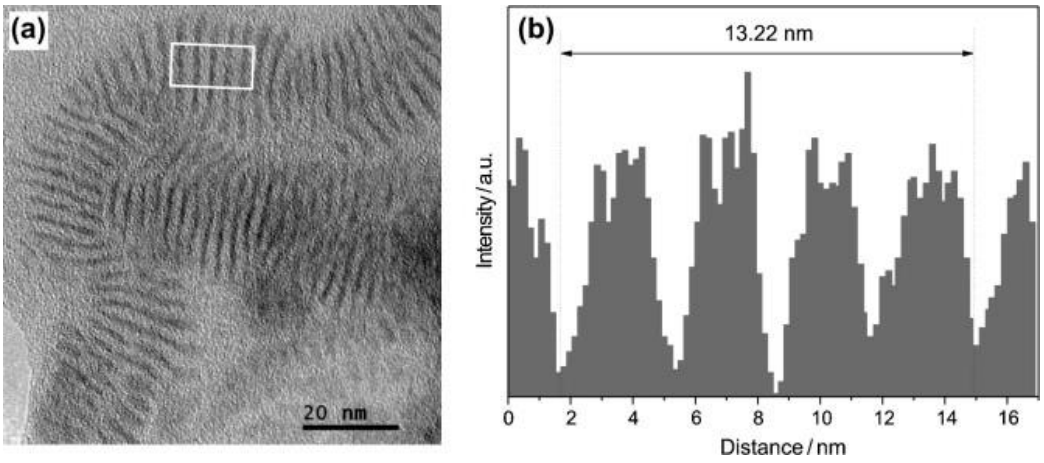

Figure 1.31. HR-TEM (a) LZH–DS exfoliated in butanol at 60 °C and deposited on a Cu grid. (b) electron density histogram of the area marked in (a). *Reprinted with permission from Demel et al.[180] Copyright 2011 Elsevier.*

1.5.3 Applications

LZHs are applied as sorbents, fire retardants, drug delivery vectors, photocatalysts and in electronic devices.[163] Due to the charged nature of the zinc hydroxide layers and the ease of anion exchange, LZHs are also interesting targets for the encapsulation of charged drugs, such as amoxicillin trihydrate and protocatechuic acid.[189, 190] The LZHs readily released the encapsulated drugs at pH 7.4, in phosphate buffer, where up to 90% release of protocatechuic acid was observed within 10 mins.[189-191] This was attributed to anion exchange between the encapsulated drug and the phosphate ions from the buffer.

The conversion of LZH, to ZnO *via* thermal degradation, provides an alternative route to access different morphologies of ZnO. In particular, thermal degradation of LZHs results in ZnO that retains the sheet-like structure of the precursor LZHs and this provides ZnO with a high surface area.[192-196] ZnO nanoplatelets, generated by the thermal degradation of LZHs, were employed as a photocatalyst for the photo-degradation of 4-chlorophenol to various compounds, such as 4-chlorocatechol and hydroquinone.[20] The photocatalyst was prepared by the inkjet-printing of LZH–DS nanosheets, followed by thermal degradation to ZnO nanosheets onto a glass substrate (80 °C, 24 h). The resulting ZnO film exhibited two times higher photocatalytic activity than films prepared by conventional sol-gel routes. The enhanced catalytic activity was attributed to the high surface area of the nanosheet morphology, as confirmed by surface gas adsorption measurements (32 vs. 4 $cm^2 g^{-1}$).

ZnO nanosheets, obtained by the thermal degradation of LZHs, were also investigated further for photovoltaic devices, such as dye-sensitised solar cells (DSSCs).[19] LZH–CO_3 was used as a precursor due to its degradation into carbon

dioxide, resulting in minimal carbon contamination in the resulting ZnO film.[195, 197] In one case, LZH–CO_3 was directly grown onto a titanium foil through chemical bath deposition.[194] A 25 μm-thick film of ZnO nanosheets (5–20 nm in size) was formed by annealing at 300 °C for 1 h. The DSSC formed using the ZnO film achieved an energy conversion efficiency (η) of 5.41%, with a V_{OC} of 0.54 V and J_{SC} of 18.9 mA cm^{-2}. It outperformed a DSSC prepared from ZnO nanoparticles (particle size of ~ 20 nm; η = 3.58%, V_{OC} = 0.47 V and J_{SC} = 12.9 mA cm^{-2}).

1.6 Thesis Aims

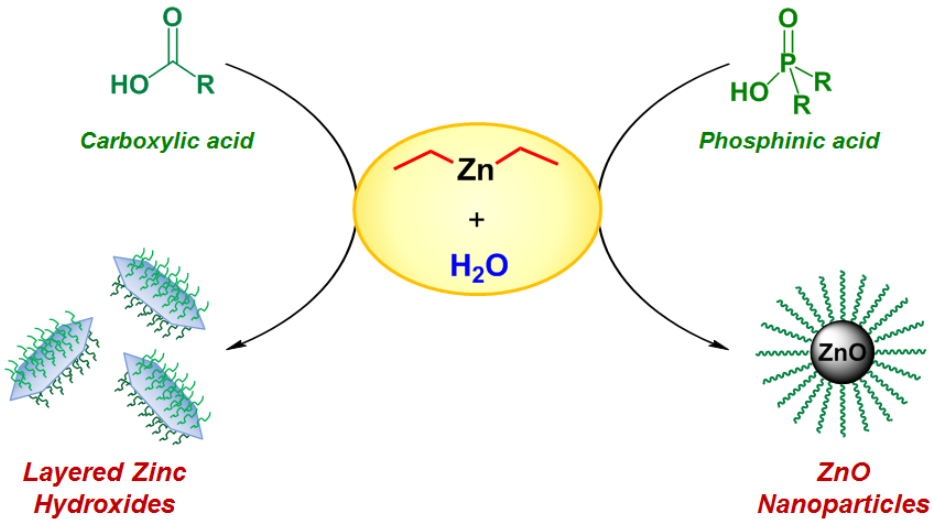

Figure 1.32. General scheme for the synthesis of colloidal ZnO nanoparticles and layered zinc hydroxides by the hydrolysis of $ZnEt_2$ in the presence of the appropriate carboxylic or phosphinic acid ligand.

This thesis focuses on the development of colloidal nanocatalysts for CO_2 hydrogenation to methanol. In order to improve the performance and gain insight into the catalysis, two synthetic parameters are investigated: the choice of ligand and dopants. As previously discussed in *section 1.4.*3, the ligand type and quantity are proposed to influence the surface sites of the Cu/ZnO nanocatalysts. The stabilisation of the nanoparticles is also essential to provide the high surface area beneficial for catalysis. Therefore, small ZnO nanoparticles which are resistant to ripening, should be useful in this catalysis. Furthermore, the promotional effects of dopants in ZnO are apparent in the heterogeneous Cu/ZnO catalyst, but have yet to be explored in colloidal Cu/ZnO nanocatalysts.[68, 147]

In order to modify the two synthetic parameters and investigate their impact on the catalysis, the hydrolysis of reactive diethylzinc will be used to prepare colloidal ZnO nanoparticles (Figure 1.32).[52, 58] One benefit of this route is that small

monodispersed ZnO nanoparticles (2–4 nm) are formed, with variable/controllable amounts of ligand.[52] The overall objectives are summarised as follows:

1. To investigate the effect of ligand loading, [COOR]/[Zn], in the reaction between diethylzinc and zinc *bis*(carboxylate) or carboxylic acid, on product distribution. Previous work demonstrated the formation of layered zinc hydroxide, along with ZnO nanoparticles, when a high loading of carboxylate ligand was employed.[198] The target is to investigate the optimal ligand loading which allows the sole formation of LZHs.

2. To modify the alkyl chain length on the phosphinate ligand for the capping of ZnO nanoparticles to investigate its effects on nanoparticle growth. In order to prevent the ripening of ZnO nanoparticles, by reaction with water, a long alkyl chain phosphinate is chosen for its hydrophobicity.

3. To introduce sub-stoichiometric amounts of a different organometallic reagent, MR_x ($M = Mg^{2+}$, Al^{3+}, Cu^{+}), to synthesise doped-ZnO nanoparticles, capped with dioctylphosphinate. The properties of the resulting doped-ZnO nanoparticles will be investigated to evaluate the efficacy of the doping strategy and to understand its effect, if any, on the catalysis.

4. To implement some of the aforementioned ZnO nanoparticles in the hydrogenation of CO_2 to methanol, in a liquid-phase reactor (Figure 1.33). The ZnO nanoparticles will be combined with Cu(0) nanoparticles to the catalyst system. Post-catalysis samples will be characterised with the goal of gaining a better understanding of the Cu/ZnO synergetic effect in catalysis.

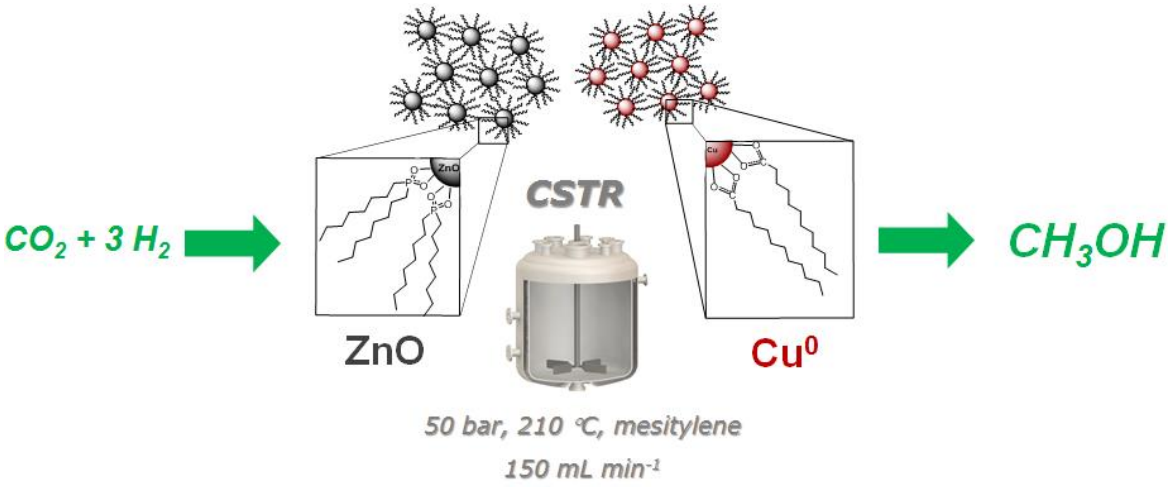

Figure 1.33. Schematic showing the hydrogenation of CO_2 to methanol, using colloidal ZnO and Cu(0) nanoparticles, in a continuous flow stirred tank reactor (CSTR; 50 bar CO_2:H_2 1:3, 210 °C, mesitylene, 150 mL min^{-1}).

1.7 References

1. S. Kango, S. Kalia, A. Celli, J. Njuguna, Y. Habibi and R. Kumar, *Prog. Polym. Sci*, 2013, **38**, 1232-1261.
2. R. L. Z. Hoye, K. P. Musselman and J. L. MacManus-Driscoll, *APL Mater.*, 2013, **1**, 060701.
3. D. Pla and M. Gómez, *ACS Catal.*, 2016, **6**, 3537-3552.
4. R. Ferrando, J. Jellinek and R. L. Johnston, *Chem. Rev.*, 2008, **108**, 845-910.
5. N. Yan, Y. Yuan and P. J. Dyson, *Dalton Trans.*, 2013, **42**, 13294-13304.
6. S. Horikoshi and N. Serpone, in *Microwaves in Nanoparticle Synthesis*, DOI: doi:10.1002/9783527648122.ch1.
7. V. Francesc, L. Yaroslava, S. Thorsten, L. M. P. A., P. Christian, S. Hans-Peter, L. Jörg, N. K. M. and G. Andreas, *Chem. Eur. J.*, 2010, **16**, 6530-6539.
8. A. P. Alivisatos, *J. Phys. Chem.*, 1996, **100**, 13226-13239.
9. V. K. LaMer and R. H. Dinegar, *J. Am. Chem. Soc.*, 1950, **72**, 4847-4854.
10. N. T. K. Thanh, N. Maclean and S. Mahiddine, *Chem. Rev.*, 2014, **114**, 7610-7630.
11. W. Z. Ostwald, *Phys. Chem.*, 1900, **34**, 495-503.
12. W. R. Lee, M. G. Kim, J. R. Choi, J.-I. Park, S. J. Ko, S. J. Oh and J. Cheon, *J. Am. Chem. Soc.*, 2005, **127**, 16090-16097.
13. A. C. S. Samia, K. Hyzer, J. A. Schlueter, C.-J. Qin, J. S. Jiang, S. D. Bader and X.-M. Lin, *J. Am. Chem. Soc.*, 2005, **127**, 4126-4127.
14. B. Ingham, T. H. Lim, C. J. Dotzler, A. Henning, M. F. Toney and R. D. Tilley, *Chem. Mater.*, 2011, **23**, 3312-3317.
15. D. Li, M. H. Nielsen, J. R. I. Lee, C. Frandsen, J. F. Banfield and J. J. De Yoreo, *Science*, 2012, **336**, 1014-1018.
16. D. Hapiuk, B. Masenelli, K. Masenelli-Varlot, D. Tainoff, O. Boisron, C. Albin and P. Mélinon, *J. Phys. Chem. C*, 2013, **117**, 10220-10227.
17. W. W. Yu, Y. A. Wang and X. Peng, *Chem. Mater.*, 2003, **15**, 4300-4308.
18. U. Özgür, Y. I. Alivov, C. Liu, A. Teke, M. A. Reshchikov, S. Doğan, V. Avrutin, S. J. Cho and H. Morkoç, *J. Appl. Phys.*, 2005, **98**, 041301.
19. S. Ueno and S. Fujihara, *J. Electrochem. Soc.*, 2011, **158**, K1.
20. J. Hynek, V. Kalousek, R. Zouzelka, P. Bezdicka, P. Dzik, J. Rathousky, J. Demel and K. Lang, *Langmuir*, 2014, **30**, 380-386.
21. H. Nishikiori, S. Nagaya, T. Takikawa, A. Kikuchi, T. Yamakami, H. Wagata, K. Teshima and T. Fujii, *Appl. Catal., B*, 2014, **160-161**, 651-657.
22. C. Li, Y. Lin, F. Li, L. Zhu, D. Sun, L. Shen, Y. Chen and S. Ruan, *RSC Adv.*, 2015, **5**, 80561-80567.
23. N. Lepot, M. K. Van Bael, H. Van den Rul, J. D'Haen, R. Peeters, D. Franco and J. Mullens, *Mater. Lett.*, 2007, **61**, 2624-2627.
24. M. Z. Ahmad, J. Chang, M. S. Ahmad, E. R. Waclawik and W. Wlodarski, *Sens. Actuators, B*, 2013, **177**, 286-294.
25. Y.-S. Fu, X.-W. Du, S. A. Kulinich, J.-S. Qiu, W.-J. Qin, R. Li, J. Sun and J. Liu, *J. Am. Chem. Soc.*, 2007, **129**, 16029-16033.
26. X. Tang, E. S. G. Choo, L. Li, J. Ding and J. Xue, *Chem. Mater.*, 2010, **22**, 3383-3388.
27. J. Pan, J. Chen, Q. Huang, Q. Khan, X. Liu, Z. Tao, Z. Zhang, W. Lei and A. Nathan, *ACS Photonics*, 2016, **3**, 215-222.
28. R. Vittal and K.-C. Ho, *Renewable Sustainable Energy Rev.*, 2017, **70**, 920-935.

29. L. J. A. Koster, W. J. van Strien, W. J. E. Beek and P. W. M. Blom, *Adv. Funct. Mater.*, 2007, **17**, 1297-1302.
30. B. W. J. E., W. M. M. and J. R. A. J., *Adv. Mater.*, 2004, **16**, 1009-1013.
31. C. B. Ong, L. Y. Ng and A. W. Mohammad, *Renewable Sustainable Energy Rev.*, 2018, **81**, 536-551.
32. C. Hariharan, *Appl. Catal., A*, 2006, **304**, 55-61.
33. T. Tsuzuki and P. G. McCormick, *Scripta Mater.*, 2001, 1731.
34. N. Salah, S. S. Habib, Z. H. Khan, A. Memic, A. Azam, E. Alarfaj, N. Zahed and S. Al-Hamedi, *Int. J. Nanomed.*, 2011, **6**, 863-869.
35. L. Janusz, Ś. Witold, D. Maciej, J. Iwona and L. Janusz, *Angew. Chem. Int. Ed.*, 2006, **118**, 4944-4947.
36. L. Janusz, D. Michał, L. Michał, Ś. Witold, Z. Karolina, J. Iwona and L. Janusz, *Angew. Chem. Int. Ed.*, 2010, **49**, 8266-8269.
37. S. Polarz, A. Orlov, A. Hoffmann, M. R. Wagner, C. Rauch, R. Kirste, W. Gehlhoff, Y. Aksu, M. Driess, M. W. E. van den Berg and M. Lehmann, *Chem. Mater.*, 2009, **21**, 3889-3897.
38. W. Bury, E. Krajewska, M. Dutkiewicz, K. Sokolowski, I. Justyniak, Z. Kaszkur, K. J. Kurzydlowski, T. Plocinski and J. Lewinski, *Chem. Commun.*, 2011, **47**, 5467-5469.
39. J. Hambrock, S. Rabe, K. Merz, A. Birkner, A. Wohlfart, R. A. Fischer and M. Driess, *J. Mater. Chem.*, 2003, **13**, 1731.
40. C. J. Brinker and G. W. Scherer, *Sol-Gel Science: The Physics and Chemistry of Sol-Gel Processing*, Academic Press, Inc,, 1990.
41. L. Spanhel and M. A. Anderson, *J. Am. Chem. Soc.*, 1991, **113**, 2826-2833.
42. L. Spanhel, *J. Sol-Gel Sci. Technol.*, 2006, **39**, 7-24.
43. C. B. Murray, D. J. Norris and M. G. Bawendi, *J. Am. Chem. Soc.*, 1993, **115**, 8706-8715.
44. A. Rodriguez, C. Amiens, B. Chaudret, M.-J. Casanove, P. Lecante and J. S. Bradley, *Chem. Mater.*, 1996, **8**, 1978-1986.
45. F. Rataboul, C. Nayral, M.-J. Casanove, A. Maisonnat and B. Chaudret, *J. Organomet. Chem.*, 2002, **643-644**, 307-312.
46. W. Kuran and M. Czernecka, *J. Organomet. Chem.*, 1984, **263**, 1-7.
47. J. A. Garden and S. D. Pike, *Dalton Trans.*, 2018, **47**, 3638-3662.
48. A. Gonzalez-Campo, K. L. Orchard, N. Sato, M. S. Shaffer and C. K. Williams, *Chem. Commun.*, 2009, 4034-4036.
49. M. Monge, M. L. Kahn, A. Maisonnat and B. Chaudret, *Angew. Chem. Int. Ed.*, 2003, **42**, 5321-5324.
50. M. L. Kahn, M. Monge, V. Collière, F. Senocq, A. Maisonnat and B. Chaudret, *Adv. Funct. Mater.*, 2005, **15**, 458-468.
51. S. D. Pike, E. R. White, M. S. Shaffer and C. K. Williams, *Nat. Commun.*, 2016, **7**, 13008.
52. K. L. Orchard, M. S. P. Shaffer and C. K. Williams, *Chem. Mater.*, 2012, **24**, 2443-2448.
53. R. J. Herold, S. L. Aggarwal and V. Neff, *Can. J. Chem.*, 1963, **41**, 1368-1380.
54. C. Lizandara-Pueyo, M. W. E. van den Berg, A. De Toni, T. Goes and S. Polarz, *J. Am. Chem. Soc.*, 2008, **130**, 16601-16610.
55. S. Inoue, M. Kobayashi and T. Tozuka, *J. Organomet. Chem.*, 1974, **81**, 17-21.
56. M. L. Kahn, T. Cardinal, B. Bousquet, M. Monge, V. Jubera and B. Chaudret, *ChemPhysChem*, 2006, **7**, 2392-2397.

57. K. L. Orchard, J. E. Harris, A. J. P. White, M. S. P. Shaffer and C. K. Williams, *Organometallics*, 2011, **30**, 2223-2229.
58. S. D. Pike, E. R. White, M. S. P. Shaffer and C. K. Williams, *Nat. Commun.*, 2016, **7**, 13008.
59. Y. Yin and A. P. Alivisatos, *Nature*, 2005, **437**, 664-670.
60. L. Manna, E. C. Scher and A. P. Alivisatos, *J. Am. Chem. Soc.*, 2000, **122**, 12700-12706.
61. K. Soulantica, L. Erades, M. Sauvan, F. Senocq, A. Maisonnat and B. Chaudret, *Adv. Funct. Mater.*, 2003, **13**, 553-557.
62. S. Zhang, G. Leem, L. O. Srisombat and T. R. Lee, *J. Am. Chem. Soc.*, 2008, **130**, 113-120.
63. C. Yannick, S. Grégory, P. Carole, C. Bruno, M. André and K. M. L., *Chem. Eur. J.*, 2012, **18**, 5384-5393.
64. S. Saliba, Y. Coppel, P. Davidson, C. Mingotaud, B. Chaudret, M. L. Kahn and J.-D. Marty, *J. Mater. Chem.*, 2011, **21**, 6821.
65. C. Pagès, Y. Coppel, M. L. Kahn, A. Maisonnat and B. Chaudret, *ChemPhysChem*, 2009, **10**, 2334-2344.
66. R. Buonsanti and D. J. Milliron, *Chem. Mater.*, 2013, **25**, 1305-1317.
67. S. T. Ochsenbein and D. R. Gamelin, *Nat. Nanotechnol.*, 2011, **6**, 112-115.
68. J. Schumann, M. Eichelbaum, T. Lunkenbein, N. Thomas, M. C. Álvarez Galván, R. Schlögl and M. Behrens, *ACS Catal.*, 2015, **5**, 3260-3270.
69. I. Hwang, H. Kim, J.-E. Kim, H. Y. Park and H. Lim, *Phys. Rev. B*, 1994, **50**, 8849-8852.
70. S. C. Erwin, L. Zu, M. I. Haftel, A. L. Efros, T. A. Kennedy and D. J. Norris, *Nature*, 2005, **436**, 91.
71. G. Galli, *Nature*, 2005, **436**, 32.
72. S. Mehra, A. Bergerud, D. J. Milliron, E. M. Chan and A. Salleo, *Chem. Mater.*, 2016, **28**, 3454-3461.
73. S. Heitz, Y. Aksu, C. Merschjann and M. Driess, *Chem. Eur. J.*, 2011, **17**, 3904-3910.
74. S. Jana, Y. Aksu and M. Driess, *Dalton Trans.*, 2009, 1516-1521.
75. K. Merz, S. Block, R. Schoenen and M. Driess, *Dalton Trans.*, 2003, 3365-3369.
76. N. Pradhan, D. Goorskey, J. Thessing and X. Peng, *J. Am. Chem. Soc.*, 2005, **127**, 17586-17587.
77. R. Buonsanti, A. Llordes, S. Aloni, B. A. Helms and D. J. Milliron, *Nano Lett.*, 2011, **11**, 4706-4710.
78. D. Chen, R. Viswanatha, G. L. Ong, R. Xie, M. Balasubramaninan and X. Peng, *J. Am. Chem. Soc.*, 2009, **131**, 9333-9339.
79. M. Behrens, S. Zander, P. Kurr, N. Jacobsen, J. Senker, G. Koch, T. Ressler, R. W. Fischer and R. Schlögl, *J. Am. Chem. Soc.*, 2013, **135**, 6061-6068.
80. S. Schimpf and M. Muhler, *Synthesis of Solid Catalysts*, 2009.
81. G. A. Olah, *Angew. Chem. Int. Ed.*, 2013, **52**, 104-107.
82. G. A. Olah, A. Goeppert and G. K. S. Prakash, *Beyond Oil and Gas: The Methanol Economy*, Wiley, 2009.
83. J. Schumann, T. Lunkenbein, A. Tarasov, N. Thomas, R. Schlögl and M. Behrens, *ChemCatChem*, 2014, **6**, 2889-2897.
84. M. Behrens and R. Schlögl, *Z. Anorg. Allg. Chem.*, 2013, **639**, 2683-2695.
85. S. G. Jadhav, P. D. Vaidya, B. M. Bhanage and J. B. Joshi, *Chem. Eng. Res. Des.*, 2014, **92**, 2557-2567.

86. J. Ma, N. Sun, X. Zhang, N. Zhao, F. Xiao, W. Wei and Y. Sun, *Catal. Today*, 2009, **148**, 221-231.
87. K. Klier, V. Chatikavanij, R. G. Herman and G. W. Simmons, *J. Catal.*, 1982, **74**, 343-360.
88. G. C. Chinchen, P. J. Denny, D. G. Parker, M. S. Spencer and D. A. Whan, *Appl. Catal.*, 1987, **30**, 333-338.
89. L. C. Grabow and M. Mavrikakis, *ACS Catal.*, 2011, **1**, 365-384.
90. K. C. Waugh, *Catal. Lett.*, 2012, **142**, 1153-1166.
91. F. Studt, M. Behrens, E. L. Kunkes, N. Thomas, S. Zander, A. Tarasov, J. Schumann, E. Frei, J. B. Varley, F. Abild-Pedersen, J. K. Nørskov and R. Schlögl, *ChemCatChem*, 2015, **7**, 1105-1111.
92. K. C. Waugh, *Catal. Today*, 1992, **15**, 51-75.
93. K. C. Waugh, *Catal. Lett.*, 1999, **58**, 163-165.
94. R. Burch, S. E. Golunski and M. S. Spencer, *J. Chem. Soc., Faraday Trans.*, 1990, **86**, 2683-2691.
95. J. C. Frost, *Nature*, 1988, **334**, 577.
96. F. Liao, Y. Huang, J. Ge, W. Zheng, K. Tedsree, P. Collier, X. Hong and S. C. Tsang, *Angew. Chem. Int. Ed.*, 2011, **50**, 2162-2165.
97. F. Liao, Z. Zeng, C. Eley, Q. Lu, X. Hong and S. C. Tsang, *Angew. Chem. Int. Ed.*, 2012, **51**, 5832-5836.
98. T. Fujitani and J. Nakamura, *Catal. Lett.*, 1998, **56**, 119-124.
99. N.-Y. Topsøe and H. Topsøe, *J. Mol. Catal. A: Chem.*, 1999, **141**, 95-105.
100. T. Lunkenbein, J. Schumann, M. Behrens, R. Schlogl and M. G. Willinger, *Angew. Chem. Int. Ed.*, 2015, **54**, 4544-4548.
101. M. K. Schroter, L. Khodeir, M. W. van den Berg, T. Hikov, M. Cokoja, S. Miao, W. Grunert, M. Muhler and R. A. Fischer, *Chem. Commun.*, 2006, **23**, 2498-2500.
102. P. L. Hansen, J. B. Wagner, S. Helveg, J. R. Rostrup-Nielsen, B. S. Clausen and H. Topsøe, *Science*, 2002, **295**, 2053-2055.
103. C. Holse, C. F. Elkjær, A. Nierhoff, J. Sehested, I. Chorkendorff, S. Helveg and J. H. Nielsen, *J. Phys. Chem. C*, 2015, **119**, 2804-2812.
104. A. Le Valant, C. Comminges, C. Tisseraud, C. Canaff, L. Pinard and Y. Pouilloux, *J. Catal.*, 2015, **324**, 41-49.
105. C. Tisseraud, C. Comminges, T. Belin, H. Ahouari, A. Soualah, Y. Pouilloux and A. Le Valant, *J. Catal.*, 2015, **330**, 533-544.
106. C. Tisseraud, C. Comminges, S. Pronier, Y. Pouilloux and A. Le Valant, *J. Catal.*, 2016, **343**, 106-114.
107. E. W. Thornton, H. Knözinger, B. Tesche, J. J. Rafalko and B. C. Gates, *J. Catal.*, 1980, **62**, 117-126.
108. I. Masaru, *Bull. Chem. Soc. Jpn.*, 1978, **51**, 2268-2272.
109. N. Koizumi, K. Murai, T. Ozaki and M. Yamada, *Catal. Today*, 2004, **89**, 465-478.
110. X. Zhou, J. Qu, F. Xu, J. Hu, J. S. Foord, Z. Zeng, X. Hong and S. C. Edman Tsang, *Chem. Commun.*, 2013, **49**, 1747-1749.
111. E. M. Fiordaliso, I. Sharafutdinov, H. W. P. Carvalho, J.-D. Grunwaldt, T. W. Hansen, I. Chorkendorff, J. B. Wagner and C. D. Damsgaard, *ACS Catal.*, 2015, **5**, 5827-5836.
112. J. Qu, X. Zhou, F. Xu, X.-Q. Gong and S. C. E. Tsang, *J. Phys. Chem. C*, 2014, **118**, 24452-24466.
113. L. Liandi, Z. Bingsen, K. Edward, F. Karin, A. Marc, S. D. Sheng, W. Wei, S. Robert and B. Malte, *ChemCatChem*, 2012, **4**, 1764-1775.

114. W. Tong, A. West, K. Cheung, K.-M. Yu and S. C. E. Tsang, *ACS Catal.*, 2013, **3**, 1231-1244.
115. M. M.-J. Li, Z. Zeng, F. Liao, X. Hong and S. C. E. Tsang, *J. Catal.*, 2016, **343**, 157-167.
116. M. M. J. Li, C. Chen, T. Ayvalı, H. Suo, J. Zheng, I. F. Teixeira, L. Ye, H. Zou, D. O'Hare and S. C. E. Tsang, *ACS Catal.*, 2018, **8**, 4390-4401.
117. N. Iwasa, T. Mayanagi, N. Ogawa, K. Sakata and N. Takezawa, *Catal. Lett.*, 1998, **54**, 119-123.
118. H. Lorenz, W. Jochum, B. Klötzer, M. Stöger-Pollach, S. Schwarz, K. Pfaller and S. Penner, *Appl. Catal., A*, 2008, **347**, 34-42.
119. M. Oliver, M. A. J., M. Cecilia, M. Sharon, S. T. F., H. Roland, D. Charlotte, C. F. Daniel and P. R. Javier, *Angew. Chem. Int. Ed.*, 2016, **55**, 6261-6265.
120. G. J. Hutchings, *Catal. Lett.*, 2001, **75**, 1-12.
121. G. Ertl, H. Knözinger, F. Schüth and J. Weitkamp, *Handbook of Heterogeneous Catalysis*, Wiley-VCH, Weinheim, Germany, 2008.
122. M. Behrens, G. Lolli, N. Muratova, I. Kasatkin, M. Havecker, R. N. d'Alnoncourt, O. Storcheva, K. Kohler, M. Muhler and R. Schlogl, *Phys. Chem. Chem. Phys.*, 2013, **15**, 1374-1381.
123. A. A. E., T. A. L. and O. H. Dermot, *Angew. Chem. Int. Ed.*, 2009, **48**, 9839-9843.
124. Y.-N. Li, R. Ma, L.-N. He and Z.-F. Diao, *Catal. Sci Technol.*, 2014, **4**, 1498-1512.
125. C. A. Huff and M. S. Sanford, *J. Am. Chem. Soc.*, 2011, **133**, 18122-18125.
126. S. Wesselbaum, V. Moha, M. Meuresch, S. Brosinski, K. M. Thenert, J. Kothe, T. v. Stein, U. Englert, M. Holscher, J. Klankermayer and W. Leitner, *Chem. Sci.*, 2015, **6**, 693-704.
127. B. Ekambaram, B. D. Yehoshoa and M. David, *Angew. Chem. Int. Ed.*, 2011, **123**, 11906-11909.
128. E. Balaraman, C. Gunanathan, J. Zhang, L. J. W. Shimon and D. Milstein, *Nat. Chem.*, 2011, **3**, 609.
129. W. Sebastian, v. S. Thorsten, K. Jürgen and L. Walter, *Angew. Chem. Int. Ed.*, 2012, **124**, 7617-7620.
130. S. Lee and A. Sardesai, *Top. Catal.*, 2005, **32**, 197-207.
131. E. C. Heydorn and P. J. A. Tijm, *Gasification Technology Council Meeting*, San Francisco, USA, 1998.
132. A. Cybulski, *Catalysis Reviews*, 1994, **36**, 557-615.
133. H. H. Kung, *Catal. Today*, 1992, **11**, 443-453.
134. X. Zhang, L. Zhong, Q. Guo, H. Fan, H. Zheng and K. Xie, *Fuel*, 2010, **89**, 1348-1352.
135. A. Sawant, M. K. Ko, V. Parameswaran, S. Lee and C. J. Kulik, *Fuel Sci. Technol. Int.*, 1987, **5**, 77-88.
136. E. C. Heydorn, B. W. Diamond and R. D. Lilly, *Commercial Scale Demonstration of the Liquid Phase Methanol (LPMEOH) Process Final Report*, 2003.
137. A. Roucoux, J. Schulz and H. Patin, *Chem. Rev.*, 2002, **102**, 3757-3778.
138. C.-J. Jia and F. Schuth, *Phys. Chem. Chem. Phys.*, 2011, **13**, 2457-2487.
139. A. Didier, L. Feng and A. J. Ruiz, *Angew. Chem. Int. Ed.*, 2005, **44**, 7852-7872.
140. K. An, S. Alayoglu, T. Ewers and G. A. Somorjai, *J. Colloid Interface Sci.*, 2012, **373**, 1-13.
141. S. Carregal-Romero, J. Pérez-Juste, P. Hervés, L. M. Liz-Marzán and P. Mulvaney, *Langmuir*, 2010, **26**, 1271-1277.

142. S. Jones, S. M. Fairclough, M. Gordon-Brown, W. Zheng, A. Kolpin, B. Pang, W. C. H. Kuo, J. M. Smith and S. C. E. Tsang, *Chem. Commun.*, 2015, **51**, 46-49.
143. M. Zahmakran and S. Ozkar, *Nanoscale*, 2011, **3**, 3462-3481.
144. S. Schimpf, A. Rittermeier, X. Zhang, Z.-A. Li, M. Spasova, M. W. E. van den Berg, M. Farle, Y. Wang, R. A. Fischer and M. Muhler, *ChemCatChem*, 2010, **2**, 214-222.
145. A. García-Trenco, E. R. White, A. Regoutz, D. J. Payne, M. S. P. Shaffer and C. K. Williams, *ACS Catal.*, 2017, **7**, 1186-1196.
146. A. García-Trenco, A. Regoutz, E. R. White, D. J. Payne, M. S. P. Shaffer and C. K. Williams, *Appl. Catal., B*, 2018, **220**, 9-18.
147. N. J. Brown, J. Weiner, K. Hellgardt, M. S. Shaffer and C. K. Williams, *Chem. Commun.*, 2013, **49**, 11074-11076.
148. M. Simon, A. Mortreux and F. Petit, *J. Chem. Soc., Chem. Commun.*, 1988, 1445-1446.
149. J. M. Corker and J. Evans, *J. Chem. Soc., Chem. Commun.*, 1994, 1027-1029.
150. V. Sascha, T. Oliver, G. Jan-Dierk, K. Christoph and S. Ferdi, *Angew. Chem. Int. Ed.*, 2005, **117**, 8192-8195.
151. N. J. Brown, A. García-Trenco, J. Weiner, E. R. White, M. Allinson, Y. Chen, P. P. Wells, E. K. Gibson, K. Hellgardt, M. S. P. Shaffer and C. K. Williams, *ACS Catal.*, 2015, **5**, 2895-2902.
152. S. Luidold and H. Antrekowitsch, *JOM*, 2007, **59**, 20-26.
153. M. A. Sliem, S. Turner, D. Heeskens, S. B. Kalidindi, G. V. Tendeloo, M. Muhler and R. A. Fischer, *Phys. Chem. Chem. Phys.*, 2012, **14**, 8170-8178.
154. A. Rittermeier, S. Miao, M. K. Schroter, X. Zhang, M. W. E. van den Berg, S. Kundu, Y. Wang, S. Schimpf, E. Loffler, R. A. Fischer and M. Muhler, *Phys. Chem. Chem. Phys.*, 2009, **11**, 8358-8366.
155. S. D. Pike, A. García-Trenco, E. R. White, A. H. M. Leung, J. Weiner, M. S. P. Shaffer and C. K. Williams, *Catal. Sci. Technol.*, 2017, **7**, 3842-3850.
156. R. Ma and T. Sasaki, *Adv. Mater.*, 2010, **22**, 5082-5104.
157. T. Sasaki and M. Watanabe, *J. Phys. Chem. B*, 1997, **101**, 10159-10161.
158. N. Sakai, Y. Ebina, K. Takada and T. Sasaki, *J. Am. Chem. Soc.*, 2004, **126**, 5851-5858.
159. K. S. Novoselov, A. K. Geim, S. Morozov, D. Jiang, Y. Zhang, S. a. Dubonos, I. Grigorieva and A. Firsov, *Science*, 2004, **306**, 666-669.
160. J. N. Coleman, M. Lotya, A. O'Neill, S. D. Bergin, P. J. King, U. Khan, K. Young, A. Gaucher, S. De and R. J. Smith, *Science*, 2011, **331**, 568-571.
161. F. Wang, J.-H. Seo, G. Luo, M. B. Starr, Z. Li, D. Geng, X. Yin, S. Wang, D. G. Fraser and D. Morgan, *Nat. Commun.*, 2016, **7**.
162. H. Yin and Z. Tang, *Chem. Soc. Rev.*, 2016, **45**, 4873-4891.
163. Q. Wang and D. O'Hare, *Chem. Rev.*, 2012, **112**, 4124-4155.
164. H. Yin, S. Zhao, K. Zhao, A. Muqsit, H. Tang, L. Chang, H. Zhao, Y. Gao and Z. Tang, *Nat Commun*, 2015, **6**, 6430.
165. H. Tang, J. Wang, H. Yin, H. Zhao, D. Wang and Z. Tang, *Adv. Mater.*, 2015, **27**, 1117-1123.
166. S. Zhao, Y. Wang, J. Dong, C.-T. He, H. Yin, P. An, K. Zhao, X. Zhang, C. Gao, L. Zhang, J. Lv, J. Wang, J. Zhang, A. M. Khattak, N. A. Khan, Z. Wei, J. Zhang, S. Liu, H. Zhao and Z. Tang, *Nat. Energy*, 2016, **1**, 16184.
167. Z. Liu, R. Ma, M. Osada, N. Iyi, Y. Ebina, K. Takada and T. Sasaki, *J. Am. Chem. Soc.*, 2006, **128**, 4872-4880.

168. R. Ma, Z. Liu, L. Li, N. Iyi and T. Sasaki, *J. Mater. Chem.*, 2006, **16**, 3809.
169. R. Allman, *Acta Cryst.*, 1968, **24**, 972-977.
170. H. F. W. Taylor, *Mineral. Mag.*, 1973, **39**, 377-389.
171. G. W. Brindley and S. Kikkawa, *Am. Mineral.*, 1979, **64**, 86-843.
172. S. Ghose, *Acta Cryst.*, 1964, **17**, 1051-1057.
173. L. Poul, N. Jouini and F. Fiévet, *Chem. Mater.*, 2000, **12**, 3123-3132.
174. Z. P. Xu and P. S. Braterman, *J. Mater. Chem.*, 2003, **13**, 268-273.
175. F. Wypych, G. G. Arizaga and J. E. da Costa Gardolinski, *J. Colloid Interface Sci.*, 2005, **283**, 130-138.
176. J. Miao, M. Xue, H. Itoh and Q. Feng, *J. Mater. Chem.*, 2006, **16**, 474-480.
177. S. Inoue and S. Fujihara, *Inorg. Chem.*, 2011, **50**, 3605-3612.
178. G. G. C. Arizaga, K. G. Satyanarayana and F. Wypych, *Solid State Ion.*, 2007, **178**, 1143-1162.
179. V. Briois, C. Giorgetti, F. Baudelet, S. Blanchandin, M. Tokumoto, S. H. Pulcinelli and C. V. Santilli, *J. Phys. Chem. C*, 2007, **111**, 3253-3258.
180. J. Demel, J. Plestil, P. Bezdicka, P. Janda, M. Klementova and K. Lang, *J. Colloid Interface Sci.*, 2011, **360**, 532-539.
181. S. Inoue and S. Fujihara, *Langmuir*, 2010, **26**, 15938-15944.
182. A. H. M. Leung, S. D. Pike, A. J. Clancy, H. C. Yau, W. J. Lee, K. L. Orchard, M. S. P. Shaffer and C. K. Williams, *Chem. Sci.*, 2018, **9**, 2135-2146.
183. A. K. Geim, *Science*, 2009, **324**, 1530-1534.
184. L. Zhao, J. Miao, H. Wang, Y. Ishikawa and Q. Feng, *J. Ceram. Soc. Jpn.*, 2009, **117**, 1115-1119.
185. H. C. Yau, M. K. Bayazit, J. H. Steinke and M. S. Shaffer, *Chem. Commun.*, 2015, **51**, 16621-16624.
186. C. Nethravathi, G. Harichandran, C. Shivakumara, N. Ravishankar and M. Rajamathi, *J. Colloid Interface Sci.*, 2005, **288**, 629-633.
187. J. T. Rajamathi, A. Arulraj, N. Ravishankar, J. Arulraj and M. Rajamathi, *Langmuir*, 2008, **24**, 11164-11168.
188. J. Machado, N. Ravishankar and M. Rajamathi, *Solid State Sci.*, 2010, **12**, 1399-1403.
189. F. Barahuie, M. Z. Hussein, S. A. Gani, S. Fakurazi and Z. Zainal, *Int. J. Nanomed.*, 2014, **9**, 3137-3149.
190. H. Nabipour, M. Hosaini Sadr and N. Thomas, *J. Exp. Nanosci.*, 2015, **10**, 1269-1284.
191. H. Nabipour and M. H. Sadr, *Bull. Mater. Sci.*, 2015, **38**, 1561-1567.
192. E. Hosono, S. Fujihara, T. Kimura and H. Imai, *J. Colloid Interface Sci.*, 2004, **272**, 391-398.
193. H. Wang and C. Xie, *J. Cryst. Growth*, 2006, **291**, 187-195.
194. Y.-H. Lai, C.-Y. Lin, H.-W. Chen, J.-G. Chen, C.-W. Kung, R. Vittal and K.-C. Ho, *J. Mater. Chem.*, 2010, **20**, 9379.
195. T. Yuki, S. Ueno, M. Hagiwara and S. Fujihara, *J. Asian Ceram. Soc.*, 2015, **3**, 144-150.
196. M.-K. Liang, M. J. Limo, A. Sola-Rabada, M. J. Roe and C. C. Perry, *Chem. Mater.*, 2014, **26**, 4119-4129.
197. H. Kajihara, M. Hagiwara and S. Fujihara, *J. Ceram. Soc. Jpn.*, 2016, **124**, 673-677.

198. K. L. Orchard, The Mild Synthesis of Zinc Oxide Nanoparticles and Nanocomposites via hydrolysis of Well-Characterised Zinc Organometallics, Imperial College London, 2011.

Chapter 2

Characterisation Techniques

2.1 Powder X-Ray Diffraction

Powder X-ray diffraction (XRD) is widely used for the identification and characterisation of crystalline solid powders. The X-ray source is diffracted by the periodically crystalline powder sample and the scattered rays constructively interfere with one another to generate characteristic diffraction features, as described by Bragg's Law:[1]

$$n\lambda = 2d \sin\theta \tag{2.1}$$

where n is an integer, λ is the wavelength of the incident radiation, d is the interplanar spacing and θ is the scattering angle. In the case of LZH, d is an important parameter; it is the interlayer spacing as dictated by (001) basal plane of the material.

Although Bragg's Law is useful, it is only accurate for ideal crystal systems with no imperfections and infinite lattice size. The size of the nanoparticles can be estimated using the Scherrer equation:[1]

$$\tau = \frac{K\lambda}{\beta \cos\theta} \tag{2.2}$$

where τ is the mean size of ordered crystalline domain, K is a dimensionless shape factor (close to unity), λ is the wavelength of the incident radiation, β is the line broadening at full width half maximum (FWHM) and θ is the scattering angle. The use of the Scherrer equation to analyse crystallite sizes is limited to nano-scale particles and it often provides the lower bound of the particle size, mainly due to the inhomogeneous strain and crystal lattice imperfections. Depending on the planes used for Scherrer analysis, the difference in the size measurement can indicate the aspect ratio of the sample. The estimated sizes of the synthesised ZnO nanoparticles

from XRD were cross-checked with sizes estimated from other techniques such as UV-Vis spectroscopy and TEM.

For phase identification, reference diffraction patterns for known materials can be obtained from the International Centre for Diffraction Data (previously known as the Joint Committee on Powder Diffraction Standards, JCPDS). For ZnO, the reference pattern has the JCPDS card number of 00-001-1136 (Figure 2.1). For data processing, all XRD patterns presented in this thesis have all been peak fitted using fitting software (Fityk, version 0.9.8).

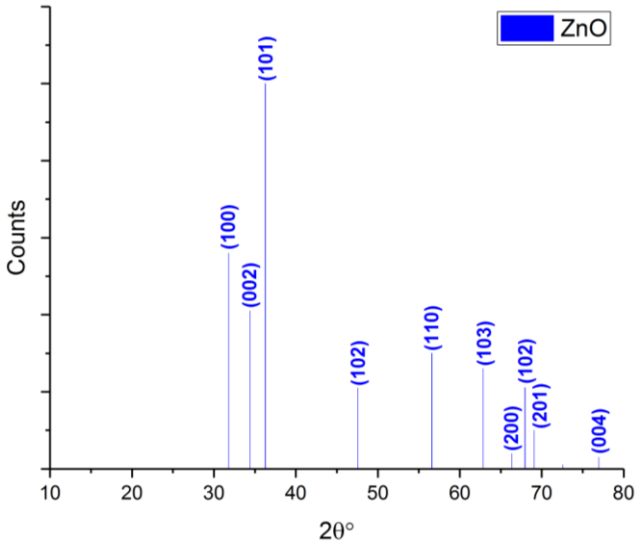

Figure 2.1. Reference line pattern for ZnO (JCPDS card number: 00-001-1136).

2.2 Small Angle X-Ray Scattering

Small angle X-ray scattering (SAXS) works on the same principle as X-ray diffraction (elastic scattering), but often operating in transmission mode. Due to the inverse relationship between the specimen size and angle of the incident beam (*rf.* Bragg's law, eqn. 2.1), SAXS provides high resolution characterisation of any

crystalline features (up to 150 nm in size) in the range of 0–10° 2θ. At small angles (<10° 2θ), information related to the shape and size of nanomaterials and any periodic spacing of partially ordered materials can be obtained. This technique was used to determine the (001) facet and the spacing of LZH–Ole as it was not observed using the powder X-ray diffractometer.

2.3 Infrared Spectroscopy

Infrared spectroscopy (IR) is a commonly used technique to probe the chemical structure of a compound. The absorbance/transmittance of infrared light passing through a sample is measured, where the vibrational frequencies of the chemical bonds match with the incoming absorbed IR frequencies.

The use of IR spectroscopy in organometallic chemistry and inorganic nanomaterials allows for the assignment of coordination modes of carboxylates or a capping ligand of choice, *e.g.* phosphinates, on zinc metal centres and surfaces of ZnO nanoparticles and layered zinc hydroxides.

2.4 Thermogravimetric Analysis

Thermogravimetric analysis (TGA) measures the weight loss of a material as a function of temperature or time (given that temperature stays constant), under a chosen atmosphere. Information such as degradation temperature, organic and inorganic contents and degradation profile can be obtained. Typically, the thermal degradation is run under an atmosphere of N_2 or synthetic air to allow oxidation. The

quantity of sample required for measurement spans from 10 mg to 150 mg, with a measureable temperature range of 25–1000 °C.

A typical thermal degradation profile of inorganic-organic hybrid materials consists of the weight loss attributed to the removal of water and hydrocarbons, from the organic components, and the remaining mass mainly composed of inorganic residue.[2-4] In this thesis, TGA, cross-checked with elemental analysis, was used to quantify the organic and inorganic content of ZnO nanoparticles and LZHs. To ensure accurate determination organic content, efficient removal of water or hydrocarbon volatiles prior to TGA was achieved by subjecting all samples to high vacuum ($< 10^{-2}$ mbar) overnight. Furthermore, for ZnO nanoparticle samples, an additional drying step of 100 °C, for 30 mins, was included in the heating regime to ensure removal of trapped toluene (synthesis solvent) in the samples. In addition, the degradation temperature of LZH was probed, using TGA, for the determination of the annealing temperature for ZnO thin film formation from LZH.

2.5 UV-Vis Spectroscopy

UV-Vis spectroscopy investigates the electronic structure of a given compound; absorption of a high wavelength photon (visible-UV-Vis region) takes place readily due to similar energies. Upon absorption of photons, ground state electrons within the sample of interest are excited to higher energy states and for semiconductors, such as ZnO, the ground state electrons (in the valence band) are excited to the conduction band. The gap between the valence and conduction band is commonly known as the bandgap of a semiconductor (E_g).

Although LZH is not active in the UV-Visible light range, in the case of ZnO nanoparticles, due to its semiconducting nature, the bandgap between conduction and valence bands has an energy in the in the same order of magnitude as range of ultraviolet wavelengths. The ZnO nanoparticles produced *via* the organozinc hydrolysis route typically are 2–4 nm in size and hence quantum confinement effects heavily influence the electronic properties of the nanoparticles. The absorption spectrum of typical ZnO nanoparticles, capped with carboxylate or phosphinate, shows the band gap signal to be in 300–400 nm region and the nanoparticles fluoresce either green or yellow when excited with UV light (Figure 2.2 & Figure 2.3). The size of ZnO nanoparticles can be estimated using an empirical method developed by Meulenkamp,[5] but it is only valid for particles of sizes between 2–6 nm.

The Meulenkamp method equates the bandgap of ZnO with the 50% absorption of the exciton peak, $\lambda_{1/2}$, to the particle sizes determined by TEM and XRD (Equation 2.3):

$$\frac{1240}{\lambda_{1/2}} = a + \frac{b}{D^2} - \frac{c}{D} \qquad (2.3)$$

where a = 3.556, b = 799.9, c = 22.64 and D is the diameter of the ZnO nanoparticles. This is only valid for nanoparticles of 2.5–6.2 nm, as the material's optical properties are mainly dominated by quantum size effects. The validity of this empirical relationship was established using several data sets reported in the literature.[5] In the case of the colloidal ZnO nanoparticles synthesised in this thesis, good agreement is generally obtained between the sizes determined from TEM and XRD with UV-Vis. In *Chapter 5*, the sizing of doped ZnO nanoparticles cannot be achieved due to the interference of dopant on the position of bandgap in UV-Vis spectroscopy.

Cu(0) nanoparticles exhibit a surface plasmon resonance (SPR) in the range of 500–700 nm (Figure 2.4). Upon oxidation to Cu_2O nanoparticles, the SPR diminishes in intensity, accompanied by a red shift.[6] UV-Vis spectroscopy enables qualitative determination of oxidative stability of the post-catalysis Cu(0) component, in comparison to the starting Cu(0) nanoparticles prior to catalysis (*see Chapter 4*).

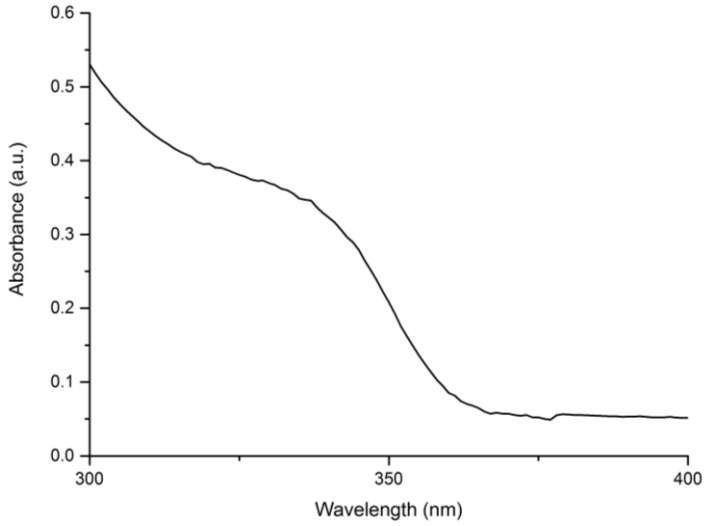

Figure 2.2. A typical UV-Vis spectrum of ZnO@carboxylate, in toluene. The allowed band gap signal is located at 351 nm (*i.e.* steepest point of signal).

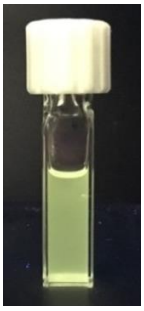

Figure 2.3. Photo of ZnO@Ole in toluene showing yellow colour emission under UV irradiation (254 nm).

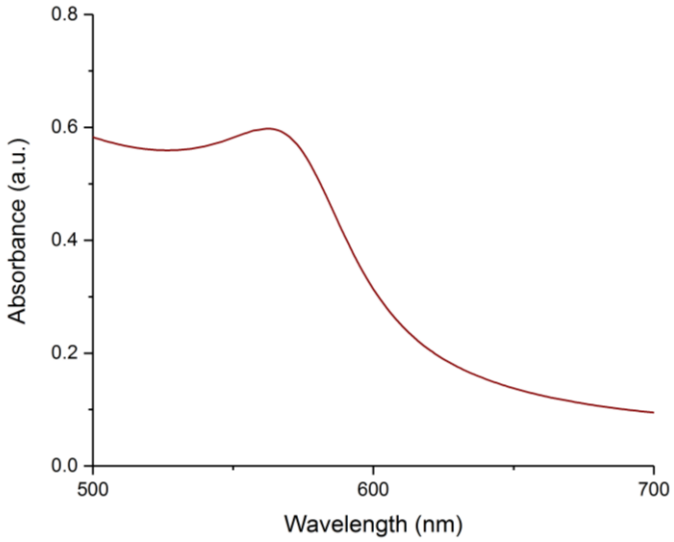

Figure 2.4. A typical UV-Vis spectrum of Cu@DOPA, in toluene. The SPR of Cu(0) is located at 564 nm (*i.e.* the maximum of the signal).

2.6 Scanning Electron Microscopy

Scanning electron microscopy (SEM) is an imaging technique to observe the surface morphology of the bulk material of interest. The electron beam scans the surface of the material in a raster scan pattern and the secondary electrons are collected by detectors to build an image. Samples are typically sputtered with a thin layer of conductive metal, such as Au or Cr, to allow good electric conductivity and avoid build-up of charge, especially on non-conductive samples.

The bulk LZHs and the thin films of LZH/ZnO were investigated using SEM to probe the surface morphology of the films, such as thickness and roughness.

In Chapter 3, SEM images were collected by Dr Adam J. Clancy (Department of Chemistry, Imperial College London).

2.7 Transmission Electron Microscopy

Transmission electron microscopy (TEM) is a powerful imaging technique which allows the analysis of specimens of nanometers in size, with atomic resolution. The principle of TEM is similar to that of optical light microscope but high energy electrons are used instead as the beam source, which generates images at atomic resolution. At high acceleration voltages, particles with shorter wavelengths are generated, *i.e.* electrons. The technique may be used to probe nanoscale morphology and crystallinity of a specimen. The beam of electrons is focused and passed through the specimen. The beam of electron is diffracted and the transmitted electrons are collected by a camera to produce an image. High resolution transmission electron microscopy (HR-TEM) is an image mode of TEM, where images with atomic

resolution are possible. In order to avoid sample damage and artefacts, specimens are typically dissolved in an appropriate solvent to form a solution of the material, with concentrations of ≤ 1 mg/mL.

Conventional and HR-TEM were used to probe the morphology of LZH and ZnO nanoparticles, but typically, the images obtained had poor contrast due to the presence of carbon-containing species, *i.e.* intercalated long-chain carboxylates, and the small size of the material. Furthermore, the poor contrast is likely to introduce systematic errors in size measurements. The incorporation of monochromator and spherical aberration (C_s) corrector (a series of magnetic lenses) in the microscope allowed high resolution imaging of nanoparticles (< 5 nm with resolution of 0.05 nm), with minimal stigmatism and good contrast.[7] Aberration-corrected TEM were used instead for imaging Cu/ZnO colloidal catalysts in *Chapters 3 & 4* as phase identification through lattice spacing analysis was required.

2.8 Scanning Transmission Electron Microscopy

Scanning transmission electron microscopy (STEM) is an imaging mode of conventional TEM. The beam of electrons that passes through the specimen is focused into one spot (spot size: 0.05–0.2 nm) and scanned through the specimen in a raster. The raster pattern of scanning allows for the use of high-angle annular dark field (HAADF), energy dispersive X-ray (EDX) and electron energy loss spectroscopy (EELS). The analytical techniques of STEM which are relevant to the analysis of ZnO nanoparticles and post-catalysis samples of Cu/ZnO systems are STEM-HAADF and EDX.

HAADF imaging, alternatively known as **z-contrast imaging**, collects the incoherently scattered electrons at the annulus around the main electron beam. These specific scattered electrons are extremely sensitive to the atomic number of the atoms in the specimen and hence the image generated from the annular dark field detector correlates with the atomic numbers.

EDX spectroscopy allows for the elemental analysis, composition and chemical identification within the specimen. The specimen is excited with an X-ray source and the generation of an inner-shell electron hole occurs, which is rapidly quenched (by an outer shell electron), to produce X-ray emission that is characteristic of a particular element. The emitted energies are collected by a detector which converts the signals into voltage (keV) to generate an EDX spectrum. Using EDX mapping on post-catalysis samples, the identification and location of ZnO and Cu particles within the specimen is possible without the need for lattice spacing analysis using HR-TEM. Furthermore, the presence of dopants was probed by such technique in *Chapter 5*.

In Chapter 4, all HR-TEM, STEM and EDX characterisations were performed by Dr Edward R. White (Department of Chemistry, Imperial College London). For Chapter 5, STEM-HAADF and EDX characterisations were performed by Dr Manfred Erwin Schuster (Johnson Matthey, Harwell).

2.9 X-ray Photoelectron Spectroscopy

X-ray photoelectron spectroscopy (XPS) is a surface-sensitive analytical spectroscopic technique, which allows for chemical composition analysis, identification and measurement of electronic states for the elements of interest. This spectroscopic technique works on the same principle as EDX spectroscopy in STEM (*section 2.8*), but more information can be obtained in terms of depth profile against elemental composition within the specimen (where the smallest penetration depth of the beam is 1–2 nm into the sample).

In this thesis, it is useful for the identification of elemental composition and distinguishing the oxidation state of Cu (0, +1 and +2) within the catalytic samples. In Chapter 5, XPS is used further to quantify the amount and location of dopants applied to ZnO nanoparticles, capped with DOPA. The comparison of Zn $2p_{3/2}$ core line to Mg 1*s* and Cu 2*p* core lines, and, Zn 3*s* to Al 2*p* were used for dopant quantification due to the close matching of the binding energies.

In Chapter 4 and 5, XPS characterisation was performed by Dr Anna Regoutz (Department of Materials, Imperial College London), in collaboration with Dr David J. Payne (Department of Materials, Imperial College London).

2.10 Atomic Force Microscopy

Atomic force microscopy (AFM) is a surface-sensitive technique and surface analysis of nanomaterials can be performed accurately with high resolution of sample heights. Three modes of AFM can be operated: contact mode, tapping mode and non-contact mode. In tapping mode, the piezoelectric cantilever oscillates at a fixed frequency, where the oscillating tip is brought close to the surface of the specimen and different interactions of forces occur. The change in amplitude of oscillation in the cantilever is related to the force dissipated by the intermittent contact of the tip and surface, hence this generates a tapping AFM image. The use of tapping mode avoids the tip sticking to the sample's surface and hence the nature of the sample is not altered due to systematic error. The LZH–Ole specimen was deposited onto a silicon wafer and the tapping mode was used to obtain images.

The use of AFM is complementary to TEM; whilst TEM gives atomic, lateral, resolution images of LZH–Ole monolayers, AFM can provide useful information regarding the thickness of the specimen, which TEM cannot provide.

In Chapter 3, AFM images were collected by Dr Hin Chun Yau (Department of Chemistry, Imperial College London).

2.11 Solid-state nuclear magnetic resonance

Solid-state NMR is an important technique for investigating molecular structures and environments in solid states, especially anisotropic interactions within a sample.

Anisotropic interactions are typically averaged in solution-state NMR as rapid molecular tumbling reduces the line broadening effect to zero. Molecules, in solid state, lack the freedom of motion and Zeeman interaction becomes a tensor property, thus, line broadening effects become prominent. Several line broadening interactions are known to induce asymmetric signals in a solid-state NMR spectrum: 1) shielding interactions, 2) dipolar interactions and 3) quadrupolar interactions.

Incorporation of magic angle spinning (MAS) allows the removal of chemical shift anisotropy and dipolar interactions and hence reducing the line broadening effects. The aforementioned interactions depend on the geometric factor of $3\cos^2\theta-1$; with the magic angle being $\theta = 54.74°$ and $3\cos^2\theta-1 = 0$, where line broadening effects are minimised. In the case of the quadrupolar nucleus, ^{27}Al ($I = \frac{5}{2}$, natural abundance = 100%), its sensitivity is high and the technique has been used extensively to determine the geometry and coordination environment of Al nuclei in heterogeneous catalysts, such as zeolites and alumina.[8] Octahedral, pentahedral and tetrahedral Al species in ^{27}Al-MAS-NMR typically fall in δ -20–20 ppm, δ 25–50 ppm and δ 50–80 ppm, respectively.[8, 9]

In Chapter 5, the solid-state ^{27}Al-MAS-NMR spectra were recorded by Dr Nick Rees (Department of Chemistry, University of Oxford).

2.12 Inductively Coupled Plasma Optical Emission Spectrometry

Inductively coupled plasma optical emission spectrometry (ICP-OES) is an analytical technique to determine elemental composition of a given sample, in bulk. The inductively coupled plasma generates flame temperatures, ranging from 6000 to 10000 K. Each emission wavelength is unique to a particular chemical element and the emission intensity varies according to the concentration of the element.

The technique is useful for its high sensitivity and complementarity to elemental analysis. It provides identification and quantification of up to 70 elements. Samples typically require digestion using an acid and the concentration for the sample solution is typically in microgram quantities (μg/L). Its accuracy lies with the element itself; certain elements have a lower detection limit than others. In this study, Al and P have high detection limits (20 μg/L and 50 μg/L), whilst Cu, Zn and Mg have lower detection limits (5 μg/L for Cu and Zn, 0.5 μg/L for Mg).

All ICP-OES measurements, in Chapter 5, were performed by Mr Alan P. Dickerson (Department of Chemistry, University of Cambridge).

2.13 References

1. B. D. Cullity, *Elements of X-ray Diffraction*, Addison-Wesley, 2nd edn., 1978.
2. T. Yuki, S. Ueno, M. Hagiwara and S. Fujihara, *J. Asian Ceram. Soc.*, 2015, **3**, 144-150.
3. H. Kajihara, M. Hagiwara and S. Fujihara, *J. Ceram. Soc. Jpn.*, 2016, **124**, 673-677.
4. K. L. Orchard, M. S. P. Shaffer and C. K. Williams, *Chem. Mater.*, 2012, **24**, 2443-2448.
5. E. A. Meulenkamp, *J. Phys. Chem. B*, 1998, **102**, 5566-5572.
6. S. D. Pike, E. R. White, A. Regoutz, N. Sammy, D. J. Payne, C. K. Williams and M. S. Shaffer, *ACS Nano*, 2017, **11**, 2714-2723.
7. F. Hosokawa, H. Sawada, Y. Kondo, K. Takayanagi and K. Suenaga, *Microscopy*, 2013, **62**, 23-41.
8. C. Pecharromán, I. Sobrados, J. E. Iglesias, T. González-Carreño and J. Sanz, *J. Phys. Chem. B*, 1999, **103**, 6160-6170.
9. J. J. Fripiat, L. J. Alvarez, J. S. Sánchez, E. M. n. Morales, J. M. Saniger and N. A. Sánchez, *Appl. Catal., A*, 2001, **215**, 91-100.

Chapter 3

Layered Zinc Hydroxide Monolayers by Hydrolysis of Organozincs

3.1 Scope

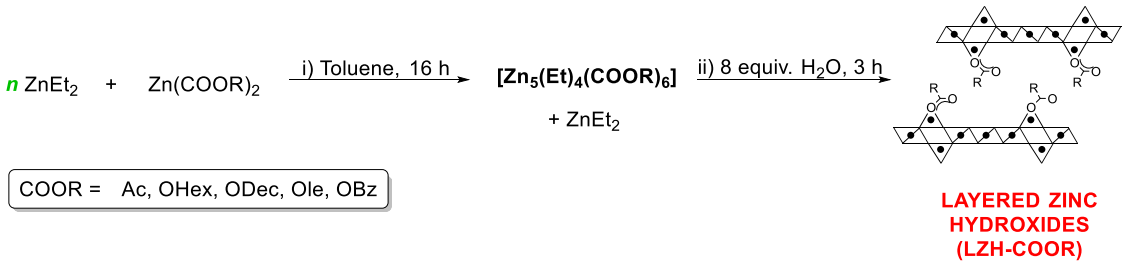

Scheme 3.1. Reaction scheme showing the general method used to target the formation of layered zinc hydroxides from diethyl zinc and zinc *bis*(carboxylate).

The aim of the chapter is determine the optimal conditions for the hydrolysis of organozincs to form layered zinc hydroxides, LZHs (Scheme 3.1).[1] The exfoliation and utilisation of the LZHs, as precursors, for thin film formation of ZnO will also be explored.

A previous study found that the controlled hydrolysis of $ZnEt_2$ with carboxylates, at a carboxylate loading of 0.33, favoured the formation of LZHs, but with ZnO nanoparticles present (confirmed by XRD).[2] Carboxylate loading is defined as the ratio of total amount of carboxylate and total amount of Zn, [COOR]/[Zn]. Here, a range of ligand stoichiometries ([COOR]/[Zn] = 0.4 – 0.6) was targeted to try to access LZHs without any ZnO. In addition, by varying the carboxylate ligand, the synthetic scope will be explored. It is hypothesised that long chain carboxylates may result in higher dispersity in organic solvents and so may facilitate the exfoliation of LZH.

3.2 Synthesis of LZHs by Hydrolysis of Organozincs

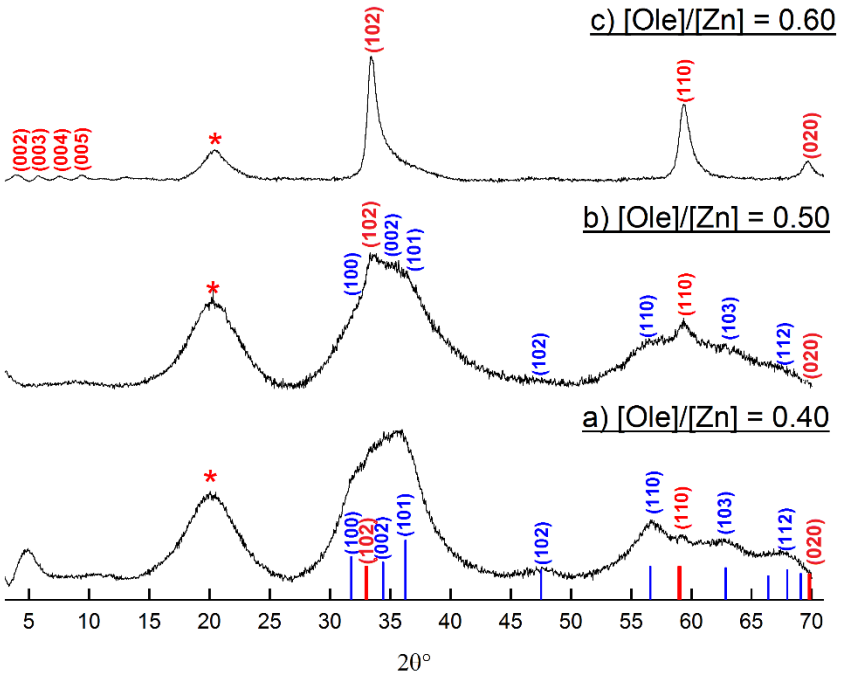

Figure 3.1. (a)-(c) Stacked XRD patterns of products from different loadings of oleate within the synthesis mixture, with (a) & (b) showing the presence of ZnO nanoparticles alongside LZH–Ole. Red vertical bars = LZH–Ole (trigonal with hexagonal unit cell, a = 3.156 Å, c = 46.535 Å). Blue vertical bars = ZnO (JCPDS: 00-001-1136) and * marks the peak caused by the lateral packing of hydrocarbon chains of oleate.

Previous work has shown that a ratio of [COOR]/[Zn] = 0.2 generates ZnO nanoparticles (3–4 nm), capped with carboxylate ligands.[1] When carboxylate/zinc molar ratios [COOR]/[Zn] = 0.33 was employed, a mixture of ZnO nanoparticles and an impurity phase, which was indexed as LZHs (reported by Poul *et al.*[3]), were formed. In order to target LZHs as the sole product from the hydrolysis of organozinc reagents, higher ratios of [COOR]/[Zn] will be explored. The ratio of [COOR]/[Zn] = 0.4 would be expected to be effective since it matches the quantities in the chemical formula of LZH, $[Zn_5(OH)_8(COOR)_2 \cdot nH_2O]$. Hence ratios of [COOR]/[Zn] ≥ 0.4 are targeted to understand the impact of ligand concentration on the distribution of ZnO and LZH within the product mixture.

The syntheses were conducted by reacting commercially available diethylzinc with the appropriate amount of zinc *bis*(carboxylate), in toluene ([Zn] = 0.15 M), to achieve [COOR]/[Zn] = 0.4, 0.5 and 0.6 (*see Chapter 7 experimental*). Water was directly added into the reaction mixture, under a dynamic flow of N_2, and the mixture was stirred for 2 h. All volatiles were removed under reduced pressure to yield white solids, where no subsequent purification steps were performed. Firstly, oleate was used to understand the influence of changing carboxylate/zinc molar ratio and the products were characterised by powder XRD. Over all the tested ratios, the presence of LZH was observed, with the presence of peaks at 33°, 59° and 70° 2θ corresponding to (100), (110) and (200) planes of LZHs. At the ratio of 0.4, ZnO Wurzite phase was also detected at 31°, 34°, 36°, 47°, 56°, 62° and 67° 2θ (Figure 3.1a). By increasing the carboxylate/zinc molar ratio to [COOR]/[Zn] = 0.5, formation of LZHs becomes favoured, with LZHs being the sole crystalline product at [COOR]/[Zn] = 0.6 (Figure 3.1b & c). The same trend of product distribution was also observed using acetate and hexanoate as the carboxylate source (*see Appendix for XRD patterns*).

Excess ligands were required to favour the selective formation of LZHs, with the higher [COOR]/[Zn] of 0.6 compared to the ratio of 0.4. The carboxylate ligands are tentatively assigned to be found as zinc *bis*(carboxylate), possibly located in between the layers. Evidence supporting this theory comes from a comparison of the IR spectra of LZH–Ole against zinc *bis*(oleate) (Figure 3.2). The comparison of the sharp C–O stretches at 1520–1550 cm^{-1} and ~ 1450 cm^{-1} suggests the presence of residual zinc *bis*(oleate) in the product, along with a new C–O stretch at 1580 cm^{-1}. As expected, excess carboxylates and the retention of original stoichiometry

([COOR]/[Zn] = 0.6), in the final product, was confirmed by elemental analysis and TGA (Table 3.1). Hence no loss of diethylzinc or ligands took place through either evaporation or washing.

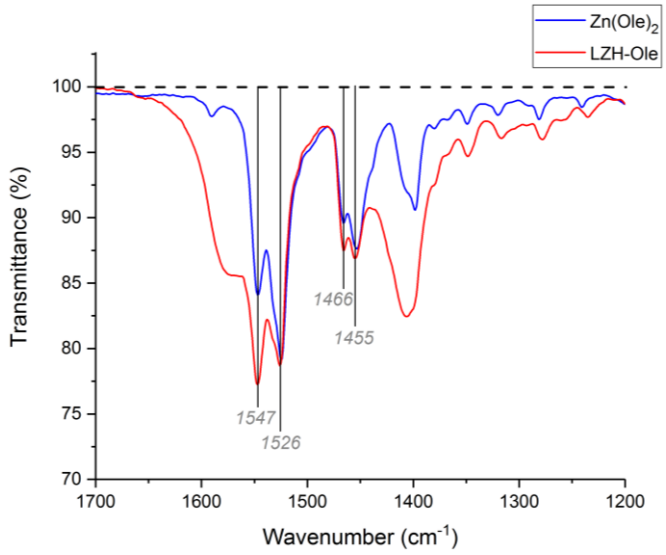

Figure 3.2. Comparison of IR spectra of LZH–Ole and zinc *bis*(oleate), focussing on the C–O bond stretch region where presence of zinc *bis*(oleate) is observed in the case of LZH–Ole.

LZH	Expected %C [a]	%C (from TGA)	%C (from elemental analysis)
LZH–Ac	11.26	10.53	12.72
LZH–OHex	26.74	23.72	27.25
LZH–ODec	36.89	35.49	36.66
LZH–Ole	49.61	49.73	46.74
LZH–OBz	30.53	29.39	30.27

Table 3.1. Table showing the comparisons between the predicted %Carbon values and %Carbon form TGA and EA for LZH–Ac, LZH–OHex and LZH–Ole.

[a] Expected wt% C calculated from the chemical formula: $[Zn_5(OH)_8(COOR)_2]$ with one molar equivalent of excess ligand taken into account.

The purity of LZHs was determined by UV-Vis spectroscopy. This showed signals attributed to ZnO nanoparticles (~20 mol% Zn or 6.4 wt% of the final product). The amount of ZnO was estimated by calibrating the extinction coefficient of pure ZnO nanoparticles, capped with oleate, against the values for the samples (ε = 755 dm^2 mol^{-1} at λ = 357 nm; Figure 3.3). Such a small quantity would be difficult to detect using powder XRD due to the low sensitivity of the technique and may explain its absences from the diffractogram. Assuming the only byproducts from the synthesis are zinc *bis*(carboxylate) and ZnO nanoparticles (identified by IR and UV-Vis spectroscopy), yields of ~63 mol% Zn were obtained for LZH–Ole (*see calculation of yields in Appendix*). The calculation of yield, based on Zn, is only reliable and accurate, given that no other known products are present within the sample.

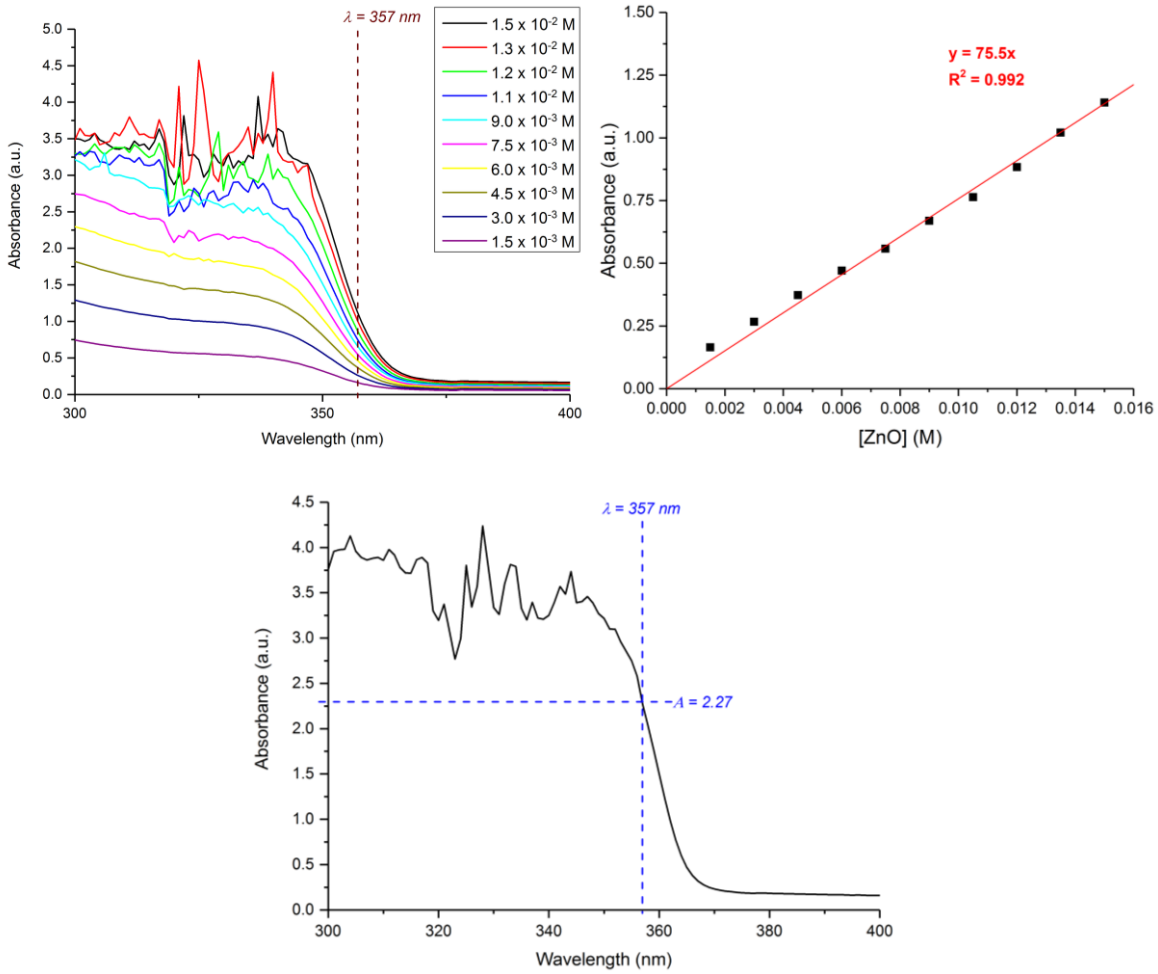

Figure 3.3. (*Top left*) The combined UV-Vis spectra for the standards of ZnO@Ole (in toluene) with the wavelength marked where the absorbance readings were taken from. (*Top right*) The calibration plot showing the linear relationship between the content of ZnO@Ole and absorbance from UV-Vis spectrum. (Bottom) UV-Vis spectrum of solution of LZH–Ole synthesised from the hydrolysis of diethyl zinc and zinc *bis*(oleate). The blue dashed lines mark the wavelength of the steepest point of the ZnO nanoparticle peak and the corresponding absorbance value.

3.2.1 Further Derivatives of LZHs

A range of carboxylate ligands were tested, in order to explore the generality of the new synthesis to LZHs. A range of alkyl chain lengths, with or without an unsaturated moiety in the chain, and aromatic substituents were tested: acetate (C_2), hexanoate (C_6), decanoate (C_{10}), oleate (C_{18}, with *cis*-alkene at C_9 position) and benzoate (C_6 aromatic ring). A ratio of [COOR]/[Zn] = 0.6 was applied for all the carboxylates to promote the sole formation of LZHs. For the synthesis of LZHs with decanoate, oleate and benzoate, neat carboxylic acids were used instead of the corresponding zinc *bis*(carboxylate) due to their low volatility and high hydrophobicity (Table 3.2).

XRD patterns of the five products are consistent with the formation of LZHs (Figure 3.4i). There are observable changes in the low angle peaks (<20° 2θ) depending on the carboxylate. Asymmetric peaks, with turbostratic character, at 33° (100), 59° (110) and 70° 2θ (200) are assigned to in-plane spacings of zinc hydroxide layers with hexagonal unit cell (a = 3.138 Å),[3] along with (102), (110) and (020) of

LZH	Carboxylate source	(001)/ ° 2θ	Basal spacing / Å
Acetate	$Zn(Ac)_2$	6.3	14.1
Hexanoate	$Zn(OHex)_2$	3.9	22.7
Decanoate	Decanoic acid	*3.0*	*29.7*
Oleate	$Zn(Ole)_2$ & oleic acid	*1.9*	*45.9*
Benzoate	Benzoic acid	4.7	18.9

Table 3.2. LZH–carboxylates (all contain hexagonal unit cell) with their corresponding (001) positions and basal spacing determined from the position of (001). The carboxylate sources are stated for clarification. In the case of LZH–Ole (a = 3.156 Å), the basal spacing was calculated from the spacing of (002), (003), (004) and (005). For LZH–ODec (a = 3.138 Å), the basal spacing was calculated from the spacing of (002) and (003).

LZH–Ole. The peak marked with '*' in the XRD patterns of LZH–Ole and LZH–ODec corresponds to the lateral packing of long hydrocarbons chains.[1, 4] Increasing the hydrocarbon chain lengths of the carboxylate changes in the basal spacing of the (001) and subsequent reflections (<20° 2θ) across the series of LZHs (Table 3.2; *Table A.1 in Appendix*).[5] In the case of LZH–Ac and LZH–OBz, the basal spacings were estimated to be 14.1 Å (6.3° 2θ) and 18.9 Å (4.7° 2θ) which are in good agreement with the data reported for the same materials, but synthesised using either base-assisted decomposition, hydrothermal route or hydrolysis in polyol media.[3, 6, 7] For LZH–OHex, the basal spacing was estimated to be 22.7 Å (3.9° 2θ). Due to the limitation of the diffractometer at low angles, the (001) peaks of LZH–ODec and LZH–Ole were not observed, but the value can be estimated using the higher reflection peaks, such as (002) and (003). The basal spacing were calculated to be 28.1 Å (3.1° 2θ) for decanoate, with the positions of (002), at 14.9 Å (5.9° 2θ), and (003), at 9.9 Å (8.6° 2θ). In the case of LZH–Ole, the features at 22.1 Å (4.0° 2θ), 15.2 Å (5.8° 2θ), 11.6 Å (7.6° 2θ) and 9.5 Å (9.3° 2θ) correspond to (002), (003), (004) and (005) planes, indicating a basal spacing of 45.9 ± 0.8 Å. The low intensities of the higher order reflections are caused by the disordered stacking of the oleate chains, this phenomenon was previously observed in analogues systems, *e.g.* LDH–Ole.[8-10] The (001) basal spacing of LZH–Ole was further investigated using SAXS and a broadly consistent spacing of 38 ± 6 Å was estimated; the high error in the data is likely due to the low measurement resolution (Figure 3.4ii & iii).

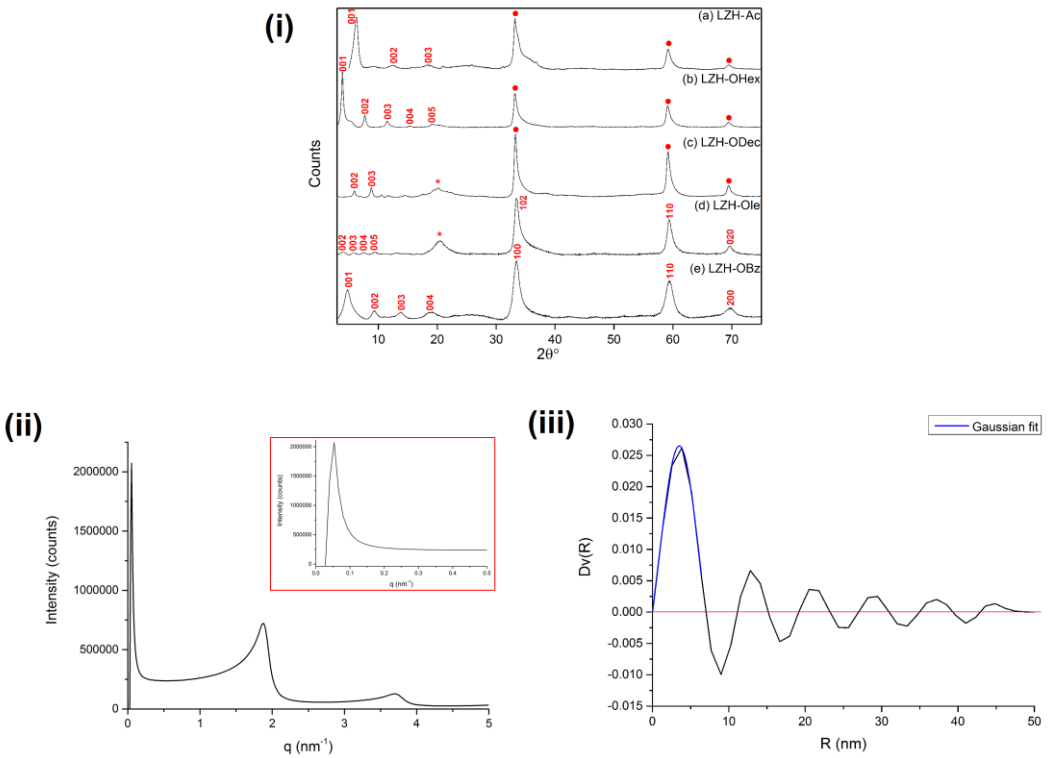

Figure 3.4. (i) XRD pattern of (a) LZH–Ac, (b) LZH–OHex, (c) LZH–ODec, (d) LZH–Ole and (e) LZH–OBz. The red circles correspond to the (100), (110) and (200) planes of LZH and * is caused by the lateral packing of aliphatic hydrocarbons. (ii) Solid-state SAXS spectrum of LZH–Ole with the inset showing the part of the spectrum where the volume-weighted size distribution (Dv(R)) calculation was taken. (iii) Graph showing the interlayer distance, R, against the volume-weighted size distribution, Dv(R), for LZH–Ole, with a Gaussian curve fit applied to the most populated peak, which corresponds to the (001) plane.

The IR spectra of LZHs show intense asymmetric and symmetric carboxylate signals at ~1600 cm^{-1} and ~1400 cm^{-1} (Figure 3.5).[11] The hydroxyl groups and intercalated water molecules show broad signals at 3100–3600 cm^{-1}.[12] The hydroxyl peak width and definition changes with carboxylate alkyl chain lengths.[3, 5, 12-14] As the length of alkyl group increases, the signals become sharper and this is especially noticeable when comparing LZH–Ac, LZH–OHex and LZH–Ole. It is proposed that longer alkyl chains increase hydrophobicity and help to maintain a more ordered layer structure; this effect is most noticeable for LZH–Ole, which showed sharp peaks at 3512 and 3395 cm^{-1}.[15]

The surface morphologies of LZH–Ac, LZH–OHex and LZH–Ole were analysed using SEM. LZH–Ac and LZH–OHex have similar platelet structures at high magnification (x 100000; Figure 3.6a & Figure 3.6b). In the case of LZH–Ole (Figure 3.6c & Figure 3.6d), particulates hundreds of nanometers wide (~350 μm) with smooth surfaces were observed. Such a structural difference might be a direct consequence of its high dispersity in organic solvents (*vide infra*).

TGA profiles of the different LZHs show an initial mass loss attributed to removal of intercalated water and partial dehydroxylation of zinc hydroxide layers at ~100 °C (endothermic), followed by the second mass loss starting at 300 °C (exothermic), which is attributed to the decomposition of organic carboxylates (Figure 3.7). As the number of carboxylate carbons increases, the second mass loss becomes more intense and LZH–Ole has the highest % weight loss. Hence the starting ratio (*i.e.* [COOR]/[Zn] = 0.6) is preserved within the final product.

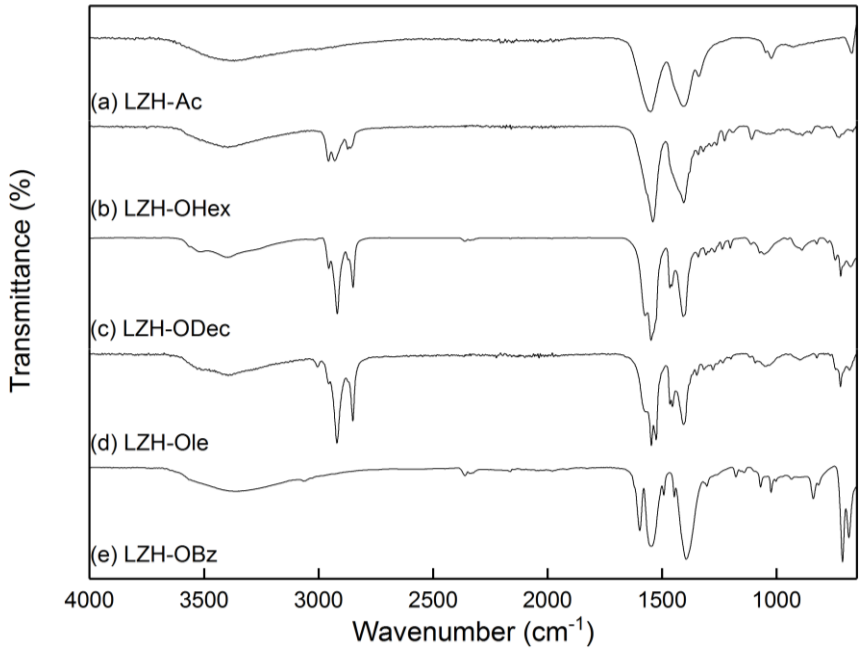

Figure 3.5. IR spectra of (a) LZH–Ac, (b) LZH–OHex, (c) LZH–ODec, (d) LZH–Ole and (e) LZH–OBz.

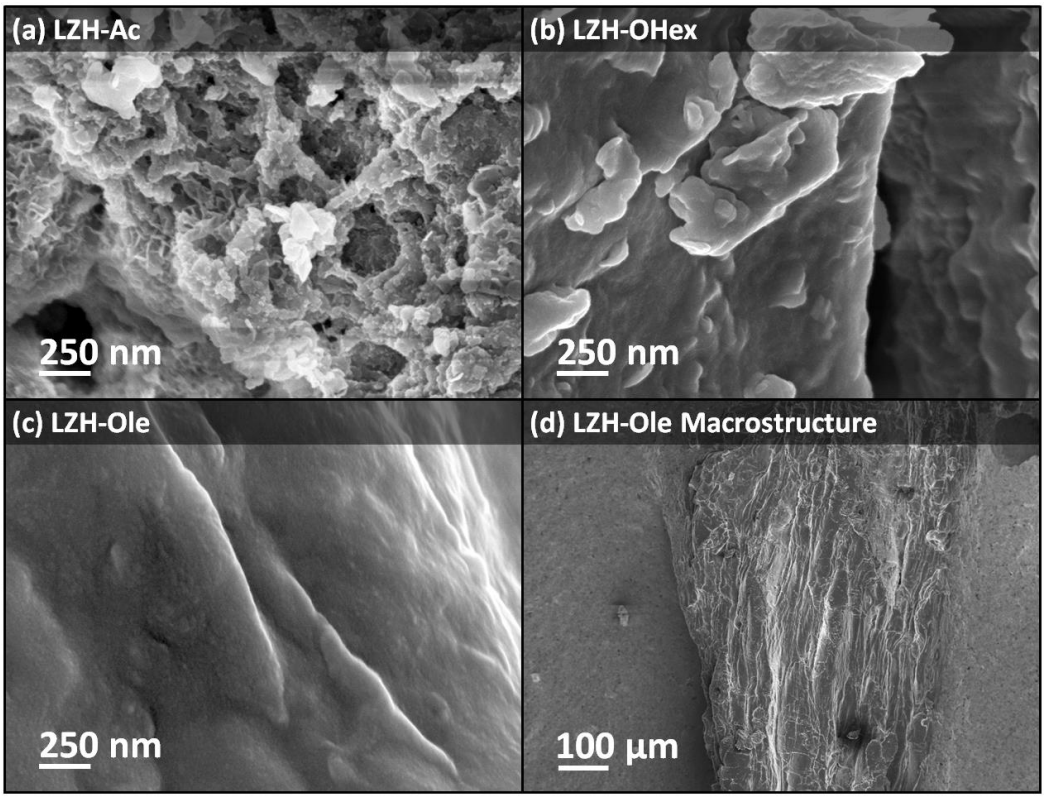

Figure 3.6. SEM images showing the surface morphology of (a) LZH–Ac, (b) LZH–OHex and (c) LZH–Ole, with (d) showing the macrostructure of LZH–Ole.

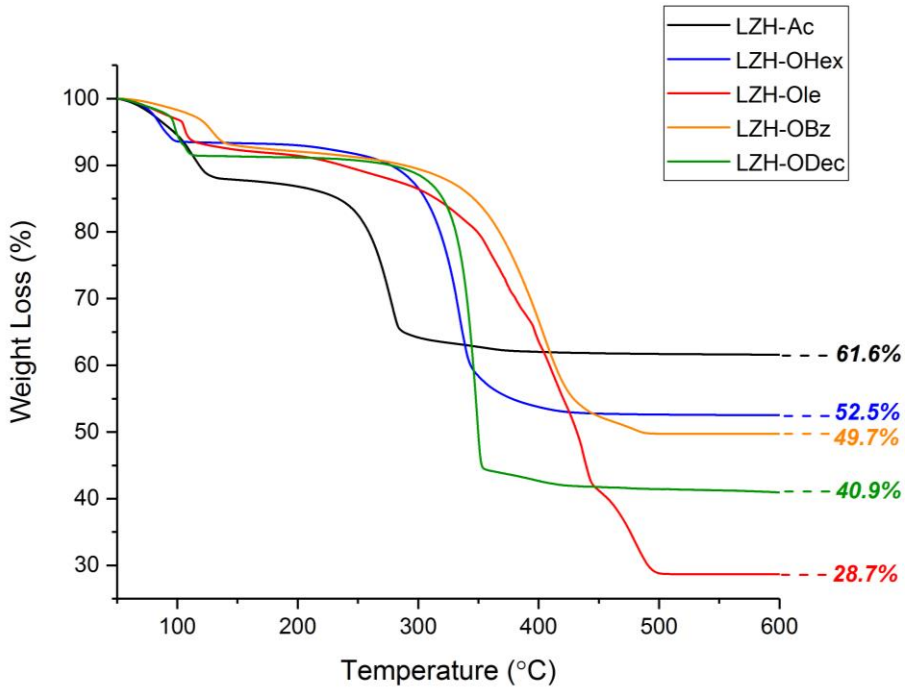

Figure 3.7. TGA profiles of LZH–Ac, LZH–OHex, LZH–ODec, LZH–Ole and LZH–OBz.

3.3 Exfoliation of LZH–Ole

Solvent	LZH–Ole Dispersed (mg/mL)
Toluene	23
Hexane	5
Chloroform	14
Dichloromethane	2
Ethanol	0
Water	0

Table 3.3. Amount of LZH–Ole dispersed in various solvents.

In order to investigate the dispersity of LZH–carboxylate, a range of solvents were tested (Table 3.3). Re-solvation of the LZHs proved difficult after isolation of dry powders, which is in line with previous reports and is attributed to the solubility of the intercalated anion in layered structures.[16] LZH–Ole was poorly dispersed in polar solvents (Table 3.3), but high dispersity was observed in toluene. Indeed, a concentration of 23 mg/mL was achieved in toluene which is unusual in this field since most LZHs are dissolved in polar solvents. It is comparable to the reported solubility of 22 mg/mL for LZH–DS in formamide.[17]

Due to its good dissolution ability in toluene, exfoliation of LZH–Ole was investigated in toluene. The LZH–Ole was stirred for 2 h in toluene, under ambient conditions. The hydrophobic nature and disrupted packing of the oleate chain (caused by the presence of the *cis*-alkene at the C_9 position) is proposed to improve swelling and infiltration of toluene. The spontaneous dissolution of LZH–Ole in toluene was also observed over 72 h without agitation. The latter exfoliation was shown by the increase in intensity of Rayleigh scattering resulting from a laser beam passed through the solution (Figure 3.8). By applying agitation, from simple magnetic

stirring, the dissolution process was shortened to 2 h. The extent of exfoliation was determined using HR-TEM and AFM on the resultant toluene solution. The solution was deposited onto a TEM grid or an AFM silicon wafer, in both cases through drop casting.

The TEM image showed a series of agglomerated sheet-like structures which are likely formed as the solution dries on the grid (Figure 3.9a; *see Appendix for more TEM images*). Within the thickest section of agglomerates, small stacks of ~5–8 layers of LZH–Ole nanoplatelets are present. For the stacks orientated parallel to the electron beam, clear diffraction fringes from the (001) layer planes are visible, marked by line profile [1] and [2] (Figure 3.9b & Figure 3.9c). The intensity of line profiles [1] and [2] show an interlayer spacing of 5.3 ± 1.3 nm (N ~30); the distance is consistent, within error, with that obtained by XRD (4.6 ± 0.1 nm) or by SAXS (solid sample: 3.8 ± 0.6 nm) for the same (001) plane. Analysis of the fast-Fourier transform (FFT) of an individual nanoplatelets, located on the edge of one of the agglomerates, revealed diffraction peaks at 33° ((100), d = 2.7 Å), 59° ((110), d = 1.5 Å) and 70° ((200), d = 1.3 Å) 2θ), which are consistent with the values for LZH–Ole by powder XRD (Figure 3.9e & d).

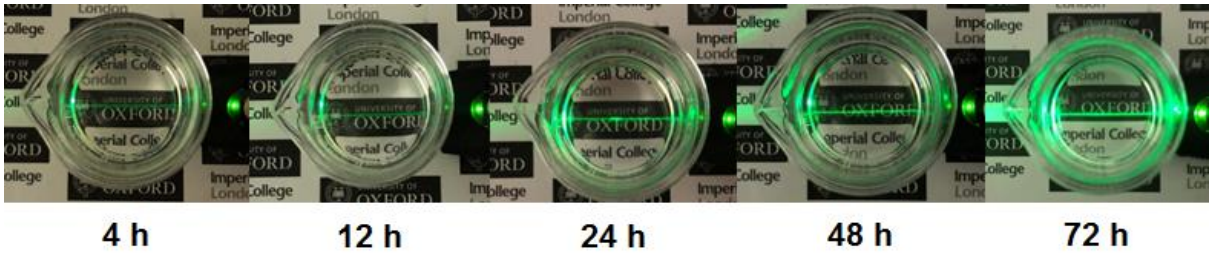

Figure 3.8. Photographs showing the spontaneous dissolution of LZH–Ole in toluene, over a period of 72 h. The increasing concentration of nanoplatelets is revealed by Rayleigh scattering from an incident laser beam which becomes stronger over time as more LZH dissolves, although the solution remains transparent.

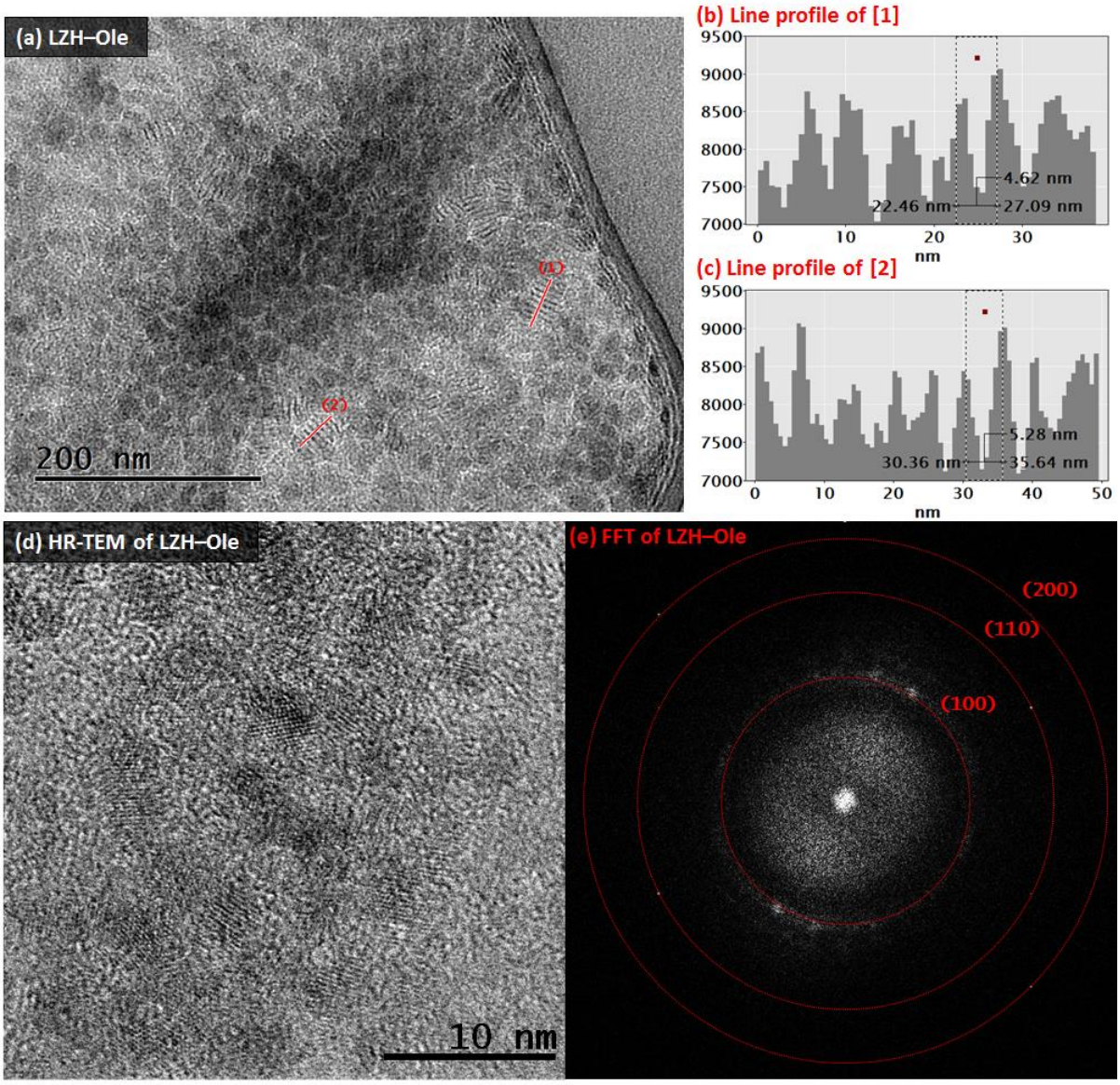

Figure 3.9. TEM image of (a) LZH–Ole after exfoliation by mechanical stirring for 2 h in toluene. Line profiles (b) & (c) correspond to lines [1] & [2] in (a), respectively. Within the line profiles, the interlayer distances are marked by the dashed line box. (d) HR-TEM image of the edge of agglomerate of LZH–Ole after exfoliation treatment (mechanical stirring, 2 h, toluene) and (e) the FFT of image (d).

AFM analysis was also performed as TEM can only provide high lateral resolution analysis of the exfoliated specimen. The typical profile of a 2D layered material was observed for individual LZH monolayers and the surface of the silicon wafer was decorated with such monolayers (Figure 3.10a & b). The average thickness of the monolayers was determined to be 3.62 ± 0.07 nm (σ = 0.75 nm, *N* = 127, Figure 3.10e & Figure 3.10f), which is in good agreement with the value obtained using solid-state SAXS (3.8 ± 0.6 nm). A small population of layers is below the thickness of 3.5 nm, which might be attributed to some layers with only carboxylate ligands present on one side of the zinc hydroxide sheet. The average radius of the monolayers is 13.25 nm (σ = 3.38 nm, *N* = 127), but due to tip convolution, this value is likely an overestimate. AFM also showed some large agglomerates similar to the ones seen in TEM (Figure 3.10c). Upon closer analysis, a height of ~3 nm (Figure 3.10d) was found which is consistent with the monolayer thickness. The gaps between the particles are too small to be resolved by AFM due to its low lateral resolution.

The TEM and AFM analyses strongly suggest the exfoliation of LZH–Ole was successful and that the material exists as exfoliated monolayers in solution. The occasional larger agglomerates are considered to be an artefact from the drying process required for these analyses.

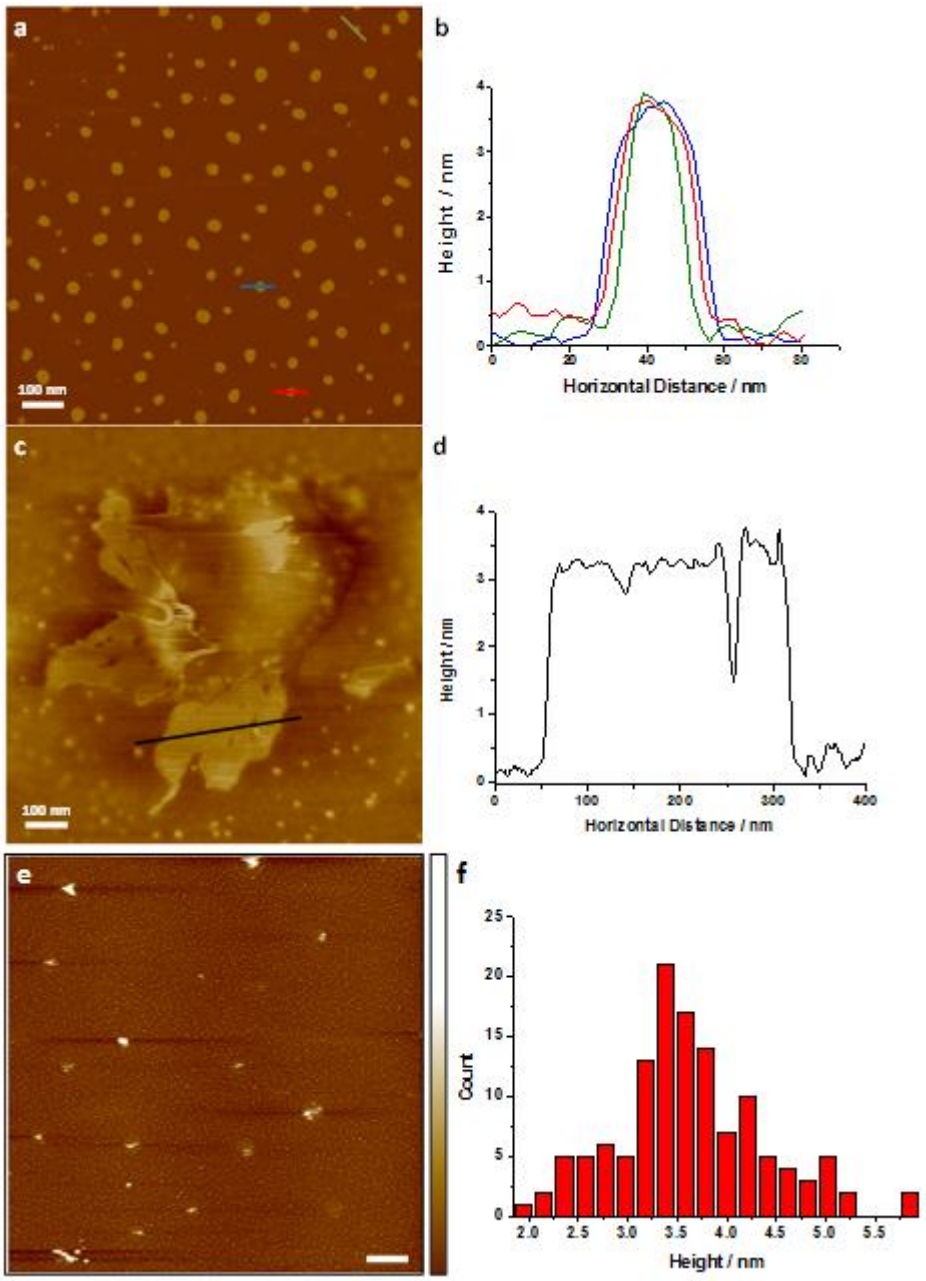

Figure 3.10. (a) AFM image of individual LZH-Ole and (b) height profiles of the individual platelets highlighted in (a). (c) AFM image of self-assembled LZH-Ole and (d) height profile of the self-assembled platelets highlighted in (d). (e) Large area AFM image of LZH-Ole and (f) height distribution of the individual platelets (N = 127, mean 3.628 ± 0.748 nm). Scale bar – horizontal: 1 μm, vertical: 10 nm.

3.4 Synthetic Pathway to LZHs

The high dispersity of the oleate nanoplatelets provides an opportunity to monitor the organometallic synthesis of LZH–Ole, *in situ*, using ^{1}H NMR spectroscopy (Figure 3.11). The ^{1}H NMR spectrum of the LZH–Ole product exhibits broad peaks that are shifted relative to the zinc *bis*(oleate) precursor.[18, 19] A broad signal at 0.53 ppm is tentatively assigned to intercalated water molecules (water in C_6D_6: 0.40 ppm) which are hydrogen-bonded to zinc hydroxide layers.

The reaction between diethyl zinc and zinc *bis*(oleate), at [COOR]/[Zn] = 0.60, leads to the formation of a pentanuclear complex, $[Zn_5(Et)_4(Ole)_6]$ (Figure 2.19a, signals marked 'C'), together with unreacted diethyl zinc (Figure 2.19a, signals marked 'X'). The zinc pentanuclear complexs has a stoichiometry in line with previously reported clusters. Indeed, prior research showed that these clusters are stable in apolar solvent. In the case of oleate, the cluster is clearly identified by the oleate signals in the range of 5.60–0.90 ppm, along with signals at 1.70 ppm due to overlap between oleate and zinc ethyl groups, and at 0.78 ppm due to zinc ethyls. The relative integrals of oleate to ethyl are 6:4, which is in line with the values expected for the pentanuclear cluster. The signals at 1.12 and 0.10 ppm correspond to the excess diethyl zinc. The relative integrals between the cluster signals at 5.52 ppm, and 0.78 ppm against the diethyl zinc signal at 0.12 ppm indicate a 1 : 1.5 (cluster : $ZnEt_2$) relative stoichiometry.

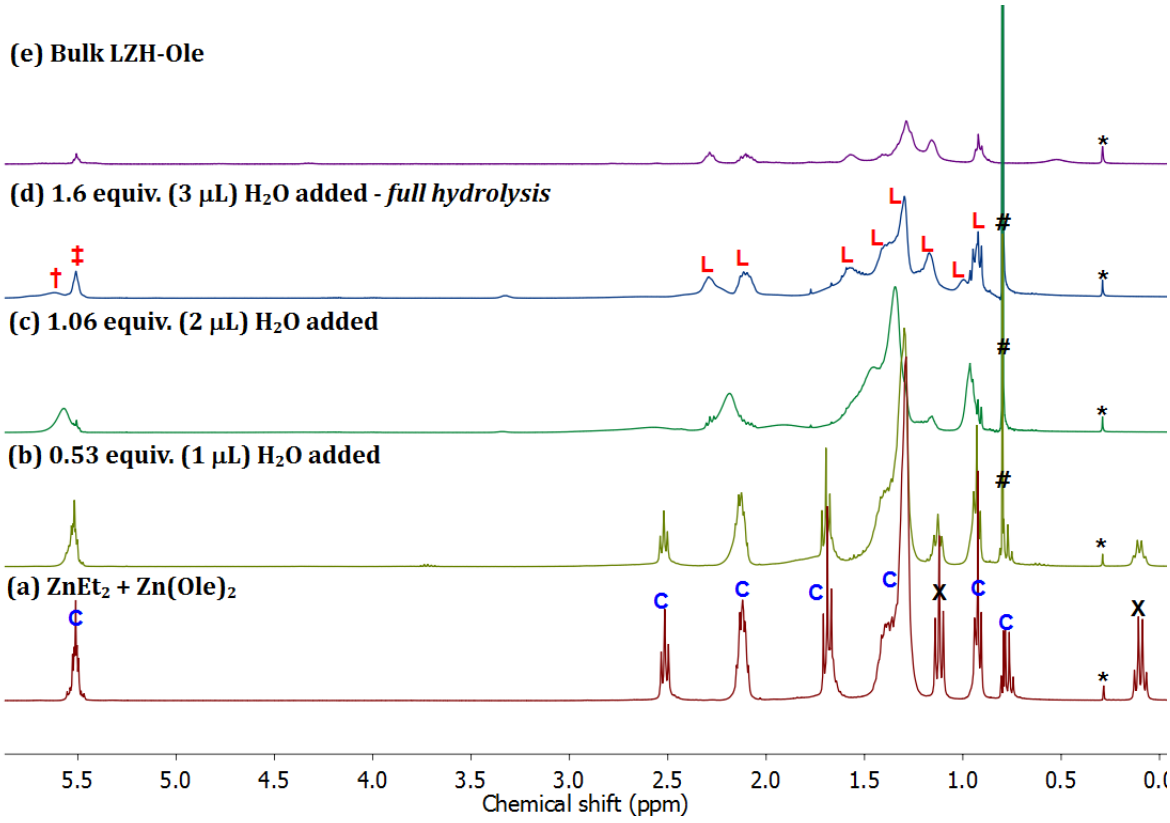

Figure 3.11. ^{1}H NMR spectra showing the progression of the synthesis of LZH–Ole from diethyl zinc and zinc *bis*(oleate) in benzene-d_6. (a) $[Zn_5(Et)_4(Ole)_6]$ and diethyl zinc, the hydrolysed products observed at (b) 0.53 equiv water added, (c) 1.06 equiv. water added, (d) 1.6 equiv. water added and (e) the bulk LZH–Ole. *: silicon grease, #: ethane (δ 0.80 ppm), C: $[Zn_5(Et)_4(Ole)_6]$, L: LZH–Ole, X: $ZnEt_2$ (δ 0.10 & 1.12 ppm), ‡ & †: alkenyl protons of oleate (δ 5.51 & 5.61 ppm).

The controlled hydrolysis of this mixture of cluster and excess $ZnEt_2$ was performed by the sequential addition of a known amount of water, under a dynamic flow of nitrogen. It is important to note that the solution remained homogenous throughout and the ^{1}H NMR spectra are therefore representative of all proton-containing species present (Figure 3.11b-d). The addition of ~0.5 equiv. of water (to total moles of zinc present) caused a decrease in the intensity of the free diethyl zinc, as expected due to its high reactivity (Figure 3.11b). When a total of ~1 equiv. of water was added, the hydrolysis of the cluster was observed as confirmed by the disappearance of its ethyl signals at 0.78 and 1.70 ppm (Figure 3.11c). The broadening of the oleate signals suggests coordination to the putative zinc hydroxide

product(s) and the changes in chemical shifts (L: 5.52, 2.30, 2.11, 1.58, 1.42, 1.40, 1.30, 1.17, 0.92 ppm) are consistent with the formation of LZH–Ole and are comparable to the ^{1}H NMR of the pure product (Figure 3.11d & e). Each addition of water to the reaction mixture resulted in evolution of ethane, as indicated by the signal at 0.80 ppm (Figure 3.11b-d). Two low intensity signals (δ 3.30 & 5.61 ppm) are present in the fully hydrolysed proton spectrum and are not present in zinc oxide coordinated by oleate or bulk LZH–Ole (Figure 3.11d). They may be tentatively assigned as intercalated water. (*See Appendix for ^{1}H NMR spectrum of ZnO@Ole*).

The hydrolysis process can be divided into three stages: 1) formation of the pentanuclear complex, $[Zn_5(Et)_4(COOR)_6]$, in equilibrium with excess diethyl zinc, 2) the hydrolysis of the free diethyl zinc and 3) the hydrolysis of the pentanuclear complex, which is followed by the formation of LZHs.

3.5 Formation of ZnO Thin Film

Given the high dispersity of LZH–Ole in toluene, solution casting of LZH–Ole onto a substrate as a precursor for the formation of ZnO thin film was tested. Thermal decompositions of LZH to ZnO films are quite well known and mainly applied in the fabrication of photovoltaic devices.[20] A solution of LZH–Ole in toluene (1 mg/mL) was deposited onto a glass substrate through evaporation of LZH–Ole solution and a uniform, 1 μm thick, optically opaque LZH film was formed (Figure 3.12a & c, Figure 3.13a). The morphology of the precursor film has a similar appearance to that of bulk LZH–Ole in SEM (Figure 3.12c). Upon annealing of the precursor film (500 °C, 15 min), the same film thickness was retained but a drastic change in surface morphology was observed, using SEM (Figure 3.12b, Figure 3.14). The surface of the resulting film was decorated with spherical nanoparticles of size ~25 nm and the film appeared to be porous and less dense compared to the precursor (Figure 3.12d & f). The film was optically transparent through visual inspection (Figure 3.13b). The nanoparticles were identified by UV-Vis spectroscopy as ZnO, with a band edge at 374 nm (Figure 3.15). The apparent retention of film the thickness and homogeneity in the ZnO film demonstrates promise for use in hybrid photovoltaic devices and transistors, where optimal thicknesses are between 100 nm to 1 μm. [21-23]

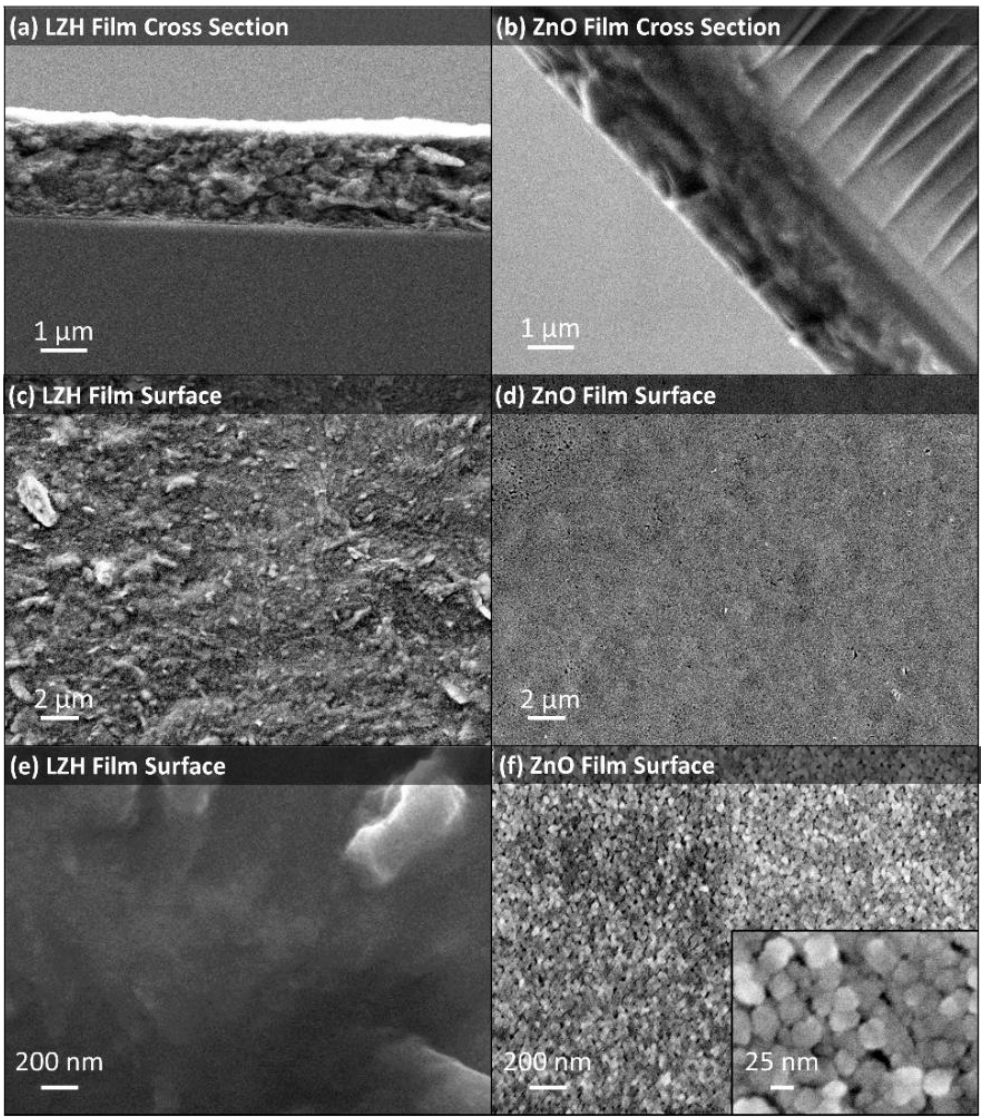

Figure 3.12. SEM images of LZH–Ole precursor film and ZnO film. (a) & (b) cross sections of LZH and ZnO films, (c) & (d) surface of LZH and ZnO films and (e) & (f) surface of LZH and ZnO films at higher magnification. Inset of (f) shows the ZnO nanoparticle size of 25 nm.

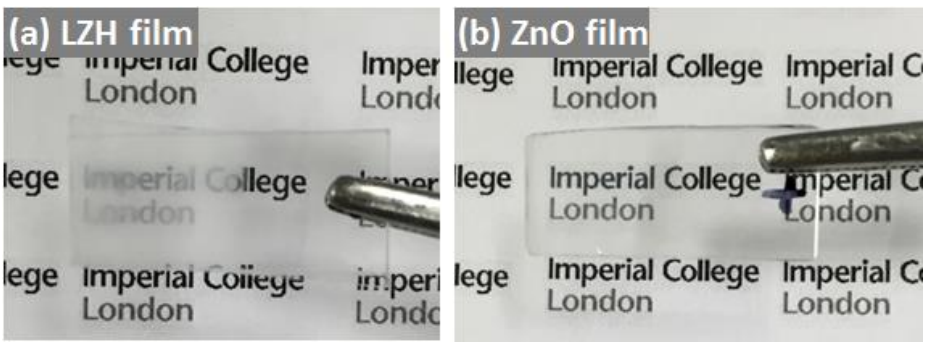

Figure 3.13. Photographs of (a) LZH film and (b) ZnO film.

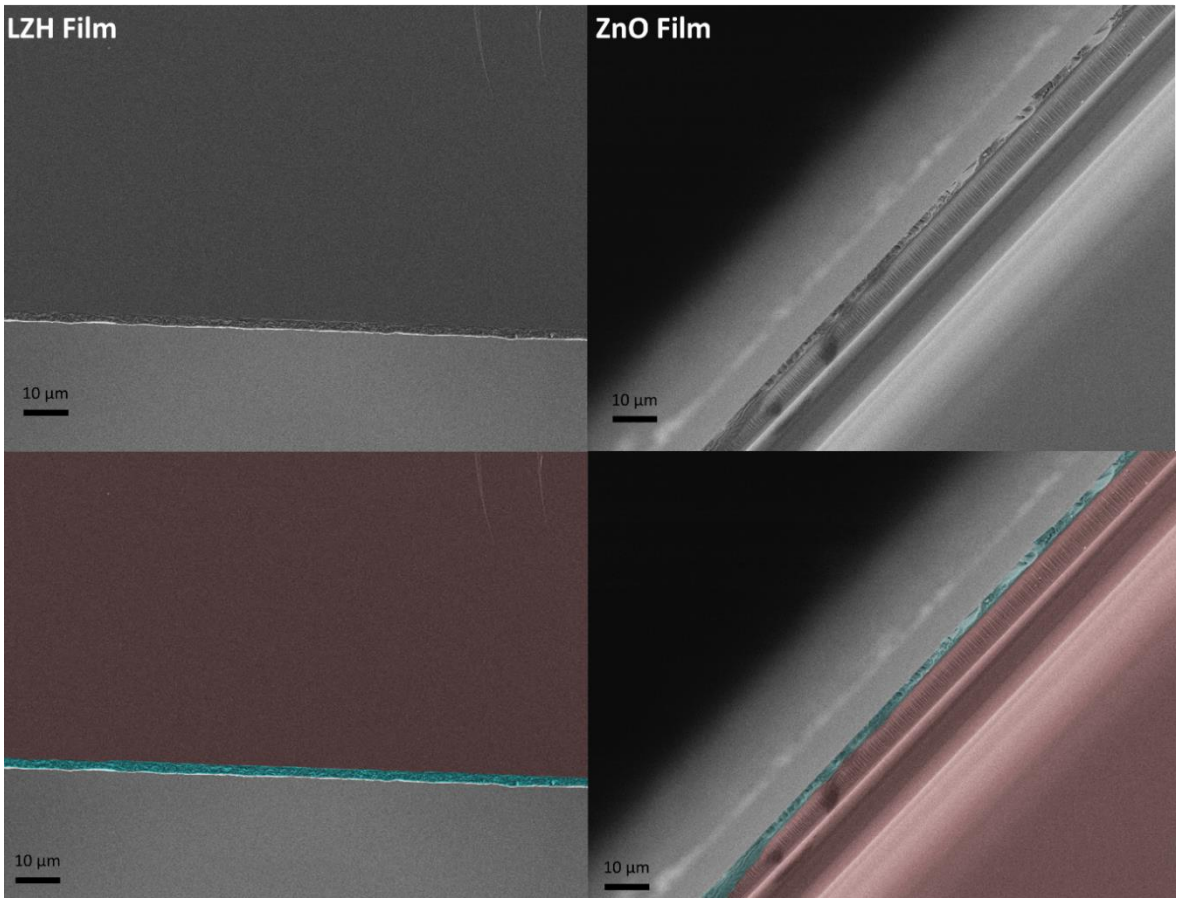

Figure 3.14. SEM images of cross sections of LZH and ZnO films, showing that the uniformity of the films were retained across the films. False colour has been applied to highlight the glass substrate (red) and ZnO film (blue).

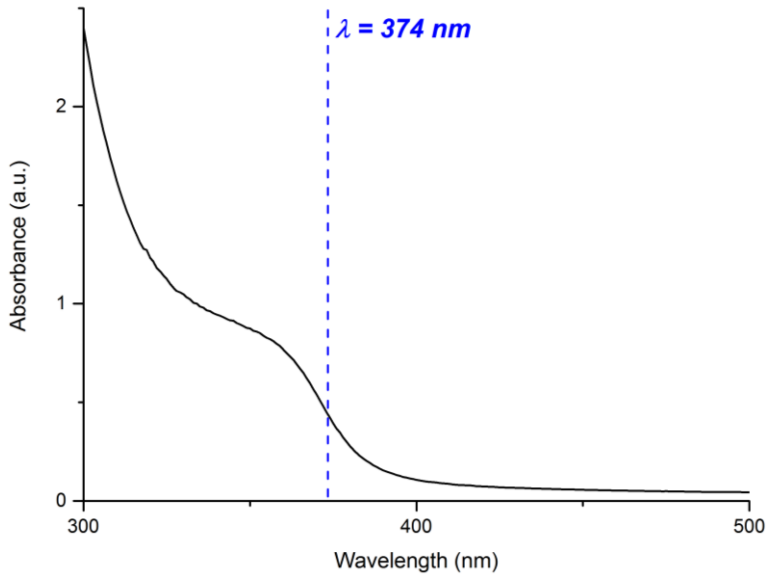

Figure 3.15. UV-Vis spectrum of ZnO film formed from annealing LZH film at 500 °C for 15 mins.

3.6 Discussion

LZH was successfully synthesised *via* the hydrolysis of diethylzinc, with an appropriate amount of carboxylate ligands (in the form of zinc *bis*(carboxylate) or neat carboxylic acid), in toluene, and at room temperature. At an optimal ratio of [COOR]/[Zn] = 0.6, sole formation of LZH was observed across all five synthesised LZH–carboxylate samples. By exploiting the high reactivity of Zn–C bonds towards water, high conversion efficiencies and selectivities were achieved.

A significant difference between the hydrolysis route and the conventional base-assisted/hydrothermal route is that no signals of a common contaminant, hydrozincite, were observed in the product powder XRD patterns. Hydrozincite is typically produced due to carbonate contamination and when urea is used as the base in synthesis. Overall, only a small amount of ZnO nanoparticles (~6.4 wt% as indexed by UV-Vis spectroscopy) and zinc *bis*(carboxylate) were identified as contaminants in the hydrolysis route. In comparison to literature, both ZnO and hydrozincite are sometimes clearly present, *e.g.* in the XRD pattern of product; Figure 3.16 without being explained by the authors.[5, 7, 17, 24-26] Despite the scarcity of yields for LZHs, most likely due to the difficulty in identification of byproducts, a yield of ~63 mol% Zn, for LZH–Ole, is comparable to ~90 mol% Zn and 60–89 mol% Zn reported for LZH–DS and LZH–OBz, respectively.[5, 27]

In the case of LZH–Ole, nanoplatelets (~3.6 nm x ~24 nm) were isolated directly and resolvated as monolayers, in apolar organic solvents. The new hydrolysis route can be considered as a bottom-up approach to LZH monolayers of which there have not yet been any other reports. In contrast with the harsh conditions needed for

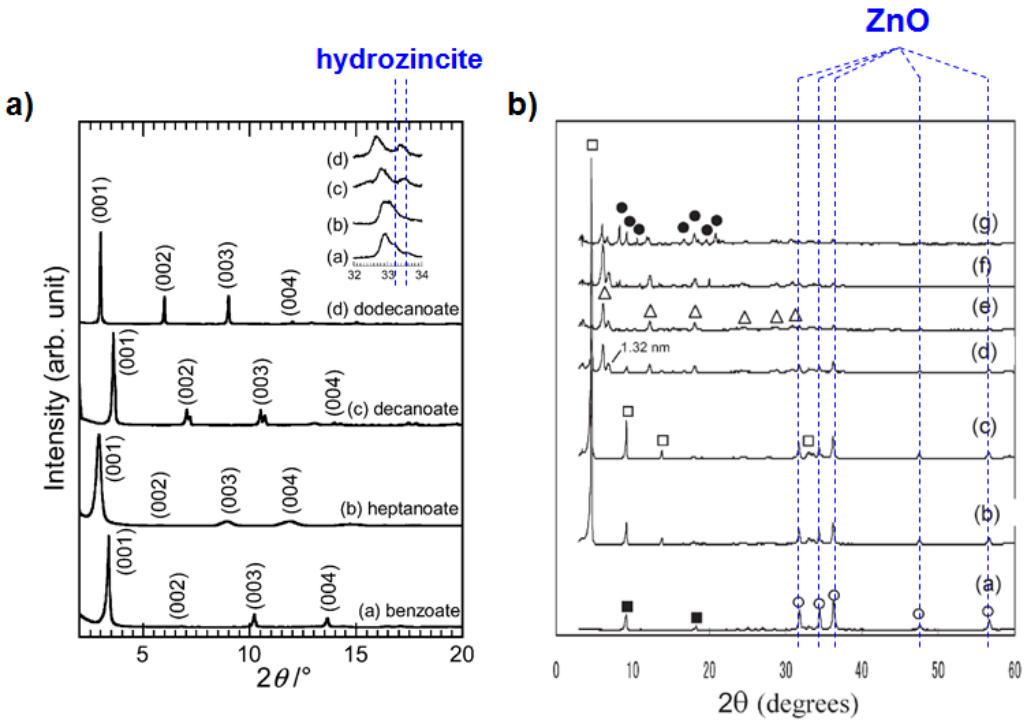

Figure 3.16. a) XRD of LZHs synthesised by using a biphasic system[5] with the presence of impurity, hydrozincite, highlighted with blue dash lines.. *Reproduced (adapted) with permission from Inoue et al.[5] Copyright 2011 American Chemical Society*. b) XRD of LZH–OBz with ZnO diffraction present across all samples synthesised using different carboxylate loadings (■: $[Zn_5(OH)_8(NO_3)_2 \bullet 2H_2O$, •: $Zn(C_6H_5COO)_2$, Δ: 1.47 nm layered phase, □: 1.93 nm layered phase).[7] *Reproduced with permission from the Royal Society of Chemistry.*[7]

conventional exfoliation, monolayers are preserved here after simple dissolution or by stirring (toluene, 2 h).

One advantage of a route to highly soluble LZH–Ole, in apolar organic solvents, is the ability to use *in-situ* ^{1}H NMR spectroscopy to investigate LZH formation. The study suggests the formation of LZH is achieved through 1) the hydrolysis of diethylzinc, 2) the hydrolysis of the ethyl bonds on cluster $[Zn_5(Et)_4(COOR)_6]$ and 3) the formation of LZH. The order of reactivity of Zn–ethyl species is hypothesised to be $ZnEt_2$ > $[Zn_5(Et)_4(COOR)_6]$ and upon hydrolysis of the pentanuclear zinc cluster, its carboxylate ligands labilised and able to stabilise LZH. The proposed hydrolysis

pathway is consistent with a detailed study on speciation during the synthesis of ZnO@phosphinate nanoparticles (*Chapter 3 & 4*).[28]

Some restrictions are imposed by the use of an organometallic precursor: 1) the need of air-sensitive handling techniques and 2) the need for organic solvents (to dissipate the heat evolved during hydrolysis). Despite these limitations, the synthesis minimalises contaminants in products, which might impact both exfoliation and application of LZHs.

ZnO films obtained from LZH pyrolysis have an apparently high porosity and retained the same film thickness, which are both desirable for high surface area adsorption of photoactive dyes in DSSCs.[6, 20, 29-31] The 1 μm-thick ZnO film formed from using LZH–Ole might not yet be ideal for DSSC (typically thicknesses >10 μm), but its porosity and thickness are in line with requirements for hybrid cells.[32] With the simple deposition method from toluene and short conversion time (< 0.5 h) to ZnO, there is potential for larger scale fabrication of uniform ZnO thin films.

3.7 Summary & Conclusion

By increasing the concentration of ligands in the previously reported synthesis of ZnO nanoparticles *via* hydrolysis, layered zinc hydroxides were obtained.[17] At an optimal molar ratio [COOR]/[Zn] = 0.6, the hydrolysis method, operating at room temperature in apolar organic solvents, provides an alternative route to layered zinc hydroxides. The synthesis was demonstrated with a range of carboxylates including acetate, hexanoate, decanoate, oleate and benzoate.

Increasing the alkyl chain length of the carboxylate allowed control of the dispersity of the resulting LZH. The oleate ligand provided good dissolution ability to the LZH in apolar organic solvents (23 mg/mL, in toluene). TEM and AFM analyses indicate that upon re-solvation in toluene, exfoliated monolayers were obtained. Finally, porous ZnO films were fabricated from layered zinc hydroxides, with oleate ligand, through annealing on glass substrate.

In order to extend the generality of the synthesis, the intercalation of phosphinate was attempted. One advantage of using phosphinate ligands would be to further increase dispersity in organic solvents (two alkyl chains per phosphorus headgroup). In addition, the phosphorous centre has good reductive stability, which might be desirable for certain applications such as hydrogenation catalysis. Unfortunately, phosphinate ligands were not successfully intercalated into LZHs (*see Appendix*). It is proposed that several products were formed, such as ZnO nanoparticles and zinc-oxo clusters containing phosphinate ligands are formed instead of LZH (XRD; *see Appendix*).[28]

3.8 References

1. K. L. Orchard, M. S. P. Shaffer and C. K. Williams, *Chem. Mater.*, 2012, **24**, 2443-2448.
2. K. L. Orchard, The Mild Synthesis of Zinc Oxide Nanoparticles and Nanocomposites via hydrolysis of Well-Characterised Zinc Organometallics, Imperial College London, 2011.
3. L. Poul, N. Jouini and F. Fiévet, *Chem. Mater.*, 2000, **12**, 3123-3132.
4. R. A. Taylor, H. A. Ellis, P. T. Maragh and N. A. S. White, *J. Mol. Struct.*, 2006, **787**, 113-120.
5. S. Inoue and S. Fujihara, *Inorg. Chem.*, 2011, **50**, 3605-3612.
6. A. Moezzi, A. McDonagh, A. Dowd and M. Cortie, *Inorg. Chem.*, 2013, **52**, 95-102.
7. J. Miao, M. Xue, H. Itoh and Q. Feng, *J. Mater. Chem.*, 2006, **16**, 474-480.
8. Z. P. Xu, P. S. Braterman, K. Yu, H. Xu, Y. Wang and C. J. Brinker, *Chem. Mater.*, 2004, **16**, 2750-2756.
9. C. Manzi-Nshuti, P. Songtipya, E. Manias, M. M. Jimenez-Gasco, J. M. Hossenlopp and C. A. Wilkie, *Polymer*, 2009, **50**, 3564-3574.
10. Y. Kameshima, H. Yoshizaki, A. Nakajima and K. Okada, *J. Colloid Interface Sci.*, 2006, **298**, 624-628.
11. J. Oomens and J. D. Steill, *J. Phys. Chem. A*, 2008, **112**, 3281-3283.
12. S. Inoue and S. Fujihara, *Langmuir*, 2010, **26**, 15938-15944.
13. J. W. Lee, W. C. Choi and J.-D. Kim, *CrystEngComm*, 2010, **12**, 3249.
14. K. Nakamoto, *Infrared and Raman spectra of inorganic and coordination compounds*, Wiley Online Library, 1986.
15. S. Musić, S. Popović, M. Maljković and Đ. Dragčević, *J. Alloys Compd.*, 2002, **347**, 324-332.
16. Q. Wang and D. O'Hare, *Chem. Rev.*, 2012, **112**, 4124-4155.
17. J. Demel, J. Plestil, P. Bezdicka, P. Janda, M. Klementova and K. Lang, *J. Colloid Interface Sci.*, 2011, **360**, 532-539.
18. Z. Hens and J. C. Martins, *Chem. Mater.*, 2013, **25**, 1211-1221.
19. M. Schönhoff, *Curr. Opin. Colloid Interface Sci.*, 2013, **18**, 201-213.
20. Y.-H. Lai, C.-Y. Lin, H.-W. Chen, J.-G. Chen, C.-W. Kung, R. Vittal and K.-C. Ho, *J. Mater. Chem.*, 2010, **20**, 9379.
21. T. Gershon, *Mater. Sci. Technol.*, 2013, **27**, 1357-1371.
22. J. S. Park, W.-J. Maeng, H.-S. Kim and J.-S. Park, *Thin Solid Films*, 2012, **520**, 1679-1693.
23. E. Fortunato, P. Barquinha, A. Pimentel, A. Gonçalves, A. Marques, L. Pereira and R. Martins, *Thin Solid Films*, 2005, **487**, 205-211.
24. F. Wypych, G. G. Arizaga and J. E. da Costa Gardolinski, *J. Colloid Interface Sci.*, 2005, **283**, 130-138.
25. G. G. C. Arizaga, K. G. Satyanarayana and F. Wypych, *Solid State Ion.*, 2007, **178**, 1143-1162.
26. V. Briois, C. Giorgetti, F. Baudelet, S. Blanchandin, M. Tokumoto, S. H. Pulcinelli and C. V. Santilli, *J. Phys. Chem. C*, 2007, **111**, 3253-3258.
27. D. Zhang, X. Liu, H. Wan, N. Zhang, S. Liang, R. Ma and G. Qiu, *ACS Sustainable Chem. Eng.*, 2017, **5**, 5869-5879.

28. S. D. Pike, E. R. White, M. S. P. Shaffer and C. K. Williams, *Nat. Commun.*, 2016, **7**, 13008.
29. T. Yuki, S. Ueno, M. Hagiwara and S. Fujihara, *J. Asian Ceram. Soc.*, 2015, **3**, 144-150.
30. H. Morioka, H. Tagaya, M. Karasu, J.-i. Kadokawa and K. Chiba, *Inorg. Chem.*, 1999, **38**, 4211-4216.
31. H. Kajihara, M. Hagiwara and S. Fujihara, *J. Ceram. Soc. Jpn.*, 2016, **124**, 673-677.
32. S. Ueno and S. Fujihara, *J. Electrochem. Soc.*, 2011, **158**, K1.

Chapter 4

Hydrogenation of CO_2 to Methanol using Colloidal Cu/ZnO Nanocatalysts

4.1 Introduction

4.1.1 Ripening Mechanisms of Nanoparticles

In the colloidal synthesis of nanoparticles, the choice of capping ligand is important as it determines the growth kinetics and stability of nanoparticles. Hens and co-workers[1] have shown that, in the hot-injection synthesis of CdSe nanoparticles, particle size decreases with increasing alkyl chain length of capping carboxylate ligands. This was proposed to be due to a change in diffusion coefficient of precursors with longer alkyl chains leading to faster particle nucleation compared growth.

Colloidal ZnO nanoparticle growth, in the solution state, is generally described by the growth/ripening mechanism called Ostwald ripening.[2-5] The mechanism proposes the growth of larger particles at the expense of smaller particles and is diffusion controlled, as described by Lifshitz-Slyozov-Wagner (LSW) theory.[6, 7] Ripening of ZnO nanoparticles readily takes place as the ZnO intrinsic defect sites, including zinc interstitials (Zn_i) and oxygen vacancies (V_O), are highly mobile, especially at grain boundaries.[4, 5, 8] Different factors can promote Ostwald ripening including: (i) concentration of nanoparticles, (ii) nature of solvent and (iii) storage conditions (*e.g.* temperature).[2] Searson and co-workers measured the kinetics of ZnO growth in 2-propanol, in the presence of H_2O, and results were in line with Ostwald ripening kinetics, with the diffusion of H_2O (as a reactant) being the limiting factor.[3, 7]

In comparison, ZnO nanoparticle growth, in the solid state, is less well studied. A study has found ZnO nanoparticles, without capping ligands, readily ripen under ambient conditions, contrary to expectation.[9] It was proposed that trace H_2O present

in the atmosphere is sufficient to promote the growth of ZnO nanoparticles, by reacting with defects sites (Zn_i and V_O). This reaction leads to diffusion of Zn and O atoms and the formation of a new ZnO layer on the nanoparticle's surface (*see section 4.3.3 for proposed mechanism*). In the absence of capping ligands, ZnO nanoparticles are more prone to ripening, in both solution and solid states, and hence the engineering of capping ligands is essential to stabilise nanoparticles.

4.2 Aims and Hypothesis

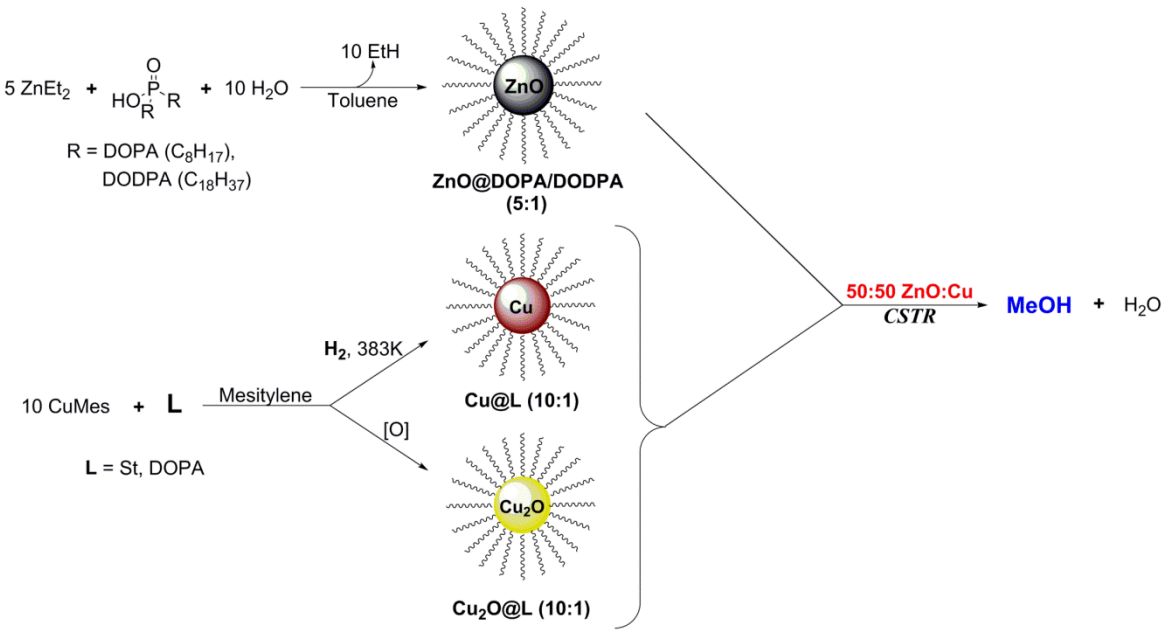

Scheme 4.1. Colloidal Cu or Cu_2O nanoparticles are combined with colloidal ZnO nanoparticles to form the nanocatalysts for the hydrogenation of CO_2 to methanol, at equivalent molar ratio of Cu:ZnO. Both ZnO and Cu-based nanoparticles are synthesised using organometallic reagents. Catalysis conditions in continuous flow stirred tank reactor (CSTR): mesitylene, 210 °C, 50 bar, 3:1 H_2:CO_2, 150 mL min^{-1} flow.

This chapter is set to explore the importance of the nanoparticle capping ligand and the nature of Cu nanoparticles upon colloidal Cu/ZnO nanocatalysts in CO_2 hydrogenation to methanol. The choice of capping ligands may influence 1) nanoparticle size and 2) nanoparticles stability against ageing processes, *e.g.* ripening and sintering, with the latter often triggered during catalysis.

Phosphinates are selected as capping ligands for ZnO and Cu(0) nanoparticles due to their high stability to the conditions of hydrogenation of CO_2 to methanol and high solubility in apolar organic solvents, *e.g.* mesitylene and squalane.[10, 11] Two phosphinates were selected for further study: dioctylphosphinic acid (DOPA–H) and di(octadecyl)phosphinic acid (DODPA–H). The optimisation of the synthesis of DODPA–H will be presented, alongside the synthesis of ZnO nanoparticles capped

with di(octadecyl)phosphinate (ZnO@DODPA). The solid state ripening of the two phosphinate-capped nanoparticles was targeted to understand the effects of increasing the alkyl chain lengths of phosphinates.

The impact of changing the Cu precursor or synthesis route on catalyst performance is investigated and post-catalysis analysis is carried out to shed light on any differences in catalytic activities (Scheme 4.1). The outputs of this investigation were applied to a further investigation into the effect of ZnO particle size on methanol production using both ZnO@DODPA and ZnO@DOPA.

4.3 Long Chain Phosphinate-capped ZnO Nanoparticles

As a capping ligand, dioctylphosphinate (DOPA) has been demonstrated to provide better reductive and size stability for ZnO nanoparticles, in comparison to carboxylates.[10, 11] It chelates as a mono-anionic group to the ZnO surface, *i.e.* stronger binding than neutral molecules as expected, and the two alkyl substituents increase solubility. Using DOPA as capping ligand enables the production of small-sized (2–4 nm), highly dispersed ZnO nanoparticles with good solubility in organic solvents.[10-12] Here, the target is to investigate the effect of chain length on ZnO stability by comparing alkyl chain lengths of 8 methylene units (DOPA) against 18 methylene units (DODPA).

4.3.1 Synthesis & Characterisation of Di(octadecyl)phosphinic Acid (DODPA–H)

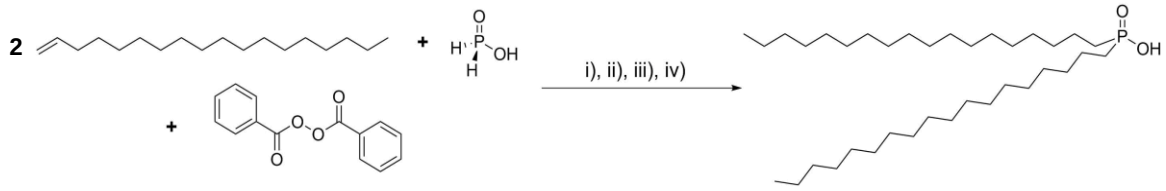

Scheme 4.2. The synthesis of DODPA–H.[13] (i) EtOH, H_2O, 100 °C, 88 h, (ii) 6 M HCl, toluene extraction, acetone wash, (iii) hot recrystallisation from heptane x 3, acetone wash and (iv) chloroform wash.

The synthesis of DODPA–H was achieved using a previously reported route for DOPA–H.[13] The reaction between 1-octadecene and hypophosphorous acid was conducted in the presence of benzoyl peroxide (5.5 mol%) and water, in ethanol (Scheme 4.2). The reaction mixture was refluxed, at 100 °C for 89 h, to allow for the thermal generation of benzoyl peroxide radicals. The resulting reaction mixture, after reflux, was cooled and an acid work up, followed by extraction with toluene, was performed to obtain the crude product.

Several purification steps were required to obtain the DODPA–H: 1) washing with acetone, 2) recrystallisation from hot heptane, three times, and 3) washing with chloroform. The first step removes any unreacted 1-octadecene, the next step also removes residual starting material, impurities (associated with byproducts from radical reactions) and small amount of mono(octadecyl)phosphinic acid (MODPA–H). The final step separates MODPA–H, from DODPA–H, as MODPA–H has higher solubility in chloroform. DODPA–H was obtained as a free-flowing white powder, with a yield of 7%, and its purity was confirmed by elemental analysis. Despite its low solubility in chloroform, it is still sufficient to enable NMR characterisation.

The ^{1}H NMR spectrum (Figure 4.1) shows alkyl signals (δ 0.90–1.70 ppm) with the signal of the methylene protons adjacent to the phosphorus centre at δ 1.50–1.70 ppm. The $^{31}P\{^{1}H\}$ NMR spectrum shows a single peak at δ 61 ppm which is in good agreement with literature, where dialkylphosphinic acids typically resonate.[13] The IR spectrum (Figure 4.2) shows the asymmetric and symmetric C–H stretches at 2914 cm^{-1} and 2847 cm^{-1}, along with C–H bend at 1466 cm^{-1}. The characteristic phosphinic acid stretches are at 1674 cm^{-1} (P–OH) and 963 cm^{-1} (P=O).

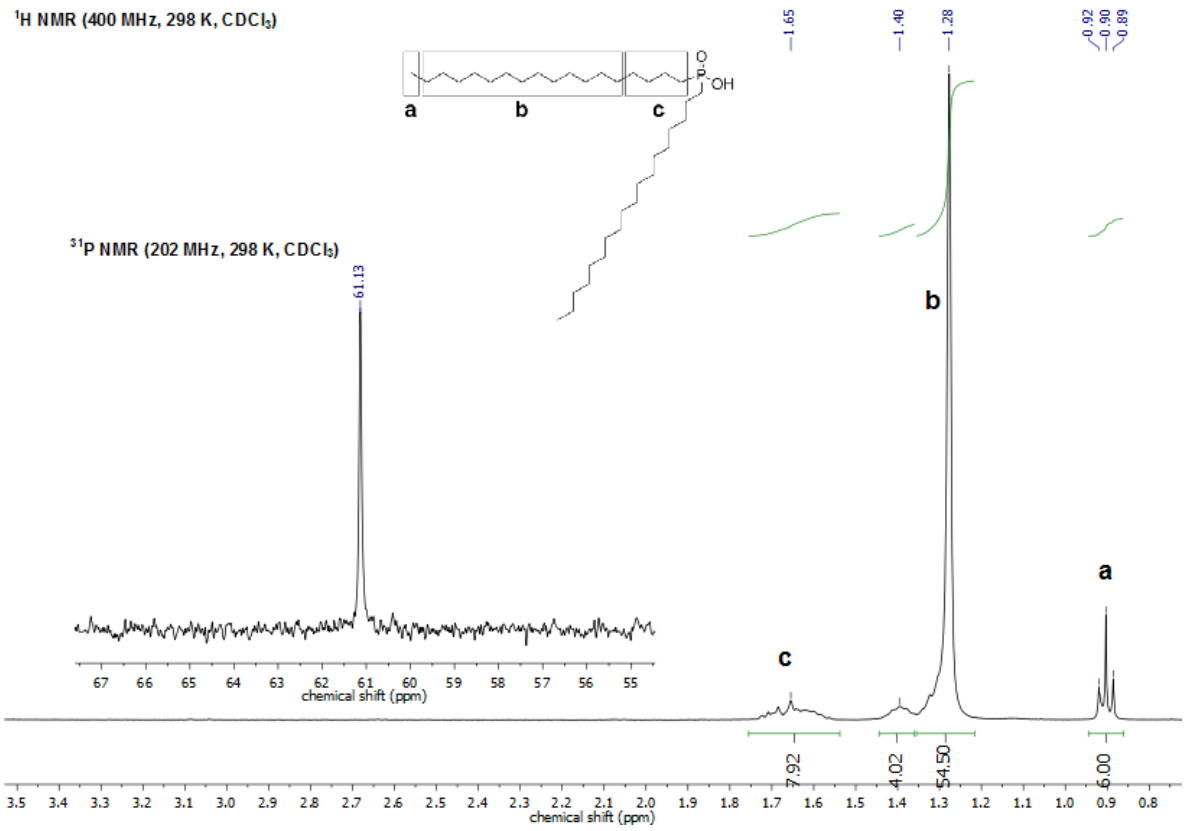

Figure 4.1. ^{1}H NMR spectrum of DODPA–H, with inset as ^{31}P NMR of DODPA–H, taken in $CDCl_3$ at 298 K.

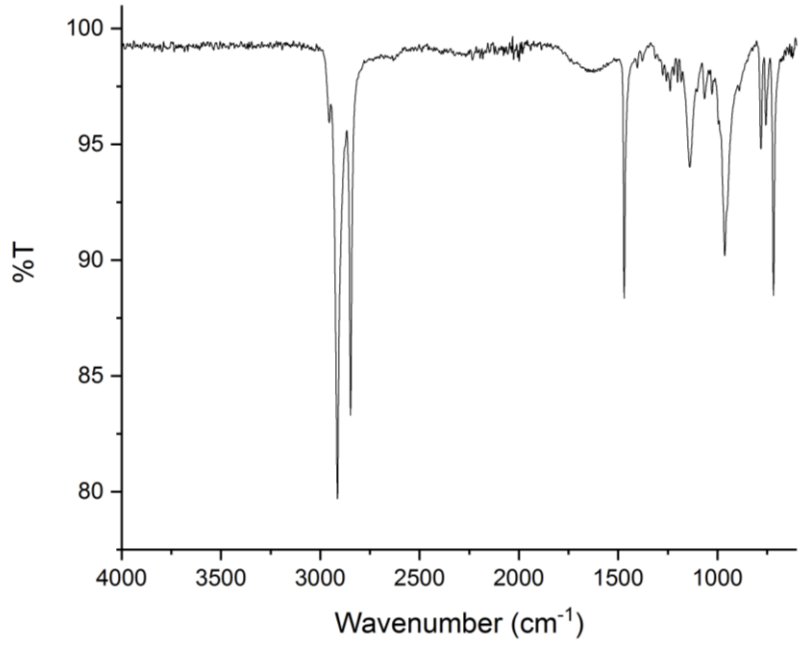

Figure 4.2. IR spectrum of DODPA–H.

4.3.2 Synthesis & Characterisation of ZnO Nanoparticles Capped with DODPA (ZnO@DODPA)

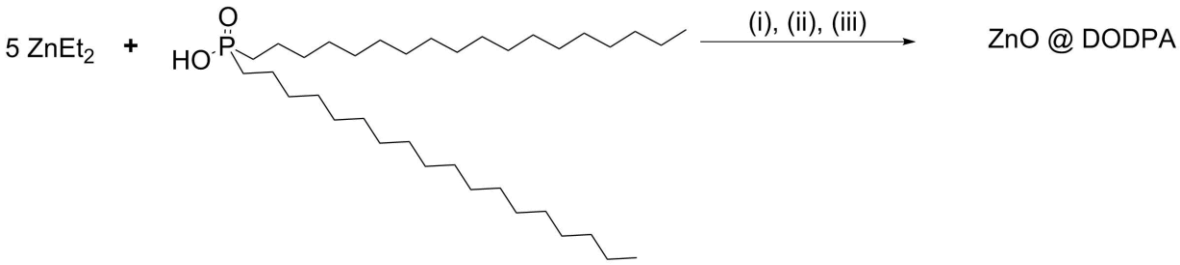

Scheme 4.3. The synthesis of ZnO nanoparticles capped with di(octadecyl)phosphinate (ZnO@DODPA) by the controlled hydrolysis of a mixture containing diethyl zinc and DODPA–H. (i) toluene, 16 h, room temperature, (ii) 0.4 M H_2O in acetone and (iii) centrifugation x 3.

ZnO@DODPA was synthesised by the modification of a previously reported route to ZnO@phosphinate nanoparticles (Scheme 4.3).[10, 11] The reagents were reacted in a 5:1 molar ratio $ZnEt_2$:DODPA–H, in toluene, and the mixture was stirred for 16 h, prior to controlled hydrolysis. The long reaction time ensures complete deprotonation of phosphinic acid, after which the resulting phosphinates have been proposed to be incorporated into zinc ethyl phosphinate clusters.[12] A solution of water in acetone (0.4 M) was added to the solution, over a period of 8 mins, resulting in the evolution of ethane gas. The formation of white precipitate, ZnO@DODPA, was immediately observed on complete hydrolysis. The nanoparticles were isolated using centrifugation (3900 rpm, 20 mins) and purified by re-dissolving them in toluene, followed by precipitation with acetone. Two further centrifugation steps (3900 rpm, 20 mins) were performed, with acetone used in the final centrifugation to assist the removal of residual toluene. After drying the sample in air overnight, a translucent pellet was formed and when crushed, a white powder was obtained (86% yield, based on Zn).

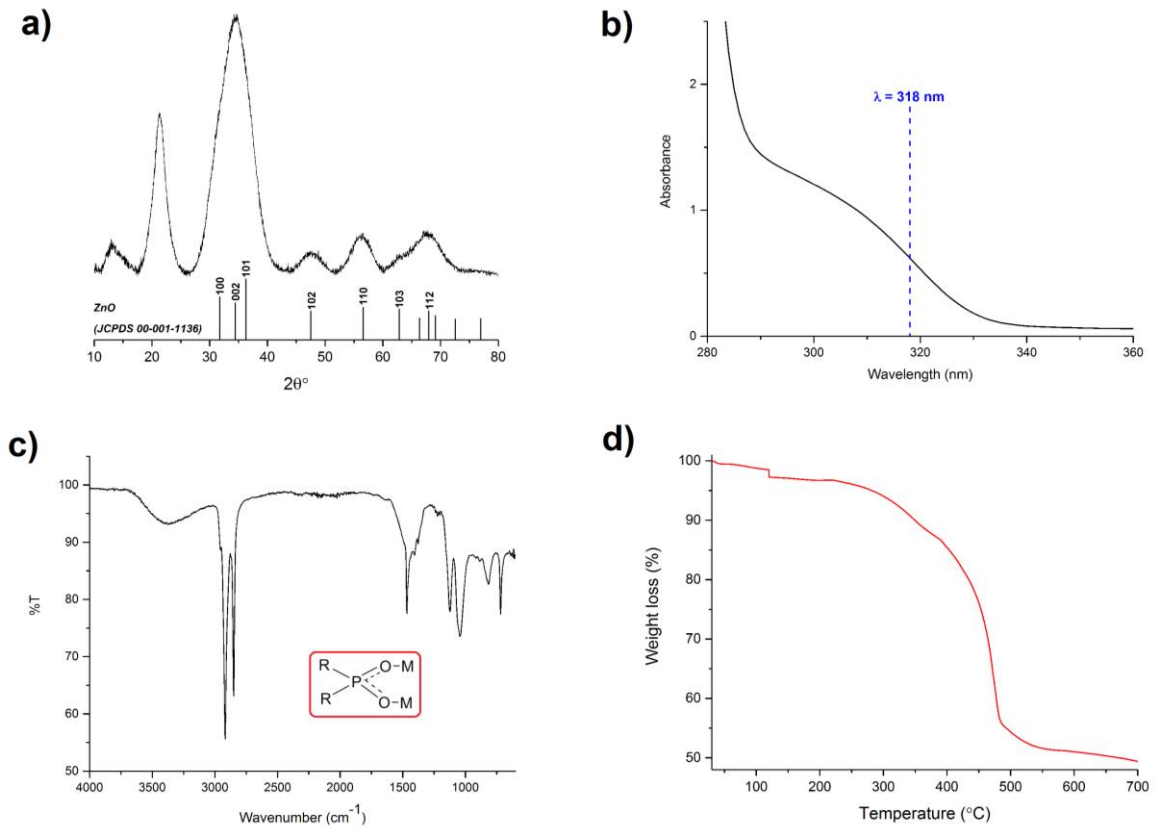

Figure 4.3. (a) XRD pattern of ZnO@DODPA, with reference lines for ZnO as black vertical bars (JCPDS 00-001-1136). (b) UV-Vis spectrum of ZnO@DODPA with wavelength taken for Meulenkamp[14] sizing method marked at 318 nm. (c) IR spectrum of ZnO@DODPA, with inset showing the coordination mode of DODPA on the surface of ZnO. (d) TGA profile of ZnO@DODPA.

The phase identification of ZnO@DODPA was performed using powder XRD and electron microscopy. Wurzite ZnO diffraction peaks are present in the XRD pattern and using Scherrer equation on (102) and (110) planes, the average crystallite size was 2.03 ± 0.06 nm, based on three samples (Figure 4.3a). The UV-Vis spectrum displays a distinctive ZnO band edge, at 318 nm; a particle size of 2.6 nm was estimated, using an empirical method developed by Meulenkamp (Figure 4.3b).[14]

The IR spectrum shows C–H stretches at 2918 cm^{-1} and 2850 cm^{-1}, with C–H bend at 1465 cm^{-1} (Figure 4.3c). The disappearance of the P=O stretch (963 cm^{-1}) and the emergence of PO_2^- stretches (1124 cm^{-1}, symm, and 1043 cm^{-1}, asymm) indicate

deprotonation of the free acid and coordination to the ZnO as a phosphinate ligand. The separation of the symmetric and asymmetric stretches of PO_2^- is 81 cm^{-1}; the binding mode between them can be inferred from this separation to be the same as that of polymeric zinc *bis*(dibutylphosphinate), reported by Gillman *et al.*[15, 16] (Figure 4.3c *inset*). The same binding mode was also proposed for ZnO@DOPA.[10]

The thermal degradation profile, from TGA, shows two step degradation with the first weight loss (1.2% at 120 °C) likely to correspond to residual toluene, and the second weight loss (47.8% from 120–700 °C) corresponding to organic ligand decomposition (Figure 4.3d). The ligand loading established by TGA is in good agreement with the value determined by elemental analysis (40.15 wt% C, 7.13 wt% H). The residue from the thermolysis consists of Zn- and P-containing species, likely to include ZnO, P_4O_{10}, $Zn(PO_3)_2$, $Zn_4P_6O_{19}$ or $Zn_2P_2O_7$ clusters.[17, 18] The particle composition was determined as 6:1 Zn:DODPA ratio, with a surface coverage of 60% (radius of 1.15 nm; *calculation outlined in Chapter 7*); the mismatch between the reagent starting ratio and particle stoichiometry may be due to the formation of minor amounts of zinc phosphinate clusters, *e.g.* $[Zn_4O(DODPA)_6]$, which would be expected to be removed during purification.[12] Pike *et al.* have demonstrated that such zinc-phosphinate clusters form readily, alongside ZnO@DOPA, in the hydrolysis of $ZnEt_2$ and DOPA–H.[12]

TEM analysis shows spherical ZnO@DODPA nanoparticles (Figure 4.4a & b). Scanning transmission electron microscopy, in high angle annular dark field mode (STEM-HAADF), shows nanoparticles with an aggregated morphology; amongst individualised spherical ZnO nanoparticles, aggregate of spherical particles, adopting a chain-like morphology, were also observed (Figure 4.4c). The particle size of the

individual ZnO nanoparticles is 2.3 ± 0.06 nm (σ = 0.31, *N* = 31, Figure 4.4d), in good agreement with XRD and UV-Vis values.

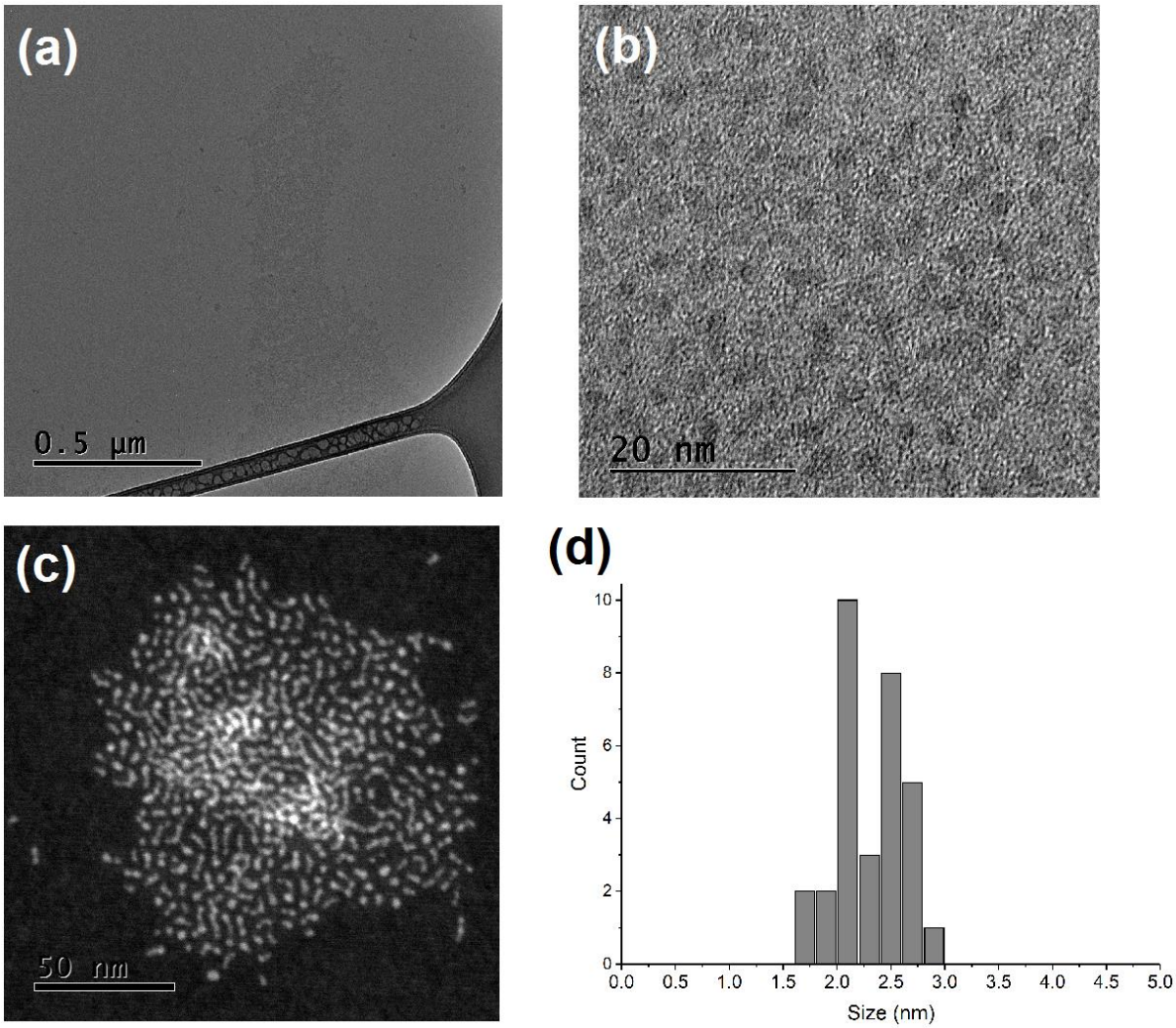

Figure 4.4. (a) TEM image of ZnO@DODPA, (b) HR-TEM image of ZnO@DODPA showing spherical nanoparticles, (c) STEM-HAADF image of ZnO@DODPA and (d) size distribution histogram of ZnO@DODPA from STEM-HAADF images.

4.3.3 Ripening of ZnO@DODPA

Previously, ZnO@DOPA was shown to ripen, in the solid state, under atmospheric conditions over a time period of 1 month.[19] The ripening was studied using UV-Vis spectroscopy and the empirical sizing method developed by Meulenkamp.[14] The nanoparticle sizes increased from 3.1 to 4.0 nm in less than 4 days, when the nanoparticles were stored in air. The size increase can be avoided by storing ZnO@DOPA under vacuum or in a dry (inert) atmosphere. One possible cause of ripening is the chemisorption of water on the ZnO surface, promoting Ostwald ripening or even an oriented attachment mechanism.[9] For example, a plausible ripening mechanism involves intrinsic defect sites of ZnO, such as V_O. Reactive hydroxyl species are generated when chemisorbed H_2O reacts with V_O on the ZnO surface[8] (Equation 4.1 & 4.2) and the hydroxyl species react further with the highly mobile Zn_i sites to form a new surface ZnO layer (Equation 4.3).[4, 5, 9] When the surface of ZnO particles are not capped with any ligands, a higher amount of intrinsic defect sites are present, promoting the growth of ZnO through ripening triggered by chemisorbed H_2O.

$$V_O^{\bullet\bullet} + O_O^x + H_2O \rightarrow OH_O^\bullet + OH_O^\bullet \quad (4.1)$$

$$OH_O^\bullet + OH_O^\bullet \rightarrow O_O^x + (OH_2)_O^{\bullet\bullet} \quad (4.2)$$

$$Zn_{Zn}^x + O_O^x \rightarrow Zn_{Zn}O_O \quad (4.3)$$

Here, the ZnO@DODPA ripening, in the solid state, was investigated over 2 weeks. Two identical batches of ZnO@DODPA were tested; one set was kept in air, whilst the other was stored in a nitrogen-filled glovebox with no trace moisture or oxygen present (H_2O <0.1 ppm and O_2 <0.1 ppm). Using UV-Vis spectroscopy, the size

of ZnO@DODPA was monitored for both samples and no changes in the sizes of any particles were observed (Figure 4.5a & b). The experiment was continued for three months, after which no detectable ripening or change in nanostructure was found even for particles stored in air (Figure 4.5c & d).

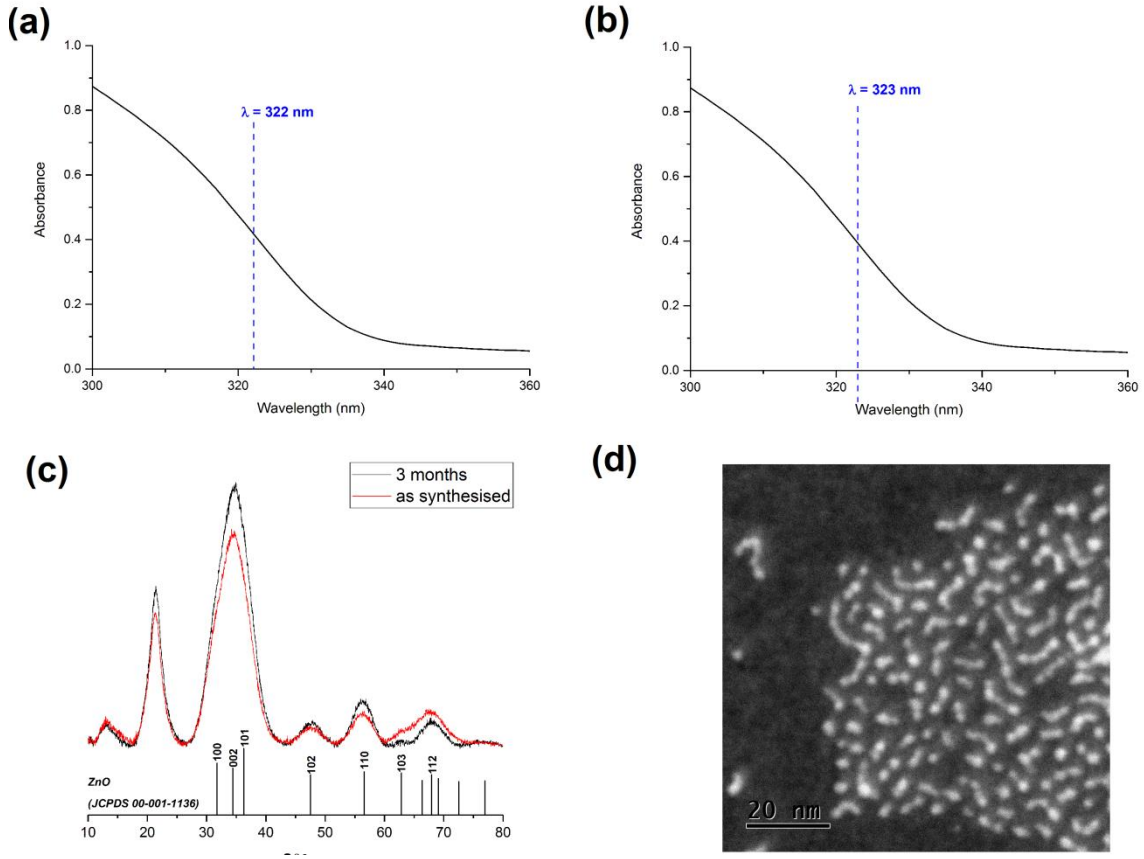

Figure 4.5. UV-Vis spectra of ZnO@DODPA in toluene for (a) sample stored in air, for 2 weeks, and (b) sample stored in a nitrogen-filled glovebox for 2 weeks. (c) XRD patterns of as-synthesised ZnO@DODPA and the same sample was stored in air for 3 months and (d) STEM-HAADF of ZnO@DODPA stored in air for 3 months.

4.3.4 Discussion

The synthesis of DODPA was successful, but the overall yield was disappointing (7%). Due to steric hindrance imposed by the long alkyl chains, the abstraction of the second proton on the phosphorus centre, by a radical species, is unfavourable and hence the attachment of the second octadecyl chain cannot occur. Despite the low yield, the overall synthetic procedure is simple and amenable to scale-up. The synthesis was carried out at 50 g scale (with respect to 1-octadecene), enabling the isolation of sufficient DODPA–H for further experiments (3.9 g).

A molar ratio of 5:1 Zn:phosphinate was necessary to provide ~95% surface coverage for particles of diameter 3.5 nm and this was chosen as the starting molar ratio for synthesis of ZnO@DODPA.[10] The surface coverage of ZnO by DODPA ligand is lower than expected (71%), potentially due to loss of ligands during particle purification, resulting in 6:1 molar ratio of Zn:DODPA, and the small size of nanoparticles. The growth and ripening mechanism of ZnO might be the key to the formation of the ZnO@DODPA chains observed in TEM and STEM. Using capping ligands, containing long alkyl chains, causes a higher rate of nucleation compared to the rate of nanoparticle growth through diffusion;[1] in the DODPA system, similar effects might occur which leads to a larger population of smaller nanoparticles (< 3 nm) where not enough ligands are present to stabilise the nanoparticles. The incomplete coverage of the ZnO surface might lead to exposure of certain reactive facets, tentatively proposed to be polar (001) facets, whereby particles in close proximity would collide and fuse to minimise surface potential energy through a process called oriented attachment (OA). OA is a known mechanism in the nucleation

and growth process of ZnO (Figure 4.6) and 1D-quasi chains are the main features of OA, similar to that of ZnO@DODPA chains.[20-23]

The observed chains of ZnO@DODPA nanoparticles suggest the particle growth might be halted at OA stage, with no occurrence of Ostwald ripening (next stage of particle size growth; Figure 4.6a). The sterically hindered and hydrophobic alkyl chains prevent H_2O chemisorption onto the surface of ZnO, inhibiting Zn and O atoms migration and consequent ripening.[12, 17-20] Such a hypothesis is further substantiated through STEM-HAADF analysis where the ZnO particles, stored in air for 3 months, show no change in particle morphology.

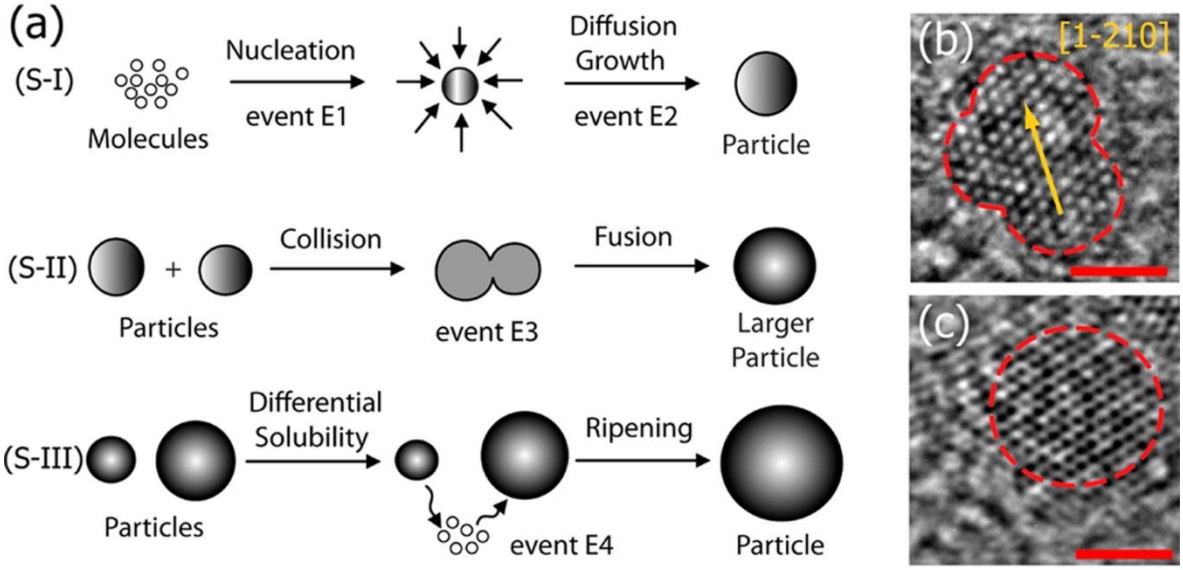

Figure 4.6. (a) Schematic of the stage wise-growth of ZnO nanocrystals (NCs) in solution: Stage S-I: nucleation [event E1] followed by diffusion growth [event E2]; stage S-II: coagulative growth by oriented attachment (OA) involving collision and fusion [event E3]; stage S-III: Ostwald ripening, OR [event E4]. (b and c) Experimental evidence from HR-TEM measurements of ZnO nanocrystals showing (b) coagulation of smaller particles at initial stages of reaction (3 min) and (c) quasi-spherical particles at later growth time (60 min). Scale bar is 2 nm. *Reprinted (adapted) with permission from Bandyopadhyaya et al.[22] Copyright 2012 American Chemical Society.*

4.4 Colloidal Cu/ZnO Nanocatalysts for CO_2 to Methanol

The synthesis and catalytic study of the catalysts were performed in collaboration with Dr Sebastian Pike and Dr Andrés García Trenco.

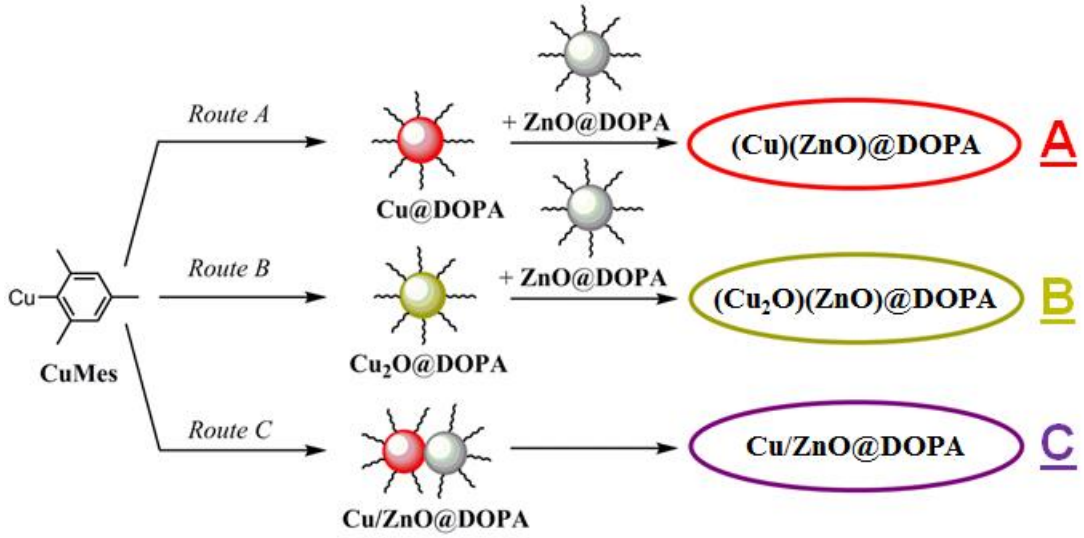

Scheme 4.4. Synthetic routes to colloidal Cu/ZnO nanoparticles for hydrogenation of CO_2 to methanol. Route A: mesitylene, 2 bar H_2, 110 °C, 2.5 h. Route B: mesitylene, air, 3 d. Route C: Zn@DOPA, 2 bar H_2, 110 °C, 2.5 h.

The formation of Cu/ZnO interfaces is crucial for methanol production from hydrogenation of CO_2.[24-27] In order to maximise Cu/ZnO interface formation, three different colloidal Cu/ZnO nanocatalysts (1:1 molar ratio Cu:Zn) systems were prepared to explore the effects of different Cu precursors on catalysis. DOPA was chosen as a capping ligand due to its enhanced reductive stability, under catalytic conditions, compared to carboxylates.[10, 11] The three new colloidal catalysts were synthesised by different synthetic routes (Scheme 4.4): Catalyst **A** is a mixture of Cu@DOPA with ZnO@DOPA nanoparticles, prepared as described previously in literature.[10, 28, 29] Catalyst **B** is a mixture of Cu_2O@DOPA and ZnO@DOPA, in order to avoid the use of air-sensitive techniques for catalyst preparation. Cu_2O@DOPA was prepared by oxidising CuMes with DOPA–H in air for three days. Catalyst **C** involves

the formation of Cu(0) nanoparticles, in the presence of ZnO@DOPA, to maximise the formation of Cu/ZnO interfaces prior to catalysis.

The standard catalysis conditions were applied, *i.e.* mesitylene as solvent, with a pressure of 50 bar (CO_2:H_2 1:3), at 210 °C, for 20 h. Mesitylene was chosen as the reaction solvent for catalysis as it has good feed gas solubility and high stability under high temperature (210 °C). Squalane is most commonly used for liquid-phase CO_2 hydrogenation to methanol, but complications with post-catalysis analysis is often encountered due to incomplete removal of squalene, using evacuation techniques, because of its low volatility.[30] Mesitylene is easier to remove compared to squalene and hence it has an added advantage of allowing better quality post-catalysis analysis.

All three colloidal Cu/ZnO nanocatalysts displayed 2-3 times higher methanol activity and comparable methanol selectivity to two benchmark catalysts, heterogeneous ternary Cu-ZnO-Al_2O_3 and colloidal Cu/ZnO@St (Figure 4.7).[11, 31] Although catalysts **A** – **C** have similar activity and selectivity, the post-catalysis characterisation revealed difference in their morphologies.

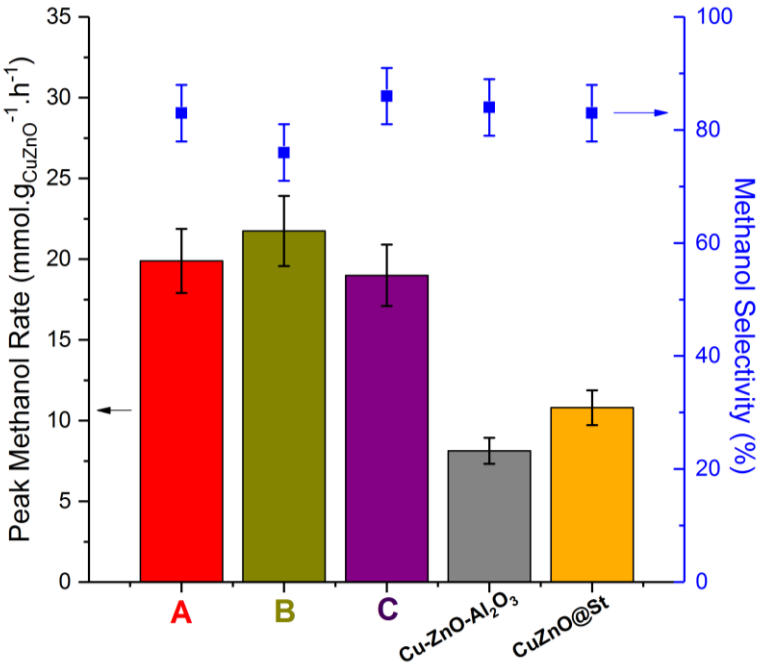

Figure 4.7. Peak methanol rate and selectivity for colloidal Cu/ZnO catalysts **A**, **B**, and **C**, and the two reference catalysts Cu-ZnO-Al_2O_3 and CuZnO@St in the hydrogenation of CO_2 to methanol. Reaction conditions: 210 °C, 50 bar, H_2 : CO_2 molar ratio 3 : 1, 150 mL min^{-1}, in mesitylene.

4.4.1 Post-catalysis analysis of colloidal Cu/ZnO nanocatalysts systems

The analysis of spent catalysts after the process of hydrogenation of CO_2 to methanol provides insight into morphological changes occurring during catalysis, and, in turn, may help explain the observed activities. In order to understand the influence, if any, of interfaces in this catalysis, several characterisation techniques, in solid and solution phase, were applied on the spent catalysts: HR-TEM, STEM-EDX, XRD and UV-Vis spectroscopy. Particles sizes were obtained from TEM, XRD and UV-Vis spectroscopy (Table 4.1).

Catalysts **A**, **B** and **C** all showed clear diffraction peaks of nanocrystalline Cu(0) phase in XRD analysis, using a polyimide tape to exclude air (Figure 4.8). An increase in the size of Cu(0) nanoparticles was observed across all three samples, with catalyst **A** exhibiting the largest change (2 to 6.4 nm). The increased size suggests sintering of the particles occurred under catalytic conditions. For the crystalline ZnO phase, a slight increase in particle size was also observed (2.3 to 3–4 nm), but crystalline ZnO was only observed in the XRD patterns of catalyst **A** and **C**.

TEM and STEM-HAADF analyses of catalyst **A** and **C** (Figure 4.10a, c, d & f) showed the presence of Cu/ZnO interfaces. Catalyst **B** (Figure 4.10b & e) exhibited a different morphology to that of **A** and **C**; instead of well-defined crystalline Cu(0) and ZnO nanoparticles being observed, the majority of Cu(0) nanoparticles were encased in an amorphous-ZnO network as identified through EDX (Figure 4.11). TEM confirmed the slight ripening of Cu(0) nanoparticles in all three post-catalysis samples (Table 4.1); the largest change was observed for catalyst **A** (2.1 to 7.2 nm) and the smallest for catalyst **B** (2.2 to 3.6 nm). Sizes from TEM are in reasonable agreement with sizes obtained from XRD.

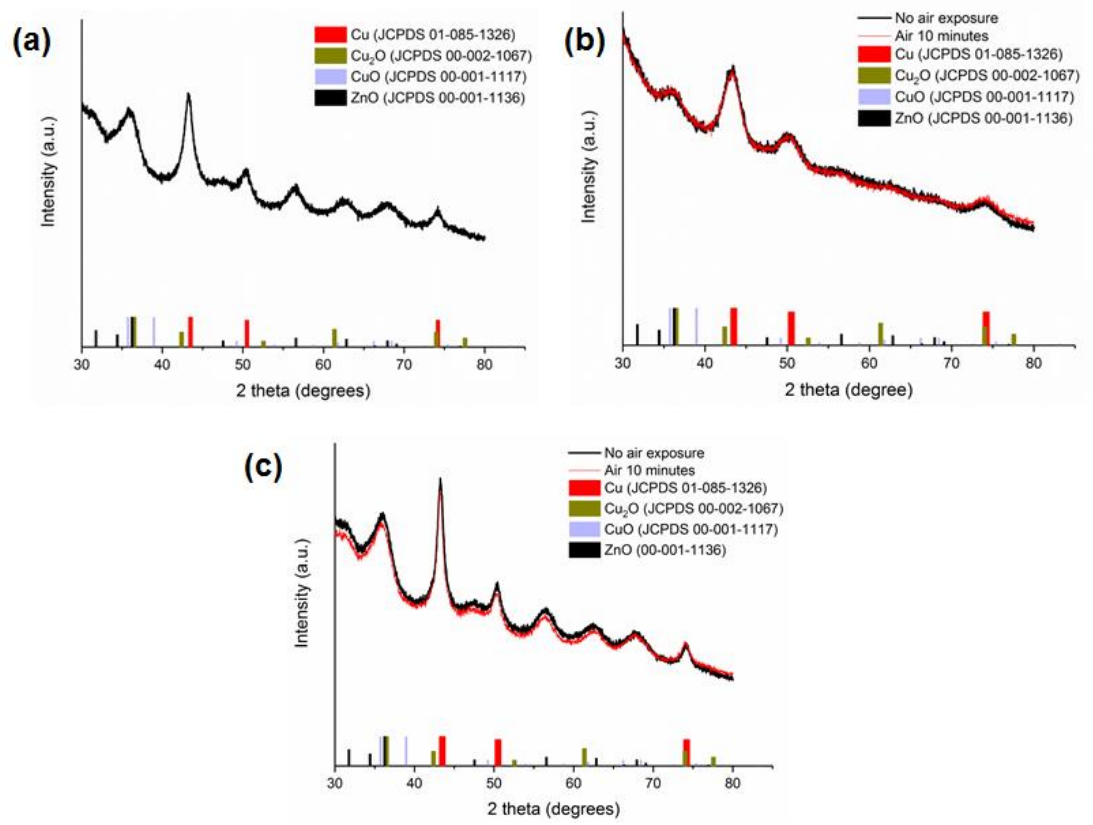

Figure 4.8. XRD patterns of post-catalysis samples for catalyst (a) **A**, (b) **B** and (c) **C**. Reference patterns: ZnO (JCPDS 00-001-1136), Cu (JCPDS 01-085-1326), Cu_2O (JCPDS 00-002-1067) and CuO (JCPDS 00-001-1117).

The oxidative stability of the catalysts was investigated using UV-Vis spectroscopy (Figure 4.9). An increase in the oxidative stability of Cu(0) was observed across all three post-catalysis samples, when compared to their pre-catalysis counterparts. The sizes of ZnO, estimated using the Meulenkamp method,[14] gave a reasonable agreement with increased sizes observed by TEM and XRD for **C** (Table 4.1), but in the case of **A** (Figure 4.9a), the size calculated from XRD was quite different to those indicated by TEM and UV-Vis spectroscopy (Table 4.1). The differences in the sizes could be attributed to the tendency to underestimate particle size using the Scherrer analysis. The absence of crystalline ZnO in **B** was further confirmed by the lack of a ZnO band edge in the UV-Vis spectrum (Figure 4.9b).

The SPR was observed across all three post-catalysis samples and upon exposure to air, its intensity did not change over 24 h but a slight red-shift was observed. The red shift is attributed to a change in the dielectric constant (ε) of the metal surface. One explanation may be that surface oxidation occurs; the DOPA (ε ~ 2.5) is replaced by an outer Cu_2O shell (ε = 7.1),[29] which causes the observed red shift of SPR.[32, 33] Due to the nanoscale of Cu(0), it preferentially oxidises to Cu_2O as the lattice expansion energy is lower compared to transforming to CuO.[29, 34, 35] In comparison, the starting Cu(0) nanoparticles undergo almost immediate oxidation, upon exposure to air (~2 min). The difference in the oxidative stabilities may also indicate the formation of a protective layer over the surface of Cu(0) which hinders further oxidation (*see section 3.4.3*).

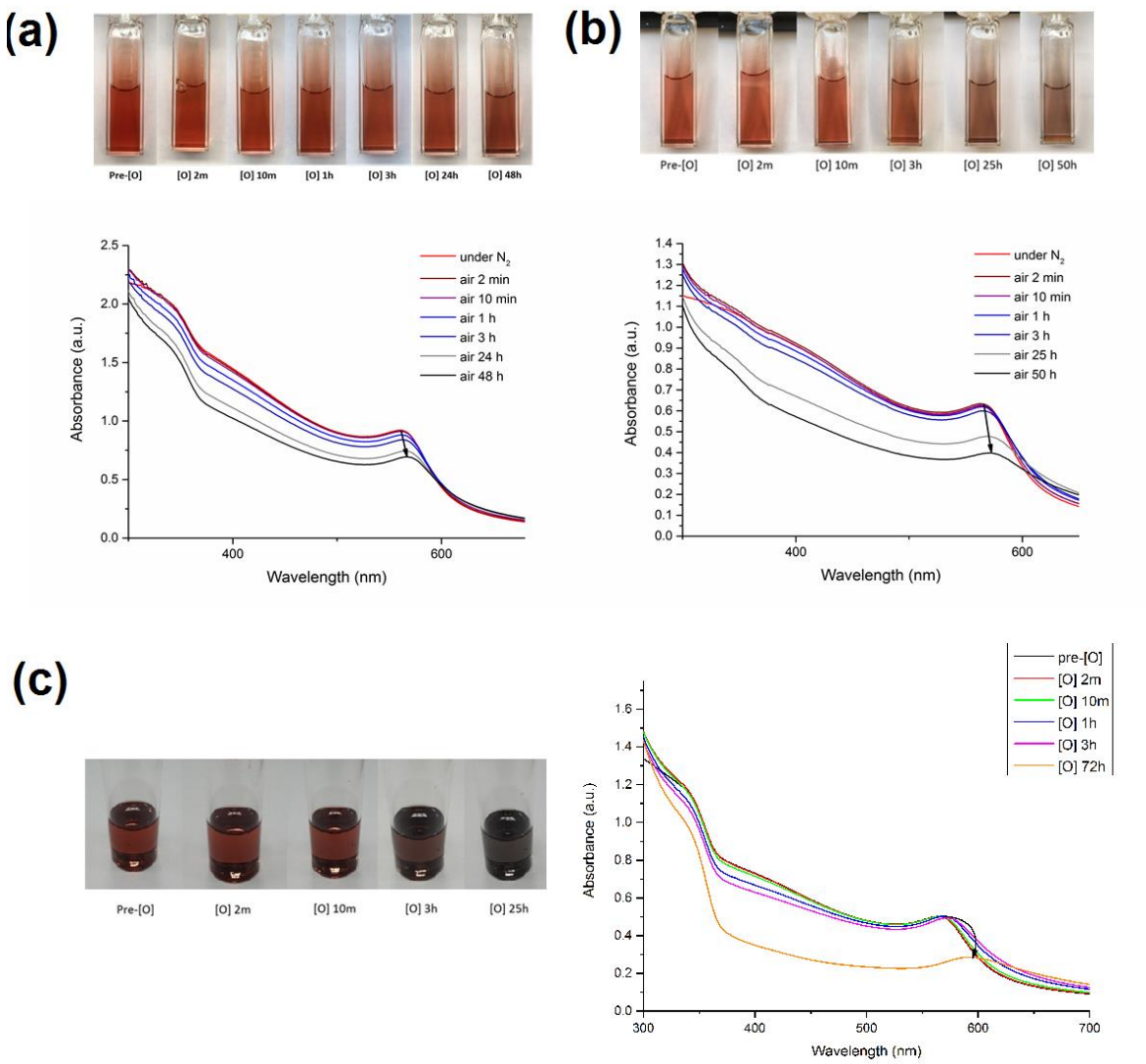

Figure 4.9. UV-Vis spectra and photographs demonstrating the increased oxidative stability over time of the post-catalysis samples for catalyst (a) **A**, (b) **B** and (c) **C**.

	ZnO (nm)						Cu (nm)			
	Pre-catalysis			Post-catalysis			Pre-catalysis		Post-catalysis	
Catalyst	**XRD**	**TEM[a]**	**UV**	**XRD**	**TEM[a]**	**UV**	**XRD**	**TEM[a]**	**XRD**	**TEM[a]**
A CuZnO@DOPA	2.3	2.8 ± 0.02 (0.6)	2.8	3.2	4.9 ± 0.1 (1.1)	4.2	-	2.1 ± 0.02 (0.9)	6.4	7.2 ± 0.2 (1.9)
B Cu_2OZnO@DOPA	2.3	2.8 ± 0.02 (0.6)	2.8	-	-	-	-	2.2 ± 0.1 (0.7)[b]	3.6	3.6 ± 0.1 (0.8)
C CuMesZnO@DOPA	2.3	2.5 ± 0.04 (0.5)	2.9	3.8	3.9 ± 0.1 (1.1)	4.1	6.8	6.2 ± 0.2 (1.7)	8.7	6.0 ± 0.5 (2.4)

[a] Average particle size ± standard error (standard deviation). The standard error of the mean is defined as standard deviation/(no. of measurements). [b] The size given is for Cu_2O@DOPA.

Table 4.1. Cu(0) and ZnO nanoparticles size data from XRD, TEM and UV-Vis spectroscopy for pre-catalysis and post-catalysis colloids.

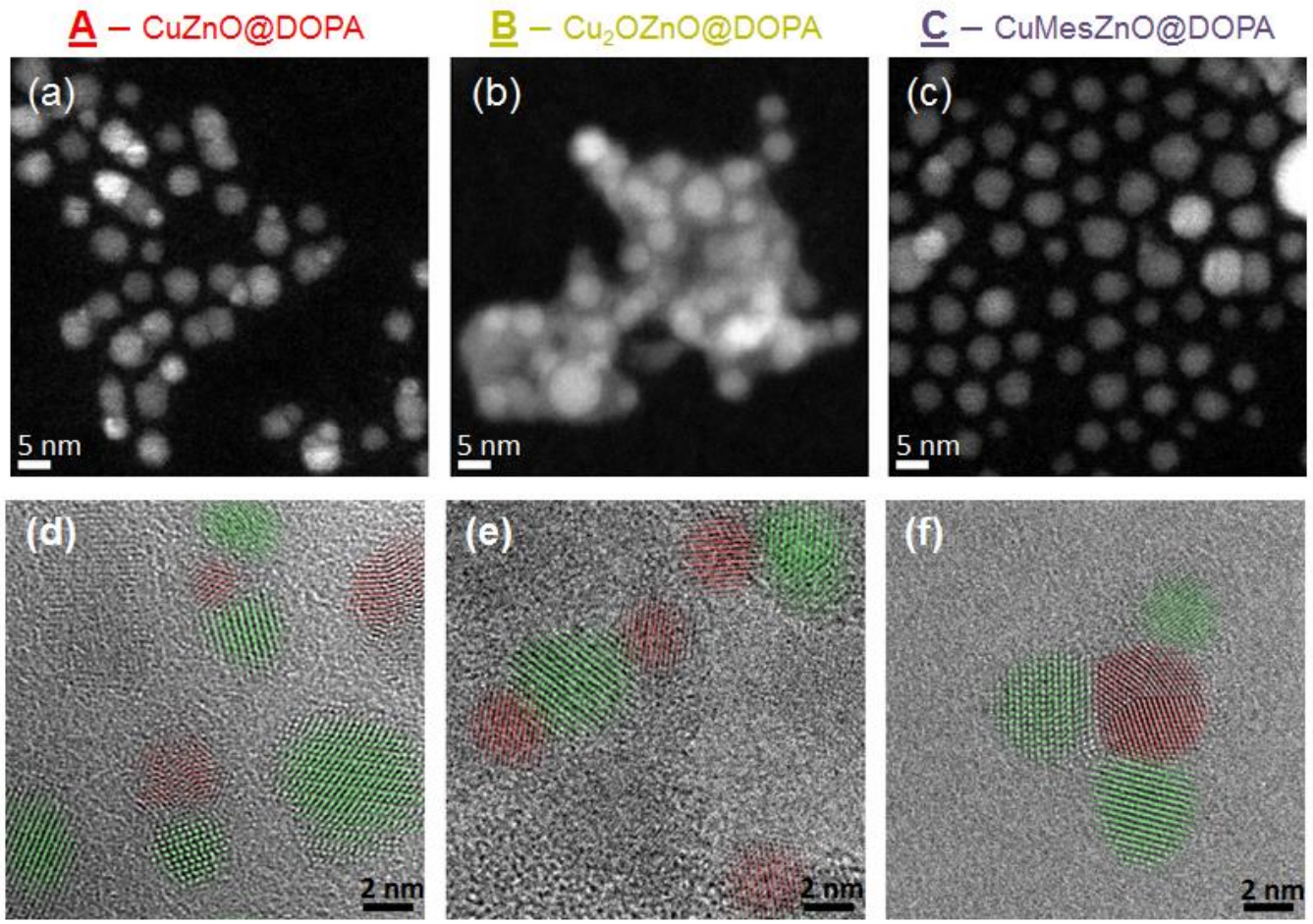

Figure 4.10. (a)-(c) STEM images of post catalysis samples of catalyst **A**, **B**, and **C**. (d)-(f) TEM images of post-catalysis samples of catalysts **A**, **B** and **C**, with green colouring represented as ZnO and red colouring represented as Cu(0). *Data collected by Dr Edward R. White.*

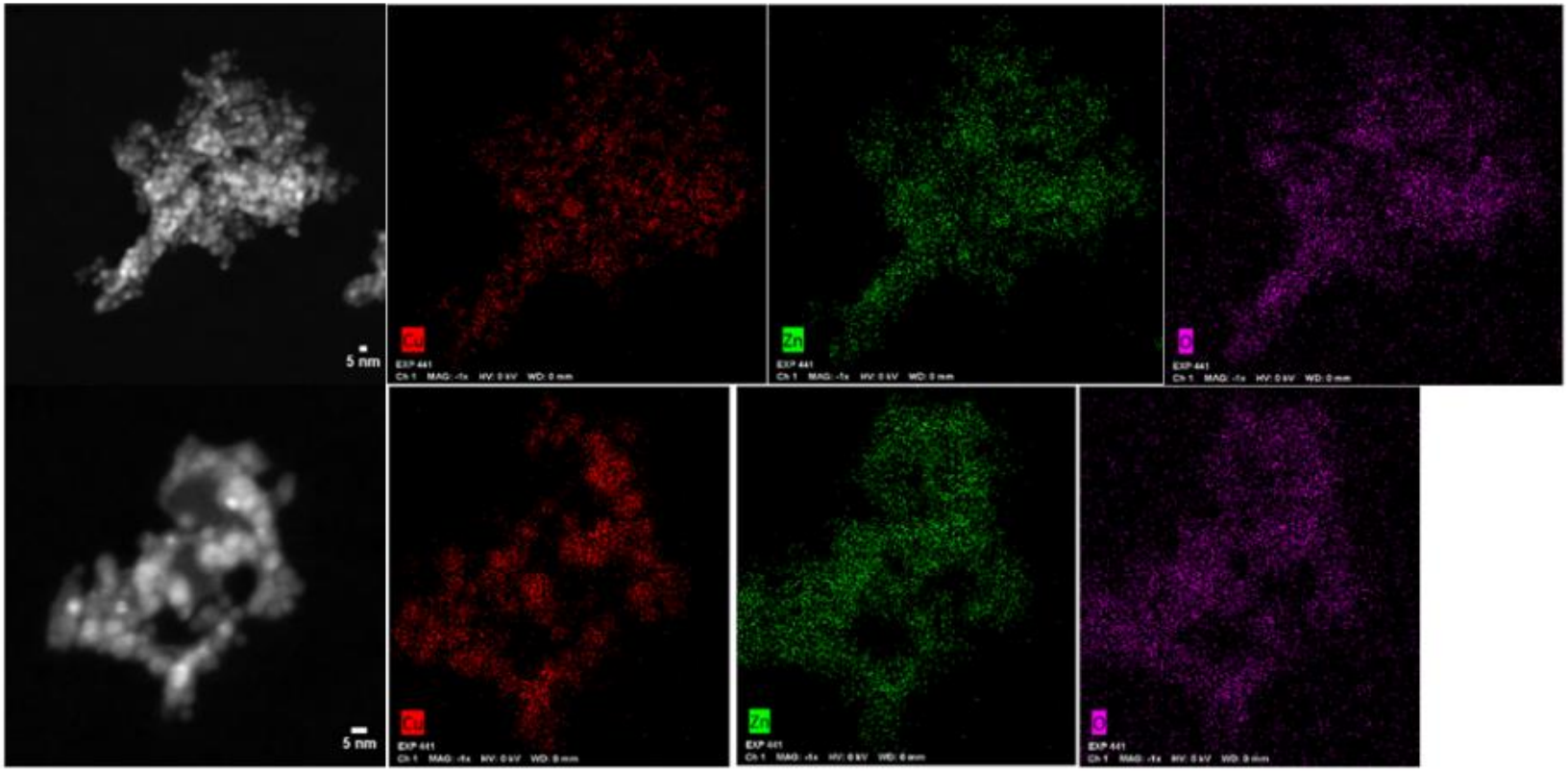

Figure 4.11. STEM-EDX mapping of post-catalysis sample of catalyst **B**. The maps show the amorphous network around nanocrystalline Cu(0) particles contains Zn and O. *Data collected by Dr Edward R. White.*

4.4.2 ZnO@DODPA catalyst systems

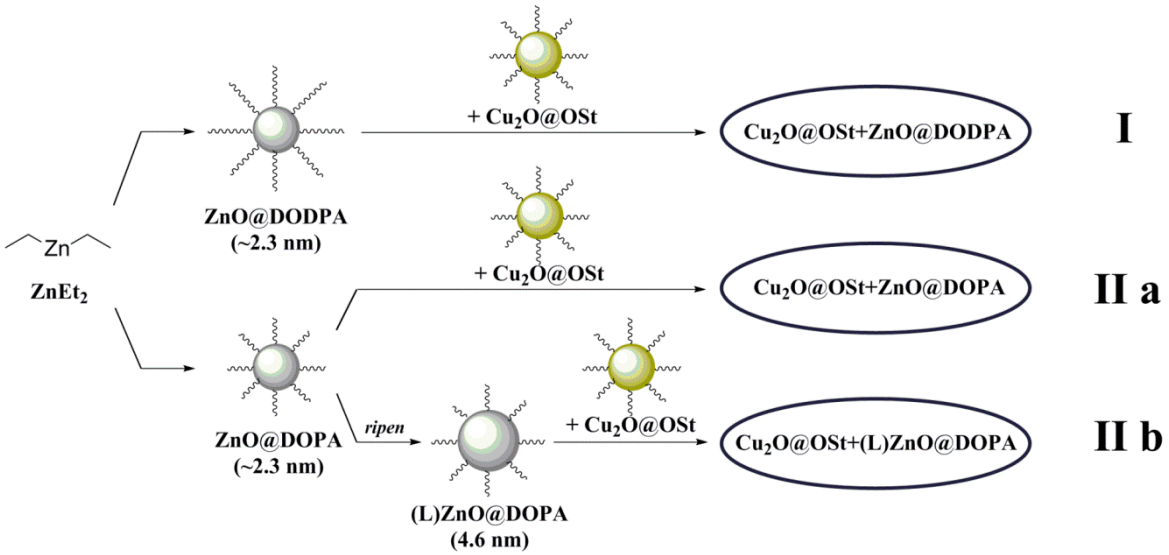

Scheme 4.5. Synthetic routes to ZnO nanoparticles capped with DOPA and DODPA, combined with Cu_2O@OSt nanoparticles to form colloidal nanocatalysts for the hydrogenation of CO_2 to methanol.

Ripening of ZnO nanoparticles may hamper the catalytic activity and to test its importance in hydrogenation of CO_2, a system with ZnO@DODPA was investigated. It was already demonstrated that the simple increase in length from octyl (C_8) to octadecyl (C_{18}) alkyl chain significantly reduced solid state nanoparticle ripening. The samples that were subjected to ripening studies in *section 4.3.3* were used in this catalytic study for the liquid-phase hydrogenation of CO_2 to methanol.

In order to investigate the influence of the ZnO with phosphinate ligands, Cu_2O nanoparticles were capped with stearate ligands (size ~ 2 nm) (Scheme 4.5). Two different ZnO components were compared: ZnO@DODPA (2.0–2.3 nm) and ZnO@DOPA, using both as synthesised (2.3 nm) and ripened (4.6 nm) particles. The standard catalysis conditions were applied, *i.e.* mesitylene as solvent, with a pressure of 50 bar (CO_2:H_2 1:3), at 210 °C, for 20 h.

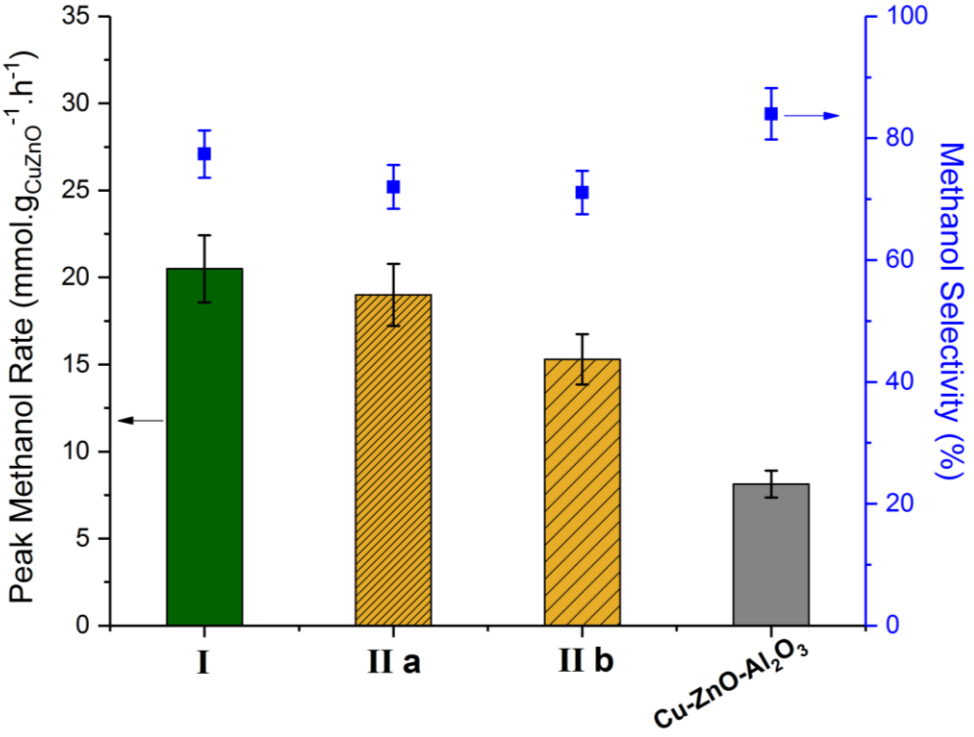

Figure 4.12. Peak methanol rate and selectivity for catalysts **I** (ZnO@DODPA + Cu_2O@OSt), **II a** (ZnO@DOPA + Cu_2O@OSt) and **II b** ((L)ZnO@DOPA + Cu_2O@OSt) in the hydrogenation of CO_2 to form methanol. Reaction conditions: 210 °C, 50 bar, H_2 : CO_2 molar ratio 3 : 1, 150 mL min^{-1}, in mesitylene.

Both catalysts **I** (ZnO@DODPA+Cu_2O@OSt) and **II a** (ZnO@DOPA+Cu_2O@OSt, ZnO = 2.3 nm) have similar activities (Figure 4.12). The catalysts show ~25% higher activity than catalyst **II b** (ZnO@DOPA+Cu_2O@OSt, ZnO = 4.6 nm) and ~60% higher than the commercial heterogeneous Cu-ZnO-Al_2O_3. Commercial Cu-ZnO-Al_2O_3 was activated prior to catalysis according to literature procedure.[36] In terms of methanol selectivity, all catalysts (**I**, **II a** and **II b)** display similar selectivity and are slightly less selective than the Cu-ZnO-Al_2O_3. It is important to note that the only byproduct is CO and no other higher number alcohols or hydrocarbons were formed. Unfortunately, due to the limited access to air-sensitive methods at the time of this study, the post-catalysis characterisation using powder XRD, electron microscopy and XPS were conducted under aerobic conditions.

The characterisation of post-catalysis sample **I** showed the same features as observed for catalyst **B.** Its powder XRD (Figure 4.13a) shows peaks due to Cu(0), Cu_2O and CuO, but no ZnO diffraction pattern was observed. The sizing of the Cu components cannot be determined due to the lack of individualised peaks to measure the FWHM for Scherrer analysis. The samples were also characterised using TEM (Figure 4.14) which showed agglomerates of nanoparticles encased in an amorphous network and by using STEM-EDX (Figure 4.15), the amorphous network was identified as ZnO encasing crystalline Cu(0) nanoparticles. Finally, an increase in its oxidative stability was also observed; the Cu(0) SPR was maintained for up to 96 h in air (Figure 4.13b). No ZnO band edge was seen in the UV-Vis spectra and this is in line with some reports of loss of absorption for amorphous ZnO as its electronic properties are altered.[37, 38] The alteration in electronic properties were mainly attributed to lack of intrinsic defect sites (*e.g.* V_O) within Wurzite ZnO.[39]

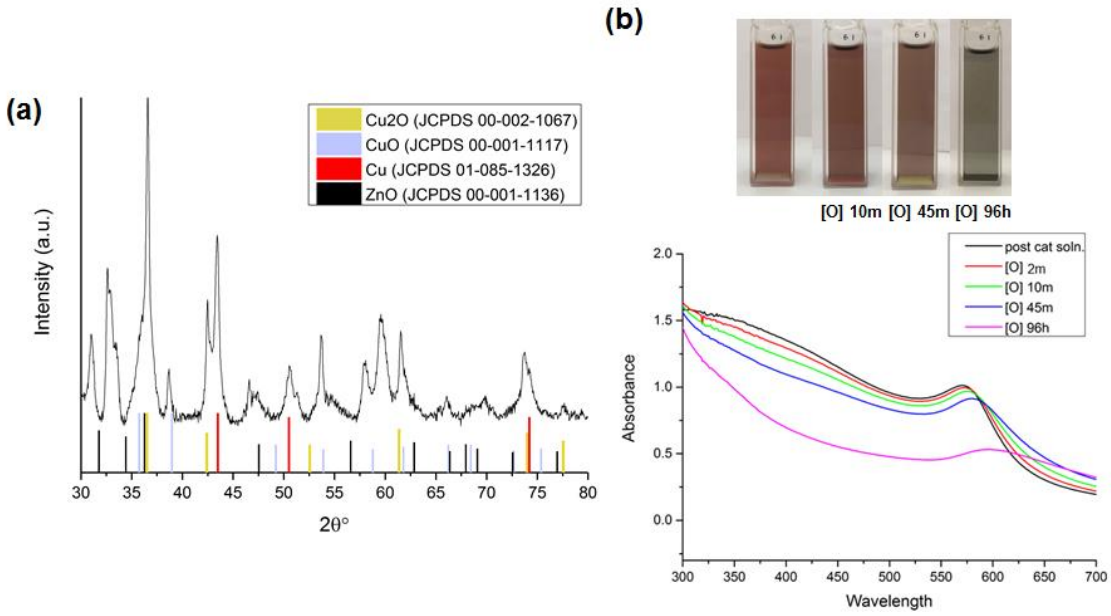

Figure 4.13. (a) XRD pattern of the post-catalysis sample of catalyst **I**. (b) UV-Vis spectra to demonstrate the increased oxidative stability of the Cu(0) nanoparticles in the post-catalysis sample of catalyst **I**.

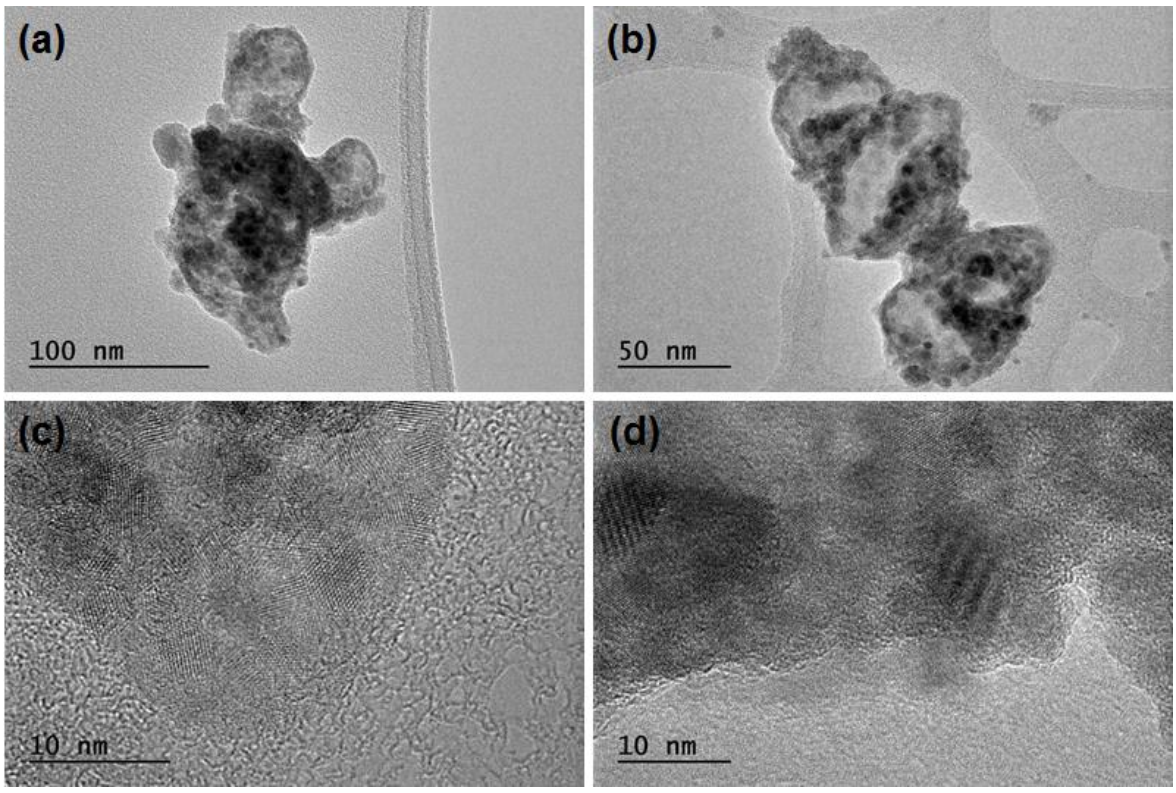

Figure 4.14. (a) & (b) TEM images of post-catalysis sample of catalyst **I**, where agglomerates were observed. (c) & (d) HE-TEM images of post-catalysis sample of catalyst **I** with crystalline particles encased in an amorphous network within the agglomerates. *Data collected by Dr Edward R. White.*

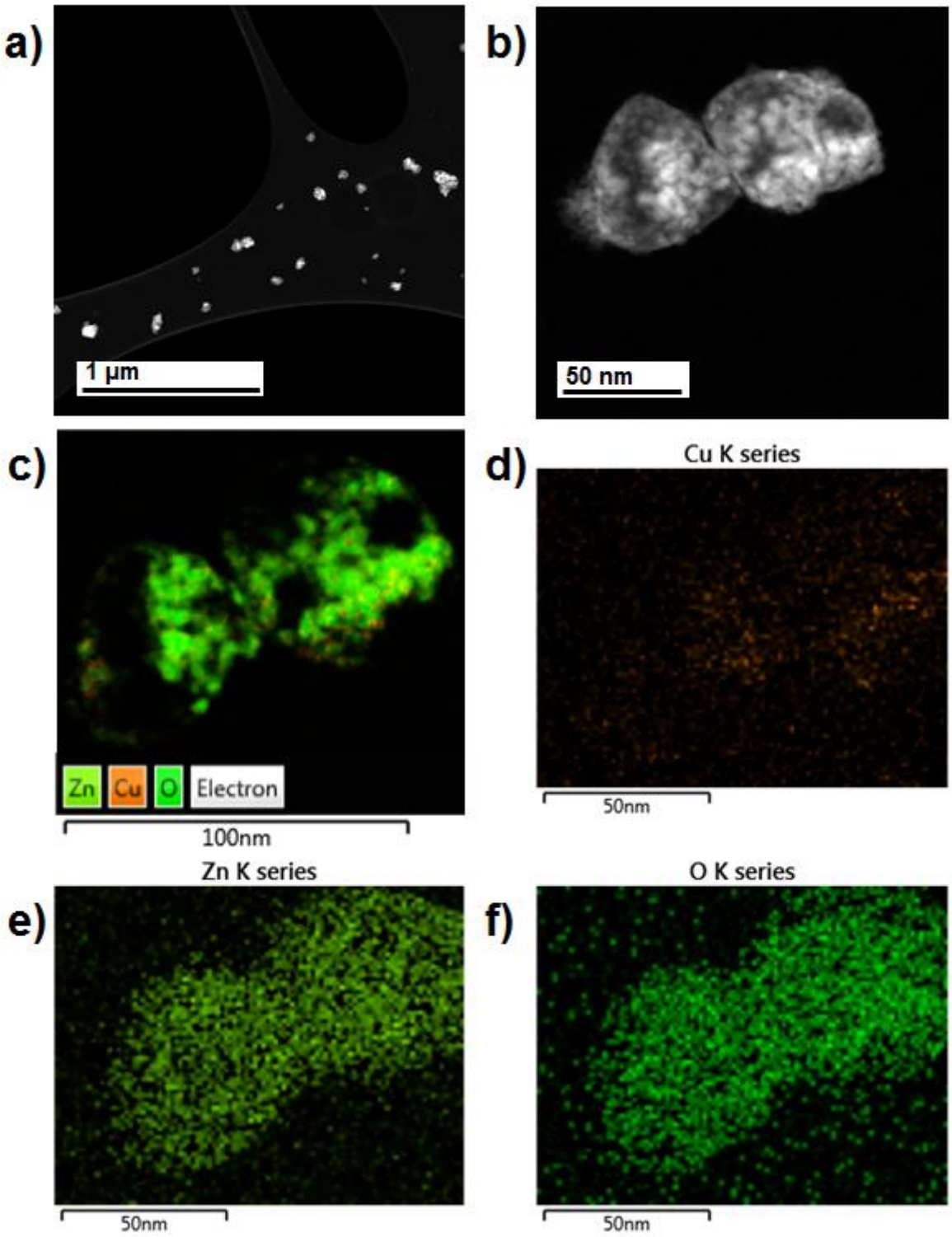

Figure 4.15. (a) STEM-HAADF image of over a large area of TEM grid showing presence of agglomerates, with (b) a magnified image of agglomerate where EDX mapping was performed to confirm the presence of (d) Cu, (e) Zn and (f) O atoms. *Data collected by Dr Edward R. White.*

4.4.3 Discussion

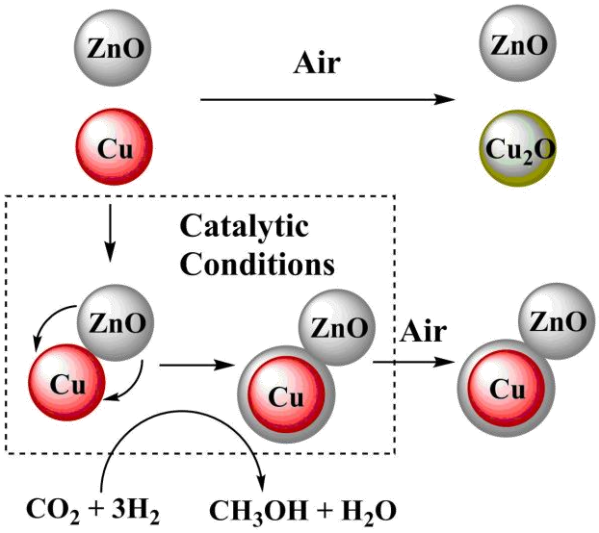

Figure 4.16. Schematic illustration proposing a possible route to rationalise the formation of a ZnO overlayer, under catalytic conditions, which offers protection to Cu(0) nanoparticles against oxidation.

The size of Cu(0) nanoparticles influences the change in intensity of the SPR signal. The Cu(0) nanoparticles sizes in **B** are significantly smaller than for **A** or **C** (using TEM), but all samples exhibited similar oxidative stability which suggests that particle size is not responsible for redox stability. One working hypothesis for the increased oxidative stability in the post-catalysis samples (**A**, **B**, **C** and **I**) is the deposition of a protective layer of ZnO over Cu(0) nanoparticles under catalytic conditions (Figure 4.16). Such a protective layer, named "graphitic ZnO" in some cases, has been proposed for other Cu/ZnO-based catalysts, including the heterogeneous Cu-ZnO-Al_2O_3 methanol synthesis catalyst.[40-43] It is proposed that it is facilitated/caused by the reduction of ZnO to ZnO_x. The intimate contact between Cu and the proposed ZnO overlayer supports the hypothesised active site, Cu/ZnO interface, and mechanism for CO_2 to methanol, *via* formate intermediates. Proposal of hydrogen spillover from Cu(0) to such ZnO overlayer (which can activate CO_2 readily)

	Crystal system	a / Å	b / Å	c / Å	α / °	β / °	γ / °	Total volume/ Å^3
Cu(0)	*Cubic*	3.61	3.61	3.61	90.00	90.00	90.00	47.24
Cu_2O	*Cubic*	4.27	4.27	4.27	90.00	90.00	90.00	77.85
CuO	*Monoclinic*	4.65	3.41	5.11	90.00	99.48	90.00	79.94
ZnO	*Hexagonal*	3.24	3.24	5.18	90.00	90.00	120.00	47.11

Table 4.2. Unit cell parameters of Cu(0) (JCPDS 01-085-1326), Cu_2O (JCPDS 00-002-1067), CuO (JCPDS 00-001-1117) and ZnO (JCPDS 00-001-1136).

promotes methanol production over CO production (*see proposed mechanism of CO_2 to methanol discussion in Chapter 1*).

In some studies, the ZnO layers were investigated using HR-TEM analysis[40] and EXAFS[41] to probe formation, speciation and location of the material. These studies suggest the ZnO_x was located on Cu(0) particle surfaces with partial coverage and hence an increase in redox stability was exhibited by the post-catalysis samples.[41] In some cases, it was proposed that a CuZn alloy species is formed nearby the ZnO_x overlayer.[40] Here, multiple unsuccessful attempts were made to identify the proposed ZnO overlayer using TEM and XPS to probe the nanostructure, crystallinity and location of the elusive overlayer.

The rearrangement of crystalline ZnO to amorphous ZnO occurs regardless of the capping ligand on Cu_2O nanoparticles and it is only observed when Cu_2O nanoparticles were used (not observed in catalysts **A** and **C**). *In situ* TEM and XPS studies of a heterogeneous Cu/ZnO catalyst indicate significant movement of atoms, tentatively proposed to be *via* diffusion, in oxidation/reduction cycles at high temperatures (150–300 °C, up to 900 mbar H_2).[44] There is a change in the unit cell upon reduction of Cu_2O to Cu(0) (Table 4.2) and it was revealed that Cu atoms

migrate to the core of the structure to form an alloy of CuZn nanoparticle (~10 nm). When the Cu/ZnO catalyst was subjected to partial reduction conditions (300 °C, 0.5 h, 1 mbar H_2), an amorphous structure, with poorly resolved lattice fringes, was reported in the catalyst with some migration of Cu and Zn being responsible for this change. Similar structures were also observed in catalysts **B** and **I**, and it could be that a similar migration of Cu and Zn atoms is taking place upon reduction in catalysis and hence causing the rearrangement of ZnO. Catalysts **B** and **I** may be viewed as the most extreme examples of the ZnO overlayer formation,[40] the crucial component appears to be the presence of Cu oxides (Cu_2O and CuO) instead of Cu(0) as a precursor. It could be that the reduction of the oxides promotes and accelerates the movement of ZnO species under reducing conditions.[40, 44] The reduction of oxides generates H_2O and H_2O chemisorption on the ZnO surface further increases the mobility of ZnO species (*see section 4.3.4*).

Larger ZnO nanoparticles, *i.e.* catalyst **II b**, showed lower activity compared to catalysts **I** and **II a** (Figure 4.17). A simple change from DOPA to DODPA, as capping ligand for ZnO nanoparticles, increases the resistance to ripening; small stable particles are desirable as they maintain a high ZnO surface area which is likely to be important for the formation of Cu/ZnO interfaces.[24-27] Comparing catalysts **I** and **II a** shows that the change in alkyl chain lengths of phosphinate ligand does not change the activity. Thus, the clear advantage of using DODPA, as a capping ligand for ZnO nanoparticles, is to prevent particle ripening and avoid the need for special storage conditions for ZnO nanoparticles.

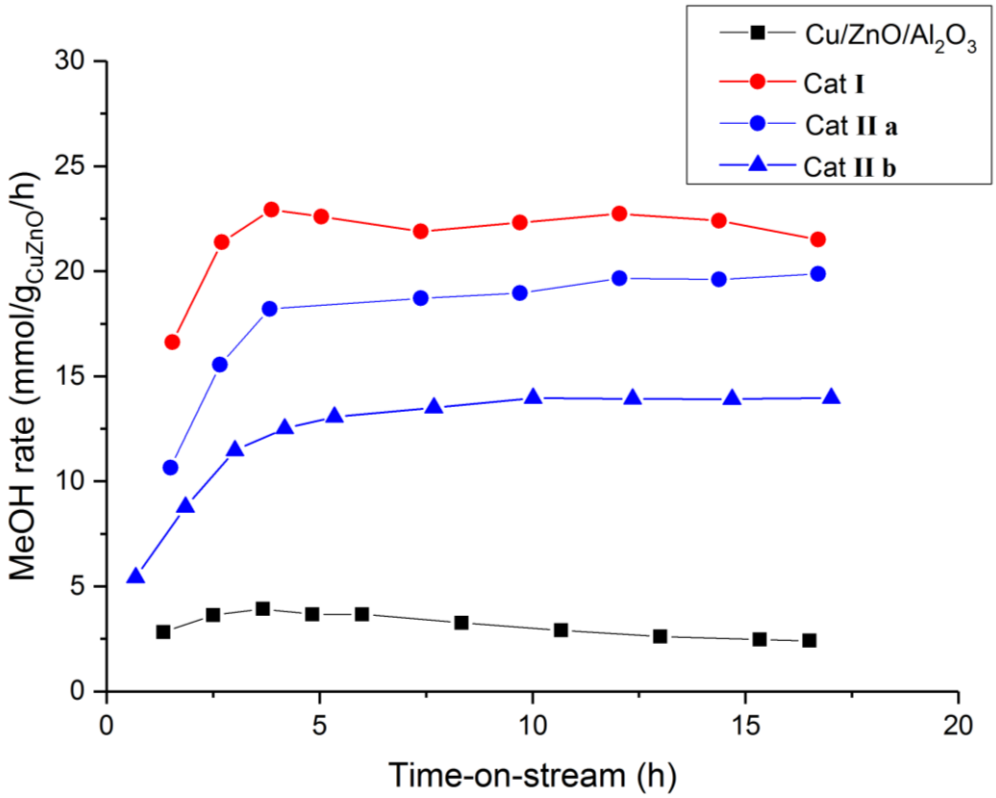

Figure 4.17. Plot of methanol rate of catalysts **I**, **II a**, **II b** and commercial Cu-ZnO-Al_2O_3 over 15 h TOS to demonstrate the stability of the catalysts.

4.5 Summary & Conclusion

The synthesis of di(octadecyl)phosphinic acid was achieved through modification to the synthetic route and purification steps reported for dioctylphosphinic acid.[13] Although the yield is low, the reaction can be performed on a multi-gram scale. Di(octadecyl)phosphinic acid was subsequently used as a capping ligand for the synthesis of ZnO nanoparticles, ZnO@DODPA (2.3 nm), with improved resistance to particle ripening over time when compared to ZnO@DOPA. Transmission electron microscopy and scanning transmission electron microscopy analyses revealed an interesting 1D quasi-chain structure of ZnO@DODPA. The structure could be consistent with nanoparticle growth being halted at the oriented attachment phase, prior to Ostwald ripening; perhaps this is caused by the bulky octadecyl chains preventing chemisorption of water on the surface of ZnO.

The colloidal Cu/ZnO catalysts, with phosphinate capping ligands, showed 2-3 times greater activity than a commercial heterogeneous methanol synthesis catalyst, Cu-ZnO-Al_2O_3, and the same improvement compared to previously tested colloidal Cu/ZnO@St catalyst (210 °C, 3:1 H_2:CO_2, 50 bar, mesitylene).[11, 31] The nature of the Cu nanoparticle precursors (Cu(0) or Cu_2O) does not affect the catalyst activity, whereas, the size of ZnO nanoparticles does. The latter findings highlight the need to slow or even prevent nanoparticle ripening. Smaller ZnO nanoparticles provided higher surface area for the formation Cu/ZnO interface formation, *i.e.* the proposed active site for methanol synthesis. It is also possible to apply ZnO@DODPA and Cu_2O@DOPA as highly active catalyst, which is advantages as both precursors are air stable and thus simplifies catalysts handling and storage.

Post-catalysis analysis of Cu/ZnO colloids showed the clear formation of Cu/ZnO interfaces and a slight ripening of Cu and ZnO nanoparticles. When using Cu_2O as precursor, the rearrangement of nanocrystalline ZnO to amorphous ZnO is promoted. The amorphous ZnO network encasing Cu nanoparticles, observed by electron microscopic techniques, is similar to structures observed upon activation/use of commercial Cu-ZnO-Al_2O_3 catalyst. UV-Vis spectroscopy showed an increased oxidative stability of the post-catalysis Cu(0) nanoparticles compared to pre-catalysis samples. Such stability might be attributed to the formation of the amorphous ZnO overlayer, but microscopic techniques, such as TEM and XPS, did not conclusively identify the putative layer. Further understanding of the rearrangement of ZnO and proposed ZnO protective layer is desirable to gain insight into the true Cu/ZnO catalytic structure (and mechanism). The colloidal catalysts show real promise in terms of catalytic performance and can be an ideal model for in-depth mechanistic studies.

4.6 References

1. K. De Nolf, R. K. Capek, S. Abe, M. Sluydts, Y. Jang, J. C. Martins, S. Cottenier, E. Lifshitz and Z. Hens, *J. Am. Chem. Soc.*, 2015, **137**, 2495-2505.
2. R. Viswanatha, H. Amenitsch and D. D. Sarma, *J. Am. Chem. Soc.*, 2007, **129**, 4470-4475.
3. R. Viswanatha, P. K. Santra, C. Dasgupta and D. D. Sarma, *Phys. Rev. Lett.*, 2007, **98**, 255501.
4. P. Erhart and K. Albe, *Appl. Phys. Lett.*, 2006, **88**, 201918.
5. T. K. Gupta and W. G. Carlson, *J. Mater. Sci.*, 1985, **20**, 3487-3500.
6. D. V. Talapin, A. L. Rogach, M. Haase and H. Weller, *J. Phys. Chem. B*, 2001, **105**, 12278-12285.
7. E. M. Wong, J. E. Bonevich and P. C. Searson, *J. Phys. Chem. B*, 1998, **102**, 7770-7775.
8. M. Kunat, S. G. Girol, U. Burghaus and C. Wöll, *J. Phys. Chem. B*, 2003, **107**, 14350-14356.
9. M. Ali and M. Winterer, *Chem. Mater.*, 2010, **22**, 85-91.
10. N. J. Brown, J. Weiner, K. Hellgardt, M. S. Shaffer and C. K. Williams, *Chem. Commun.*, 2013, **49**, 11074-11076.
11. S. D. Pike, A. García-Trenco, E. R. White, A. H. M. Leung, J. Weiner, M. S. P. Shaffer and C. K. Williams, *Catal. Sci. Technol.*, 2017, **7**, 3842-3850.
12. S. D. Pike, E. R. White, M. S. P. Shaffer and C. K. Williams, *Nat. Commun.*, 2016, **7**, 13008.
13. F. Wang, R. Tang and W. E. Buhro, *Nano Lett.*, 2008, **8**, 3521-3524.
14. E. A. Meulenkamp, *J. Phys. Chem. B*, 1998, **102**, 5566-5572.
15. H. D. Gillman, *Inorg. Chem.*, 1974, **13**, 1921-1924.
16. H. D. Gillman and J. L. Eichelberger, *Inorg. Chem.*, 1976, **15**, 840-843.
17. C. G. Lugmair, T. D. Tilley and A. L. Rheingold, *Chem. Mater.*, 1997, **9**, 339-348.
18. R. Pothiraja, S. Shanmugan, M. G. Walawalkar, M. Nethaji, R. J. Butcher and R. Murugavel, *Eur. J. Inorg. Chem.*, 2008, **2008**, 1834-1845.
19. S. D. Pike and Z. Goodwin, *Unpublished work*.
20. C. Lizandara-Pueyo, M. W. E. van den Berg, A. De Toni, T. Goes and S. Polarz, *J. Am. Chem. Soc.*, 2008, **130**, 16601-16610.
21. D. Hapiuk, B. Masenelli, K. Masenelli-Varlot, D. Tainoff, O. Boisron, C. Albin and P. Mélinon, *J. Phys. Chem. C*, 2013, **117**, 10220-10227.
22. A. Layek, G. Mishra, A. Sharma, M. Spasova, S. Dhar, A. Chowdhury and R. Bandyopadhyaya, *J. Phys. Chem. C*, 2012, **116**, 24757-24769.
23. D. Li, M. H. Nielsen, J. R. I. Lee, C. Frandsen, J. F. Banfield and J. J. De Yoreo, *Science*, 2012, **336**, 1014-1018.
24. A. Le Valant, C. Comminges, C. Tisseraud, C. Canaff, L. Pinard and Y. Pouilloux, *J. Catal.*, 2015, **324**, 41-49.
25. S. Kattel, P. J. Ramírez, J. G. Chen, J. A. Rodriguez and P. Liu, *Science*, 2017, **355**, 1296-1299.
26. E. K. Poels and D. S. Brands, *Appl. Catal., A*, 2000, **191**, 83-96.
27. S. Schimpf, A. Rittermeier, X. Zhang, Z.-A. Li, M. Spasova, M. W. E. van den Berg, M. Farle, Y. Wang, R. A. Fischer and M. Muhler, *ChemCatChem*, 2010, **2**, 214-222.
28. K. L. Orchard, M. S. P. Shaffer and C. K. Williams, *Chem. Mater.*, 2012, **24**, 2443-2448.

29. S. D. Pike, E. R. White, A. Regoutz, N. Sammy, D. J. Payne, C. K. Williams and M. S. Shaffer, *ACS Nano*, 2017, **11**, 2714-2723.
30. E. C. Heydorn, B. W. Diamond and R. D. Lilly, *Commercial Scale Demonstration of the Liquid Phase Methanol (LPMEOH) Process Final Report*, 2003.
31. N. J. Brown, A. García-Trenco, J. Weiner, E. R. White, M. Allinson, Y. Chen, P. P. Wells, E. K. Gibson, K. Hellgardt, M. S. P. Shaffer and C. K. Williams, *ACS Catal.*, 2015, **5**, 2895-2902.
32. K. P. Rice, E. J. Walker, M. P. Stoykovich and A. E. Saunders, *J. Phys. Chem. C*, 2011, **115**, 1793-1799.
33. O. Peña-Rodríguez and U. Pal, *J. Opt. Soc. Am. B*, 2011, **28**, 2735-2739.
34. M. Yin, C.-K. Wu, Y. Lou, C. Burda, J. T. Koberstein, Y. Zhu and S. O'Brien, *J. Am. Chem. Soc.*, 2005, **127**, 9506-9511.
35. P. Kanninen, C. Johans, J. Merta and K. Kontturi, *J. Colloid Interface Sci.*, 2008, **318**, 88-95.
36. A. Sawant, M. K. Ko, V. Parameswaran, S. Lee and C. J. Kulik, *Fuel Sci. Technol. Int.*, 1987, **5**, 77-88.
37. B. S. Zou, V. V. Volkov and Z. L. Wang, *Chem. Mater.*, 1999, **11**, 3037-3043.
38. A. van Dijken, E. A. Meulenkamp, D. Vanmaekelbergh and A. Meijerink, *J. Phys. Chem. B*, 2000, **104**, 1715-1723.
39. H. Zhang, G. Chen, G. Yang, J. Zhang and X. Lu, *J. Mater. Sci.: Mater. Electron.*, 2007, **18**, 381-384.
40. T. Lunkenbein, J. Schumann, M. Behrens, R. Schlogl and M. G. Willinger, *Angew. Chem. Int. Ed.*, 2015, **54**, 4544-4548.
41. M. K. Schroter, L. Khodeir, M. W. van den Berg, T. Hikov, M. Cokoja, S. Miao, W. Grunert, M. Muhler and R. A. Fischer, *Chem. Commun.*, 2006, **23**, 2498-2500.
42. F. Liao, Y. Huang, J. Ge, W. Zheng, K. Tedsree, P. Collier, X. Hong and S. C. Tsang, *Angew. Chem. Int. Ed.*, 2011, **50**, 2162-2165.
43. C. Tisseraud, C. Comminges, T. Belin, H. Ahouari, A. Soualah, Y. Pouilloux and A. Le Valant, *J. Catal.*, 2015, **330**, 533-544.
44. C. Holse, C. F. Elkjær, A. Nierhoff, J. Sehested, I. Chorkendorff, S. Helveg and J. H. Nielsen, *J. Phys. Chem. C*, 2015, **119**, 2804-2812.

Chapter 5

Colloidal M:ZnO Nanoparticles (M = Mg, Al, Cu) in Hydrogenation of CO_2 to Methanol

5.1 Scope

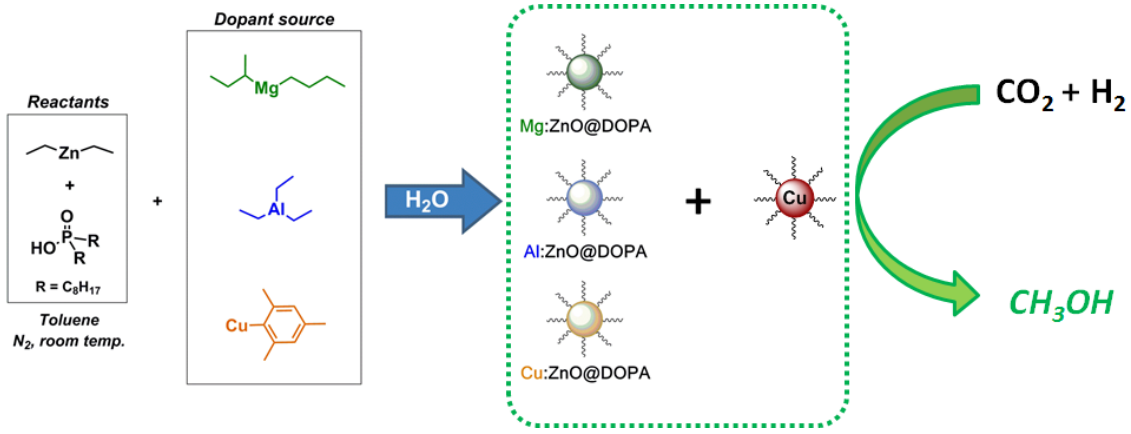

Scheme 5.1. General reaction scheme to synthesising M:ZnO@DOPA (M = Mg, Al, Cu). The synthesised doped ZnO nanoparticles are combined with Cu nanoparticles, capped with DOPA, are used as nanocatalysts for the hydrogenation of CO_2 to methanol.

It has previously been observed that the introduction of small quantities of dopants (3–5 mol%) can have either beneficial or detrimental effects on the hydrogenation of CO_2 to methanol (*section 1.4.2*). Here, the motivation is to explore the effects of doping colloidal Cu/ZnO nanocatalysts upon catalytic performance. In order to achieve substitutional doping of ZnO, the addition of organometallic dopant reagent into the pre-hydrolysis synthetic mixture is targeted.[1-3] This strategy follows an established route to Mg-doped ZnO nanoparticles (10 mol% Mg, 10–15 nm by TEM) by the hydrolysis of diethylzinc and (*n*-butyl)(*sec*-butyl) magnesium, in the presence of oleic acid.[4] The resulting nanoparticles, capped with oleate, were used as antimicrobial agent in polyurethane.

Herein, ZnO nanoparticles with different dopants and featuring DOPA capping ligands are synthesised (M:ZnO@DOPA; M = Mg, Al, Cu) to test the generality of the method described above. A 5 mol% dopant incorporation *via* substitution is targeted and the chosen dopants are the following: Mg(II) for isovalent doping, Al(III) for *n*-type doping and Cu(I) for *p*-type doping of ZnO (Scheme 5.1).

5.2 M:ZnO@DOPA Nanoparticles (M = Mg, Al, Cu)

5.2.1 Synthesis of M:ZnO@DOPA Nanoparticles

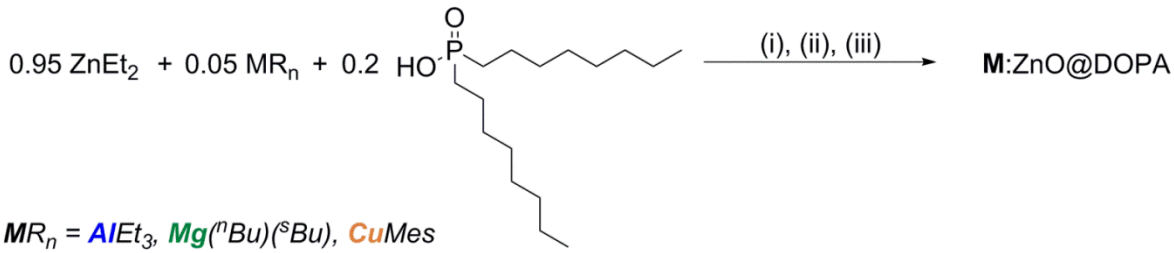

Scheme 5.2. The synthesis of doped-ZnO nanoparticles, capped with dioctylphosphinate (M:ZnO@DOPA), by the controlled hydrolysis of a mixture containing diethylzinc, DOPA–H and the dopant source. (i) toluene, 16 h, room temperature, (ii) 0.4 M H_2O in acetone and (iii) centrifugation x 3.

The synthesis of doped-ZnO nanoparticles (M:ZnO@DOPA) was achieved by modification to the synthetic route to colloidal ZnO@DOPA, *via* the controlled hydrolysis of an organozinc mixture.[2, 4] Alkyl metal reagents of the desired dopants were used: (*n*-butyl)(*sec*-butyl)magnesium (0.7 M hexane solution), triethylaluminium and mesitylcopper (I). All dopant sources generate volatile inert hydrocarbons upon hydrolysis, which are easily removed during the subsequent centrifugation purification/isolation of the nanoparticles.

The reaction mixture containing diethylzinc, dopant reagent and DOPA–H in toluene, with a starting (Zn+dopant):DOPA ratio of 5:1, was left to stir overnight under inert conditions to ensure complete deprotonation of DOPA–H (Scheme 5.2). A solution of water in acetone (0.4 M) was added and the reaction was stirred for 2 h. Several centrifugation steps (3 x 3900 rpm, 20 mins) were performed on the resulting suspension to isolate and purify the nanoparticles. After centrifugation, the nanoparticles were left to dry, under air overnight, to form dry waxy pellets. Upon

crushing the waxy pellets, Mg:ZnO@DOPA and Al:ZnO@DOPA were yielded as free-flowing white powders and Cu:ZnO@DOPA as a free-flowing dark green powder. Yields, based on Zn, were 87–92%. The missing Zn is likely removed as soluble Zn-phosphinate molecular clusters in the centrifugation steps.[5]

5.2.2 Characterisation of M:ZnO@DOPA Nanoparticles

M:ZnO samples	Size (nm)		(101) facet		
	XRD	TEM [a]	2θ°	*d*/Å	Δ*d*/ Å
ZnO@DOPA	2.3	2.8 ± 0.02 (0.6)	34.62	2.59	-
Mg:ZnO@DOPA	2.0	2.7 ± 0.04 (0.5)	34.31	2.61	**+0.02**
Al:ZnO@DOPA	2.3	2.7 ± 0.06 (0.9)	35.75	2.51	**-0.08**
Cu:ZnO@DOPA	2.2	2.6 ± 0.03 (0.4)	34.82	2.58	**-0.01**

[a] Average particle size ± standard error (standard deviation).

Table 5.1. Table showing the sizes of M:ZnO@DOPA and ZnO@DOPA (determined by XRD and TEM). The positions of (101) facet were determined using Gaussian fits to the peaks in the range of 30–35° 2θ. *See Appendix for particle size distribution graphs.*

The powder XRD patterns of the M:ZnO@DOPA confirmed the formation of nanocrystalline ZnO without any crystalline byproducts, such as dopant oxides or hydroxides (Figure 5.1). Crystallite sizes of 2.0–2.5 nm were obtained by Scherrer analysis (Table 5.1). Examination of the (101) zinc-rich facet of M:ZnO@DOPA revealed changes to the Wurzite lattice depending on the dopant atom (Table 5.1). In each case, the position of the (101) facet was determined using a Gaussian fit (Figure 5.2). Al:ZnO@DOPA showed a contraction of the (101) facet, which is consistent with incorporation of dopant ion, Al(III), into the Wurzite lattice (*i.e.* a change in ionic radii from Zn^{2+} r_{ion} = 0.74 Å to Al^{3+} r_{ion} = 0.53 Å).[6, 7] No clear changes were observable for Cu(I) and Mg(II) in (101) facet when compared to ZnO@DOPA. One explanation for

this might be the rather high peak broadness, resulting from the nanoscale sizes.[8] Additionally, any lattice parameter changes would likely be indistinguishable due to the similar ionic radii of Mg(II) (Mg^{2+} r_{ion} = 0.71 Å) and Cu(I) (Cu^{+} r_{ion} = 0.74 Å; Cu^{2+} r_{ion} = 0.71 Å) to Zn(II).[6] This observation is consistent with Mg-doped ZnO nanoparticles synthesised by co-precipitation (12 nm, 3 mol% Mg) and base-assisted hydrolysis (4.7 nm, 5–20 mol% Mg).[8, 9]

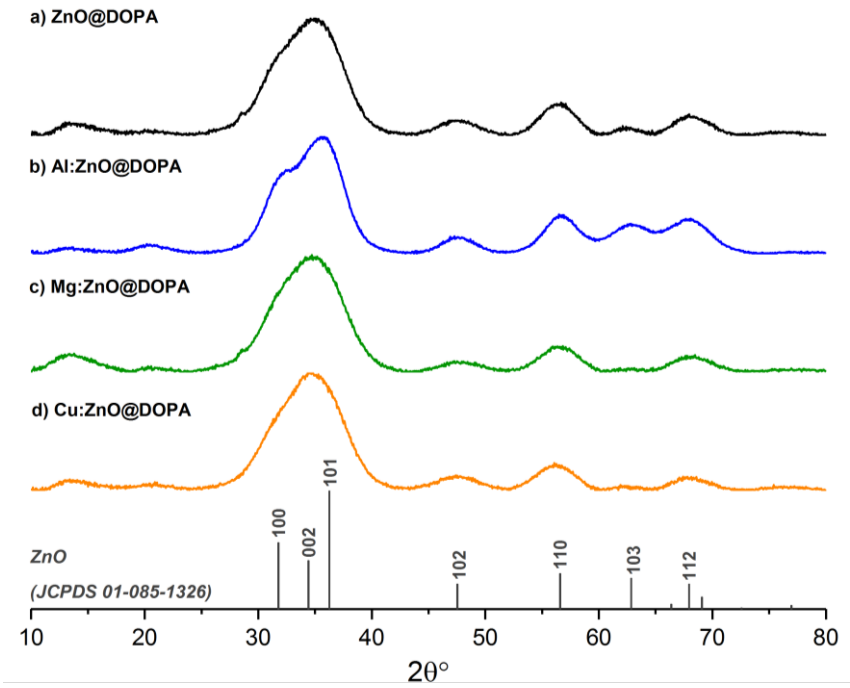

Figure 5.1. XRD patterns of (a) ZnO@DOPA, (b) Al:ZnO@DOPA, (c) Mg:ZnO@DOPA and (d) Cu:ZnO@DOPA, with reference lines for ZnO as grey vertical bars (JCPDS 01-085-1326).

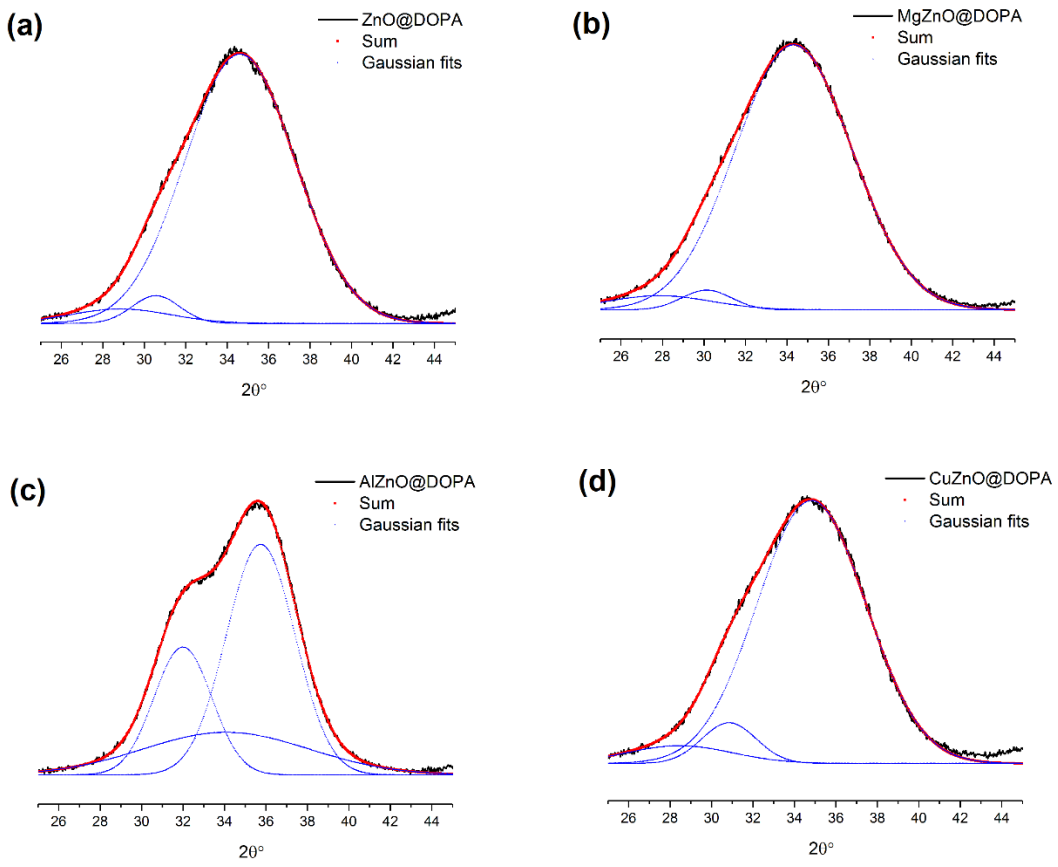

Figure 5.2. Gaussian fits applied to the XRD peaks in the range of 30–35° 2θ to determine the position of (101) facets for (a) ZnO@DOPA, (b) Mg:Zno@DOPA, (c) Al:ZnO@DOPA and (d) Cu:ZnO@DOPA.

HAADF-STEM analysis of all samples shows uniaxial, non-agglomerated particles with narrow size dispersity (in dark field mode; Figure 5.3b). The sizes of M:ZnO@DOPA were Mg:ZnO@DOPA = 2.73 ± 0.04 nm (σ = 0.50, *N* = 175), Al:ZnO@DOPA = 2.69 ± 0.06 nm (σ = 0.88, *N* = 202) and Cu:ZnO@DOPA = 2.63 ± 0.03 nm (σ = 0.38, *N* = 275). The presence of dopant atoms is confirmed by bright spots located on the doped ZnO nanoparticles in the HAADF-STEM images.

ICP-OES revealed 5.0 mol% doping of Al and Cu, but 3.8 mol% for Mg, which is lower than the target value. The amount of dopant was also probed using XPS through comparison of relevant core lines (Table 5.2, Figure 5.3). Reasonable agreement between ICP-OES and XPS dopant quantity was observed for

Al:ZnO@DOPA, whereas XPS detected a higher content of Mg. XPS is a surface-sensitive technique and thus the higher Mg content suggests a greater quantity of Mg resides on nanoparticles' surfaces. Such a hypothesis would be consistent with previous observations, made by Gamelin and co-workers, where localisation of Mg^{2+} on the surface of ZnO nanoparticles (5 mol%) led to altered electronic properties.[8] Furthermore, the dopant core levels revealed that for both Mg 1s and Al 2p, there are species corresponding to Mg–O and Al–O species. The presence of dopant–oxygen species suggests the replacement of some tetrahedral Zn^{2+} by the dopant in the Wurzite lattice. An asymmetric core line, at 932.3 eV, coupled with a shoulder (933.7 eV) at higher binding energy, is indicative of Cu(0)/Cu(I) and Cu(II) species present within Cu:ZnO@DOPA. The distinction between Cu(0) and Cu(I) from the Cu LMM Auger line is not possible due to overlap with stronger Zn LMM lines.

M:ZnO@DOPA	**Dopant quantity (mol %)**		**Optical bandgap (eV)**
	ICP-OES	**XPS** [a]	**UV-Vis** [c]
ZnO@DOPA	-	-	3.71
Mg:ZnO@DOPA	3.77 ± 0.05	4.5	3.84
Al:ZnO@DOPA	4.96 ± 0.07	5.0 [b]	3.65
Cu:ZnO@DOPA	5.05 ± 0.07	3.3	3.67

[a] Measurements taken from comparison of Zn $2p_{3/2}$ against Cu 2*p* and Mg 1*s*. Error of ± 0.5%, derived from peak fitting. [b] Measurements taken from comparison of Zn 3s core line against Al 2*p* core line due to better matching of binding energies. Error of ± 0.5%, derived from peak fitting. [c] Error of ±0.04 eV, derived from uncertainty of linear fits.

Table 5.2. Table showing the dopant quantities, obtained by ICP-OES and XPS, and optical bandgaps of ZnO@DOPA, Mg:ZnO@DOPA, Al:ZnO@DOPA and Cu:ZnO@DOPA.

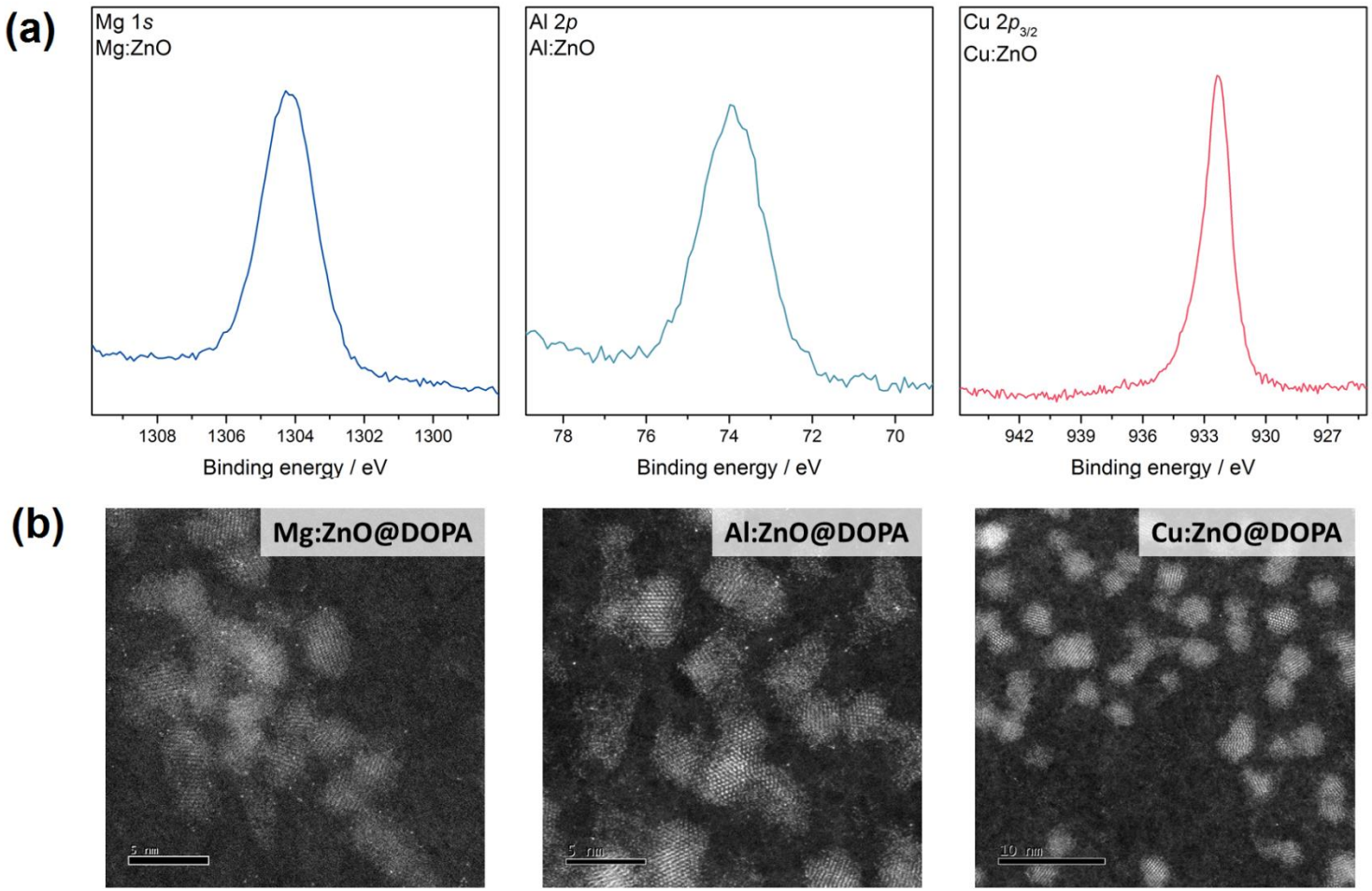

Figure 5.3. (a) XPS showing the Mg 1s core line of Mg:ZnO@DOPA, Al 2p core line of Al:ZnO@DOPA and Cu2p$_{3/2}$ core line of Cu:ZnO@DOPA. (b) HADDF-STEM images of Mg:ZnO@DOPA, Al:ZnO@DOPA and Cu:ZnO@DOPA. Scale bar for Mg:ZnO@DOPA and Al:ZnO@DOPA is 5 nm and Cu:ZnO@DOPA is 10 nm.

The optical bandgaps of M:ZnO@DOPA were estimated from Tauc plots, generated from UV-Vis spectra (in toluene; Figure 5.4b & c), and compared to ZnO@DOPA (Table 5.2). The successful incorporation of Mg^{2+} induces an increase in bandgap (3.84 eV). This finding is consistent with previously reported Mg-doped ZnO nanoparticles (5–20 mol%), where an increase of bandgap up to 0.2 eV was observed.[8-11] Al^{3+} incorporation into ZnO (Al doping level of up to 10 mol%) has been reported to induce the formation of a shallow donor state due to an increase in free charge carriers. Such a feature manifests itself in smaller bandgap for Al-doped ZnO and Al:ZnO@DOPA.[9, 12] A small decrease in the optical bandgap for Cu:ZnO@DOPA suggests successful substitution and may be attributed to the addition of shallow acceptor levels in the band structure, where Cu^{+}/Cu^{2+} dopants increases the density of holes.[13, 14] From XPS, the presence of Cu(0), or Cu(I), implies not all Cu atoms were incorporated into the Wurzite lattice and no formation of CuZn alloy is indicated. The free Cu atoms might exist as Cu(0) species which are not detectable by XRD and TEM due to the low dopant quantity. Nevertheless, evidence for the successful doping of ZnO with Mg and Al is proven by XRD, ICP-OES, XPS and UV-Vis spectroscopy.

The location of Al(III) was further probed by using ^{27}Al-MAS-NMR (Figure 5.4a). Al(III) ions were detected in all three possible coordination environments; tetrahedral Al(III) is confirmed by a sharp signal at δ 55 ppm, and hence substitutional doping is implied. Nonetheless, pentahedral (δ 47 ppm) and octahedral Al(III) (δ -16 and 16 ppm) are also observed which could be due to surface Al species.[9, 15, 16]

TGA indicates a mass loss of around 25–30%, for all the M:ZnO@DOPA, which is attributed to the loss of DOPA hydrocarbon chains (Figure 5.4d; Table 5.3). The residual mass is composed of ZnO and phosphorus-containing species, most likely P_4O_{10}, $Zn(PO_3)_2$, $Zn_4P_6O_{19}$ and $Zn_2P_2O_7$ clusters, which are not sufficiently volatile.[17, 18] The particle:ligand ratios were calculated as close to 6:1 MZnO:DOPA for all samples as expected due to small losses of Zn. The Zn atoms are likely to be incorporated into zinc-phosphinate clusters, a known byproducts of the nanoparticle synthesis, that are likely removed during centrifugation (Table 5.3).[3]

The IR spectra of nanoparticles show both C–H stretches (2800–3000 cm^{-1}) and phosphinate stretches (~1047 cm^{-1}, asymm; ~1126 cm^{-1}, symm). The separation between the two phosphinate stretches is 79–81 cm^{-1}, which may suggest a bridging coordination mode, similar to that observed for ZnO@DOPA and ZnO@DODPA (Figure 5.4e; *Chapter 3*).[18] The presence of an O–H stretch, at 3380 cm^{-1}, is indicative of surface hydroxyl species and is consistent with surface hydroxyl species on ZnO@Stearate.[19]

M:ZnO@DOPA	**EA (wt%)**			**TGA (wt%)**	**Estimated M:ZnO/DOPA**
	C	**H**	**$POOR_2$**	**Residual**	
Mg:ZnO@DOPA	25.96	5.09	39.08	69.1	5.6
Al:ZnO@DOPA	24.46	5.11	36.84	74.5	5.8
Cu:ZnO@DOPA	24.57	4.57	37.00	70.9	5.9

Table 5.3. Table showing the weight percentage of carbon and hydrogen obtained from EA, the residual mass from TGA and the estimated ratio between M:ZnO to the ligand for Mg:ZnO@DOPA, Al:ZnO@DOPA and Cu:ZnO@DOPA.

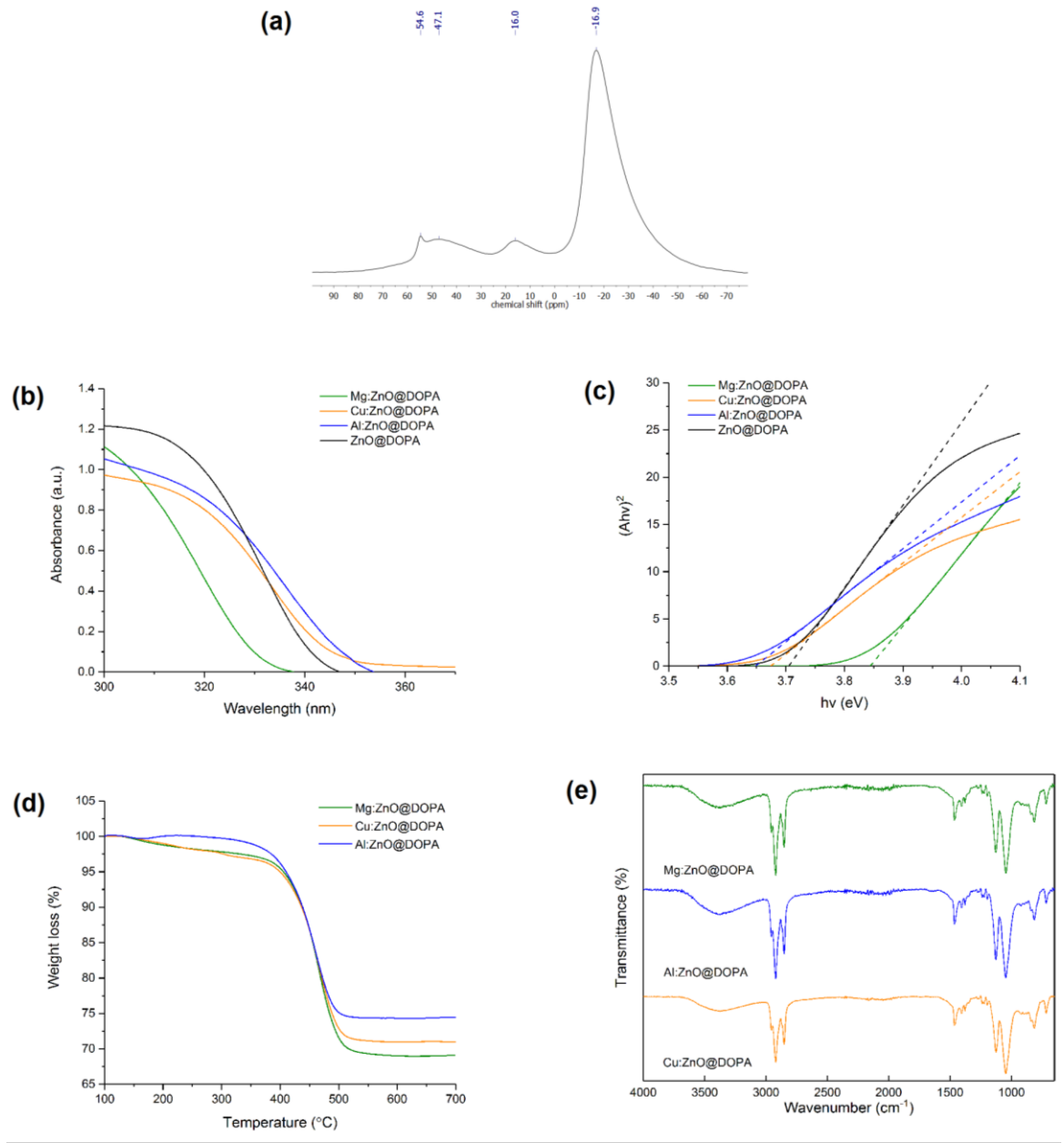

Figure 5.4. (a) ^{27}Al-MAS-NMR spectrum of Al:ZnO@DOPA. (b) UV-Vis spectra of ZnO@DOPA. Mg:ZnO@DOPA, Al:ZnO@DOPA and Cu:ZnO@DOPA, (c) Tauc plots, that were derived from (b), used for the determination of optical bandgap of ZnO@DOPA. Mg:ZnO@DOPA, Al:ZnO@DOPA and Cu:ZnO@DOPA, (d) TGA profiles of Mg:ZnO@DOPA, Al:ZnO@DOPA and Cu:ZnO@DOPA and (e) IR spectra of Mg:ZnO@DOPA, Al:ZnO@DOPA and Cu:ZnO@DOPA.

5.3 Doped-ZnO Nanoparticles for CO_2 to Methanol

5.3.1 Catalyst Preparation Methods

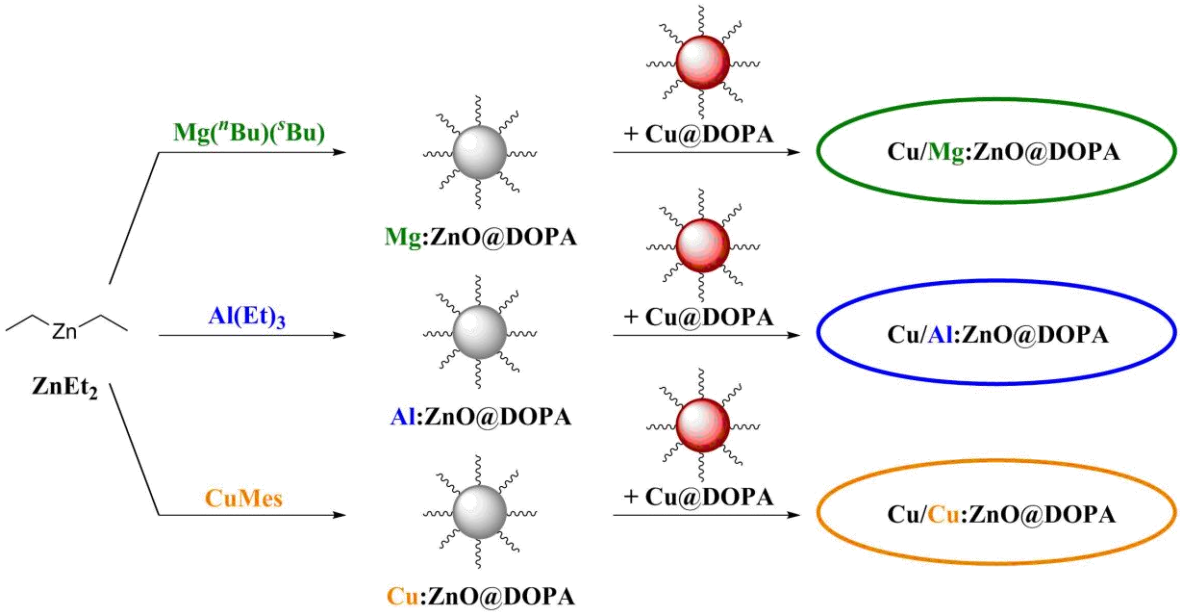

Scheme 5.3. Scheme showing the preparation of three different colloidal Cu/M:ZnO catalysts for the hydrogenation of CO_2 to methanol.

The M:ZnO@DOPA (M = Mg, Al, Cu) nanoparticles were combined with Cu@DOPA, in a 1:1 Cu:Zn molar ratio, and tested as catalysts for the liquid-phase hydrogenation of CO_2 to methanol (Scheme 5.3). The benchmark catalysts were undoped ZnO@DOPA and a slurry of the pre-activated heterogeneous Cu-ZnO-Al_2O_3 catalyst. Standard activation of the heterogeneous Cu-ZnO-Al_2O_3 catalyst was performed, in mesitylene, using a 4.5 bar 5% H_2/N_2 stream, at 240 °C for 3 h.[20] The use of Cu(0), instead of Cu_2O nanoparticles, is to try to limit any rearrangement from crystalline to amorphous ZnO (Chapter 3, *vide supra*).[21] The Cu@DOPA nanoparticle solution was prepared using a literature procedure[21, 22] and its transfer into the reactor was achieved by injection, under a dynamic flow of nitrogen. Next, the reactor was charged with CO_2:H_2 (1:3) at 50 bar and heated to 210 °C. All catalytic runs were performed for 20 h TOS and the product was analysed with an online-GC (for details,

refer to *section 6.2.5*). Each catalyst was tested twice for methanol production from CO_2, with an initiation period of 2–3 h to reach peak activity (Figure 5.5). The peak methanol rates and selectivity, shown in Figure 5.6, were calculated by averaging the peak methanol rate and selectivity of repeated runs for each catalyst. For the error analysis, the standard deviation and standard error for each catalyst were obtained from all repeat runs and hence providing the error bars observed in Figure 5.6. The standard error is defined as standard deviation. An induction period is generally observed in the first 5 hrs due to the uptake of feed gas by reaction solvent.

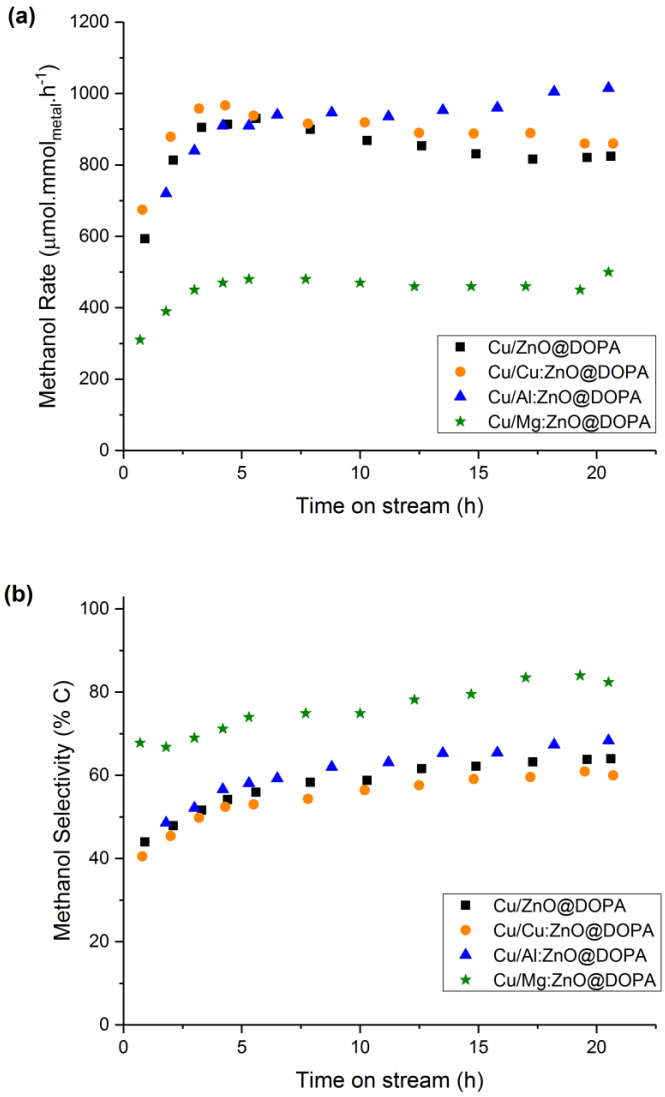

Figure 5.5. (a) Methanol rates and (b) selectivity of the tested colloidal Cu/ZnO nanocatalysts in the hydrogenation of CO_2 over 20 h time-on-stream (210 °C, 50 bar CO_2:H_2 1:3, 150 mL min^{-1}).

5.3.2 Catalytic Results & post-catalysis analysis

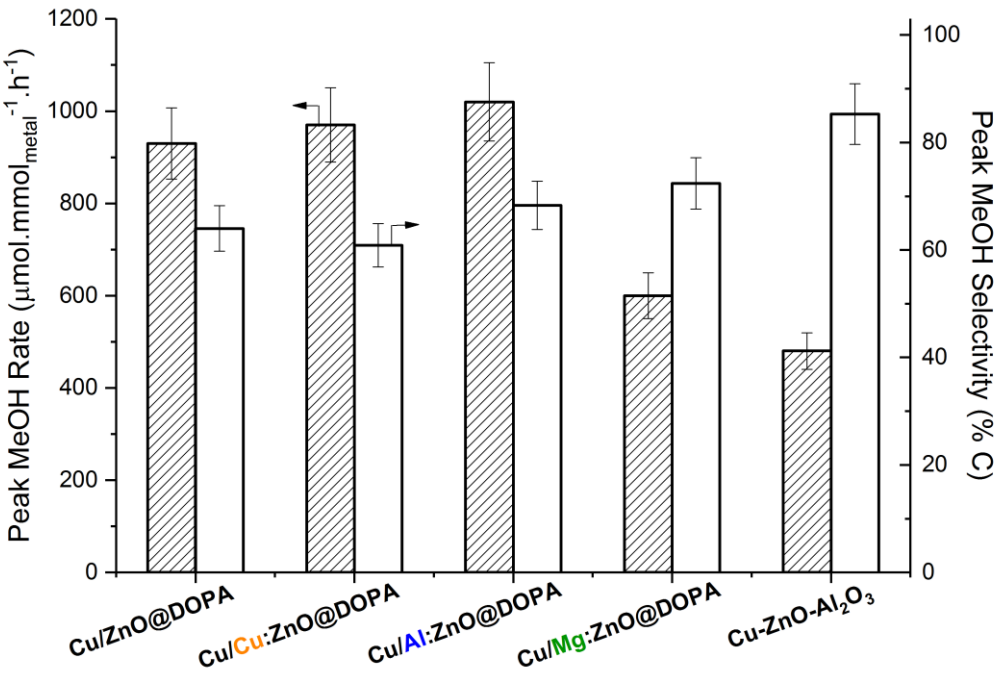

Figure 5.6. Peak methanol rate and selectivity for colloidal Cu/M:ZnO catalysts, Cu/ZnO@DOPA and the reference catalyst Cu-ZnO-Al_2O_3. Reaction conditions: 210 °C, 50 bar, H_2 : CO_2 molar ratio 3 : 1, 150 mL min^{-1}, in mesitylene.

All the colloidal nanocatalysts showed higher activity compared to the heterogeneous catalyst, Cu-ZnO-Al_2O_3 (Figure 5.6). Whilst Cu/ZnO@DOPA, Cu/Cu:ZnO@DOPA and Cu/Al:ZnO@DOPA were twice as active, which is in line with previous reports of colloidal Cu/ZnO nanocatalysts,[2, 21] the Cu/Mg:ZnO@DOPA catalyst was only slightly more active. The methanol selectivity is high (~ 70%) and comparable to Cu-ZnO-Al_2O_3 (~ 80 %), with only CO as the byproduct. The CO was likely to be generated by the rWGS reacti Each dopant had a different effect on catalysis. Whilst Al-doping led to a slight improvement in methanol production, Mg-doping was detrimental for it. No conclusive difference can be drawn for Cu-doping, with the activity being within the error that of the undoped catalyst.

For the Cu-doped catalyst, some ripening of the ZnO nanoparticles was indicated by post-catalysis XRD (3.3 nm), whilst the Cu(0) nanoparticles (~ 2 nm) show almost no ripening. Both Cu/Al:ZnO@DOPA and Cu/Mg:ZnO@DOPA also show ripening of both ZnO and Cu(0) nanoparticle crystallites (Figure 5.7; Table 5.4). A significant ripening of Cu(0) nanoparticles (2.1 nm to 4.4 nm) was especially notable for Mg-doped catalyst.

Particle sizing from TEM also demonstrated the ripening of ZnO and Cu(0) nanoparticles post-catalysis (Table 5.4). In addition, the nanostructures of the two catalysts (Al-doped & Mg-doped), as characterised by HR-TEM, are very different. Cu/Mg:ZnO@DOPA shows more isolated, well-defined, nanoparticles and fewer Cu/ZnO interfaces (Figure 5.8 & Figure 5.9). Whereas Cu/Al:ZnO@DOPA shows interfaces between Cu(0) and ZnO nanoparticles. Also, the nanocrystalline particles appear to be surrounded by an amorphous network, which EDX indicated is rich in Al (Figure 5.8 & Figure 5.10).

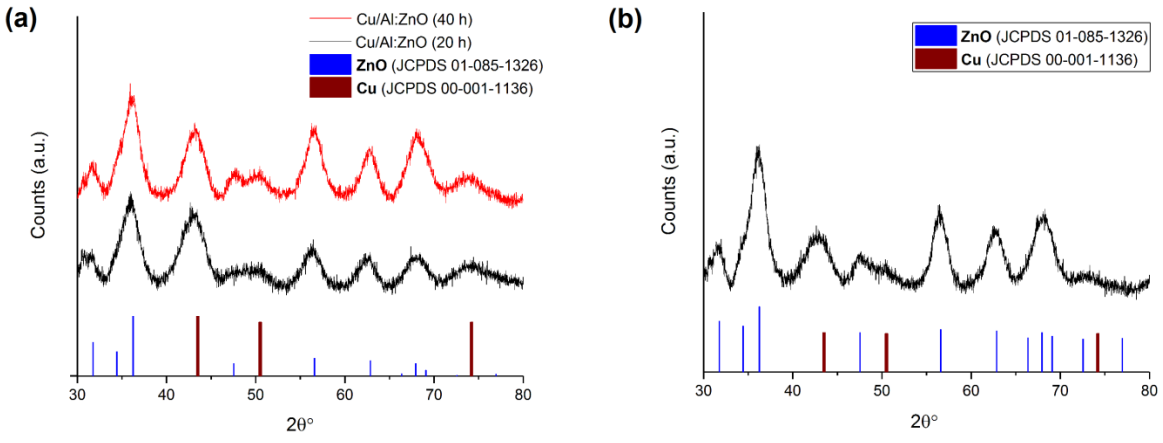

Figure 5.7. XRD patterns of post-catalysis samples of (a) Cu/Al:ZnO@DOPA and (b) Cu/Mg:ZnO@DOPA. Reference patterns of ZnO (blue vertical bars; JCPDS 01-085-1326) and Cu(0) (red vertical bars; JCPDS 00-001-1136) shown in the bottom of patterns.

XPS analysis of Cu/Al:ZnO@DOPA (Figure 5.11) reveals the formation of an alumina surface coating after catalysis (95.0 : 5.0 *vs* 43.1 : 56.9 for Zn : Al, before and after catalysis). In combination with the observed morphological change in TEM, the amorphous network is proposed to be composed of alumina which surrounds the ZnO and Cu nanoparticles.

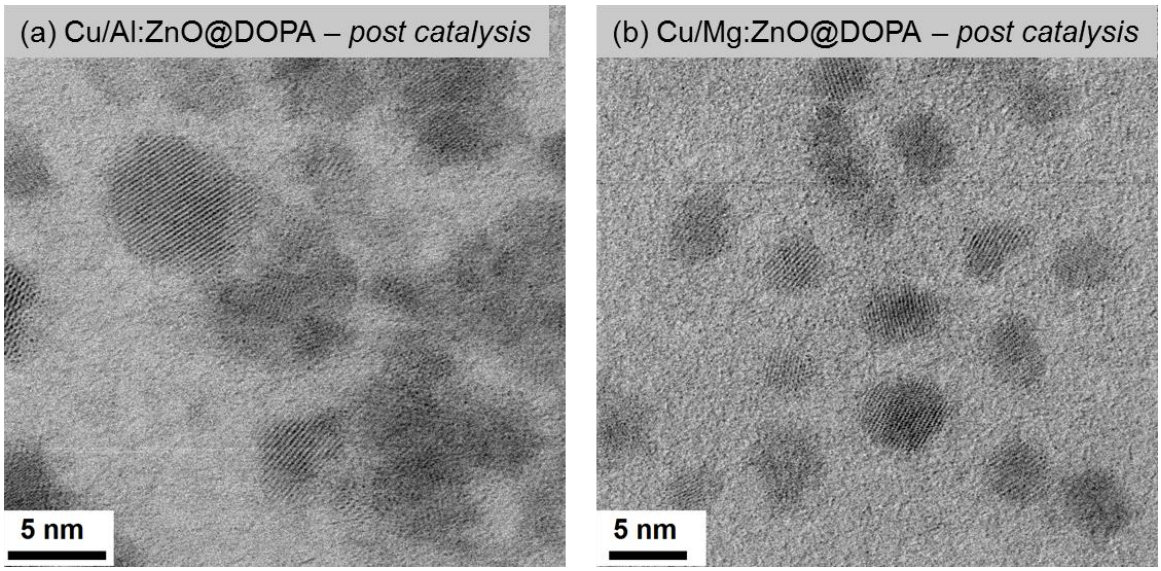

Figure 5.8. HR-TEM images of the post-catalysis sample of (a) Cu/Al:ZnO@DOPA and (b) Cu/Mg:ZnO@DOPA.

	ZnO (nm)				Cu (nm)			
	Pre-catalysis		Post-catalysis		Pre-catalysis		Post-catalysis	
Catalyst	**XRD**	**TEM[a]**	**XRD**	**TEM[a]**	**XRD**	**TEM[a]**	**XRD**	**TEM[a]**
Cu/ZnO@DOPA[b]	2.3	2.8 ± 0.02 (0.6)	3.2	4.9 ± 0.1 (1.1)	-	2.1 ± 0.02 (0.9)	6.4	7.2 ± 0.2 (1.9)
Cu/**Al**:ZnO@DOPA[c]	2.3	2.7 ± 0.06 (0.9)	3.6 (*3.1*)[d]	4.5 ± 0.07 (1.3)	-	2.1 ± 0.02 (0.9)	3.0 (*2.4*)[d]	4.6 ± 0.02 (1.1)
Cu/**Mg**:ZnO@DOPA	2.0	2.7 ± 0.04 (0.5)	2.3	3.5 ± 0.04 (0.4)	-	2.1 ± 0.02 (0.9)	4.4	4.3 ± 0.06 (0.6)
Cu/**Cu**:ZnO@DOPA	2.2	2.6 ± 0.03 (0.4)	3.3	-	-	2.1 ± 0.02 (0.9)	2.0	-

[a] Average particle size ± standard error (standard deviation). The standard error of the mean is defined as standard deviation/(no. of measurements). [b] The sizing measurement is taken from previously published system.[21] [c] Measurement taken from 40 TOS study. [d] Crystallite size of catalyst after 20 h TOS.

Table 5.4. Cu(0) and ZnO nanoparticles size data from XRD and TEM for pre-catalysis and post-catalysis colloids.

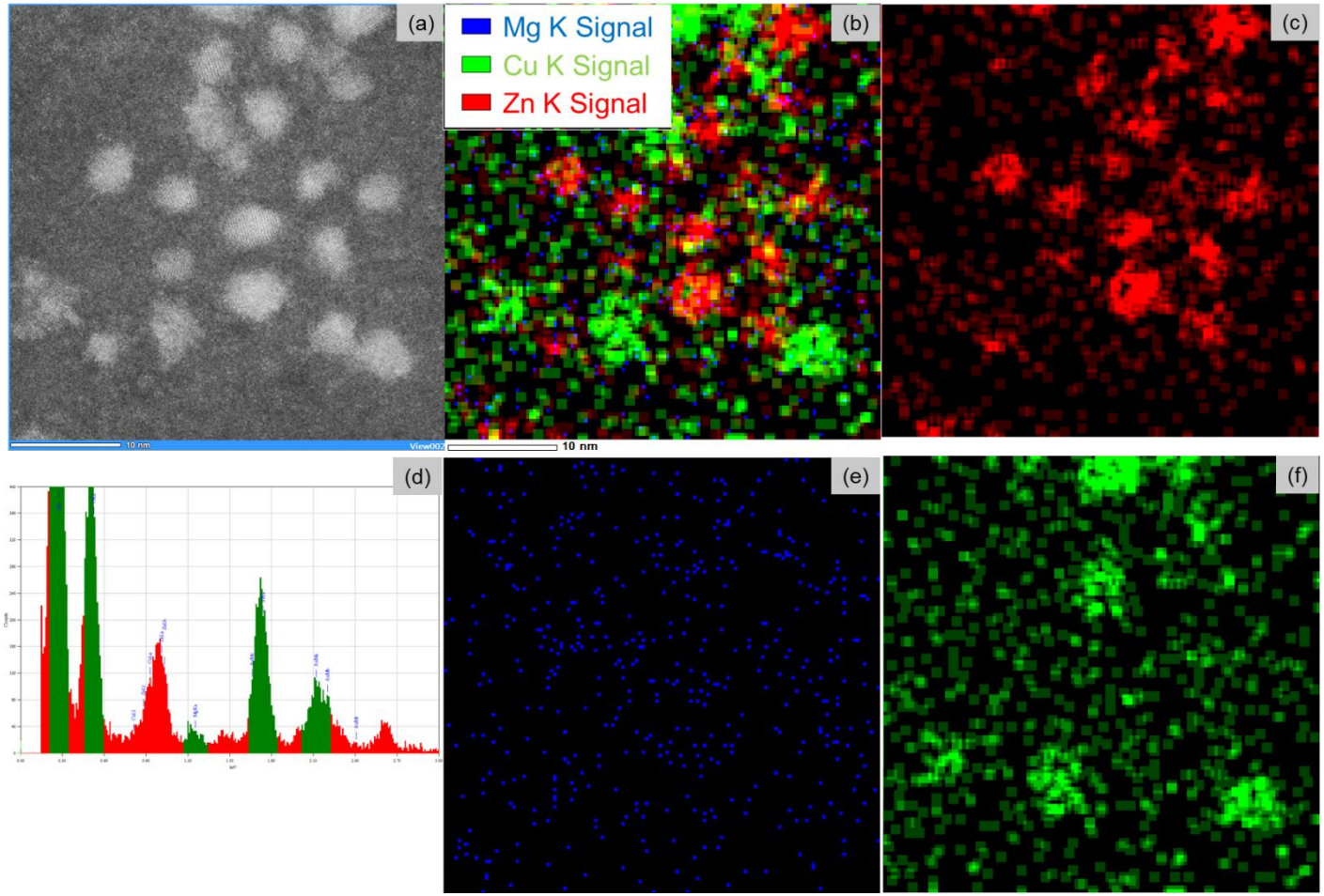

Figure 5.9. BF-STEM image (a) of post-catalysis sample of Cu/Mg:ZnO@DOPA, along with EDX maps showing the location of zinc (c), magnesium (e) and copper (f). (b) shows an RGB overlay of the Zn(red), Cu(green) and Mg(blue) EDX maps; EDX spectra in (d) indicates the Mg K peak used for fitting.

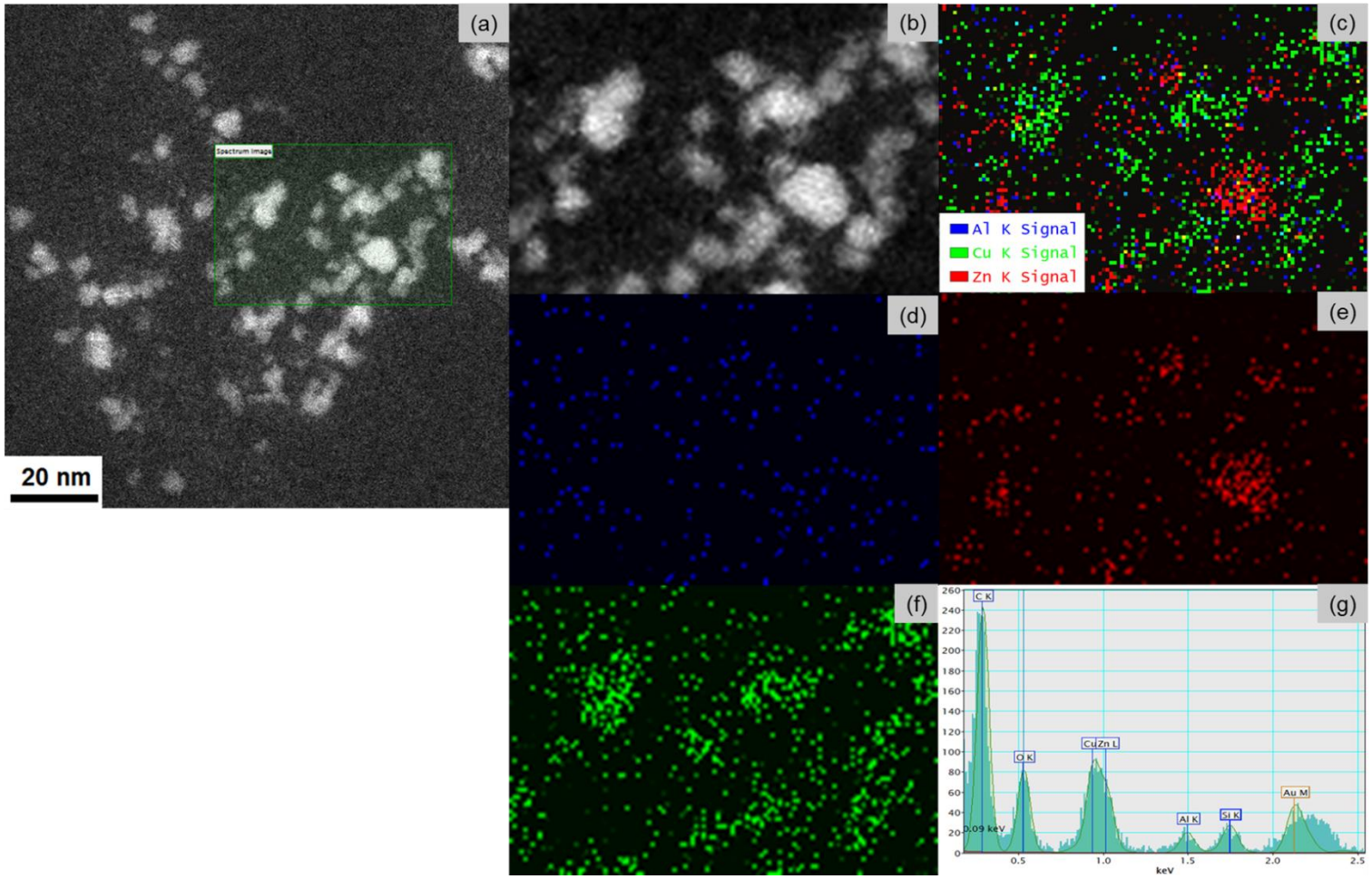

Figure 5.10. BF-STEM image (*a*,*b*) of post-catalysis sample of Cu/Al:ZnO@DOPA, along with EDX maps showing the location of aluminium (d), zinc (e) and copper (f). (c) shows an RGB overlay of the Zn(red), Cu(green) and Al(blue) EDX maps; EDX spectra in (g) indicates the Al K peak used for fitting.

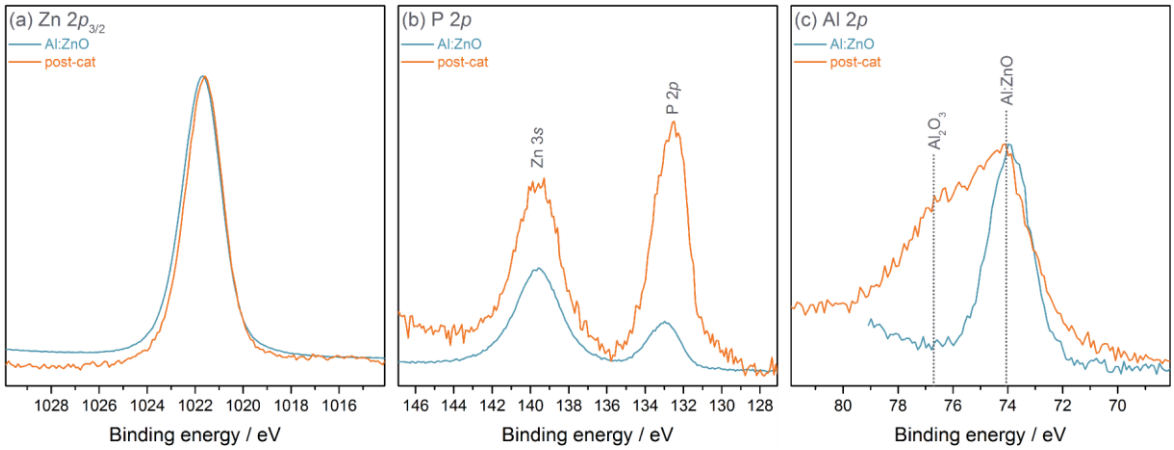

Figure 5.11. XPS of post-catalysis sample of Cu/Al:ZnO@DOPA (orange) and pre-catalysis sample of Al:ZnO@DOPA (blue), with core lines of (a) Zn $2p_{3/2}$, (b) P 2*p* and (c) Al 2*p*. An extra species is observed in Al 2p core line of the post-catalysis sample at a higher binding energy compared to the pre-catalysis sample.

5.3.3 Catalytic Stability of Colloidal Cu/Al:ZnO Nanocatalyst

In the case of some colloidal Cu/ZnO systems, agglomeration and sintering of particles have been tentatively proposed to be the main deactivation routes.[2, 23, 24] Previous investigations using Cu/ZnO@stearate or PdIn nanoparticles, have demonstrated 20–30% decrease in methanol rate after 25 h and subsequently maintained the same methanol rate over 80 h TOS.[24, 25] It is tentatively proposed that the use of ligands may hinder ripening.

The lifetime of the colloidal Cu/ZnO@phosphinates, developed by our group, has not been explored and here, both colloidal Al-doped and the heterogeneous Cu/Al:ZnO@DOPA catalysts were tested over 40 h time-on-stream. Al-doped catalyst displayed good stability, showing <10% decrease in methanol rate from time points of 5 to 40 h time-on-stream (Figure 5.12a), whilst the Cu-ZnO-Al_2O_3 catalyst experienced ~30% loss in methanol rate (Figure 5.12c). Both catalysts show similar selectivity from 20 h to 40 h time-on-stream (Figure 5.12b).

The Cu/Al:ZnO@DOPA catalyst was examined after reaction using XRD and a slight coarsening of the ZnO (3.1 nm to 3.6 nm) and Cu(0) nanoparticles (2.4 nm to 3.0 nm) was observed. Two runs were performed for the colloidal Al-doped catalyst, where the end time points were 20 h and 40 h time-on-stream. The majority of the catalyst coarsening took place in the first 20 h, suggesting catalyst stability was achieved after 20 h time-on-stream. The catalyst stability might be attributed to the presence of ligands and possibly the structural support provided by the surface alumina network as they both may prevent the sintering and agglomeration of the nanoparticles.

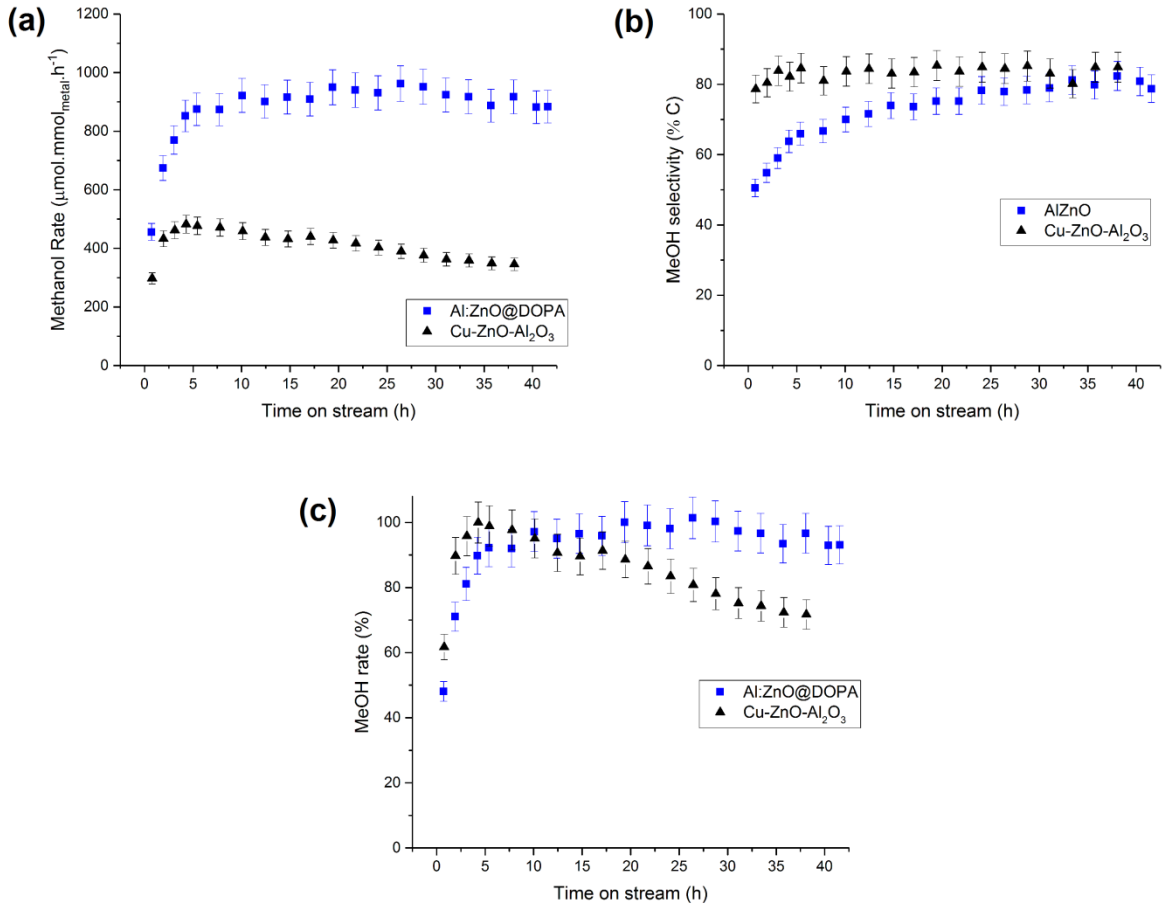

Figure 5.12. (a) Methanol rate, (b) methanol selectivity and (c) percentage of catalyst deactivation of Cu/Al:ZnO@DOPA and commercial heterogeneous Cu-ZnO-Al_2O_3, over 40 h TOS.

5.4 Discussion

The synthetic strategy for targeting M:ZnO@DOPA was successful, with yields of ~90% for all three doped ZnO samples obtained. By having the dopant in the pre-hydrolysis mixture of the nanoparticles, it maximises the chance of dopant incorporation during the nanoparticle nucleation and growth processes. Despite the success of both Al- and Mg-doping of ZnO nanoparticles, the efficacy of Cu-doping is questionable.

Cu-doping of ZnO is inherently difficult, partly due to the low solubility of Cu ions in ZnO (determined by X-ray diffraction and absorption spectroscopy) and the intrinsic donor defects of ZnO (V_O and Zn_i) cancelling the characteristics of *p*-type doping.[26] By conducting the growth of the nanoparticles under an oxygen-rich environment, the formation of defect sites in ZnO is supressed, leading to a lower energy barrier for Zn substitution with Cu.[27] In the case of Cu:ZnO@DOPA, some oxygen might have arguably been provided by the hydrolysis process as water and acetone were used without de-gassing, but an incomplete incorporation of Cu ions was suggested by ICP-OES and XPS. This might be attributed to the ease of reduction of Cu(I) species to Cu(0) as metallic Cu cannot be substituted into the Wurzite lattice. It is known that mesitylcopper(I) can be readily reduced to Cu(0) nanoparticles, a process achieved by hydrogenation at elevated temperature.[37, 38, 50] It is also reported that diethylzinc may serve as a reactant to produce Cu(0) nanoparticles.[23, 28, 29] Due to the low doping levels employed, any formation of Cu(0) or Cu_2O discrete nanoparticles would be almost impossible to detect as such levels would be below the resolution limit of both powder XRD and transmission electron microscopy.

Indeed, the very similar catalytic activity for Cu-doped and undoped catalysts might be caused by a lack of Cu doping.

Generally, the catalytic activity of Cu/ZnO catalysts is proposed to arise at interfaces between Cu and ZnO particles. One theory proposed that the formation of a Schottky junction accelerates electron transfer from ZnO to Cu(0). This promotes the formation of oxygen vacancies on ZnO along with the migration of Zn atoms onto Cu.[30-32] Doping ZnO with Al^{3+} acts as a structural and electronic promoter by promoting the migration of Zn atoms onto Cu.[9, 33] The incorporation of Al^{3+} in the ZnO lattice is proposed to enhance the *n*-type conductivity, which is consistent with changes to UV-Vis spectrum and optical bandgap. Such *n*-type doping increases electron density through the introduction of a shallow donor level in the band structure of ZnO which results in a smaller optical bandgap. The high electron density promotes the transfer of electrons from ZnO to Cu(0) and hence migration of Zn atoms to Cu. Furthermore, the formation of surface alumina, as observed by TEM and XPS, is consistent with studies of the heterogeneous Al-doped Cu/ZnO catalyst, where Al^{3+} migrates to the surface of ZnO under H_2/CO_2 (molar ratio of 3:1) environment.[9, 15, 33] The mobility of Al^{3+} may be promoted by the higher density of oxygen vacancies on ZnO. Al^{3+} ions might act as a surface stabiliser for the catalyst, and thus, it is tentatively proposed to be acting as a structural promoter.[32, 33]

The lack of Cu/ZnO interfaces in the Mg-doped catalyst is tentatively assigned to the formation of surface Mg^{2+} species, as suggested by XPS (*vide supra*). Such a Mg coating may prevent the formation of Cu/ZnO interfaces and it was already proposed that Mg-doping causes ZnO to be more insulating (suggested by TPR).[9] Furthermore, a larger optical bandgap was observed in Mg:ZnO@DOPA, and the lower electron

density might hamper the formation of Cu/ZnO interfaces. With the lack of Cu/ZnO interfaces, the ripening of Cu may be accelerated, as indicated by XRD of the post-catalysis sample.

5.5 Summary & Conclusion

The scope of organometallic synthesis of colloidal ZnO nanoparticles (2–3 nm), capped with dioctylphosphinate, has been broadened, simply by the addition of sub-stoichiometric amount of dopant organometallic reagents (Mg^{2+}, Al^{3+}, Cu^{+}; 5 mol%) into the pre-hydrolysis mixture. This approach appears to allow close proximity between the dopant and the host prior to nanoparticle growth, but without the need to use a heterometallic precursor.

All the doped-ZnO nanoparticles were combined with colloidal Cu(0) nanoparticles, capped with dioctylphosphinate, and used as catalysts for the hydrogenation of CO_2 to methanol. All systems have outperformed the benchmark heterogeneous Cu-ZnO-Al_2O_3 catalyst. Mg-doping was detrimental to activity (600 μmol $mmol_{metal}^{-1}$ h^{-1}), whilst Al-doping was beneficial and the catalyst was stable for 40 h time-on-stream (1020 μmol $mmol_{metal}^{-1}$ h^{-1}). Such promising results warrant further investigation into elucidating the Al-doped catalyst. The further characterisation of the Al-doped catalyst is warranted to understand the surface mobility of Al^{3+}. One characterisation technique that might allow such investigation would be *in-situ* environmental TEM, where the temperature and atmosphere of the sample can be controlled. As such, studies at variable temperatures and under H_2 or CO_2 atmosphere may provide more insight into the mobility of Al and Zn species, and therefore, it might lead to further understanding of the formation and synergistic effects of Cu/ZnO interface.

5.6 References

1. K. L. Orchard, M. S. P. Shaffer and C. K. Williams, *Chem. Mater.*, 2012, **24**, 2443-2448.
2. N. J. Brown, J. Weiner, K. Hellgardt, M. S. Shaffer and C. K. Williams, *Chem. Commun.*, 2013, **49**, 11074-11076.
3. S. D. Pike, E. R. White, M. S. P. Shaffer and C. K. Williams, *Nat. Commun.*, 2016, **7**, 13008.
4. S. K. Sehmi, S. Noimark, S. D. Pike, J. C. Bear, W. J. Peveler, C. K. Williams, M. S. P. Shaffer, E. Allan, I. P. Parkin and A. J. MacRobert, *ACS Omega*, 2016, **1**, 334-343.
5. S. D. Pike, E. R. White, M. S. Shaffer and C. K. Williams, *Nat. Commun.*, 2016, **7**, 13008.
6. R. Shannon, *Acta Crystallogr., Sect. A*, 1976, **32**, 751-767.
7. S. Mehra, A. Bergerud, D. J. Milliron, E. M. Chan and A. Salleo, *Chem. Mater.*, 2016, **28**, 3454-3461.
8. A. W. Cohn, K. R. Kittilstved and D. R. Gamelin, *J. Am. Chem. Soc.*, 2012, **134**, 7937-7943.
9. J. Schumann, M. Eichelbaum, T. Lunkenbein, N. Thomas, M. C. Álvarez Galván, R. Schlögl and M. Behrens, *ACS Catal.*, 2015, **5**, 3260-3270.
10. V. Etacheri, R. Roshan and V. Kumar, *ACS Appl. Mater. Interfaces*, 2012, **4**, 2717-2725.
11. S. Heitz, Y. Aksu, C. Merschjann and M. Driess, *Chem. Eur. J.*, 2011, **17**, 3904-3910.
12. K. J. Chen, T. H. Fang, F. Y. Hung, L. W. Ji, S. J. Chang, S. J. Young and Y. J. Hsiao, *Appl. Surf. Sci.*, 2008, **254**, 5791-5795.
13. X. Peng, J. Xu, H. Zang, B. Wang and Z. Wang, *J. Lumin.*, 2008, **128**, 297-300.
14. M. Suja, S. B. Bashar, M. M. Morshed and J. Liu, *ACS Appl. Mater. Interfaces*, 2015, **7**, 8894-8899.
15. M. Behrens, G. Lolli, N. Muratova, I. Kasatkin, M. Havecker, R. N. d'Alnoncourt, O. Storcheva, K. Kohler, M. Muhler and R. Schlogl, *Phys. Chem. Chem. Phys.*, 2013, **15**, 1374-1381.
16. S. Miao, R. N. d'Alnoncourt, T. Reinecke, I. Kasatkin, M. Behrens, R. Schlögl and M. Muhler, *Eur. J. Inorg. Chem.*, 2009, **2009**, 910-921.
17. C. G. Lugmair, T. D. Tilley and A. L. Rheingold, *Chem. Mater.*, 1997, **9**, 339-348.
18. R. Pothiraja, S. Shanmugan, M. G. Walawalkar, M. Nethaji, R. J. Butcher and R. Murugavel, *Eur. J. Inorg. Chem.*, 2008, **2008**, 1834-1845.
19. I. P. Silverwood, C. W. Keyworth, N. J. Brown, M. S. P. Shaffer, C. K. Williams, K. Hellgardt, G. H. Kelsall and S. G. Kazarian, *Appl. Spectrosc.*, 2014, **68**, 88-94.
20. A. Sawant, M. K. Ko, V. Parameswaran, S. Lee and C. J. Kulik, *Fuel Sci. Technol. Int.*, 1987, **5**, 77-88.
21. S. D. Pike, A. García-Trenco, E. R. White, A. H. M. Leung, J. Weiner, M. S. P. Shaffer and C. K. Williams, *Catal. Sci. Technol.*, 2017, **7**, 3842-3850.
22. S. D. Pike, E. R. White, A. Regoutz, N. Sammy, D. J. Payne, C. K. Williams and M. S. Shaffer, *ACS Nano*, 2017, **11**, 2714-2723.
23. N. J. Brown, A. García-Trenco, J. Weiner, E. R. White, M. Allinson, Y. Chen, P. P. Wells, E. K. Gibson, K. Hellgardt, M. S. P. Shaffer and C. K. Williams, *ACS Catal.*, 2015, **5**, 2895-2902.

24. A. García-Trenco, A. Regoutz, E. R. White, D. J. Payne, M. S. P. Shaffer and C. K. Williams, *Appl. Catal., B*, 2018, **220**, 9-18.
25. S. Schimpf, A. Rittermeier, X. Zhang, Z.-A. Li, M. Spasova, M. W. E. van den Berg, M. Farle, Y. Wang, R. A. Fischer and M. Muhler, *ChemCatChem*, 2010, **2**, 214-222.
26. Z. Jin, T. Fukumura, M. Kawasaki, K. Ando, H. Saito, T. Sekiguchi, Y. Z. Yoo, M. Murakami, Y. Matsumoto, T. Hasegawa and H. Koinuma, *Appl. Phys. Lett.*, 2001, **78**, 3824-3826.
27. Y. Yan, M. M. Al-Jassim and S.-H. Wei, *Appl. Phys. Lett.*, 2006, **89**, 181912.
28. M. K. Schroter, L. Khodeir, M. W. van den Berg, T. Hikov, M. Cokoja, S. Miao, W. Grunert, M. Muhler and R. A. Fischer, *Chem. Commun.*, 2006, **23**, 2498-2500.
29. S. Vukojević, O. Trapp, J.-D. Grunwaldt, C. Kiener and F. Schüth, *Angew. Chem. Int. Ed.*, 2005, **117**, 8192-8195.
30. J. C. Frost, *Nature*, 1988, **334**, 577.
31. F. Liao, Y. Huang, J. Ge, W. Zheng, K. Tedsree, P. Collier, X. Hong and S. C. Tsang, *Angew. Chem. Int. Ed.*, 2011, **50**, 2162-2165.
32. F. Liao, Z. Zeng, C. Eley, Q. Lu, X. Hong and S. C. Tsang, *Angew. Chem. Int. Ed.*, 2012, **51**, 5832-5836.
33. M. Behrens, S. Zander, P. Kurr, N. Jacobsen, J. Senker, G. Koch, T. Ressler, R. W. Fischer and R. Schlögl, *J. Am. Chem. Soc.*, 2013, **135**, 6061-6068.

Chapter 6

Summary & Outlook

6.1 Summary

Generally, organometallic routes to colloidal crystalline ZnO nanoparticles require the thermal degradation of precursors or elevated reaction temperatures. Alternatively, a one-step, controlled hydrolysis route has been developed that produces these materials, at room temperature.[1] The work presented in this thesis broadens the scope of this hydrolysis method and use it to prepare both uniaxial crystalline ZnO nanoparticles and exfoliated layered zinc hydroxide nanosheets (LZH).

The method applies $ZnEt_2$:carboxylate mixtures and by increasing the carboxylate ligand loading to 0.6, the formation of layered zinc hydroxide was achieved (at lower loadings, ZnO nanoparticles are produced). The use of oleate as the ligand provided a high solubility, of 23 mg/mL in toluene, for the layered zinc hydroxide monolayers, which allowed the investigation of the synthetic pathway using solution-state NMR spectroscopy. The reaction is proposed to proceed by hydrolysing free $ZnEt_2$ first and then the hydrolysis of a pentanuclear zinc cluster complex, $[Zn_5(Et)_4(COOR)_6]$. The solution-casting of the LZH monolayers as a thin film (1 μm thick) produced an optically transparent ZnO film upon annealing (500 °C).

The properties of the colloidal ZnO nanoparticles (prepared by hydrolysis of 5:1 $ZnEt_2$:phosphinate) were altered by modifying the capping ligand or adding dopant. For instance, changing the phosphinate ligand from having octyl chains to octadecyl chains halted the ZnO nanoparticles growth at the stage of oriented attachment (STEM). It is proposed that this occurred because the long aliphatic chains of DODPA

excluded moisture from the ZnO nanoparticles surface. This prevented the solid-state ripening of the nanoparticles over a period of three months.

Three synthetic routes were explored for colloidal Cu/ZnO nanocatalysts and the high surface area of nanoparticles is crucial for the formation of active catalysts in the hydrogenation of CO_2 to methanol. Cu/ZnO synergistic effects appear to be responsible for methanol production from CO_2, with Cu/ZnO interfaces (proposed active site) clearly identified (HR-TEM) for all active catalysts. Regardless of the oxidation state of Cu component, *i.e.* Cu(0) or Cu(I), similar catalytic activity and selectivity were achieved with the colloidal Cu/ZnO nanocatalysts. The use of Cu_2O nanoparticles, instead of Cu(0), has led to some rearrangement of ZnO, which is tentatively attributed to the reduction of ZnO to ZnO_x during catalysis. Furthermore, the use of small ZnO nanoparticles (< 3 nm) led to higher methanol activity catalyst than larger particles (> 4 nm).

The successful doping of ZnO nanoparticles, with Mg^{2+}, Al^{3+} and Cu^{+} ions (5 mol%), has led to changes in the electronic properties (UV-Vis). The application of doped ZnO nanoparticles in the catalytic hydrogenation of CO_2 to methanol showed different activities, proposed to be due to electronic and structural changes upon doping. The formation of an amorphous alumina network was observed (HR-TEM) for Al-doped ZnO/Cu nanocatalysts, likely caused by the migration of Al^{3+} to the catalyst's surface. In addition, the localisation of Mg^{2+} on the surface of Mg-doped ZnO nanoparticles was observed (XPS). Such a Mg surface layer was tentatively proposed as detrimental for catalysis as it prevented Cu/ZnO interface formation.

6.2 Outlook

6.2.1 Layered zinc hydroxides

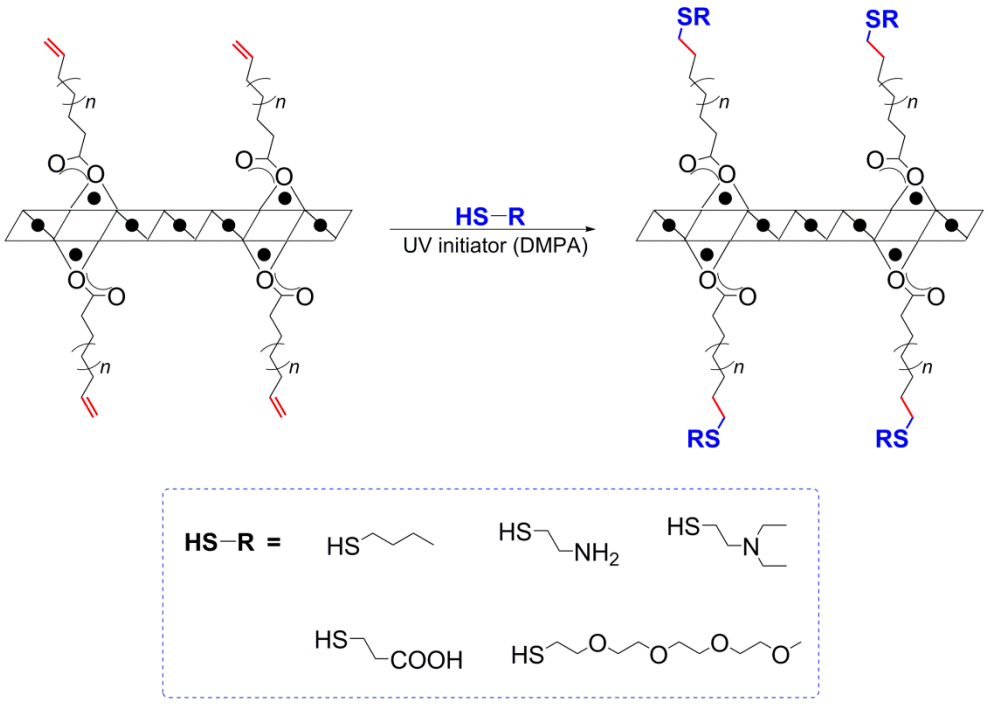

Figure 6.1. The post-modification of LZH, intercalated with terminal olefin-carboxylate, using thiolene reaction. An UV-initiated radical initiator, 2,2-dimethoxy-2-phenylacetophenone (DMPA) and various thiols can be used in the reaction.

The post-modification of the LZH monolayers would be an interesting avenue to explore in order to modify the material properties. By manipulating the periphery of the monolayers (*i.e.* ligand shell), minimal disruption on the zinc hydroxide sheets might be possible and thus maintaining the structural integrity of the inorganic sheets.

The functional group tolerance of the synthetic route should allow for the incorporation of a reactive group on the intercalated carboxylate ligand. Subsequent reactions, such as thiol-ene reactions, can be performed to install various functionalities on the carboxylate ligand (Figure 6.1). One advantage of this post-

modification strategy would be to tailor the solubility of LZH monolayers. Similar concepts have been shown for Au and CdSe/CdS nanoparticles, *via* Schiff base reactions and Huisgen cycloaddition, to achieve water solubility.[2, 3] For LZH monolayers, achieving solubility in water or other aqueous- based solvents might broaden the scope of the material in biomedical applications, such as drug encapsulation and delivery.[4, 5]

The incorporation of a second metal ion would be another interesting future direction to generate mixed metal oxides through thermal degradation. The sub-stoichiometric addition of another iso-valent metal ion, such as Cu^{2+} and Ni^{2+}, has already proven successful so as to prepare doped LZHs.[6-8] The extension to tri-valent ions might provide a feasible synthesis of exfoliated layered double hydroxides (LDHs).

The organometallic synthesis shows good compatibility with preparation of nanocomposite materials, such as the ZnO/epoxy nanocomposite prepared from hydrolysis of a precursor solution of $ZnEt_2$ and $Zn(COOR)_2$ in epoxy resin.[9] With the expansion of organometallic synthesis scope to 2D materials, similar one-pot approach to LZH or LDH nanocomposites might be possible.

6.2.2 Doped-ZnO nanoparticles

Other dopants are worth exploring to expand the range of optical and electronic properties for the ZnO. Dopants, such as $Co^{2/3+}$, Ga^{3+} and In^{3+}, have been introduced into Wurzite ZnO nanoparticles.[10-12] The addition of other transition metals (Ni^{2+} and $Cr^{2/3+}$) as dopants to promote methanation, instead of methanol synthesis, could provide another avenue for investigation.[13]

The catalytic results suggest that Al-doped ZnO nanoparticles gave a slight increase in activity compared to other colloidal catalysts (Chapter 5). A range of doping levels should be tested (1–10 mol%) and the influence on activity for the hydrogenation of CO_2 to methanol measured to determine the optimal doping level.

6.2.3 Hydrogenation of CO_2 to methanol

Throughout this thesis, the techniques used for the characterisation and analyses of post-catalysis samples were all *ex-situ* techniques. The exact mechanisms and any additional changes to the colloidal Cu/ZnO nanocatalysts, under operation, cannot be probed. The use of *in-situ* or operando techniques would be interesting to probe the rearrangement of ZnO nanoparticles in catalytic systems where Cu_2O nanoparticles were employed instead of Cu(0) nanoparticles.

This may be achieved using *in-situ* TEM. By using an environmental TEM holder, air-sensitive samples and the feed gas for catalysis (3: 1 molar ratio of H_2:CO_2) can be introduced into the sample to observe *in-situ* changes of the catalyst under catalytic conditions. Environmental TEM experiments have been conducted on heterogeneous Cu/ZnO catalysts to observe the migration of Cu and ZnO between interfaces.[14] A similar experimental set-up can be used to understand the mechanism and the rearrangement process of ZnO. In addition, near-ambient pressure XPS might be complementary to environmental TEM experiment. With the surface sensitivity of XPS, any changes in the ratio of Zn and Cu on the surface, under catalytic conditions, might further elucidate the rearrangement of ZnO and the nature of the newly formed ZnO species.

Furthermore, both extended X-ray absorption fine structure (EXAFS) and X-ray absorption near edge structure (XANES) might help gain further insight into the nature of the amorphous ZnO network (for Cu_2O/ZnO nanocatalysts) and the alumina network (for Cu/Al:ZnO@DOPA). Fischer and co-workers showed both XANES and EXAFS were able to distinguish the formation of a new ZnO species that was not observed using electron microscopic techniques.[15] All suggested *in-situ* techniques would further the understanding of the Cu/ZnO interactions in the liquid-phase hydrogenation of CO_2 to methanol.

6.3 References

1. K. L. Orchard, M. S. P. Shaffer and C. K. Williams, *Chem. Mater.*, 2012, **24**, 2443-2448.
2. W. Edwards, N. Marro, G. Turner and E. R. Kay, *Chem. Sci.*, 2018, **9**, 125-133.
3. Y. Chen, J. M. Cordero, H. Wang, D. Franke, O. B. Achorn, F. S. Freyria, I. Coropceanu, H. Wei, O. Chen, D. J. Mooney and M. G. Bawendi, *Angew. Chem. Int. Ed.*, 2018, DOI: 10.1002/anie.201801113.
4. H. Nabipour, M. Hosaini Sadr and N. Thomas, *J. Exp. Nanosci.*, 2015, **10**, 1269-1284.
5. F. Barahuie, M. Z. Hussein, S. A. Gani, S. Fakurazi and Z. Zainal, *Int. J. Nanomed.*, 2014, **9**, 3137-3149.
6. X. Zou, A. Goswami and T. Asefa, *J. Am. Chem. Soc*, 2013, **135**, 17242-17245.
7. G. G. C. Arizaga, K. G. Satyanarayana and F. Wypych, *Solid State Ion.*, 2007, **178**, 1143-1162.
8. E. Kandare and J. M. Hossenlopp, *Inorg. Chem.*, 2006, **45**, 3766-3773.
9. A. Gonzalez-Campo, K. L. Orchard, N. Sato, M. S. Shaffer and C. K. Williams, *Chem. Commun.*, 2009, 4034-4036.
10. S. Mehra, A. Bergerud, D. J. Milliron, E. M. Chan and A. Salleo, *Chem. Mater.*, 2016, **28**, 3454-3461.
11. E. Della Gaspera, M. Bersani, M. Cittadini, M. Guglielmi, D. Pagani, R. Noriega, S. Mehra, A. Salleo and A. Martucci, *J. Am. Chem. Soc.*, 2013, **135**, 3439-3448.
12. B. Martínez, F. Sandiumenge, L. Balcells, J. Arbiol, F. Sibieude and C. Monty, *Phys. Rev. B*, 2005, **72**, 165202.
13. W. Wang, X. Li, Y. Zhang, R. Zhang, H. Ge, J. Bi and M. Tang, *Catal. Sci Technol.*, 2017, **7**, 4413-4421.
14. C. Holse, C. F. Elkjær, A. Nierhoff, J. Sehested, I. Chorkendorff, S. Helveg and J. H. Nielsen, *J. Phys. Chem. C*, 2015, **119**, 2804-2812.
15. M. K. Schroter, L. Khodeir, M. W. van den Berg, T. Hikov, M. Cokoja, S. Miao, W. Grunert, M. Muhler and R. A. Fischer, *Chem. Commun.*, 2006, **23**, 2498-2500.

Chapter 7

Experimental

7.1 General Materials & Methods

The syntheses of LZHs and ZnO nanoparticles were carried out in a dry nitrogen-filled glovebox and Schlenk line techniques were used for hydrolysis of the organometallic precursors. All solvents were purchased from VWR, UK, and Sigma Aldrich. Chemicals were purchased from Sigma Aldrich, Fisher Scientific and Alfa Aesar and used as supplied unless otherwise stated. Toluene used in the syntheses of LZHs and ZnO nanoparticles was dried and distilled by refluxing over metallic Na and then degassed by freeze-thaw cycles (x3) to remove oxygen and stored over activated molecular sieves (4 Å). Mesitylene used in the hydrogenation of mesitylcopper(I), with dioctylphosphinic acid, was degassed by freeze-thaw cycles (x3) to remove oxygen and stored over activated molecular sieves (4 Å). Diethylzinc is a highly pyrophoric and volatile liquid where extreme caution must be taken when using the chemical. HPLC-grade water was used for the controlled hydrolysis of LZH and ZnO nanoparticles synthesis mixtures. Deuterated solvents were dried by placing over calcium hydride, distilled under vacuum, degassed by freeze-thaw cycles (x3) to remove oxygen and stored over activated molecular sieves (4 Å). Zinc *bis*(hydroxide) was prepared by salt metathesis of $ZnCl_2$ and NaOH (1 M) in aqueous solution.

The following chemicals were used without further purification for syntheses of LZHs and ZnO nanoparticles: zinc *bis*(acetate), hexanoic acid, benzoic acid, decanoic acid, oleic acid, stearic acid, 1-octene, 1-octadecene, benzoyl peroxide, *n*-butyl-*sec*-butylmagnesium solution (0.7 M, hexane) and triethylaluminium. All chemicals were purchased from Sigma Aldrich.

Zinc *bis*(hexanoate),[1] zinc *bis*(oleate),[2] mesitylcopper (I)[3] and dioctylphosphinic acid[4] (DOPA–H) and ZnO@DOPA[5] were synthesised using reported routes.

Mesitylcopper (I) can also be purchased commercially (Strem) and recrystallisation in toluene (x3) was performed to remove magnesium halide impurities, with product purity assessed by elemental analysis.

7.1.1 Characterisation Techniques

Elemental analysis (EA) was carried out by Mr Steven Boyer, London Metropolitan University, and **inductively coupled plasma optical emission spectrometry (ICP-OES)** was carried out by Mr Alan P. Dickerson, University of Cambridge.

^{1}H NMR spectra were recorded at 400 MHz using Bruker Av400 spectrometer operating at 9.4 T in C_6D_6 unless otherwise stated. The recycle delays (*D1*) for all spectra were 1 s, with 16 scans per spectrum. Chemical shifts are expressed in parts per million (ppm) and referenced to residual solvent resonance. **^{31}P{^{1}H} NMR** spectra were recorded at 202 MHz using Bruker Av400 spectrometer in C_6D_6 unless otherwise stated. **Solid state ^{27}Al-MAS-NMR** spectra were recorded on a Bruker Avance III HD in 4mm OD rotors, at 104.26 MHz with a spin speed of 8.5 kHz.

Fourier transform infrared (FT-IR) spectra were recorded using a Perkin-Elmer Spectrum 100 spectrometer, fitted with an ATR attachment, and each spectrum was collected with 32 scans, with a resolution of 4 cm^{-1}.

Powder X-ray diffraction (XRD) was performed using a PANalytical X'Pert PRO diffractometer at an operating voltage of 40 kV, with a step size of 0.033° 2θ, scan step time of 70 s and scan range of 3–80° 2θ. The machine was used in theta/theta reflection mode, fitted with a nickel filter, 0.04 rad Soller slit, 10 mm mask, 1/4° fixed divergence slit, and 1/2° fixed anti-scatter slit. The diffraction

patterns were analysed using Fityk (version 0.9.8; Marcin Wojdyr, 2010); the peaks were fitted to a SplitPearson7 function and the particle sizes were calculated using the fitted FWHM for the Scherrer equation. For air-sensitive samples, samples were loaded onto silicon XRD plates in a nitrogen-filled glovebox and a polyimide adhesive tape was used to cover the samples, in order to exclude air and moisture. The peak fitting of (101) facet for M:ZnO@DOPA was performed using Fityk (version 0.9.8; Marcin Wojdyr, 2010) with Gaussian function.

Small angle X-ray scattering (SAXS) measurements were performed using a PANalytical Empyrean diffractometer, equipped with ScatterX[78] module, from 0–5° 2θ, using a step size of 0.039° 2θ and scan step time of 195 s. Data analysis was performed using PANalytic EasySAXS software and error given is derived from instrumental resolution.

Thermogravimetric analysis (TGA) and **differential thermal analysis (DTA)** were carried out using a Mettler Toledo TGA/DSC 1, under a flow of dry air, with flow rate of 60 mL min^{-1}, from 50–600°C, at a heating rate of 5 °C/min.

UV-Vis absorption spectra of ZnO nanoparticles were recorded using Perkin-Elmer Lambda 950 spectrometer in transmission mode, from 300–500 nm and with a scan speed of 1 nm s^{-1}. The ZnO nanoparticle diameters were estimated from the UV-Vis spectra using the empirical method developed by Meulenkamp.[6]

Scanning electron microscopy (SEM) samples were prepared by adhering samples to stubs with silver paint and sputtering with a 10 nm layer of chromium. Micrographs were taken with a LEO Gemini 1525 FEGSEM (field emission gun SEM)

with an accelerating voltage of 5 keV and a 30 μm aperture, using an in-lens secondary electron detector.

Transmission electron microscopy (TEM) samples were drop-cast (toluene solution, 0.05 mg/mL) onto 300 mesh Au grids, with a 3 nm ultra-thin carbon film and holey carbon support (Agar Scientific). For *Chapter 3*, TEM images were obtained on a JEOL JEM 2100F scanning transmission electron microscope, equipped with an Oxford X-Max 80 SDD EDX detector, at an operating voltage of 200 kV in bright field imaging mode. For *Chapter 4*, **STEM and conventional TEM images** were acquired on an FEI Titan 80-300 microscope operated at 300 kV. For the air-sensitive samples, a Gatan environmental sample holder was used to avoid any air exposure, with the sample preparation and loading of the sample into holder being performed in a dry nitrogen-filled glovebox. **EDX mapping** was performed on a JEOL JEM 2100F scanning transmission electron microscope, equipped with an Oxford X-Max 80 SDD EDX detector, at an operating voltage of 200 kV. For *Chapter 5*, **bright field (BF) and HAADF-STEM** images were acquired with a probe corrected ARM200F, at the ePSIC facility (Diamond Light Source), with an acceleration voltage of 200 keV. Measurement conditions were a CL aperture of 30 μm, convergence semiangle of 24.3 mrad, beam current of 12 pA, and scattering angles of 0-10 and 35-110 mrad, for BF and HAADF-STEM respectively. Particle size measurement for LZH was performed manually. For the sizing of Cu and ZnO nanoparticles separately, automated size analysis was performed on STEM images and they were carried out by *Dr Edward R. White (Imperial College London) and Dr Manfred Schuster (Johnson Matthey).*

X-ray photoelectron spectroscopy (XPS) was used to characterise the surface of M:ZnO@DOPA and post-catalysis samples of Cu/M:ZnO@DOPA. The spectra were

recorded on a Thermo Scientific K-Alpha+ X-ray photoelectron spectrometer system operating at $2x10^{-9}$ mbar base pressure. This system incorporates a monochromated, microfocused Al Kα X-ray source (hν = 1486.6 eV) and a 180° double focusing hemispherical analyser with a 2D detector. The X-ray source was operated at 6 mA emission current and 12 kV anode bias and a flood gun was used to minimize sample charging. Samples were mounted using conductive carbon tape and transferred to the spectrometer using a special glove box module which ensured that samples were never exposed to air. Data were collected at 200 eV pass energy for survey spectra and 20 eV pass energy for core levels. Data was collected over six measurement positions using an X-ray spot size of 400 μm to avoid beam damage affecting the results. Data was then averaged across the different measurement positions. All data were analysed using the Avantage software package and performed by *Dr Anna Regoutz (Imperial College London).*

Atomic force microscopy (AFM) samples were prepared on silicon wafer pre-cleaned in 3:1 mixture of H_2SO_4 (98 %) and H_2O_2 (30 %). Samples were drop-cast (0.05 mg/mL in toluene) onto the Si wafer and dried under vacuum for 16 h at room temperature. AFM measurements were performed with tapping mode on a Bruker Digital Instruments Multimode VIII AFM with Nanoscope IV Digital Instruments AFM controller. All AFM micrographs were recorded with a resolution of 512 lines and with a typical scanning speed of 1 Hz, and processed using Bruker NanoScope Analysis v1.40 (R2Sr). Height profiles were recorded from individual particle maximum heights (N = 127) for LZH–Ole.

7.2 Experimental Procedure & Characterisation Data

7.2.1 Synthesis & Exfoliation of LZHs

Carboxylate loading [COOR]/[Zn]	Molar Ratio $ZnEt_2$:$Zn(COOR)_2$	Moles of $ZnEt_2$/ mmol	Moles of $Zn(COOR)_2$/ mmol
0.40	4:1	1.09	0.27
0.50	3:1	1.02	0.34
0.60	2.3:1	0.95	0.41

Table 7.1. Table showing the corresponding molar ratios and moles of $ZnEt_2$ and $Zn(COOR)_2$ required for the synthesis of LZH at different carboxylate loading.

The carboxylate loading ([COOR]/[Zn]) was varied (the molar ratios and moles of reagents, for each loading, are listed in Table 7.1), whilst maintaining the total concentration of zinc at 0.15 M and total moles of Zn at 1.37 mmol. For the yields of LZHs, they were calculated to be ~ 63 mol% Zn (*see Appendix*).

LZH–OAc. $ZnEt_2$ (0.118 g, 0.952 mmol) was added dropwise to a suspension of $Zn(OOC(CH_3))_2$ (0.075 g, 0.414 mmol) in toluene (9.1 mL). The mixture was stirred for 16 h at room temperature, which yielded a clear solution. Under a flow of N_2, HPLC-grade water (39 µL, 2.18 mmol, 1.6 equiv. to the total moles of Zn of 1.37 mmol) was directly added to the reaction and the mixture was stirred for 3 h, where the formation of white solid was observed after 1 h. All volatiles were removed *in vacuo*, which yielded LZH–OAc as a fine white powder. FT-ATR-IR (υ/cm^{-1}): 3367 (*O–H*), 1550 $(COO)_{asymm}$, 1406 $(COO)_{symm}$. Elemental analysis: $C_6H_{17}O_{12}Zn_5$, expected 11.26 %C, 2.68 %H; found 12.72 %C, 2.27 %H.

LZH–OHex. $ZnEt_2$ (0.118 g, 0.952 mmol) was added dropwise to a suspension of $Zn(OOC(CH_2)_4CH_3)_2$ (0.122 g, 0.414 mmol) in toluene (9.1 mL). The mixture was stirred for 16 h at room temperature, which yielded a clear solution. Under a flow of N_2, HPLC-grade water (39 μL, 2.18 mmol, 1.6 equiv. to the total moles of Zn of 1.37 mmol) was directly added to the reaction and the mixture was stirred for 3 h, where the formation of white solid was observed after 2 h. All volatiles were removed *in vacuo*, which yielded LZH–OHex as a fine white powder. FT-ATR-IR (υ/cm^{-1}): 3395 (*O–H*), 2956 ($C–H)_{asymm}$, 2929 ($C–H)_{asymm}$, 2872 ($C–H)_{symm}$, 1540 ($COO)_{asymm}$, 1405 ($COO)_{symm}$. Elemental analysis: $C_{18}H_{41}O_{12}Zn_5$, expected 26.74 %C, 5.11 %H; found 27.25 %C; 4.25 %H.

LZH–Ole. $ZnEt_2$ (0.118 g, 0.952 mmol) was added dropwise to a suspension of $Zn(OOC(CH_2)_7HC{=}CH(CH_2)_7CH_3)_2$ (0.260 g, 0.414 mmol) in toluene (9.1 mL). The mixture was stirred for 16 h at room temperature, which yielded a clear solution. Under a flow of N_2, HPLC-grade water (39 μL, 2.18 mmol, 1.6 equiv. to the total moles of Zn of 1.37 mmol) was directly added to the reaction and the mixture was stirred for 3 h. A clear solution remained after stirring and all volatiles were removed *in vacuo*, which yielded LZH–Ole as a white, glassy solid. *The synthesis of LZH–Ole can also be achieved using neat oleic acid rather than $Zn(OOC(CH_2)_7HC{=}CH(CH_2)_7CH_3)_2$ as the source of carboxylate ligand.* FT-ATR-IR (υ/cm^{-1}): 3389 (*O–H*), 3003 ($=C–H)_{asymm}$, 2920 ($C–H)_{asymm}$, 2851 ($C–H)_{symm}$, 1570 ($COO)_{asymm}$, 1465 ($C–H)_{symm}$, 1411 ($COO)_{symm}$. ^{1}H NMR (400 MHz, C_6D_6, 298 K, *see Appendix for proton assignment*): δ 5.52 (*cis*-alkene H, H_e), 2.30 (H_a), 2.11 (H_d), 1.58 (H_b), 1.42 (H_c), 1.40 (H_c), 1.30 (H_c), 1.17 (H_c),

0.92 (terminal CH_3 of oleate, H_f). Elemental analysis: $C_{54}H_{107}O_{12}Zn_5$, expected 49.61 %C, 8.25 %H; found 46.74 %C, 8.34 %H.

For the synthesis of LZH–ODec and LZH–OBz, neat decanoic acid and benzoic acid were used instead of the zinc *bis*(carboxylate) salt form:

LZH–ODec. $ZnEt_2$ (0.169 g, 1.37 mmol) was added to a solution of decanoic acid (0.141 g, 0.818 mmol) in toluene (9.1 mL) and the mixture was stirred for 16 h. Under a flow of N_2, HPLC-grade water (39 µL, 3.23 mmol) was directly added to the reaction and the mixture was stirred for 3 h. A clear solution remained after stirring and all volatiles were removed *in vacuo*, which yielded LZH–ODec as a white, glassy solid. FT-ATR-IR (υ/cm^{-1}): 3396 (O–H), 2920 (C–H)$_{asymm}$, 2850 (C–H)$_{symm}$, 1573 (COO)$_{asymm}$, 1465 (C–H)$_{symm}$, 1407 (COO)$_{symm}$. Elemental analysis: $C_{20}H_{46}O_{12}Zn_5$, expected 29.82 %C, 5.76 %H; found 36.66 %C, 7.06 %H.

LZH–OBz. $ZnEt_2$ (0.169 g, 1.37 mmol) was added to a solution of benzoic acid (0.100 g, 0.818 mmol) in toluene (9.1 mL) and the mixture was stirred for 16 h. Under a flow of N_2, HPLC-grade water (39 µL, 3.23 mmol) was directly added to the reaction and the mixture was stirred for 3 h, where the formation of white solid was observed after 1 h. All volatiles were removed *in vacuo*, which yielded LZH–OBz as a white fine powder. FT-ATR-IR (υ/cm^{-1}): 3382 (O–H), 1598 (C=C), 1546 (COO)$_{asymm}$, 1394 (COO)$_{symm}$. Elemental analysis: $C_{14}H_{18}O_{12}Zn_5$, expected 23.85 %C, 2.57 %H; found 30.27 %C, 2.91 %H.

Solubility test of LZH–Ole. The solubility of LZH–Ole was assessed by gradual addition to 1 mL of aliquots toluene, hexane, chloroform, dichloromethane, ethanol and water. The point of saturation was determined to be when insoluble solid was seen in solution. A second method of solubility measurement of LZH–Ole in toluene was achieved by obtaining an over-saturated solution of LZH–Ole (50 mg) in toluene (2 mL), undissolved solids was allowed to settle and an aliquot of solution (1 mL) was taken and solvent was removed under a flow of N_2. The weight of the sample from the aliquot was measured and the solubility of LZH–Ole in toluene was determined to be 22 mg/mL.

Exfoliation of LZH–Ole in toluene. LZH–Ole (10 mg) was added to toluene (10 mL) and the mixture was mechanically stirred for 2 h at room temperature. A clear colloidal solution of LZH–Ole in toluene was obtained. The solution was then diluted to concentration of 0.05 mg/mL and then drop-cast onto TEM grids and Si wafers for TEM and AFM.

Fabrication of ZnO thin film using LZH–Ole. Glass microscope slides were used as substrates for deposition of thin films of LZH–Ole. Slides were placed vertically into a solution of LZH–Ole in toluene (1 mg/mL), the solution was then evaporated under a stream of nitrogen overnight and a uniform film of LZH–Ole was deposited on substrate. For the production of ZnO thin films on glass substrates, slides coated with LZH–Ole were annealed in a three-zone tube furnace (PTF 12/38/500, Lenton Ltd, UK) at 500 °C, with a heating ramp rate of 50 °C/min, for 15 mins, under a flow of air. All fabricated films were characterised by SEM and UV-Vis spectroscopy in transmission mode.

7.2.2 Synthesis of DODPA & ZnO@DODPA

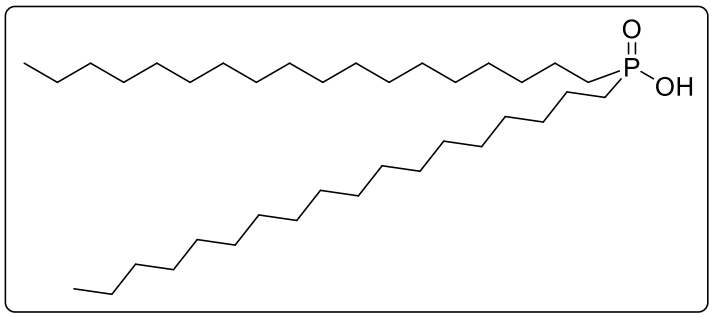

Di-(octadecyl)phosphinic acid (DODPA–H).[4] 1-octadecene (50 g, 198 mmol), hypophosphorous acid (6.535 g, 99 mmol) and benzoyl peroxide (1.319 g, 5.45 mmol) were suspended in EtOH (30 mL) with H_2O (6.5 mL). The reaction mixture was refluxed at 100 °C for 89 h. A two-phase mixture was observed after reflux with white precipitate suspended in the organic layer. HCl (6 M, 40 mL) was added and toluene (200 mL) was introduced to dissolve all white precipitate. The aqueous layered was separated and extracted with toluene (2 x 50 mL). All organic layers were combined and the solvent was removed *in vacuo*, yielding the crude product as a white precipitate. The white precipitate was recrystallized from hot heptane three times and washed with acetone and chloroform. The undissolved white solid is di-(octadecyl)phosphinic acid (3.887 g, 6.81 mmol, 6.9%). ^{1}H ($CDCl_3$, 400 MHz, 298 K): δ 3.71 (br s, $R_2POO\mathit{H}$), 1.65 (m, 8H, $HO_2P((C\mathit{H}_2)_2CH_2(CH_2)_{14}CH_3)_2$, 1.40 (m, 4H, $HO_2P((CH_2)_2C\mathit{H}_2(CH_2)_{14}CH_3)_2$, 1.28 (m, 56H, $HO_2P((CH_2)_2CH_2(C\mathit{H}_2)_{14}CH_3)_2$, 0.90 (t, 6H, $HO_2P((CH_2)_2CH_2(CH_2)_{14}C\mathit{H}_3)_2$); $^{31}P\{^1H\}$ (CDCl3, 202 MHz, 298 K): δ 61.17 ($R_2\mathit{P}OOH$). AT-IR (cm^{-1}): ν 2914 ($(C–H)_{asymm}$), 2847 ($(C–H)_{symm}$), 1674 (P–OH), 1466 ($(C–H)_{asymm}$), 963 (P=O). Elemental analysis: $C_{36}H_{75}O_2P$, expected 75.73 %C, 13.24 %H; found 75.83 %C, 13.13 %H.

ZnO@DODPA nanoparticles. DODPA–H (0.200 g, 0.350 mmol) was suspended in toluene (12 mL) and diethylzinc (0.216 g, 1.750 mmol) was added to the suspension. The reaction mixture was left to stir for 18 h. A 0.4 M solution of water (63 mg) in acetone (8.75 mL) was introduced to the reaction mixture over a period of 8 min. Upon the addition of water in acetone, the mixture went from a colourless solution, *via* a white gel-phase, to a solution with suspended white precipitate and the mixture was stirred for 2 h. The separation of white precipitate was achieved through centrifugation (3900 rpm, 20 min) of the mixture. The white precipitate was isolated, washed with toluene (3 mL) and re-precipitated with acetone (12 mL), and finally washed with acetone only, with centrifugation after each washing-precipitation step. The white precipitate was left to dry overnight under air, yielding ZnO@DODPA (0.217 g, 86%). $^{31}P\{^{1}H\}$ (CDCl3, 202 MHz, 298 K): δ 62 (br, ZnO@R_2*P*OO). AT-IR: ν 3372 (O–H), 2918 ($(C–H)_{asymm}$), 2850 ($(C–H)_{symm}$), 1465 ($(C–H)_{asymm}$), 1124 ($(PO_2^-)_{symm}$), 1043 ($(PO_2^-)_{asymm}$). Elemental analysis: found 40.15 %C, 7.13 %H.

7.2.3 Synthesis of doped-ZnO nanoparticles

All syntheses of doped-ZnO nanoparticles were performed using the general procedure outline below, where some modifications were applied to a previously reported literature procedure.[5, 7] Introduction of dopants into ZnO nanoparticles was achieved using the following reagents: *n*-butyl-*sec*-butylmagnesium solution (0.7 M, hexane) for Mg:ZnO, triethylaluminium for Al:ZnO and mesitylcopper (I) for Cu:ZnO.

M:ZnO@DOPA (M = Mg, Al, Cu). DOPA–H (0.2 g, 0.689 mmol) was added to a Schlenk flask, with a stirrer bar, and the flask was subjected to vacuum for 2 h. Toluene (23 mL) was added to the flask. For 5 mol% doping of ZnO, diethylzinc (0.404 g, 3.273 mmol) was added dropwise to the solution, followed by the addition of dopant source (0.172 mmol, *amounts of doping reagent added are found in Table 7.2*). The mixture was stirred overnight under static nitrogen atmosphere. A 0.4 M solution of HPLC-grade water (0.123 g) in acetone (17.2 mL) was added to the reaction mixture, dropwise, over a period of 8 mins. Upon the addition of water in acetone, the mixture went from a colourless solution, *via* a gel-phase, to a solution with suspended precipitate and the mixture was stirred for further 2 h. The separation of precipitate was achieved through centrifugation (3900 rpm, 20 min) of the mixture. The precipitate was isolated, re-dissolved in toluene (3 mL) and re-precipitated with acetone (12 mL), and finally washed with acetone only, where centrifugation is needed after each washing-precipitation step. The precipitate was left to dry overnight under air, yielding Mg:ZnO@DOPA (0.426 g) and Al:ZnO@DOPA (0.440 g) as white powders and a dark green powder for Cu:ZnO@DOPA (0.438 g).

M:ZnO@DOPA	Dopant source	Doping reagent added	Yield[a] (%)
Mg:ZnO@DOPA	Mg(^{n}Bu)(^{s}Bu) (0.7 M in hexane)	0.246 mL	87
Al:ZnO@DOPA	$AlEt_3$	19 mg	89
Cu:ZnO@DOPA	CuMes	31 mg	92

[a] Yields were calculated based on Zn content.

Table 7.2. Table showing the amount of doping reagent required to achieve 5 mol% doping in M:ZnO @DOPA.

7.2.4 Synthesis of Cu(0) nanoparticles *via* hydrogenation

All metallic copper and copper(I) oxide nanoparticles were synthesised according to reported procedure.[8] J. Young flasks (50 mL, GPE Scientific) were used for all hydrogenation of Cu(I) precursors and the resultant deep red Cu@DOPA solutions were used in the catalytic hydrogenation of CO_2 to methanol.

Cu@DOPA. DOPA–H (11.7 mg, 0.04 mmol) was added to the J Young flask and was subjected to vacuum on Schlenk line for 30 min. In a nitrogen-filled glovebox, mesitylcopper (I) (73.3 mg, 0.40 mmol) was added to the flask and mesitylene (11 mL) was used to dissolve both DOPA and mesitylcopper (I), where then the mixture was stirred for 10 min. The reaction was degassed by freeze-thaw cycles (x2). The reaction solution was re-frozen and vacuum was applied. The reaction vessel, fully submerged in liquid N_2, was then charged with hydrogen gas (open to mercury bubbler) and the reaction mixture was thawed to room temperature to obtain 2 bar of hydrogen within flask. The reaction was heated to 110 °C for 2.5 h in the sealed J Young flask resulting in the formation of a deep red solution. The solution was cooled and short vacuum/refill cycles (x4) were performed to remove excess hydrogen gas from flask (care: do not remove solvent during vacuum cycles). The solution of Cu@DOPA was stored in the glovebox to prevent oxidation.

Cu_2O@L, (L = DOPA, St). L–H (0.04 mmol) and mesitylcopper (I) (73.3 mg, 0.40 mmol) were dissolved in mesitylene (11 mL) and the solution was exposed to air overnight, with stirring. The resulting solution has a dark yellow/brown colour, occasionally with some black precipitate.

7.2.5 Catalytic experiments for the hydrogenation of CO_2 to methanol

The methanol synthesis experiments were performed in a 300 mL continuous flow stirred-tank reactor (CSTR, Parr) which was mechanically stirred at 1500 r.p.m. and with vertical baffles to ensure homogeneous mixing of the liquid and gas phase. Any air stable precursors (ZnO@DOPA, ZnO@DODPA, M:ZnO@DOPA [M = Mg, Al, Cu] or Cu_2O nanoparticles), were added directly to the reactor vessel, and then, the reactor was filled with mesitylene up to a total volume of 100 mL. The solution mixture was subsequently stirred and degassed by flowing N_2 (400 mL.min-1) for 30 minutes. All colloidal, air-sensitive, solutions of Cu@DOPA NPs were added by syringe under a flow of nitrogen, always giving a total reaction volume of 100 mL. 0.4 mmol each of Zn and Cu were added in all cases to achieve a ratio of 1:1 Zn:Cu. Finally, the reactor was pressurized to 5.0 MPa using a gas mixture comprising 3:1 H_2:CO_2 (96 vol%, with 4 vol% Ar used as internal standard for GC analysis) and heated to 210 °C. The experiments were performed under a flow of 150 mL min^{-1} for 20 h.

The commercial CuO-ZnO-Al_2O_3 precursor of the methanol synthesis catalyst from Alfa Aesar (45776, mass composition CuO; 63.5%, ZnO; 25.1%, Al_2O_3; 10.1%, MgO; 1.3%), ground to a fine powder, was tested as a reference material. The choice of catalyst loading was dictated by normalisation considerations, making sure that the total moles of Cu and Zn metals was the same as in the Cu/ZnO colloids. Before any catalytic experiment was conducted, the reference catalyst was activated using a diluted H_2 stream (5 vol% H_2/N_2) at 0.45 MPa and 240°C (ramp 2 °C min^{-1}) for 3 h, according to a standard activation protocol for the ternary Cu-ZnO-Al_2O_3 methanol

synthesis catalyst in slurry reactors.[9] Finally, the catalytic run was performed under the same conditions described before.

The reaction products and unreacted material were monitored by an online gas chromatograph (Bruker 450 GC), equipped with a thermal conductivity detector (TCD), for the quantification of CO, CO_2 and Ar, and a flame ionization detector (FID), for the quantification of MeOH, and other oxygenates or hydrocarbons (if produced). To avoid any product condensation during the experiments, the lines from the reactor to the GC were heated to 180 °C. (Scheme 7.1, Figure 7.1)

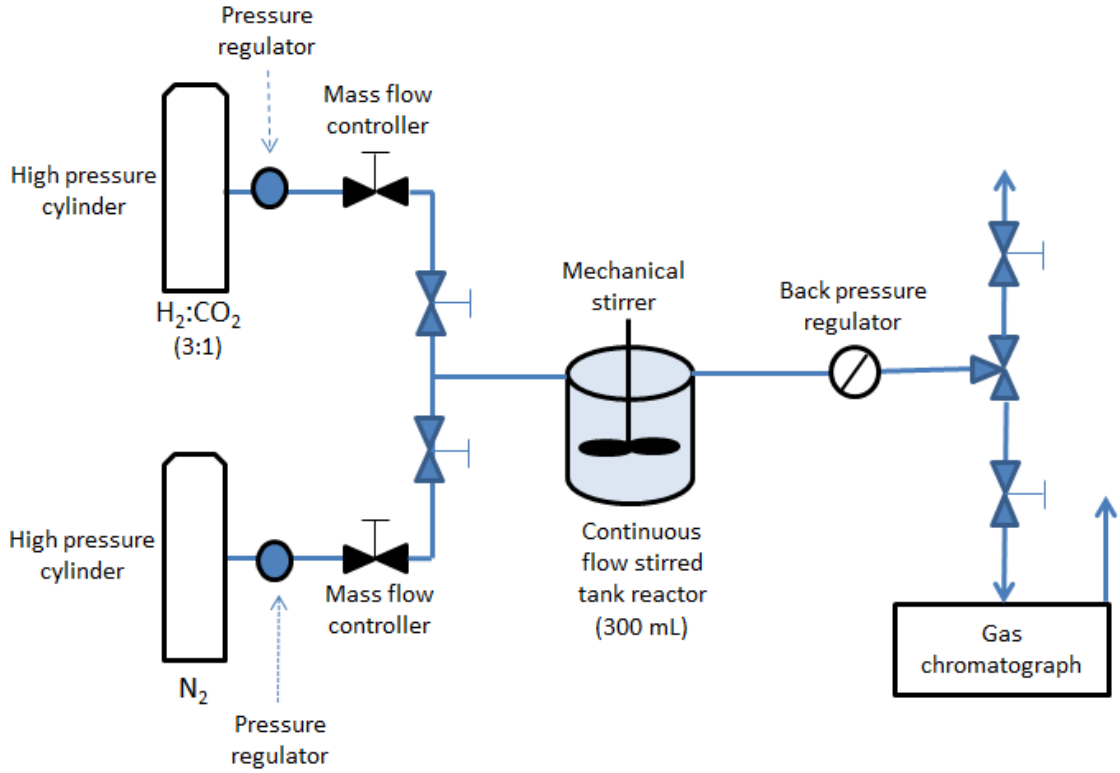

Scheme 7.1. Schematic set-up of the continuous flow stirred tank reactor (300 mL) with the online gas chromatograph connected to the reactor.

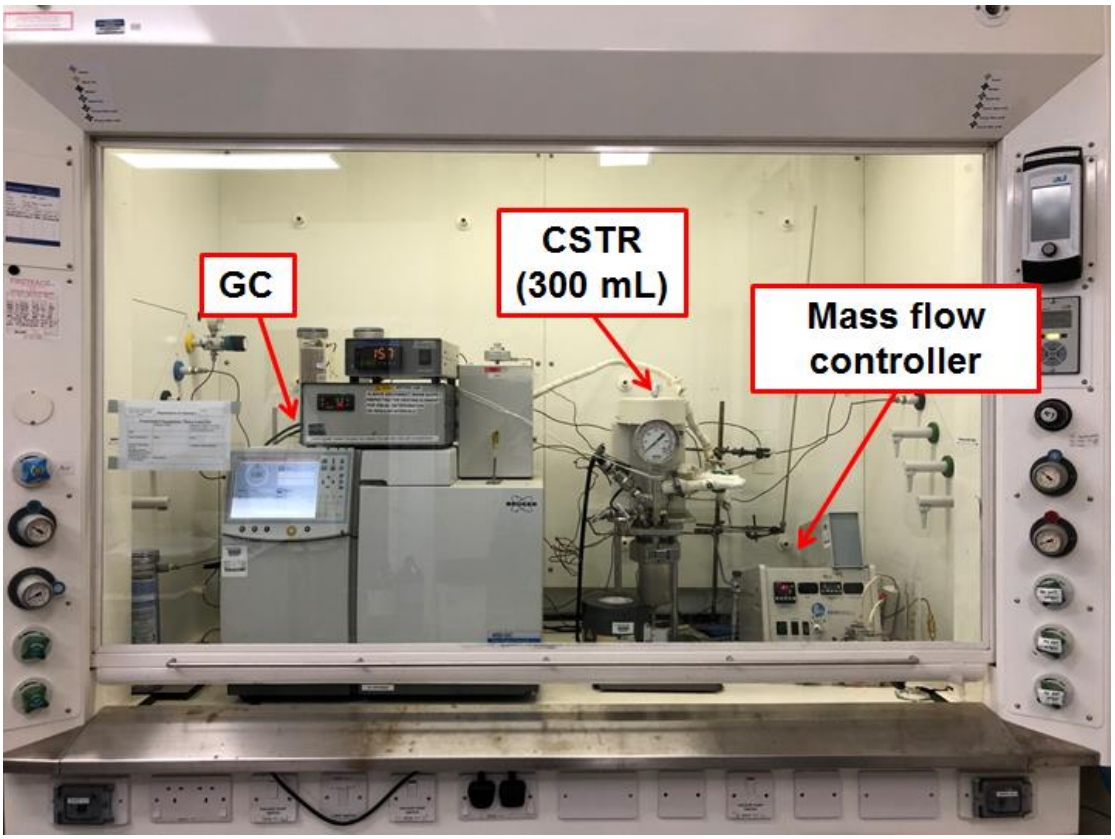

Figure 7.1. Photograph of continuous flow stirred tank reactors.

7.3 Surface Coverage Calculations

For calculating the surface coverage of ZnO nanoparticles, elemental analysis is used in order to obtain the weight percentage of ZnO and capping ligand, respectively. The theoretical total surface area of ZnO nanoparticles at a given size (S_T) is:

$$S_T = S_P \times N_P \tag{7.1}$$

where S_P is the surface area per particle and N_P is the total number of particles, given by:

$$N_P = \frac{nV_m}{V_P} \tag{7.2}$$

with n being the number of moles of ZnO, V_m as the molar volume of ZnO (1.4353×10^{25} Å^3 mol^{-1}) and V_P is the volume per particle. Assuming that the particles are perfect spheres, rearrangement of equations 6.1 and 9.2 would give the following:

$$\frac{S_T}{S_P} = \frac{nV_m}{V_P} \rightarrow \frac{S_T}{4\pi r^2} = \frac{nV_m}{(\frac{4}{3}\pi r^3)} \rightarrow \boldsymbol{S_T = \frac{3nV_m}{r}} \tag{7.3}$$

where r is the radius of the particles (average of measurements by XRD, HR-TEM and UV-Vis analysis) with n = 1.

The number of moles of organics per mole of ZnO, n_c, is the following:

$$n_c = \frac{\left({W_o}/{M_o}\right)}{\left({W_{ZnO}}/{M_{ZnO}}\right)} \tag{7.4}$$

W_O and W_{ZnO} being the weight percentage (wt%) of organics and ZnO present in the sample. M_o and M_{ZnO} are the molecular weight of phosphinate and ZnO, respectively.

For each phosphinate headgroup,[5, 7, 10] the surface area was estimated to be 24.4 Å^2. The theoretical surface area that can be occupied by the phosphinates (S_S) is:

$$\boldsymbol{S_S = Z \times n_c \times 24.4} \quad (7.5)$$

with Z as Avogadro's number. The ratio of S_S to S_T gives the percentage coverage of ligand on ZnO nanoparticles.

7.4 Determining Yields of ZnO Nanoparticles

The Zn yields of ZnO and M:ZnO nanoparticles were determined by obtaining the mass and the Zn wt% of the final product. The mass of Zn, in grams, within a sample of ZnO nanoparticles was calculated. The theoretical mass of Zn, in grams, was determined by the quantity of Zn-based starting materials. For example, below details the calculations of the Zn yield of Mg:ZnO@DOPA. The final product mass is 0.426 g, with Zn wt% of 46.01%, and the moles of Zn starting material is 3.445 mmol:

$$\textbf{Mass of Zn} = 0.426 \text{ x } 0.46 = 0.196 \text{ g}$$

$$\textbf{Theoretical mass of Zn} = \frac{3.445}{1000} \times 65.38 = 0.225 \text{ g}$$

$$\textbf{Zn yield of Mg:ZnO@DOPA} = \frac{0.196}{0.225} \times 100 = \mathbf{87}\%$$

7.5 References

1. O. Berkesi, I. Dreveni, J. Andor and J. Mink, *Inorg. Chim. Acta*, 1992, **195**, 169-173.
2. S. Barman and S. Vasudevan, *J. Phys. Chem. B*, 2007, **111**, 5212-5217.
3. T. Tsuda, T. Yazawa, K. Watanabe, T. Fujii and T. Saegusa, *J. Org. Chem.*, 1981, **46**, 192-194.
4. F. Wang, R. Tang and W. E. Buhro, *Nano Lett.*, 2008, **8**, 3521-3524.
5. N. J. Brown, J. Weiner, K. Hellgardt, M. S. Shaffer and C. K. Williams, *Chem. Commun.*, 2013, **49**, 11074-11076.
6. E. A. Meulenkamp, *J. Phys. Chem. B*, 1998, **102**, 5566-5572.
7. S. D. Pike, A. García-Trenco, E. R. White, A. H. M. Leung, J. Weiner, M. S. P. Shaffer and C. K. Williams, *Catal. Sci. Technol.*, 2017, **7**, 3842-3850.
8. S. D. Pike, E. R. White, A. Regoutz, N. Sammy, D. J. Payne, C. K. Williams and M. S. Shaffer, *ACS Nano*, 2017, **11**, 2714-2723.
9. A. Sawant, M. K. Ko, V. Parameswaran, S. Lee and C. J. Kulik, *Fuel Sci. Technol. Int.*, 1987, **5**, 77-88.
10. K. L. Orchard, M. S. P. Shaffer and C. K. Williams, *Chem. Mater.*, 2012, **24**, 2443-2448.

Appendix

A. Figures & Tables

Chapter 3: Layered Zinc Hydroxide Monolayers by Hydrolysis of Organozincs

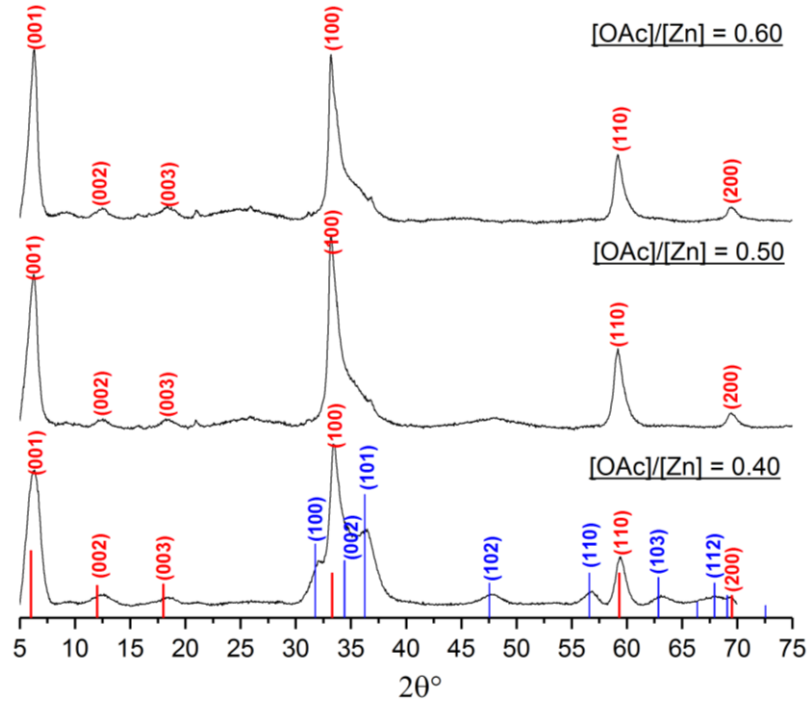

Figure A.1. Stacked XRD patterns of products from different loadings of acetate within the synthesis mixture.

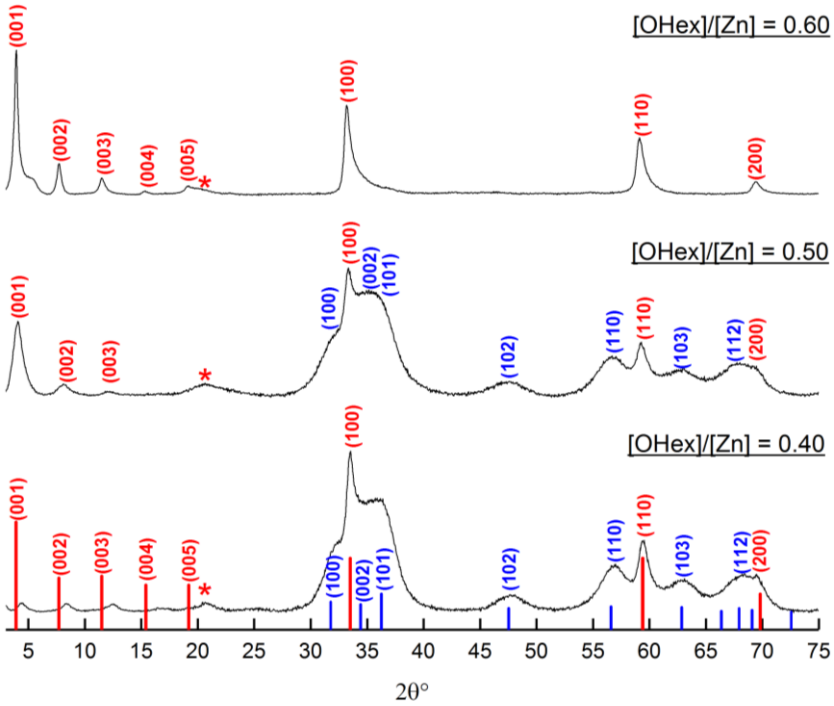

Figure A.2. Stacked XRD patterns of products from different loadings of hexanoate within the synthesis mixture.

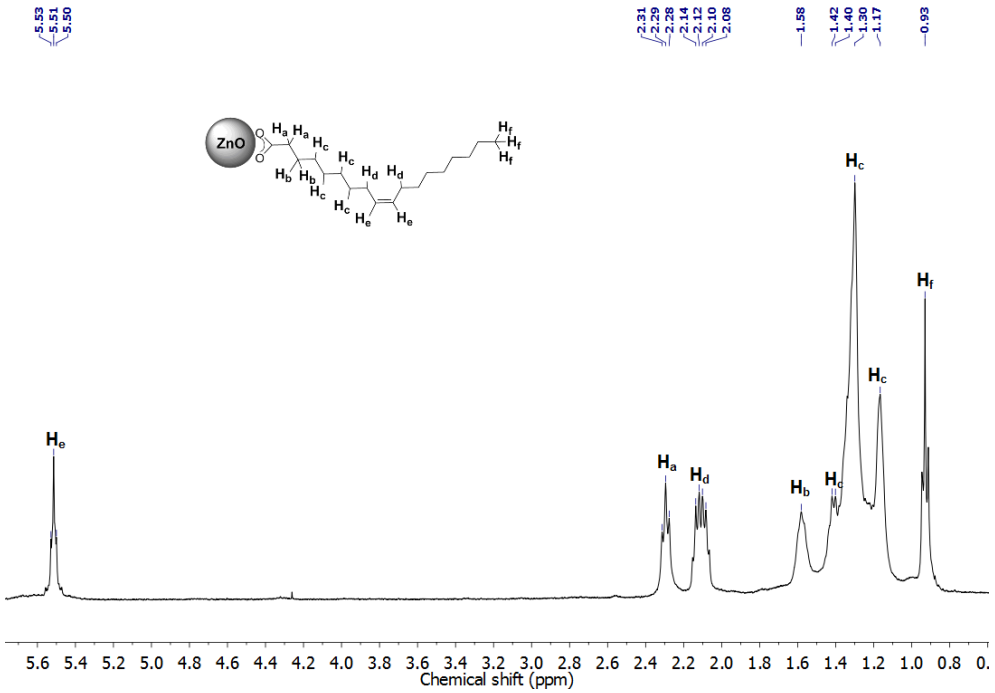

Figure A.3. ^{1}H NMR spectrum (C_6D_6, 400 MHz, 298 K) of ZnO@Ole, with the assignments of protons indicated for the oleate ligand.

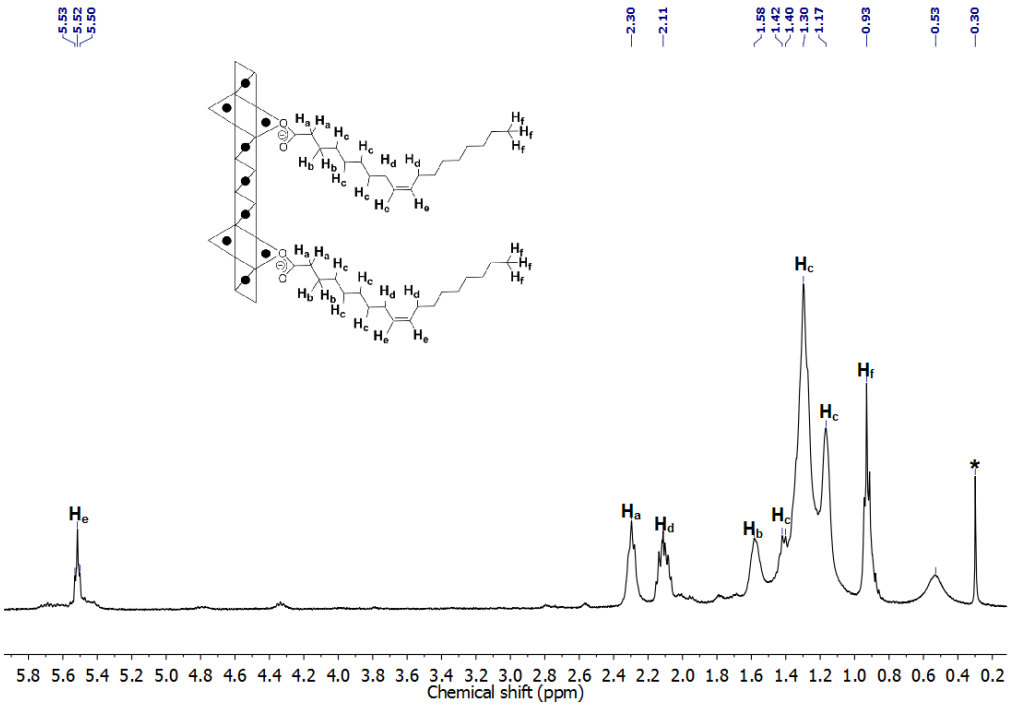

Figure A.4. ^{1}H NMR spectrum (C_6D_6, 400 MHz, 298 K) of LZH–Ole, with the assignments of protons indicated for the oleate ligand.

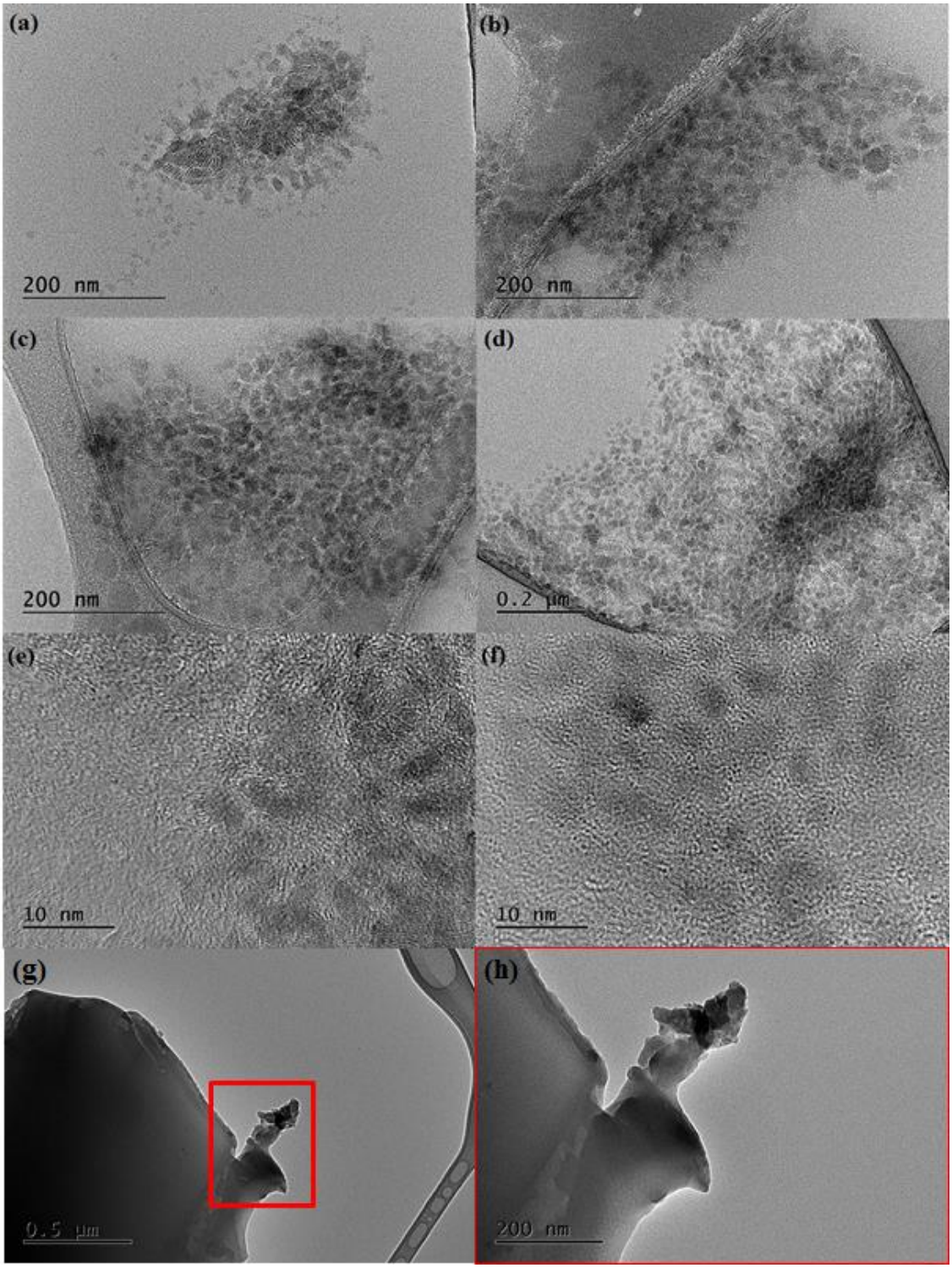

Figure A.5. (a)-(f) TEM images showing the agglomerates exfoliated LZH–Ole nanoplatelets (2 h, stirred in toluene). (g) TEM image of the unexfoliated LZH–Ole (briefly shaken in toluene), with (h) showing the higher magnification of the area highlighted with a red box in (g).

LZH	Basal plane	°2θ	Spacing/ Å
OAc	(001)	6.3	14.1
	(002)	12.6	7.0
	(003)	18.9	4.7
OHex	(001)	3.9	22.7
	(002)	7.7	11.5
	(003)	11.5	7.7
	(004)	15.4	5.8
	(005)	19.2	4.6
ODec	*(001)*	*2.97*	*29.7 ± 0.1*
	(002)	5.9	14.9
	(003)	8.9	9.9
Ole	*(001)*	*1.92*	*45.9 ± 0.8*
	(002)	4.0	22.1
	(003)	5.8	15.2
	(004)	7.6	11.6
	(005)	9.3	9.5
OBz	(001)	4.7	18.9
	(002)	9.3	9.5
	(003)	13.7	6.4
	(004)	18.9	4.7

Table A.1. Table showing the spacing for the planes of LZH–OAc, LZH–OHex, LZH–ODec, LZH–Ole and LZH–OBz. For LZH–Ole, the spacing for (001) is predicted from the (002), (003), (004) and (005) peaks. For LZH–ODec, the spacing of (001) is predicted from the (002) and (003) peaks.

Determining the yield of LZH–Ole

For a synthesis containing 1.366 mmol of Zn and 0.8196 mmol COOR (1:0.6) in total, UV-Vis spectroscopy (above) shows that 20 mol% is in the form of ZnO. Assuming that the remaining Zn (1.093 mmol) are incorporated as x $[Zn_5(OH)_8(COOR)_2]$ + y $Zn(COOR)_2$ two constraints apply:

from Zn balance:

$$5\,x + y = 1.093 \quad (1)$$

and COOR balance:

$$2\,x + 2\,y = 0.8196 \quad (2)$$

Solving these simultaneous equations indicates that there are 0.854 mmol of Zn in LZH, and 0.239 mmol of Zn in $Zn(COOR)_2$, hence the molar yield of LZH-Ole is 62.5 mol% Zn, and the mass content of ZnO is 6.4 wt%.

Species in products	**Molar proportions/ mol% Zn**	**Mass per Zn/ mg**	**Mass proportions in product/ mg**	**wt% in product**
LZH-Ole[a]	62.5	205.1	128.2	50.4
$Zn(Ole)_2$	17.5	627.3	109.8	43.2
ZnO	20.0	81.3	16.3	**6.4**

[a] chemical formula of $[Zn_5(OH)_8(COOR)_2]$

Table A.2. Table showing the estimation of ZnO wt% in the final product from LZH-Ole synthesis.

Attempted Synthesis of LZH with intercalated phosphinates

$ZnEt_2$ (0.169 g, 1.37 mmol) was added dropwise to a suspension of diphenylphosphinic acid (0.178 g, 0.818 mmol) in toluene (9.1 mL). The mixture was stirred for 16 h at room temperature, which yielded a clear solution. Under a flow of N_2, HPLC-grade water (39 µL, 2.18 mmol, 1.6 equiv. to the total moles of Zn of 1.37 mmol) was directly added to the reaction and the mixture was stirred for 3 h, where the formation of white solid was observed after 1 h. All volatiles were removed *in vacuo*, which yielded a fine white powder. Powder XRD pattern indicated no formation of LZHs with the absence of in-plane peaks at 33°, 59° and 70° 2θ.

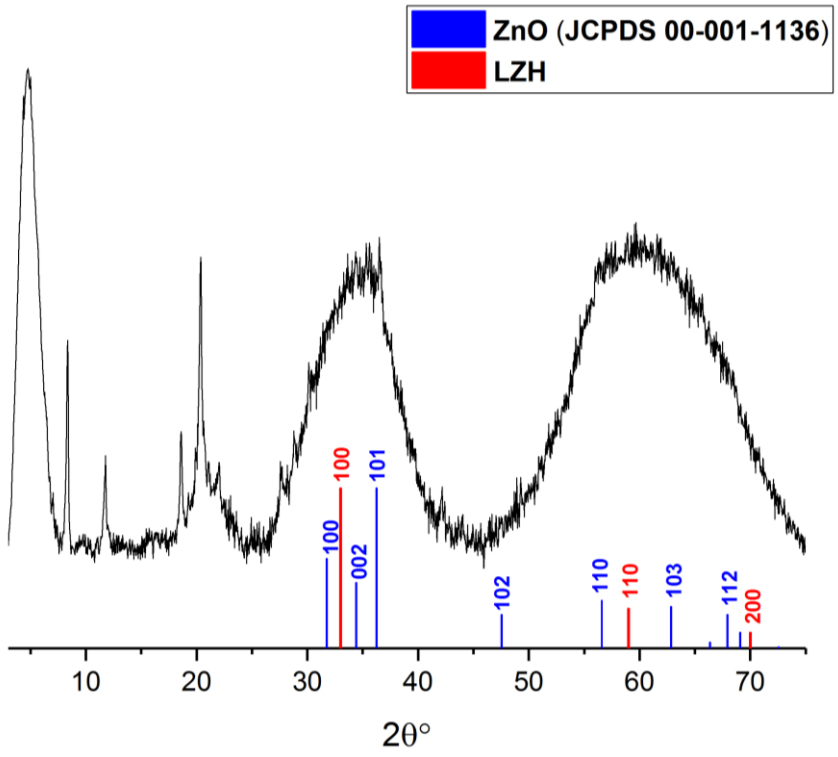

Figure A.6. XRD pattern of the product produced from the hydrolysis of mixture containing $ZnEt_2$ and diphenylphosphinic acid, in toluene. Reference patterns: ZnO (blue, JCPDS 00-001-1136) and LZH (red, taken from Poul *et al.*).[1]

Chapter 5: Colloidal M:ZnO Nanoparticles (M = Mg, Al, Cu) in Hydrogenation of CO_2 to Methanol

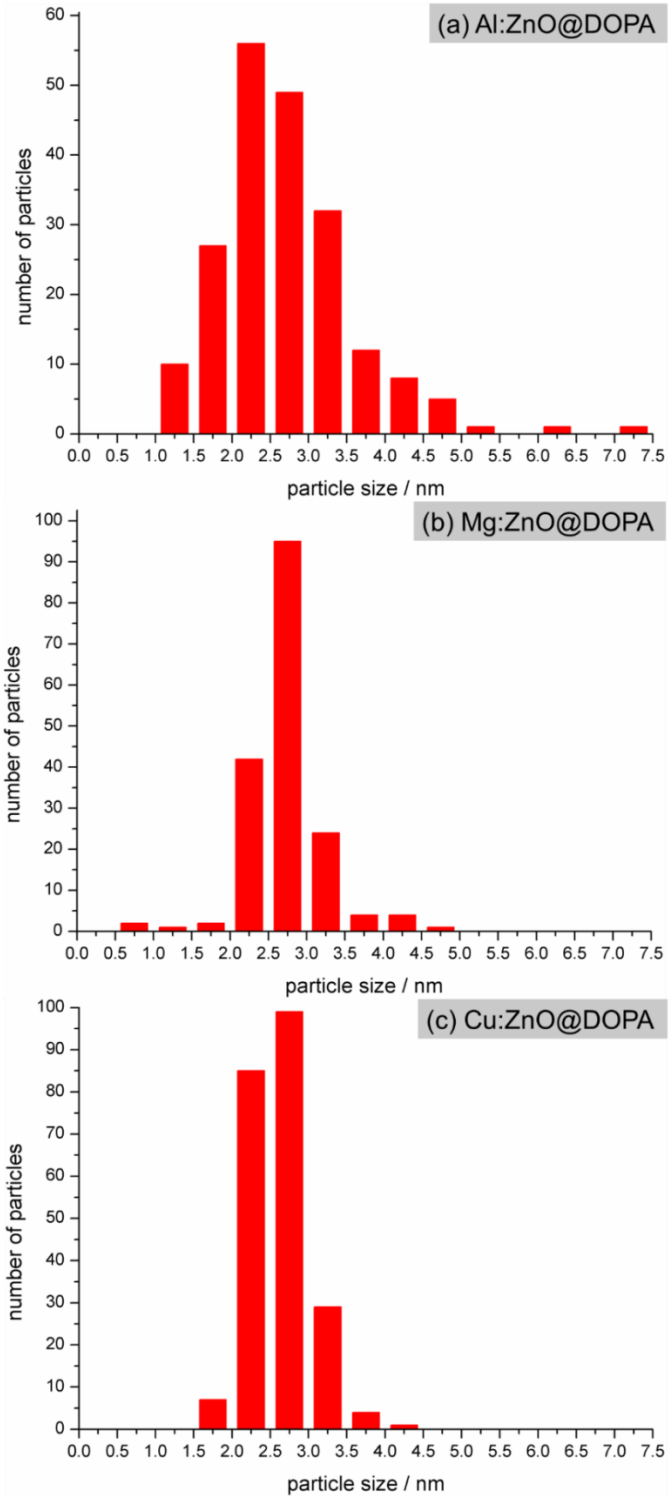

Figure A.7. Particle size distributions, obtained from TEM analysis, of (a) Al:ZnO@DOPA, (b) Mg:ZnO@DOPA and (c) Cu:ZnO@DOPA.

Chapter 7: Experimental

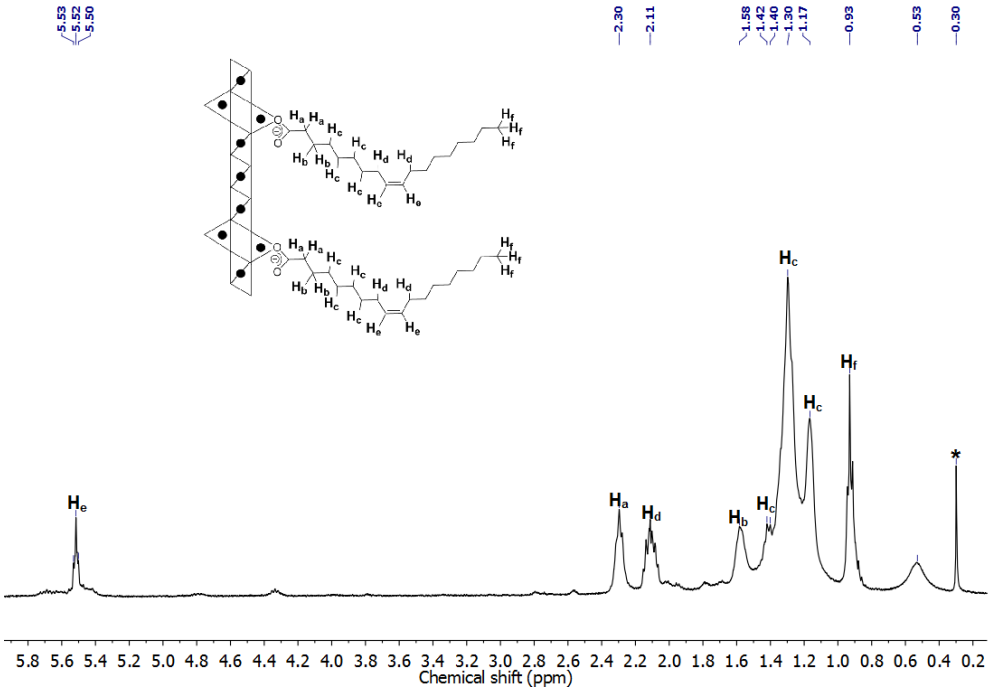

Figure A.8. ^{1}H NMR spectrum (C_6D_6, 400 MHz, 298 K) of LZH–Ole, with the assignments of protons indicated for the oleate ligand.

References

1. L. Poul, N. Jouini and F. Fiévet, *Chem. Mater.*, 2000, **12**, 3123-3132.

B. Licenses for reproducing figures

Article Title	Journal	Type of Use	License
Synthesis of Inorganic–Organic Layered Compounds Using Immiscible Liquid–Liquid Systems under the Distribution Law	*Langmuir, ACS*	Thesis/ Dissertation	*See below*
Layered zinc hydroxide salts: Delamination, preferred orientation of hydroxide lamellae, and formation of ZnO nanodiscs	*J. Colloid Interface Sci., Elsevier*	Thesis/ Dissertation	4225460538484
Synthesis, Anion Exchange, and Delamination of Co–Al Layered Double Hydroxide: Assembly of the Exfoliated Nanosheet/Polyanion Composite Films and Magneto-Optical Studies	*J. Am. Chem. Soc., ACS*	Thesis/ Dissertation	*See below*
A Generalized Three-Stage Mechanism of ZnO Nanoparticle Formation in Homogeneous Liquid Medium	*J. Phys. Chem. C, ACS*	Thesis/ Dissertation	*See below*
Theory, Production and Mechanism of Monodispersed Hydrosols	*J. Am. Chem. Soc., ACS*	Thesis/ Dissertation	*See below*
Oriented Attachment of ZnO Nanocrystals	*J. Phys. Chem. C, ACS*	Thesis/ Dissertation	*See below*
Performance Improvement of Nanocatalysts by Promoter-Induced Defects in the Support Material: Methanol Synthesis over Cu/ZnO:Al	*J. Am. Chem. Soc., ACS*	Thesis/ Dissertation	*See below*
The Cu–ZnO synergy in methanol synthesis Part 3: Impact of the composition of a selective Cu@ZnO_x core–shell catalyst on methanol rate explained by experimental studies and a concentric spheres model	*J. Catal., Elsevier*	Thesis/ Dissertation	4325930898831

Article Title	Journal	Type of Use	License
Promoting Strong Metal Support Interaction: Doping ZnO for Enhanced Activity of Cu/ZnO:M (M = Al, Ga, Mg) Catalysts	*ACS Catal., ACS*	Thesis/ Dissertation	*See below*
Chemistry of Colloidal Doped Nanocrystals	*Chem. Mater., ACS*	Thesis/ Dissertation	*See below*
tert-Butylzinc hydroxide as an efficient predesigned precursor of ZnO nanoparticles	*Chem. Commun., RSC*	Thesis/ Dissertation	4365910883891
Nucleation and Growth of ZnO in Organic Solvents - an in Situ Study	*J. Am. Chem. Soc., ACS*	Thesis/ Dissertation	*See below*
Liquid crystal based on hybrid zinc oxide nanoparticles	*J. Mater. Chem., RSC*	Thesis/ Dissertation	*4366530005907*
An Alternative of CdSe Nanocrystal Emitters: Pure and Tunable Impurity Emissions in ZnSe Nanocrystals	*J. Am. Chem. Soc., ACS*	Thesis/ Dissertation	*See below*
Tunable Infrared Absorption and Visible Transparency of Colloidal Aluminum-Doped Zinc Oxide Nanocrystals	*Nano Lett., ACS*	Thesis/ Dissertation	*See below*
Temperature Dependence of "Elementary Processes" in Doping Semiconductor Nanocrystals	*J. am. Chem. Soc., ACS*	Thesis/ Dissertation	*See below*

Table B.1. Table of licenses and permission for copyrighted figures in publications.

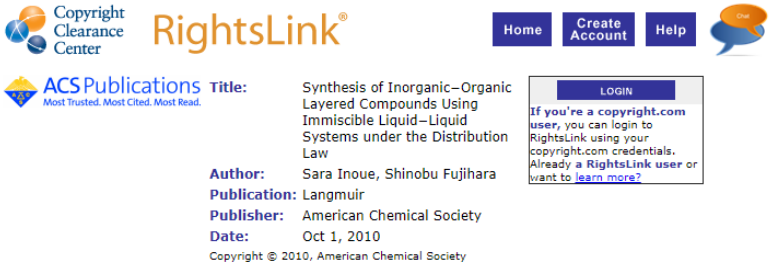

Copyright Clearance Center RightsLink®

Home | Create Account | Help

ACS Publications Most Trusted. Most Cited. Most Read.

Title: Synthesis of Inorganic–Organic Layered Compounds Using Immiscible Liquid–Liquid Systems under the Distribution Law

Author: Sara Inoue, Shinobu Fujihara

Publication: Langmuir

Publisher: American Chemical Society

Date: Oct 1, 2010

Copyright © 2010, American Chemical Society

LOGIN

If you're a copyright.com user, you can login to RightsLink using your copyright.com credentials. Already a RightsLink user or want to learn more?

PERMISSION/LICENSE IS GRANTED FOR YOUR ORDER AT NO CHARGE

This type of permission/license, instead of the standard Terms & Conditions, is sent to you because no fee is being charged for your order. Please note the following:

- Permission is granted for your request in both print and electronic formats, and translations.
- If figures and/or tables were requested, they may be adapted or used in part.
- Please print this page for your records and send a copy of it to your publisher/graduate school.
- Appropriate credit for the requested material should be given as follows: "Reprinted (adapted) with permission from (COMPLETE REFERENCE CITATION). Copyright (YEAR) American Chemical Society." Insert appropriate information in place of the capitalized words.
- One-time permission is granted only for the use specified in your request. No additional uses are granted (such as derivative works or other editions). For any other uses, please submit a new request.

If credit is given to another source for the material you requested, permission must be obtained from that source.

BACK | CLOSE WINDOW

Copyright Clearance Center RightsLink®

Home | Create Account | Help

ACS Publications Most Trusted. Most Cited. Most Read.

Title: Synthesis, Anion Exchange, and Delamination of Co–Al Layered Double Hydroxide: Assembly of the Exfoliated Nanosheet/Polyanion Composite Films and Magneto-Optical Studies

Author: Zhaoping Liu, Renzhi Ma, Minoru Osada, et al

Publication: Journal of the American Chemical Society

Publisher: American Chemical Society

Date: Apr 1, 2006

Copyright © 2006, American Chemical Society

LOGIN

If you're a copyright.com user, you can login to RightsLink using your copyright.com credentials. Already a RightsLink user or want to learn more?

PERMISSION/LICENSE IS GRANTED FOR YOUR ORDER AT NO CHARGE

This type of permission/license, instead of the standard Terms & Conditions, is sent to you because no fee is being charged for your order. Please note the following:

- Permission is granted for your request in both print and electronic formats, and translations.
- If figures and/or tables were requested, they may be adapted or used in part.
- Please print this page for your records and send a copy of it to your publisher/graduate school.
- Appropriate credit for the requested material should be given as follows: "Reprinted (adapted) with permission from (COMPLETE REFERENCE CITATION). Copyright (YEAR) American Chemical Society." Insert appropriate information in place of the capitalized words.
- One-time permission is granted only for the use specified in your request. No additional uses are granted (such as derivative works or other editions). For any other uses, please submit a new request.

If credit is given to another source for the material you requested, permission must be obtained from that source.

BACK | CLOSE WINDOW

Title: A Generalized Three-Stage Mechanism of ZnO Nanoparticle Formation in Homogeneous Liquid Medium

Author: Arunasish Layek, Gargi Mishra, Archana Sharma, et al

Publication: The Journal of Physical Chemistry C

Publisher: American Chemical Society

Date: Nov 1, 2012

PERMISSION/LICENSE IS GRANTED FOR YOUR ORDER AT NO CHARGE

This type of permission/license, instead of the standard Terms & Conditions, is sent to you because no fee is being charged for your order. Please note the following:

- Permission is granted for your request in both print and electronic formats, and translations.
- If figures and/or tables were requested, they may be adapted or used in part.
- Please print this page for your records and send a copy of it to your publisher/graduate school.
- Appropriate credit for the requested material should be given as follows: "Reprinted (adapted) with permission from (COMPLETE REFERENCE CITATION). Copyright (YEAR) American Chemical Society." Insert appropriate information in place of the capitalized words.
- One-time permission is granted only for the use specified in your request. No additional uses are granted (such as derivative works or other editions). For any other uses, please submit a new request.

If credit is given to another source for the material you requested, permission must be obtained from that source.

Title: Theory, Production and Mechanism of Formation of Monodispersed Hydrosols

Author: Victor K. LaMer, Robert H. Dinegar

Publication: Journal of the American Chemical Society

Publisher: American Chemical Society

Date: Nov 1, 1950

PERMISSION/LICENSE IS GRANTED FOR YOUR ORDER AT NO CHARGE

This type of permission/license, instead of the standard Terms & Conditions, is sent to you because no fee is being charged for your order. Please note the following:

- Permission is granted for your request in both print and electronic formats, and translations.
- If figures and/or tables were requested, they may be adapted or used in part.
- Please print this page for your records and send a copy of it to your publisher/graduate school.
- Appropriate credit for the requested material should be given as follows: "Reprinted (adapted) with permission from (COMPLETE REFERENCE CITATION). Copyright (YEAR) American Chemical Society." Insert appropriate information in place of the capitalized words.
- One-time permission is granted only for the use specified in your request. No additional uses are granted (such as derivative works or other editions). For any other uses, please submit a new request.

If credit is given to another source for the material you requested, permission must be obtained from that source.

Title: Oriented Attachment of ZnO Nanocrystals

Author: Dimitri Hapiuk, B. Masenelli, Karine Masenelli-Varlot, et al

Publication: The Journal of Physical Chemistry C

Publisher: American Chemical Society

Date: May 1, 2013

PERMISSION/LICENSE IS GRANTED FOR YOUR ORDER AT NO CHARGE

This type of permission/license, instead of the standard Terms & Conditions, is sent to you because no fee is being charged for your order. Please note the following:

- Permission is granted for your request in both print and electronic formats, and translations.
- If figures and/or tables were requested, they may be adapted or used in part.
- Please print this page for your records and send a copy of it to your publisher/graduate school.
- Appropriate credit for the requested material should be given as follows: "Reprinted (adapted) with permission from (COMPLETE REFERENCE CITATION). Copyright (YEAR) American Chemical Society." Insert appropriate information in place of the capitalized words.
- One-time permission is granted only for the use specified in your request. No additional uses are granted (such as derivative works or other editions). For any other uses, please submit a new request.

If credit is given to another source for the material you requested, permission must be obtained from that source.

Title: Performance Improvement of Nanocatalysts by Promoter-Induced Defects in the Support Material: Methanol Synthesis over Cu/ZnO:Al

Author: Malte Behrens, Stefan Zander, Patrick Kurr, et al

Publication: Journal of the American Chemical Society

Publisher: American Chemical Society

Date: Apr 1, 2013

PERMISSION/LICENSE IS GRANTED FOR YOUR ORDER AT NO CHARGE

This type of permission/license, instead of the standard Terms & Conditions, is sent to you because no fee is being charged for your order. Please note the following:

- Permission is granted for your request in both print and electronic formats, and translations.
- If figures and/or tables were requested, they may be adapted or used in part.
- Please print this page for your records and send a copy of it to your publisher/graduate school.
- Appropriate credit for the requested material should be given as follows: "Reprinted (adapted) with permission from (COMPLETE REFERENCE CITATION). Copyright (YEAR) American Chemical Society." Insert appropriate information in place of the capitalized words.
- One-time permission is granted only for the use specified in your request. No additional uses are granted (such as derivative works or other editions). For any other uses, please submit a new request.

If credit is given to another source for the material you requested, permission must be obtained from that source.

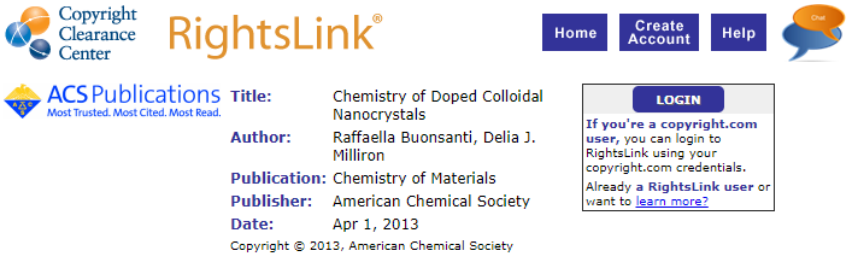

Copyright Clearance Center RightsLink®

Home | Create Account | Help

ACS Publications Most Trusted. Most Cited. Most Read.

Title: Chemistry of Doped Colloidal Nanocrystals
Author: Raffaella Buonsanti, Delia J. Milliron
Publication: Chemistry of Materials
Publisher: American Chemical Society
Date: Apr 1, 2013
Copyright © 2013, American Chemical Society

LOGIN
If you're a copyright.com user, you can login to RightsLink using your copyright.com credentials.
Already a RightsLink user or want to learn more?

PERMISSION/LICENSE IS GRANTED FOR YOUR ORDER AT NO CHARGE

This type of permission/license, instead of the standard Terms & Conditions, is sent to you because no fee is being charged for your order. Please note the following:

- Permission is granted for your request in both print and electronic formats, and translations.
- If figures and/or tables were requested, they may be adapted or used in part.
- Please print this page for your records and send a copy of it to your publisher/graduate school.
- Appropriate credit for the requested material should be given as follows: "Reprinted (adapted) with permission from (COMPLETE REFERENCE CITATION). Copyright (YEAR) American Chemical Society." Insert appropriate information in place of the capitalized words.
- One-time permission is granted only for the use specified in your request. No additional uses are granted (such as derivative works or other editions). For any other uses, please submit a new request.

If credit is given to another source for the material you requested, permission must be obtained from that source.

BACK | CLOSE WINDOW

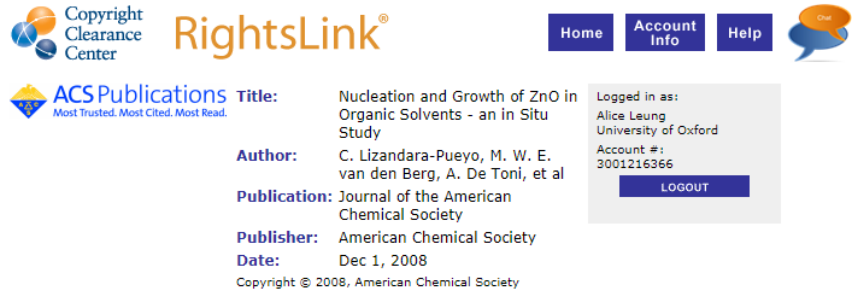

Copyright Clearance Center RightsLink®

Home | Account Info | Help

ACS Publications Most Trusted. Most Cited. Most Read.

Title: Nucleation and Growth of ZnO in Organic Solvents - an in Situ Study
Author: C. Lizandara-Pueyo, M. W. E. van den Berg, A. De Toni, et al
Publication: Journal of the American Chemical Society
Publisher: American Chemical Society
Date: Dec 1, 2008
Copyright © 2008, American Chemical Society

Logged in as:
Alice Leung
University of Oxford
Account #: 3001216366
LOGOUT

PERMISSION/LICENSE IS GRANTED FOR YOUR ORDER AT NO CHARGE

This type of permission/license, instead of the standard Terms & Conditions, is sent to you because no fee is being charged for your order. Please note the following:

- Permission is granted for your request in both print and electronic formats, and translations.
- If figures and/or tables were requested, they may be adapted or used in part.
- Please print this page for your records and send a copy of it to your publisher/graduate school.
- Appropriate credit for the requested material should be given as follows: "Reprinted (adapted) with permission from (COMPLETE REFERENCE CITATION). Copyright (YEAR) American Chemical Society." Insert appropriate information in place of the capitalized words.
- One-time permission is granted only for the use specified in your request. No additional uses are granted (such as derivative works or other editions). For any other uses, please submit a new request.

If credit is given to another source for the material you requested, permission must be obtained from that source.

BACK | CLOSE WINDOW

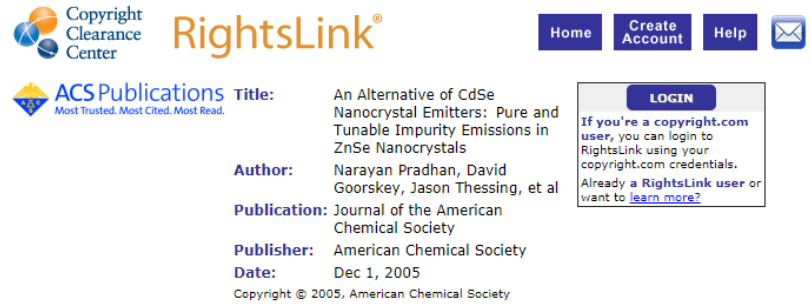

Copyright Clearance Center RightsLink®

Home | Create Account | Help

ACS Publications Most Trusted. Most Cited. Most Read.

Title: An Alternative of CdSe Nanocrystal Emitters: Pure and Tunable Impurity Emissions in ZnSe Nanocrystals

Author: Narayan Pradhan, David Goorskey, Jason Thessing, et al

Publication: Journal of the American Chemical Society

Publisher: American Chemical Society

Date: Dec 1, 2005

Copyright © 2005, American Chemical Society

LOGIN

If you're a copyright.com user, you can login to RightsLink using your copyright.com credentials.

Already a RightsLink user or want to learn more?

PERMISSION/LICENSE IS GRANTED FOR YOUR ORDER AT NO CHARGE

This type of permission/license, instead of the standard Terms & Conditions, is sent to you because no fee is being charged for your order. Please note the following:

- Permission is granted for your request in both print and electronic formats, and translations.
- If figures and/or tables were requested, they may be adapted or used in part.
- Please print this page for your records and send a copy of it to your publisher/graduate school.
- Appropriate credit for the requested material should be given as follows: "Reprinted (adapted) with permission from (COMPLETE REFERENCE CITATION). Copyright (YEAR) American Chemical Society." Insert appropriate information in place of the capitalized words.
- One-time permission is granted only for the use specified in your request. No additional uses are granted (such as derivative works or other editions). For any other uses, please submit a new request.

If credit is given to another source for the material you requested, permission must be obtained from that source.

BACK | CLOSE WINDOW

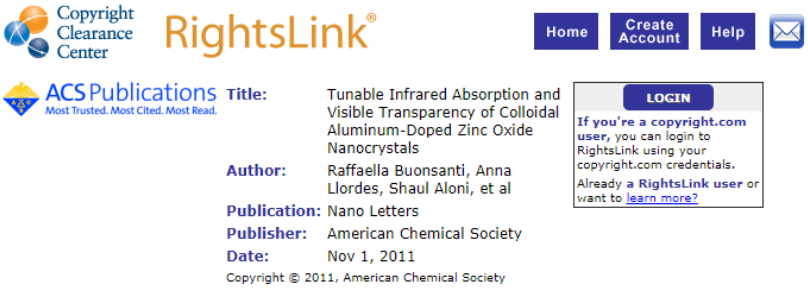

Copyright Clearance Center RightsLink®

Home | Create Account | Help

ACS Publications Most Trusted. Most Cited. Most Read.

Title: Tunable Infrared Absorption and Visible Transparency of Colloidal Aluminum-Doped Zinc Oxide Nanocrystals

Author: Raffaella Buonsanti, Anna Llordes, Shaul Aloni, et al

Publication: Nano Letters

Publisher: American Chemical Society

Date: Nov 1, 2011

Copyright © 2011, American Chemical Society

LOGIN

If you're a copyright.com user, you can login to RightsLink using your copyright.com credentials.

Already a RightsLink user or want to learn more?

PERMISSION/LICENSE IS GRANTED FOR YOUR ORDER AT NO CHARGE

This type of permission/license, instead of the standard Terms & Conditions, is sent to you because no fee is being charged for your order. Please note the following:

- Permission is granted for your request in both print and electronic formats, and translations.
- If figures and/or tables were requested, they may be adapted or used in part.
- Please print this page for your records and send a copy of it to your publisher/graduate school.
- Appropriate credit for the requested material should be given as follows: "Reprinted (adapted) with permission from (COMPLETE REFERENCE CITATION). Copyright (YEAR) American Chemical Society." Insert appropriate information in place of the capitalized words.
- One-time permission is granted only for the use specified in your request. No additional uses are granted (such as derivative works or other editions). For any other uses, please submit a new request.

If credit is given to another source for the material you requested, permission must be obtained from that source.

BACK | CLOSE WINDOW

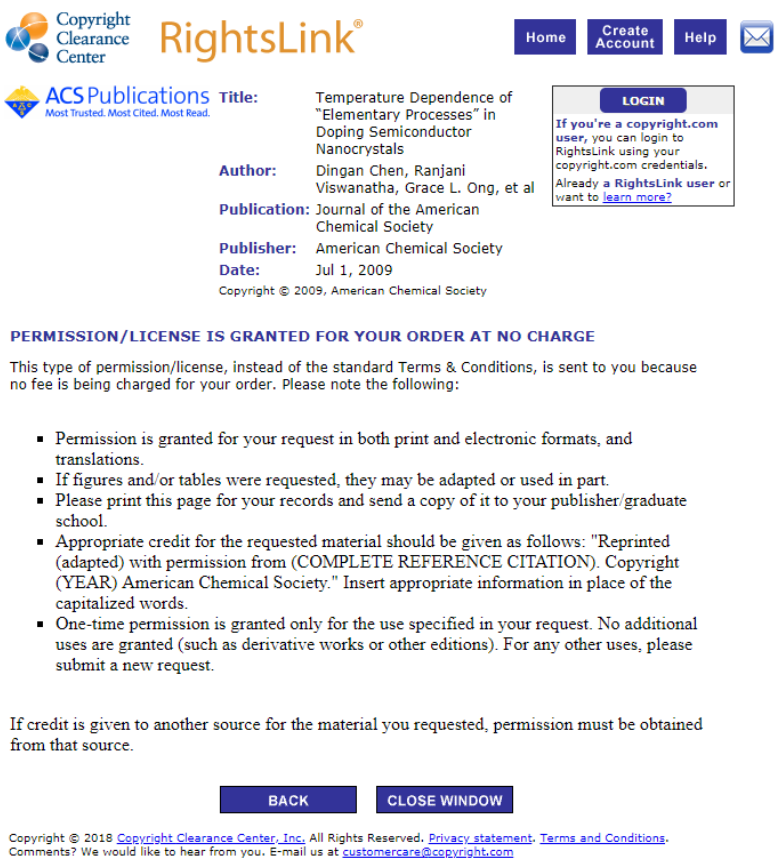

Copyright Clearance Center RightsLink®

Home | Create Account | Help

ACS Publications
Most Trusted. Most Cited. Most Read.

Title: Temperature Dependence of "Elementary Processes" in Doping Semiconductor Nanocrystals

Author: Dingan Chen, Ranjani Viswanatha, Grace L. Ong, et al

Publication: Journal of the American Chemical Society

Publisher: American Chemical Society

Date: Jul 1, 2009

Copyright © 2009, American Chemical Society

LOGIN

If you're a copyright.com user, you can login to RightsLink using your copyright.com credentials.

Already a RightsLink user or want to learn more?

PERMISSION/LICENSE IS GRANTED FOR YOUR ORDER AT NO CHARGE

This type of permission/license, instead of the standard Terms & Conditions, is sent to you because no fee is being charged for your order. Please note the following:

- Permission is granted for your request in both print and electronic formats, and translations.
- If figures and/or tables were requested, they may be adapted or used in part.
- Please print this page for your records and send a copy of it to your publisher/graduate school.
- Appropriate credit for the requested material should be given as follows: "Reprinted (adapted) with permission from (COMPLETE REFERENCE CITATION). Copyright (YEAR) American Chemical Society." Insert appropriate information in place of the capitalized words.
- One-time permission is granted only for the use specified in your request. No additional uses are granted (such as derivative works or other editions). For any other uses, please submit a new request.

If credit is given to another source for the material you requested, permission must be obtained from that source.

BACK | CLOSE WINDOW

Copyright © 2018 Copyright Clearance Center, Inc. All Rights Reserved. Privacy statement. Terms and Conditions.
Comments? We would like to hear from you. E-mail us at customercare@copyright.com